Muon signatures in ATLAS

A search for new physics in $\mu^{\pm}\mu^{\pm}$ events

Nicole Manuela Ruckstuhl

Dutch title: Muon signalen in ATLAS
Een zoektocht naar nieuwe fysica in $\mu^{\pm}\mu^{\pm}$
Cover: Bakabaka Design www.bakabaka.nl
Drawing by Esther van Rijnstra
Print: Wöhrmann Print Service Zutphen
ISBN: 978-94-6203-062-6

FOM

NWO
Netherlands Organisation for Scientific Research

This work is part of the research program of the Foundation for Fundamental Research on Matter (FOM), which is part of the Netherlands Organization for Scientific Research (NWO). The research has been supported by VIDI grant 680-47-219 of Dr. I.B. van Vulpen.

Muon signatures in ATLAS

A search for new physics in $\mu^{\pm}\mu^{\pm}$ events

ACADEMISCH PROEFSCHRIFT

ter verkrijging van de graad van doctor
aan de Universiteit van Amsterdam
op gezag van de Rector Magnificus
prof. dr. D.C. van den Boom
ten overstaan van een door het college van promoties ingestelde
commissie, in het openbaar te verdedigen in de Agnietenkapel
op donderdag 28 juni 2012, te 16:00 uur

door

Nicole Manuela Ruckstuhl

geboren te Los Angeles, Verenigde Staten van Amerika

Promotor:	Prof. dr. S.C.M. Bentvelsen
Co-Promotor:	Dr. I.B. van Vulpen
Overige leden:	Prof. dr. ir. E.N. Koffeman
	Prof. dr. ir. P.J. de Jong
	Prof. dr. E.L.M.P. Laenen
	Prof. dr. M.H.M. Merk
	Dr. ir. P.M. Kluit
	Dr. S. Caron
	Dr. G. Salamanna

Faculteit der Natuurwetenschappen, Wiskunde en Informatica

Contents

Introduction

To understand the universe around us, it is important to know the characteristics of all the fundamental building blocks of matter as well as their interactions. Our current knowledge of these elementary particles is contained within the Standard Model [1–3].

The Standard Model of particle physics was first established in the 1960's. In the last 50 years it has been thoroughly tested using a wide range of experimental data. This includes the discovery of predicted particles, such as the W- and Z-boson and the top quark, but also the measurement of interaction rates between the elementary particles. At present, the only particle of the Standard Model which has not been experimentally verified is the Higgs-boson, although current results at the LHC show indications of a Higgs-boson-like particle with a mass of approximately 125 GeV [4–6].

Although the Standard Model is able to correctly describe and predict all currently measured particle interactions and properties there is some indirect evidence for physics beyond the Standard Model. The most famous evidence is provided by astronomical observations that indicate that only 17% of the mass of the universe consists of known visible matter [7]. The remaining 83% are referred to as dark matter. As none of the Standard Model particles can account for all this dark matter, the vast majority of the mass of the universe should consist of new non-Standard Model particles.

One way to obtain direct evidence of such new elementary particles is to try to create them in controlled high energy particle collisions using a particle accelerator. A wide range of such accelerators has been built, varying greatly in the maximum possible collision energy, the collision rate and the types of particles colliding. As so far no evidence for physics beyond the Standard Model has been found at any of these accelerators, strong limits can be set on the properties of possible new particles. However, as the collisions must create sufficient energy to produce such new particles, the detection and exclusion range of accelerators is always limited to particles with a mass smaller than the collision energy. For direct searches of new particles, it is therefore important to study collisions with as high energy as possible.

At present the most powerful accelerator in the world is the Large Hadron Collider (LHC) which has collided protons with a center of mass energy of 7 TeV. This is more than 3.5 times the maximum energy of any other accelerator. In this thesis we study such collisions at the LHC, detected using the ATLAS detector, to search for evidence of new heavy particles.

The expected signature for physics beyond the Standard Model in ATLAS depends strongly on the properties of these new particles. Many theoretical extensions of the Standard Model have been proposed predicting a wide range of such new particles, most of which are expected to decay before reaching the detector. These particles can therefore only be discovered through their decay products. In this thesis we focus exclusively on one possible decay product, the muon, which is experimentally relatively easy to identify.

Multiple processes can lead to the production of muons at the LHC. As our main goal is to search for new physics particles, which typically decay before propagating a significant distance, we are searching for muons produced at the interaction point, called prompt muons. While many particles can decay to muons, only a few Standard Model particles can result in the creation of prompt muons: top quarks, W-bosons, Z-bosons and off-shell photons[1]. Pairs of prompt muons are even more rare and can only be produced in the decay of Z-bosons and off-shell photons, or in collision events containing at least two different decay chains, such as W^+W^- production. As most such production processes create a particle anti-particle pair, with one resulting in the production of a muon and the other with an anti-muon, and since both the Z-boson and photon are electrically neutral, the vast majority of prompt muon pairs produced in ATLAS consists of muons with opposite electric charge.

Prompt muon pairs with equal electric charge, same-sign muons, are, according to the Standard Model, almost exclusively produced in ZZ and ZW events, both with a relatively small cross-section. On the other hand, a wide range of physics theories beyond the Standard Model predict additional signatures of prompt same-sign muon pairs in ATLAS which, in some cases, have a production rate similar or even larger than predicted by the Standard Model. The main goal of this thesis is to determine the cross-section for prompt same-sign muon pairs in ATLAS and compare it with the Standard Model expectation, in the hope of finding evidence for physics beyond the Standard Model.

Outline

In Chapter 1 we describe the Standard Model of particle physics as well as a possible extension in the form of supersymmetry and use it to motivate our search for prompt same-sign muon pairs. This search is performed using data provided by the LHC and collected by the ATLAS detector, both of which are discussed in Chapter 2 including a description of the ATLAS trigger, reconstruction and simulation software used in the rest of the thesis. Together, Chapter 1 and 2 should provide all relevant background information necessary to understand the analyses presented in this thesis.

In Chapter 3 we study the muon reconstruction performance of ATLAS, specifically the muon momentum scale and resolution during the first few months of data-taking. One of the particularities of the analysis in Chapter 3 is that we need to separate the contribution from muons from pion and kaon decays to that of other muons. This is done using a template fitting method. In Chapter 4 we use a slightly modified version of this method to study the contribution of muons from pion and kaon decays to the invariant mass distribution of muon pairs in ATLAS.

As we are interested in prompt muon pairs, we furthermore need to be able to separate prompt muons from muons produced in the decay of b- and c-quarks and taus. This is

[1]The Higgs-boson would also be capable of producing prompt muons. However, even if the Higgs-boson exists, the corresponding cross-section is too small to affect the results in this thesis.

achieved using a different template fitting method, exploiting the difference in impact parameter distributions between the considered muon types. This method is described and validated in Chapter 5.

In Chapter 6 we use the methods developed in the earlier chapters to determine the inclusive prompt same-sign muon cross-section in ATLAS, which we compare with the Standard Model predictions. The results of this analysis are also interpreted in terms of exclusion limits for a simplified supersymmetric model.

Chapter 1

From the Standard Model to supersymmetry

One of the main goals in this thesis is to search for physics beyond the Standard Model by looking for anomalous same-sign dimuon signatures in ATLAS. In this chapter we motivate our search for such signatures by introducing one possible extension to the Standard Model of elementary particles, called supersymmetry (SUSY) [8–10].

The Standard Model (SM) [1–3] describes all elementary particles known today as well as their interactions under the strong, the electromagnetic and the weak force. Many of the properties of this model, including the interactions between particles, are coupled to symmetries of the theory. This is described in Section 1.1, including how part of this symmetry is broken by the so-called Higgs-mechanism. Although no direct evidence of physics beyond the SM has been found yet, some open questions remain. Some of these questions can be answered by introducing an additional symmetry, supersymmetry, to the SM. The exact form of this symmetry, as well as its consequences in terms of new particles and their interactions is described in Section 1.2.

The expected signatures from SUSY particles at a proton-proton collider such as the Large Hadron Collider (LHC)[1] are discussed in Section 1.3, focussing specifically on same-sign muon pair production.

1.1 The Standard Model

1.1.1 Introduction

Before providing a more thorough description of the SM in terms of symmetries, we first give a general introduction to the particles and forces of the SM and the relevant quantum numbers involved.

[1]The LHC is introduced in Chapter 2.

Particles of the Standard Model

The particles of the SM can be separated into two groups depending on their spin. The first group, the fermions, have half integer spin and are the building blocks of matter. The bosons, which have integer spin, mediate the forces of natures.

The fermions can be classified into three families of four particles. Each family is similar to the other two, except for the masses of the particles. The first family contains two quarks, the up- and down-quark (u and d), and two leptons, the electron (e^-) and the electron-neutrino (ν_e). The up- and down-quarks bind together to form protons and neutrons which, together with the electrons, form the atoms. All matter around us consists of these three types of particles. The electron-neutrino is a neutral, almost massless particle that interacts only weakly with other particles.

The second family consists of the charm- and strange-quark (c and s), the muon (μ^-) and the muon-neutrino (ν_μ) while the third family contains the top- and bottom-quark (t and b), the tau (τ^-) and the tau-neutrino (ν_τ).

All fermions except for the neutrinos come in two helicity states, known as left- and right-handed particles. The left-handed leptons and quarks of each family are grouped in doublets which interact together under part of the electroweak force.

Apart from the electric charge each quark also carries colour charge; a quantum number with three charges, generally named red, blue and green. This means that each type of quarks come in three colour flavours.

In addition to the fermions, the SM also contains bosons. The photon (γ), the Z-boson (Z), two charged W-bosons (W^+, W^-) and the gluon (g) mediate the three forces of the SM. The gluon carries a colour and anti-colour charge and comes in eight different colour combinations. The last boson of the SM is called the Higgs-boson (H) and is necessary to generate mass for the other particles (see Section 1.1.3).

The particles of the SM are listed in Table 1.1.

In addition to the particles mentioned above, each fermion has an anti-particle with exactly the same mass, but opposite charge (electric and colour) and helicity. There are two ways to denote anti-particles. The first is by writing the electric charge of the particle as a superscript. The anti-particle of the electron e^-, the positron, is denoted by e^+. This method is generally only used for particles with unit charge. The other notation is to add a bar on the symbol of the particle. For example, the anti-top-quark is denoted by $\bar{t}$.

In principle the bosons also have anti-particles however this does not introduce any new particles. The photon, Z-boson and Higgs-boson are their own anti-particles. The two charged W-bosons are each-others anti-particles, as are the eight gluons.

Forces of the Standard Model

Within the SM, forces are mediated through the exchange of bosons. Three of the four fundamental forces of nature have successfully been incorporated into the SM. The weakest force, gravity, would be mediated by the so-called graviton, however no successful quantum description of gravity exists at present. As gravity is, for distances smaller than the size of an atom, many orders of magnitude weaker than the other three forces, it is not relevant in the field of high energy physics.

	Particles			Spin	Electric charge	Hyper-charge	Colour
Quarks	$(u,d)_L$	$(c,s)_L$	$(t,b)_L$	$(\frac{1}{2},\frac{1}{2})$	$(\frac{2}{3},-\frac{1}{3})$	$\frac{1}{3}$	Yes
	u_R	c_R	t_R	$\frac{1}{2}$	$\frac{2}{3}$	$\frac{4}{3}$	Yes
	d_R	s_R	b_R	$\frac{1}{2}$	$-\frac{1}{3}$	$-\frac{2}{3}$	Yes
Leptons	$(\nu_e,e^-)_L$	$(\nu_\mu,\mu^-)_L$	$(\nu_\tau,\tau^-)_L$	$(\frac{1}{2},\frac{1}{2})$	(0,-1)	-1	No
	e_R^-	μ_R^-	τ_R^-	$\frac{1}{2}$	-1	-2	No
Bosons	g			1	0	0	Yes
	$W^\pm$ and Z			1	± 1 and 0	0	No
	γ			1	0	0	No
	H			0	0	1	No

Table 1.1: The particles of the Standard Model, listed with their spin, electric charge, hypercharge and colour charges. The subscripts L and R denote left- and right-handedness respectively. We note that the quarks carry colour charge and thus also come in three different colours. The gluon has eight different colour states.

The three forces of the SM are: the strong force, the electromagnetic force and the weak force.

- **The strong force** is mediated by gluons (g), massless particles which couple to colour charge. The strong force therefore only affects quarks and gluons, while leptons and the other SM bosons are unaffected. It is responsible for binding quarks into nuclei.

- **The electromagnetic force** is mediated through the photon (γ). The photon is a massless, neutral particle which couples to the electric charge and therefore does not affect neutral particles.

- **The weak force** is mediated by the neutral Z- and charged W-bosons (Z, W^+, W^-). These bosons are massive and can decay. The consequence of this is that the weak force has a limited range of the order of hundredths of fermi.

1.1.2 Symmetries of the Standard Model

The three forces of the SM follow directly from imposing a set of specific local gauge symmetries on a non-interacting theory. To understand this, it is necessary to consider the SM as a quantum field theory, in which all elementary particles are described as quantum fields. We start by showing that imposing a simple local $U(1)$ symmetry on a non-interacting fermion field (ψ), leads to interaction terms involving a new photon-like boson. We then continue to the full symmetries of the SM.

Local gauge symmetries and forces

The Lagrangian density for a non-interacting fermion field, ψ, with mass m, is given by the free Dirac Lagrangian:

$$\mathscr{L}_{\psi}^{\text{Dirac}} = \overline{\psi}\gamma^{\mu}\partial_{\mu}\psi - m\overline{\psi}\psi, \tag{1.1}$$

where $\overline{\psi} \equiv i\psi^{\dagger}\gamma^{0}$ denotes the Dirac conjugate of the field ψ, γ^{μ} the Dirac gamma matrices and ∂_{μ} is the partial derivative. The exact form and properties of the γ matrices, except for them being space-time independent, are not important for the current discussion. The first term of $\mathscr{L}_{\psi}^{\text{Dirac}}$ corresponds to the kinetic term while the second term is the mass term.

Imposing a global $U(1)$ symmetry on Equation 1.1 requires the Lagrangian to remain invariant under the transformation

$$\psi \to e^{i\alpha}\psi, \tag{1.2}$$

and therefore

$$\overline{\psi} = i\psi^{\dagger}\gamma^{0} \to i(e^{i\alpha}\psi)^{\dagger}\gamma^{0} = e^{-i\alpha}\overline{\psi}, \tag{1.3}$$

where α is some transformation parameter. Clearly both the kinetic and mass terms are invariant.

It is also possible to impose a local $U(1)$ symmetry, meaning that the transformation parameter α can be space-time dependent. The relevant transformation is then:

$$\psi \to e^{i\alpha(x)}\psi, \tag{1.4}$$

where x denotes a four dimensional space-time vector.

Under this local transformation the mass term remains invariant, but the kinetic term does not. The reason for this is that the partial derivative does not commute with the transformation parameter:

$$\partial_{\mu}(e^{i\alpha(x)}\psi) \neq e^{i\alpha(x)}\partial_{\mu}\psi. \tag{1.5}$$

To form a kinetic term which is invariant under local $U(1)$ symmetry the partial derivative in Equation 1.1 must be replaced by a new derivative operator. This new derivative operator, D_{μ}, called a covariant derivative, must commute with the transformation parameter.

Take:

$$D_{\mu} \equiv \partial_{\mu} - igB_{\mu}, \tag{1.6}$$

where g is some constant and B_{μ} is a new vector field. If, under local gauge transformation, this fields transforms as,

$$B_{\mu} \to B_{\mu} + \frac{1}{g}\partial_{\mu}\alpha(x), \tag{1.7}$$

the following term is invariant under local $U(1)$ transformation:

$$\mathscr{L}_{\psi} = \overline{\psi}\gamma^{\mu}D_{\mu}\psi - m\overline{\psi}\psi. \tag{1.8}$$

Although in this notation this new Lagrangian for field ψ seems very similar to Equation 1.1, it no longer describes a non-interacting field. This can be seen by rewriting it to:

$$\overline{\psi}\gamma^{\mu}D_{\mu}\psi - m\overline{\psi}\psi = \overline{\psi}\gamma^{\mu}\partial_{\mu}\psi - ig\overline{\psi}\gamma^{\mu}B_{\mu}\psi - m\overline{\psi}\psi. \tag{1.9}$$

The first and last terms on the right hand side describe the non-interacting fermion field. The additional term involves both the fermion field ψ and the vector field B_{μ}. It describes a force mediated by the vector field B_{μ} acting on ψ.

More complex gauge symmetries

Imposing local gauge symmetries on a non-interacting theory requires the introduction of new vector fields and consequently interaction terms between these vector fields and the original fermion fields. The new vector fields mediate the forces of nature. The number of force carriers depends on the dimension of the symmetry; the number of generators needed to describe all possible symmetry-transformations. A more general form of the transformation given by Equation 1.4, applicable to more complex local gauge symmetries than $U(1)$, is:

$$\psi \to e^{i\alpha(x)t_a}\psi, \tag{1.10}$$

with t_a the a different generators of the symmetry. In the case of $U(1)$ this is simply the identity matrix.

The general form of the covariant derivative related to the transformation of Equation 1.10 is:

$$D_{\mu} \equiv \partial_{\mu} + ig\Lambda^{a}_{\mu}t_a, \tag{1.11}$$

with Λ^{a}_{μ} the a different gauge bosons associated with the symmetry.

Local gauge symmetries of the SM

A full description of the SM local gauge symmetry group and the resulting Lagrangian is beyond the scope of this thesis. For the discussion in this chapter it is sufficient to know that the full gauge symmetry group of the SM is given by:

$$SU(3)_{\mathrm{colour}} \otimes SU(2)_{\mathrm{left}} \otimes U(1)_{\mathrm{hypercharge}}. \tag{1.12}$$

The $SU(3)$ symmetry only applies to fields with colour-charge and is therefore responsible for the strong force. The dimension of $SU(3)$ is 8, leading to 8 new vector-fields. These fields are massless, have no electric charge, but contain both a colour and an anti-color charge. As mentioned in Section 1.1.1 these fields are called gluons (g).

The $SU(2)$ symmetry only applies to left-handed particle doublets. It is a dimension 3 symmetry. The three massless bosons of this symmetry have electric charge 0, +1 and -1 and are named W^0, W^+ and W^-.[2]

The $U(1)$ symmetry yields interaction terms proportional to the hypercharge of particles. It introduces one new massless neutral vector field, denoted by B^0.

[2]In most text books these bosons are first introduced as W^1, W^2 and W^3, where W^1 and W^2 mix to form W^+ and W^- and $W^3 \leftrightarrow W^0$.

$SU(2)$ and $U(1)$ together are responsible for the electroweak force. This symmetry is discussed further in Section 1.1.3.

Other symmetries of the Standard Model

Apart from these local gauge symmetries, the SM contains a number of other symmetries. Two of these, both considered fundamental, are relevant here. The first is the space-time equivalent of translation and rotation symmetry which leads to Lorentz-invariance. This is a fundamental symmetry in general relativity which guarantees energy and momentum conservation.

The second symmetry is a discrete symmetry imposed by the use of a quantum field theory. This symmetry, called CPT, states that if simultaneously the sign of all quantum numbers, the spacial directions and the time ordering is reversed, the physics must remain unchanged. This symmetry ensures that each particle has an anti-particle with exactly the same mass, but with opposite sign charge, both electromagnetic and colour.

1.1.3 Electroweak symmetry breaking

In Section 1.1.2 we showed that imposing the local gauge symmetry group of the SM on non-interacting fields automatically introduces the strong and electroweak force and their mediating bosons. Unfortunately this symmetry group prohibits mass-terms for all fermions and vector-bosons. As most of the SM particles are massive, part of this symmetry must be broken.

Mass terms and electroweak symmetry

Direct mass terms for the fermions and bosons of the SM violate electroweak symmetry. To prove this we show explicitly that such mass terms are not $SU(2)_{\text{left}} \otimes U(1)_{\text{hypercharge}}$ invariant.

A mass term for a fermion with field ψ would have the form:

$$m\overline{\psi}\psi = m\overline{\psi}_L\psi_R + m\overline{\psi}_R\psi_L, \tag{1.13}$$

where the subscript L indicates the left-handed and R the right-handed particle.

Because a right-handed fermion is a singlet under $SU(2)$ transformations while a left-handed fermion is a doublet, this term is not $SU(2)$-invariant and therefore not allowed within this theory.

A mass term for a boson field would also break gauge invariance. As an example take the field B_μ which changes according to Equation 1.7 under gauge transformations. A mass term for this field changes under a local $U(1)$ symmetry according to:

$$m^2 B_\mu B^\mu \to m^2 B'_\mu B'^\mu = m^2((B_\mu + \frac{i}{g}\partial_\mu \alpha(x))(B^\mu + \frac{i}{g}\partial^\mu \alpha(x))) \neq m^2 B_\mu B^\mu. \tag{1.14}$$

This is clearly not gauge invariant. Similar arguments can be used to prove that none of the SM vector-bosons can have explicit mass terms without breaking the $SU(2)_{\text{left}} \otimes U(1)_{\text{hypercharge}}$ symmetry.

The Higgs-mechanism

As all fermions as well as some of the vector-boson are massive, the electroweak symmetry must be broken. The way this symmetry breaking is currently understood is through the so-called Higgs-mechanism [11]. In this mechanism $SU(2)_{\text{left}} \otimes U(1)_{\text{hypercharge}}$ is spontaneously broken into $U(1)_{\text{electromagnetic}}$. In this context, spontaneously broken means that the general Lagrangian remains $SU(2)_{\text{left}} \otimes U(1)_{\text{hypercharge}}$ invariant, but that in the vacuum expectation value of the fields, this symmetry is hidden. In other words, at high energy the SM retains electroweak symmetry, but at low energy the symmetry is broken.

In the Higgs-mechanism this symmetry breaking is achieved by introducing an additional complex scalar field ϕ:

$$\phi = \begin{pmatrix} \phi^+ \\ \phi^0 \end{pmatrix}, \tag{1.15}$$

which is a doublet under $SU(2)_{\text{left}}$ and has hypercharge $Y_\phi = 1$. It adds the following terms to the SM Lagrangian:

$$\mathscr{L}_\phi = (D^\mu \phi)^\dagger D^\mu \phi - \mu^2 \phi^\dagger \phi - \lambda \left(\phi^\dagger \phi\right)^2, \tag{1.16}$$

where μ^2 and λ are coupling constants and D^μ is the covariant derivative of the SM. As the field ϕ does not contain colour charge the generators of $SU(3)$ need not be included, which is why gluons remain massless.

$$D_\mu = \left(\partial_\mu - i\frac{g'}{2} Y_\phi B_\mu + i\frac{g}{2} W_\mu^a \sigma^a\right), \tag{1.17}$$

where g and g' are the coupling constants of $SU(2)_{\text{left}}$ and $U(1)_{\text{hypercharge}}$ respectively and a is an index indicating the three generators of $SU(2)$. The factors of two and the sign of g and g' are conventional. The first term on the right hand side of Equation 1.17 is the partial derivative, while the second and third terms give the coupling to the vector bosons of the $U(1)_{\text{hypercharge}}$ and the $SU(2)_{\text{left}}$ symmetry respectively. To simplify further calculations a specific base for the $SU(2)_{\text{left}}$ symmetry is chosen, such that the generators σ^a are the Pauli matrices. The fields $W_\mu^{(1,2,3)}$ are the vector fields corresponding to this base. W_μ^1 and W_μ^2 can be rotated to form the W_μ^+ and W_μ^- fields introduced in Section 1.1.2 by choosing a different base:

$$W_\mu^\pm = \frac{1}{\sqrt{2}}\left(W_\mu^1 \mp i W_\mu^2\right). \tag{1.18}$$

Whether this new field ϕ can spontaneously break the $SU(2)_{\text{left}} \otimes U(1)_{\text{hypercharge}}$ symmetry depends on the values of the couplings constants μ^2 and λ which define the potential of this field. If both constants are positive, this potential in a normal (four-dimensional) parabola with a minimum at $\phi^\dagger\phi = 0$ and the theory describes massless vector bosons interacting with a massive complex scalar field. If on the other hand $\mu^2 < 0$ and $\lambda > 0$ the point $\phi^\dagger\phi = 0$ is no longer the global minimum, but a local maximum. The minimum is now at $|\phi^\dagger\phi| = \frac{\mu^2}{2\lambda}$, which is no longer a single point. The shape of this potential is often illustrated as a (four-dimensional) Mexican hat. At any point along the minimum, the potential no longer appears symmetric. The symmetry is said to be hidden or spontaneously broken in this minimum.

We define $v = \sqrt{\frac{-\mu^2}{\lambda}}$ and choose the minimum:

$$\langle \phi \rangle = \frac{1}{\sqrt{2}} \begin{pmatrix} 0 \\ v \end{pmatrix}. \tag{1.19}$$

At this minimum the kinetic term of Equation 1.16 contains the terms:

$$(D^\mu \phi)^\dagger D^\mu \phi \longrightarrow \ldots + \frac{1}{8} \begin{pmatrix} 0 & v \end{pmatrix} \left(g' Y_\phi B_\mu + g W^a_\mu \sigma^a \right) \left(g' Y_\phi B^\mu + g W^{\mu b} \sigma^b \right) \begin{pmatrix} 0 \\ v \end{pmatrix} \tag{1.20}$$

$$\longrightarrow \ldots + \left[\left(\frac{gv}{2} \right)^2 W^+_\mu W^-_\mu + \frac{(g^2 + g'^2)}{2} \left(\frac{v}{2} \right)^2 (Z^0_\mu)^2 \right]. \tag{1.21}$$

In the last step a neutral gauge boson field was introduced:

$$Z^0_\mu = \frac{1}{\sqrt{g^2 + g'^2}} \left(g W^3_\mu - g' B_\mu \right). \tag{1.22}$$

The W- and Z-bosons are now massive, with masses $M_W = \frac{1}{2} v g$ and $M_Z = \frac{1}{2} v \sqrt{g^2 + g'^2}$, while the remaining neutral gauge boson A_μ remains massless:

$$A_\mu = \frac{1}{\sqrt{g^2 + g'^2}} \left(g' W^3_\mu + g B_\mu \right). \tag{1.23}$$

A_μ is known as the photon and couples to the electric charge of particles. It is the mediator of the remaining $U(1)_{\text{electromagnetic}}$ symmetry.

We have shown that introducing a new scalar field with a potential with non-trivial minima can spontaneously break the electroweak symmetry to form the electromagnetic force mediated by massless photons. In this process the three bosons of the weak force become massive. This is known as the Higgs-mechanism.

The same mechanism can be used to give mass to the SM fermions, by allowing them to interact with the field ϕ. As an example take the following interaction term between ϕ and an electron:

$$\mathscr{L}_e^{\text{mass}} = c \overline{\psi}_e \phi \psi_e = c (\overline{\psi}_{e_L} \phi \psi_{e_R} + \overline{\psi}_{e_R} \phi \psi_{e_L}), \tag{1.24}$$

where c is some constant, ψ_{e_R} denotes the right-handed electron field while ψ_{e_L} is the left-handed electron-neutrino electron doublet $(\nu_e, e)_L$. At the vacuum expectation value of the field ϕ this interaction term becomes:

$$\mathscr{L}_e^{\text{mass}} = \frac{cv}{\sqrt{2}} (\overline{e}_L e_R + \overline{e}_R e_L), \tag{1.25}$$

which is clearly a mass term. In a similar way all the charged leptons and quarks become massive.

The Higgs-boson

Counting the degrees of freedom before and after symmetry breaking, we see that three of the four degrees of freedom of the field ϕ have been "eaten" by the vector fields in order to become massive. The remaining degree of freedom takes the form a massive real scalar field known as the Higgs-boson, H, which describes the quantum fluctuations of the field ϕ around the chosen minimum:

$$\phi(x) = \frac{1}{\sqrt{2}} \begin{pmatrix} 0 \\ v + H(x) \end{pmatrix} \tag{1.26}$$

1.1.4 Shortcomings of the Standard Model

At present, all SM particles (except the Higgs-boson) have been discovered experimentally and the correspondence between SM predictions and experimental data is excellent. Although this theory is obviously very successful there are still some open questions that hint at the need for physics beyond the SM. The two best known "problems" of the SM are the hierarchy problem and dark matter, which we describe below.

The Hierarchy Problem

The hierarchy problem is one of the main motivations for theories beyond the SM. The "problem" lies in the large relative difference in energy between the energy scales associated to the electroweak theory and to grand unified theories (GUTs).

The electroweak scale (M_{weak}) corresponds to the energy at which the electroweak symmetry is broken ($M_{\text{weak}} \sim 10^2$ GeV) while the grand unified theory scale (M_{GUT}) represents the energy at which the SM is expected to no longer hold. This scale is generally taken to be at $M_{\text{GUT}} \sim 10^{16}$ GeV, the energy scale where the three forces of the SM have approximately the same strength. It is at this energy where grand unified theories, theories that combine the three forces of the SM into one unifying force, become relevant.

The reason this difference in energy scale poses a problem, is that it affects the mass of the Higgs-boson. This mass, like any mass in the SM, is only partially determined by its bare mass, discussed in Section 1.1.3. Loop corrections to the Higgs-boson propagator also contribute.

Figure 1.1 shows a one loop correction to the Higgs-boson propagator. The contribution of this diagram to the Higgs-boson mass is of the order of $\lambda\Lambda$, where λ is the coupling constant and Λ is some cut-off value for the allowed momentum of the particle forming the loop. Since the diagram itself gives no restrictions on this momentum, the only reasonable cut-off is at an energy where the theory changes fundamentally, M_{GUT}. With $\Lambda \sim 10^{16}$ GeV and $\lambda \sim 10^{-1}$ GeV, the one-loop corrections to the Higgs-boson mass are of the order of 10^{15} GeV.

As the Higgs-boson is a result of the breaking of the electroweak symmetry, its mass must be of the order M_{weak}. This means that these corrections must be cancelled (at least in 13 orders of magnitude). As loop corrections can introduce both a positive and negative contribution to the effective mass, this can be achieved by other one-loop corrections with opposite sign. However, this requires the coupling constants to be fine-tuned to exactly cancel each other. Since there is no fundamental principle that relates these coupling constants this fine-tuning is considered unnatural.

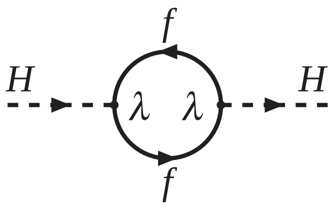

Figure 1.1: A one loop correction to the Higgs-boson mass. Solid lines are fermion lines, dashed lines represent the scalar Higgs-boson field. λ denotes the coupling constance of the two vertices.

Dark Matter

Dark matter is one of the most famous mysteries of modern physics. Astronomical observations as well as cosmological models have determined that only 17% of the mass of the universe is in the form of known baryonic matter [7]. The remaining 83% is known as dark matter. Cosmological models indicate that this matter probably consists of weakly interacting massive particles, WIMPs, where weakly interacting means that these particles have no electric or colour charge. They must furthermore be stable, or have lifetimes in the order of the age of the universe. The only possible candidate in the SM is the neutrino. However, upper limits for the neutrino masses, as well as measurements of neutrino densities, exclude them as the main source of DM. This suggests the existence of at least one new, non-SM, elementary particle.

1.2 Supersymmetry

In Section 1.1 we described the SM and its two main shortcomings, the hierarchy problem and dark matter. We showed that many of the properties of the SM are the consequence of fundamental symmetries. It seems therefore natural to solve the "problems" of the SM by introducing an additional symmetry. One way of doing this is to introduce a symmetry between fermions and bosons, called a supersymmetry.

In this section we discuss the consequences of imposing supersymmetry (SUSY) on the SM and show that this indeed solves both the hierarchy and dark matter problem. We start by defining the SUSY transformation operator and how it acts on SM fields. By extending the SM to a SUSY invariant theory it turns out to be necessary to at least double the number of fundamental particles (see Section 1.2.2), although no new forces are introduced. Although this doubling of the number of elementary particles might seem drastic, we show, in Section 1.2.3, that it does solve the hierarchy problem.

Unfortunately, as will be discussed in Section 1.2.4, current experimental data have already excluded an unbroken supersymmetry, which implies that SUSY, if it exists, must be a broken symmetry. This has consequences both in terms of particle masses and new interactions but has the added benefit that one of the SUSY particles becomes a prime dark matter candidate.

In our current understanding of SUSY, it is not possible to predict the masses of the SUSY particles after symmetry breaking. Therefore a general SUSY model introduces a large number of free parameters. To restrict the number of such parameters, simplified models have been derived. One of these models, called mSUGRA, is introduced in Section 1.2.5.

1.2.1 Supersymmetric transformations

Supersymmetry is based on a symmetry between bosons and fermions. An infinitesimal SUSY transformation turns a boson field (B) into a fermion field (f) and vice versa.

$$\delta B = \varepsilon \cdot f, \tag{1.27}$$

with ε an infinitesimal transformation parameter. Because boson fields commute and fermion fields anti-commute the SUSY transformation parameter must be anti-commuting:

$$\{f, f\} = 0, \quad [B, B] = 0 \quad \rightarrow \quad \{\varepsilon, \varepsilon\} = 0. \tag{1.28}$$

For the SUSY Lagrangian to remain gauge and Lorentz invariant, the SUSY operators must commute with the gauge operators as well as with the momentum operator. This means that while the SUSY operators changes the spin of a particle, the other characteristics of that particle such as its mass, the way it behaves under gauge transformations and its number of degrees of freedom, remain the same.

One of the main consequences of the SUSY operator being anti-commuting, is that applying it twice, annihilates the particle.

$$\{\varepsilon, \varepsilon\} = 0 \rightarrow \varepsilon \cdot \varepsilon = 0 \tag{1.29}$$

Therefore, instead of being able to produce a similar particle with exceedingly large spin, the SUSY operator creates pairs of particles that differ only by their spin and only by an amount equal to $\frac{1}{2}$. Particles that are related in such a way are called superpartners.

1.2.2 Supersymmetric particles

Since superpartners are identical, except for their spin, it should be clear that none of the SM particles can be each other superpartners. Therefore SUSY at least doubles the number of particles of the theory.

In minimal supersymmetric models, MSSMs, the amount of non-SM degrees of freedom is minimized. In these models the non-SM particles are limited to the superpartner of SM particles with the addition of a second Higgs-doublet and its superpartner, necessary to cancel some gauge anomalies in the theory. As these two SM Higgs-doublets have a total of eight degrees of freedom, three of which are ”used” in the electroweak symmetry breaking to give mass to the Z- and W-bosons, MSSMs contain five different Higgs-bosons, generally

	Particles			Spin	Electric charge	Colour
Squarks	$(\widetilde{u},\widetilde{d})_L$	$(\widetilde{c},\widetilde{s})_L$	$(\widetilde{t},\widetilde{b})_L$	$(0,0)$	$(\frac{2}{3}, -\frac{1}{3})$	Yes
	$\widetilde{u}_R$	$\widetilde{c}_R$	$\widetilde{t}_R$	0	$\frac{2}{3}$	Yes
	$\widetilde{d}_R$	$\widetilde{s}_R$	$\widetilde{b}_R$	0	$-\frac{1}{3}$	Yes
Sleptons	$(\widetilde{\nu}_e,\widetilde{e}^-)_L$	$(\widetilde{\nu}_\mu,\widetilde{\mu}^-)_L$	$(\widetilde{\nu}_\tau,\widetilde{\tau}^-)_L$	$(0,0)$	$(0,-1)$	No
	$\widetilde{e}_R^-$	$\widetilde{\mu}_R^-$	$\widetilde{\tau}_R^-$	0	-1	No
Gauginos	$\widetilde{g}$			$\frac{1}{2}$	0	Yes
	$\widetilde{W}^\pm$ and $\widetilde{Z}$			$\frac{1}{2}$	± 1 and 0	No
	$\widetilde{\gamma}$			$\frac{1}{2}$	0	No
Higgs-doublets	H^0, H^+			0	0 and 1	No
Higgsino-doublets	$\widetilde{H}^0$, $\widetilde{H}^+$			$\frac{1}{2}$	0 and 1	No

Table 1.2: The non-SM particles of the MSSM, listed with their spin, electric and colour charges. The subscripts L and R denotes the left- and right-handedness of the SM partner. H^0, H^+, $\widetilde{H}^0$ and $\widetilde{H}^+$ represent to the Higgs-boson doublets and their superpartners. The SM particles are listed in Table 1.1.

denoted by: h^0, H^0, A^0, H^+ and H^-. The lightest MSSM Higgs-boson, h^0, behaves very similar to the SM Higgs-boson. Table 1.2 list all non-SM particles in MSSMs.

As (most of) these new particles are the partners of known SM particles, all their characteristics are fully fixed by the SM and SUSY symmetries.

Sfermions: The superpartners of SM fermions are called sfermions. Each SM fermion has two superpartners. This can be understood by considering how the SM fermions react under gauge transformations. Under the $SU(2)_{\text{left}}$ symmetry the left and right handed fermion react in a fundamentally different way. Since sfermions must act under gauge transformation in the same way as their superpartner, we separate the superpartner of the left-handed fermion to that of the right handed fermion. These sfermions are denoted by $\widetilde{f}_L$ and $\widetilde{f}_R$, where the subscript L and R denotes the handedness of corresponding SM partner.

A priori the sfermion could have either spin 0 or 1. Massive spin 1 particles have three degrees of freedom. Since both the left- and right-handed fermions have only two degrees of freedom, spin 1 particles can not be the superpartner of SM fermions. Therefore sfermions must be spin 0 particles, described by complex scalar fields.

Gauginos: The superpartners of massless SM gauge bosons are called gauginos and have spin $\frac{1}{2}$ and two degrees of freedom. As there are no massive gauge bosons before electroweak symmetry breaking, there is no need to consider the partners of massive vector fields. The gauginos differ from SM fermions in that they must act, under gauge transformations, identical to the vector bosons. This means that the gauginos mediate the same forces of nature as their SM partners.

Higgsinos: The superpartners of the Higgs-bosons are spin $\frac{1}{2}$ fermions, called higgsinos.

1.2.3 SUSY as a solution to the Hierarchy problem

Due to the introduction of superpartners, which ensures an equal number of degrees of freedom from bosonic and fermionic particles, the hierarchy problem is automatically solved. This is because from Fermi statistics, fermionic loops get an extra minus sign compared to bosonic loops. Therefore, in SUSY, for each bosonic loop contributing to the Higgs-boson mass, there is a corresponding fermionic loop, which, since superpartners are equal in every way except for spin, precisely cancel the bosonic loop. Figure 1.2 shows how sfermion loops cancel the divergence from SM-fermion loops and gaugino loops cancel gauge boson loops.

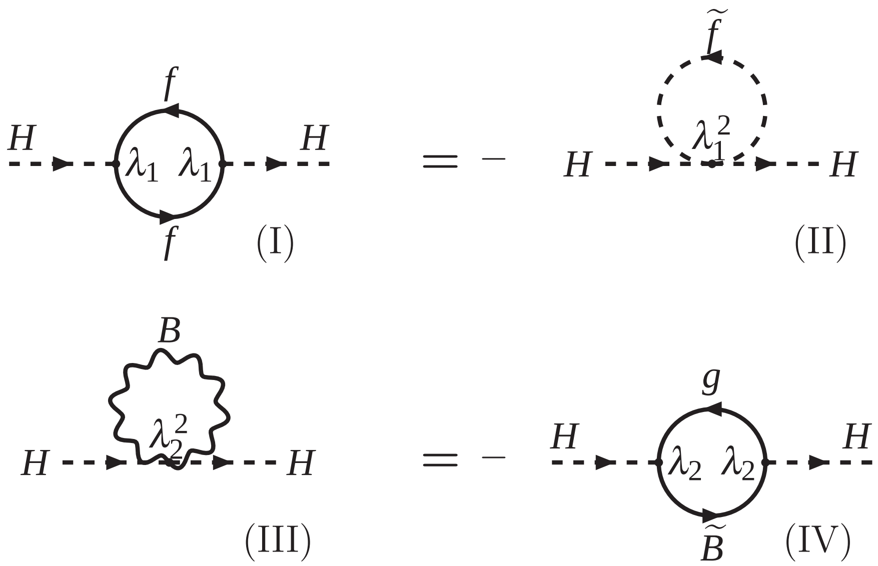

Figure 1.2: Four one-loop corrections to the Higgs-bosons mass. Solid straight lines, dashed lines and oscillating lines represent fermion, scalar and gauge boson fields. λ_1 and λ_2 are coupling constants. The divergence from fermion loops, diagram I, is cancelled by sfermion loops, diagram II. The divergence from gauge boson loops, diagram III, is cancelled by gaugino loops, diagram IV.

1.2.4 Supersymmetry breaking

We have shown, in Section 1.2.3, that introducing supersymmetry into the SM automatically solves the Hierarchy problem. In the process it was necessary to more than double the amount of fundamental particles. This might seem extreme, but is not much different from the effect of the CPT-symmetry introduced in Section 1.1.2 which ensures that each particle has a corresponding anti-particle. The superpartners of SM particles, their characteristics and interactions, are fully fixed by the symmetry. This means that, except for a mixing parameter in the Higgs-sector, introduced by the requirement of a second Higgs-doublet, no new free parameters are introduced in MSSMs.

Unfortunately supersymmetry, as discussed so far, is excluded by experimental data. If supersymmetric particles have the same mass as their SM partners, and interact in the same way, they should have been created at previous accelerators. Since none of the SUSY particles have been detected, we can conclude that SUSY, if it exist, must be a broken symmetry.

This in itself is not a problem. We have shown in Section 1.1.3 that the symmetries of the SM are also partially broken, allowing for terms in the Lagrangian which are not $SU(2)_{\mathrm{left}} \otimes U(1)_{\mathrm{hypercharge}}$ invariant. The exact form of these additional terms is fixed by the breaking mechanism, in this case the Higgs-mechanism.

In the case of a broken supersymmetry the breaking mechanism is unknown. Therefore general MSSMs must consider all SUSY violating terms which can be added to the Lagrangian without breaking either the SM symmetries or cause unrenormalizable effects. This introduces some new interactions, but perhaps more importantly, it allows for direct mass-terms for the supersymmetric particles.

MSSM particle masses

As mentioned in Section 1.1.3, the mass of SM particles is generated through coupling to the Higgs-field. In a non-broken supersymmetry, SUSY particles acquire their mass in the same way. However in a broken symmetry they can, in addition, have a direct mass term. Sfermions (ϕ) are scalar fields, and can therefore have the following mass term:

$$\mathscr{L}_{\phi}^{\mathrm{mass}} = m^2 \varphi^* \varphi. \tag{1.30}$$

Gauginos (ψ) are real Weyl-spinors which cannot be separated in a left- and a right-handed part. The following mass term is therefore allowed:

$$\mathscr{L}_{\psi}^{\mathrm{mass}} = m \overline{\psi} \psi. \tag{1.31}$$

Because of these direct mass terms, the SUSY particles can have larger masses than their SM partners.

The coupling constants m, in Equation 1.30 and 1.31 can be determined or restricted by the breaking mechanism. Since this mechanism is unknown there are currently no restrictions on these values, which could differ substantially for different particles. The mass term for sfermions can furthermore be extended to contain the 3 families of sfermions. m is then a 3x3 matrix which, if not diagonal, introduces mixing between the families.

Due to these additional mass terms, SUSY breaking introduces a large number of free parameters leading to an equally large variety of mass-spectra for the SUSY particles.

MSSM particle content

Massive particles with identical quantum number can mix into mass-eigenstates that are a linear combination of the possible gauge eigenstates. One example of this from the SM is the mixing of B_μ and W_μ^3 into the Z-boson and the photon, described in Equation 1.22 and 1.23. The same principle occurs in a broken MSSM.

The neutral gauginos and higgsinos mix together to form four neutralinos denoted by $\widetilde{\chi}_1^0$, $\widetilde{\chi}_2^0$, $\widetilde{\chi}_3^0$, and $\widetilde{\chi}_4^0$, where $\widetilde{\chi}_1^0$ is the lightest and $\widetilde{\chi}_4^0$ the heaviest neutralino. The charged winos and higgsinos also mix to two pairs of chargino, $\widetilde{\chi}_1^\pm$ and $\widetilde{\chi}_2^\pm$.

In the sfermions sector the partners of the left- and right-handed fermions can mix to states that are generally denoted as $\widetilde{f}_1$ and $\widetilde{f}_2$.

The mass-eigenstates of MSSMs are listed in Table 1.3.

	Fields			Mass Eigenstates		
Squarks	$(\widetilde{u},\widetilde{d})_L$	$(\widetilde{c},\widetilde{s})_L$	$(\widetilde{t},\widetilde{b})_L$	$\widetilde{u}_1,\widetilde{u}_2$	$\widetilde{c}_1,\widetilde{c}_2$	$\widetilde{t}_1,\widetilde{t}_2$
	$\widetilde{u}_R$	$\widetilde{c}_R$	$\widetilde{t}_R$	$\widetilde{d}_1,\widetilde{d}_2$	$\widetilde{s}_1,\widetilde{s}_2$	$\widetilde{b}_1,\widetilde{b}_2$
	$\widetilde{d}_R$	$\widetilde{s}_R$	$\widetilde{b}_R$			
Sleptons	$(\widetilde{\nu}_e,\widetilde{e})_L$	$(\widetilde{\nu}_\mu,\widetilde{\mu})_L$	$(\widetilde{\nu}_\tau,\widetilde{\tau})_L$	$\widetilde{\nu}_e$	$\widetilde{\nu}_\mu$	$\widetilde{\nu}_\tau$
	$\widetilde{e}_R$	$\widetilde{\mu_R}$	$\widetilde{\tau}_R$	$\widetilde{e}_1,\widetilde{e}_2$	$\widetilde{\mu}_1,\widetilde{\mu}_1$	$\widetilde{\tau}_1,\widetilde{\tau}_2$
Gauginos	$\widetilde{g}$			$\widetilde{g}$		
	$\widetilde{B},\widetilde{W}_1,\widetilde{W}_2,\widetilde{W}_3$			$\widetilde{\chi}_{1,2}^\pm$ (Charginos)		
Higgsino-doublets	$\widetilde{H}^0,\widetilde{H}^+$			$\widetilde{\chi}_{1,2,3,4}^0$ (Neutralinos)		

Table 1.3: The MSSM particles mass-eigenstates (right) are mixtures of the fields. The L- and R-squarks and -sleptons can mix into two states, denoted simply by their increasing mass with 1,2. The gauginos, except for the gluinos, and Higgsinos mix into the charginos and neutralinos.

Supersymmetric interactions and R-parity

In an unbroken supersymmetric theory the SUSY particles interact in the same way as SM particles. In a broken symmetry new interactions are possible. These interactions, like the known SM interactions, must be gauge invariant and renormalizable. This means that all SM interactions are allowed, as well as a number of new interactions, all involving one or more SUSY particles.

If all renormalizable and gauge invariant interactions are possible, the diagrams of Figure 1.3 are allowed, leading to lepton and baryon number violation. In particular, these diagrams allow for fast proton decay through the channel shown in Figure 1.4, which is in contradiction with experimental observations [12].

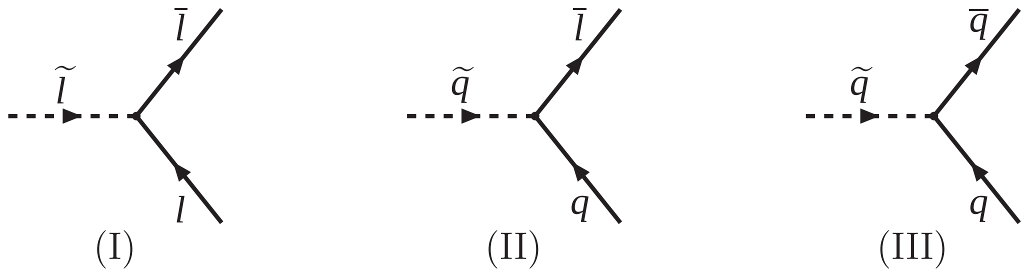

Figure 1.3: Diagrams introduced by SUSY breaking. Diagram I and II violate lepton number, while diagram III violates baryon number.

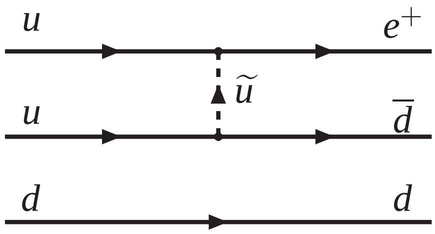

Figure 1.4: One possible diagram by which proton can decay to a pion and a positron in R-parity violating SUSY theories. This diagram includes diagram II and III of Figure 1.3.

To solve this problem a new multiplicative quantum number is introduced, R-parity, which assigns a factor 1 to all SM particles and a factor -1 to all SUSY particles. R-parity conservation therefore ensures that SUSY particles are always formed in pairs, and only decay to an other SUSY particles, making the lightest SUSY particle (LSP) stable.

All the new interactions that R-parity conserving SUSY introduces to the SM are shown in Figure 1.5. The coupling constants belonging to these interactions are, in the case of the supersymmetric equivalent of a SM interaction, equal to those of the SM. For example, the gluino mediates the strong interaction, same as the gluon, and therefore it interacts with the same constant α_S. In new interactions without a SM equivalent, the coupling is a free parameter, although, as was the case for the value of m in the SUSY mass-terms, the value of these couplings could be restricted by the SUSY breaking mechanism.

Dark Matter

In R-parity conserving supersymmetry the lightest superpartner is stable. If the LSP is the lightest neutralino, $\tilde{\chi}_1^0$, as is the case is most of the SUSY phase-space, this particle becomes a prime DM candidate.

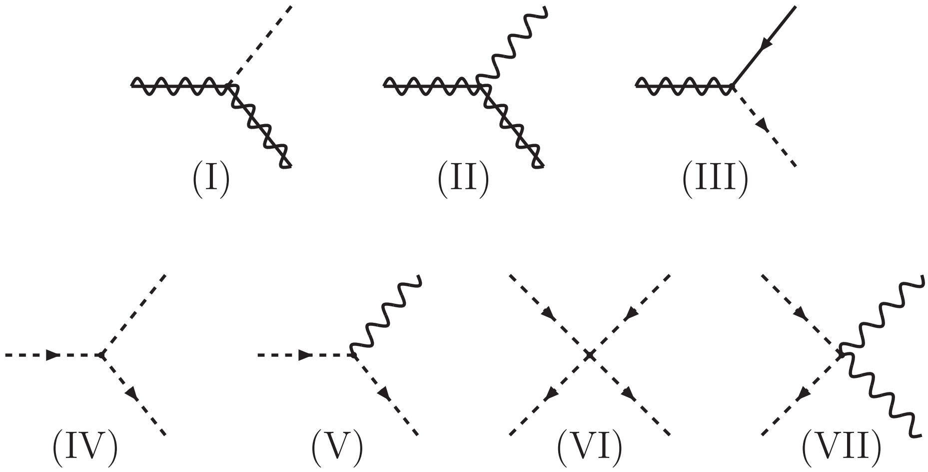

Figure 1.5: All non-SM interaction in R-parity conserving MSSM. Solid straight arrows, oscillating lines and dashed line represent fermion, gauge boson and Higgs-boson fields respectively. Dashed arrows and oscillating lines traversed by a straight line represent sfermions and gauginos/higgsinos.

The Hierarchy problem

In a broken SUSY model, the contribution of superpartners to the Higgs-boson effective mass no longer automatically cancel. The question therefore arises whether, if SUSY is indeed broken, it still solves the hierarchy problem. Fortunately, to solve the Hierarchy problem, the cancellation of the loop terms does not have to be exact, but "only" in about 13 orders of magnitude. This allows for some difference in mass between the superpartners but limits this mass difference, the values of m (or the components of m), to about 1 TeV. Therefore it is likely that, if SUSY exists, the masses of the SUSY particles are within the production range of the LHC[3].

1.2.5 mSUGRA

It is clear that a realistic SUSY theory introduces a large number of free parameters because of SUSY breaking. Even in a minimal supersymmetric model, where the number of fields is minimized, the mass terms of Equation 1.30 and 1.31 together with the interaction terms of Figure 1.5, introduce over a hundred free parameters. A theory with so many free parameters has very poor predictive power. In particular, since there is no correlation between the mass terms, there is no restriction on the SUSY mass spectrum.

To restrict the number of free parameters and thereby facilitate predictions of the effect of supersymmetry on theoretical models and experimental results, multiple simplified

[3]The possible SUSY signatures at the LHC are discussed in Section 1.3.

SUSY models have been proposed. The model most commonly used by experimentalists is named mSUGRA.

mSUGRA was initially introduced as a simplification of supergravity models. In this type of models, SUSY is broken is a so-called hidden sector containing particles which interact only through the gravitational force with the particles of the MSSM. To simplify calculations, certain assumption are made for SUSY masses and couplings at the Planck scale, $M_{\mathrm{P}} = 10^{19}$ GeV, the scale where the gravity mediated SUSY breaking takes place. These simplifications, discussed later in this section, lead to a minimum supergravity model, mSUGRA. The masses and interactions of the MSSM particles at M_{P} can then be translated to the electroweak scale.

Although mSUGRA is introduced as a supergravity model, the actual breaking mechanism has no influence on the resulting theory. Any model with the same particle content and the same assumptions for masses and interactions at the Planck scale, leads to the same SUSY model at the electroweak scale. For this reason we shall not discuss the breaking mechanism in more detail.

It was mentioned in Section 1.1.4 that the SM and its SUSY extension are not expected to describe nature at energies beyond the grand unified theory scale, M_{GUT}. Since the relevant theory at energies between M_{GUT} and M_{P} is unknown, there is no reliable way to relate couplings at the Planck scale to the electroweak scale. Therefore, in practice, the mSUGRA model makes assumptions for MSSM masses and interactions at the GUT scale, instead of at the Planck scale.

mSUGRA assumptions and parameters

In mSUGRA the following assumptions are made on the MSSM masses and interactions at the GUT energy scale:

- Mixing between the three families of sfermions is neglected; the mass matrices are diagonal.
- The direct masses of the sfermions are unified. This mass is denoted by m_0.
- The direct non-SM contribution to masses of the gauginos and higgsinos are unified. This mass is denoted by $m_{\frac{1}{2}}$.
- The values of the non-SM trilinear couplings are unified to A_0 at the GUT energy scale, which means that all the new interactions are proportional to the Yukawa couplings.

In addition to these three parameters ($m_{\frac{1}{2}}$, m_0 and A_0) mSUGRA contains two additional parameters from the extended SM Higgs-boson sector. The first consists of a mixing parameter between the two SM Higgs-doublets. This parameter is usually chosen to be $\tan(\beta)$, the ratio between the vacuum expectation values of the two Higgs-doublets. The last parameter is the sign of μ introduced in Equation 1.16.

In total mSUGRA has therefore 5 free parameters: $m_{\frac{1}{2}}$, m_0, A_0, $\tan(\beta)$ and $sign(\mu)$.

The mSUGRA mass spectrum

Like the coupling constants of the SM, the SUSY mass and interaction parameters are not constant, but depend on the energy scale. This means that although the masses of sfermions and the masses of all gauginos and higgsinos are unified at the GUT scale, this is not the case at the electroweak scale. As an example Figure 1.6 shows the masses of different SUSY particles as a function of the energy scale for one point in the mSUGRA phase-space. This running of the masses and therefore the mass-spectrum of the particles at the electroweak scale is fully determined by the five mSUGRA parameters.

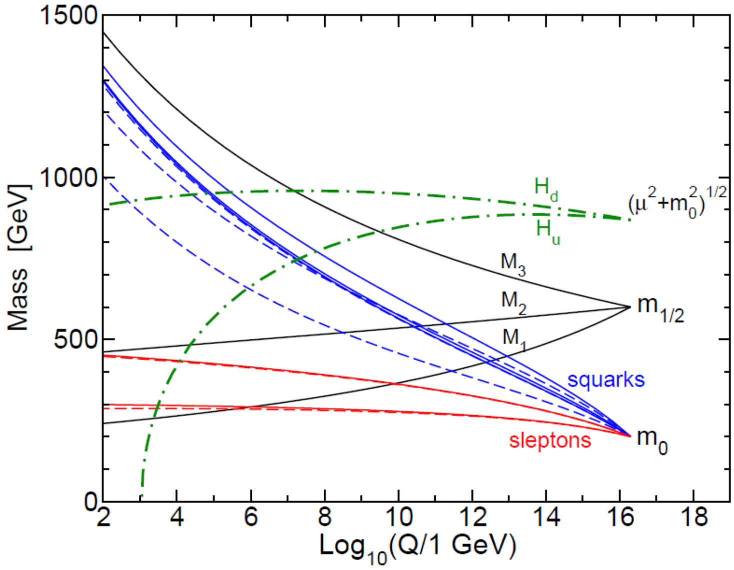

Figure 1.6: The scalar and gaugino mass parameters in mSUGRA as a function of the energy scale for point: $m_0 = 200$ GeV, $m_{\frac{1}{2}} = 600$ GeV, $A_0 = -600$ GeV, $\tan(\beta) = 10$ and $\mu > 0$ [13]. The red (blue) lines denotes the slepton (squark) masses with the full line indicating the first and second family sfermions and the dashed-line their third family equivalent. The black lines indicate the gaugino masses, with M_3 indicating the gluino. The green lines correspond to the two SM higgsino doublets.

Gaugino and higgsino masses: The gaugino and higgsino masses at the electroweak scale depend almost exclusively on the value of $m_{\frac{1}{2}}$. This almost linear dependence is shown in the left plot of Figure 1.7 where the gluino, neutralino and chargino masses are shown as a function of $m_{\frac{1}{2}}$ for $m_0 = 200$ GeV, $A_0 = 0$ GeV, $\tan(\beta) = 10$ and $\mu > 0$. From these plots we can conclude that the gluino is the heaviest gaugino and that the masses of $\widetilde{\chi}_2^0$ and $\widetilde{\chi}_1^\pm$ as well as masses of $\widetilde{\chi}_3^0$, $\widetilde{\chi}_4^0$ and $\widetilde{\chi}_2^\pm$ are almost degenerate. This is true for most of the mSUGRA phase-space.

Beside the dependence on $m_{\frac{1}{2}}$, the only other dependence of these masses is an increase in the higgsino masses for high absolute values of A_0, due to radiative corrections in the running of these couplings. For relatively low mass SUSY, $m_0 < 600$ GeV and $m_{\frac{1}{2}} < 600$ GeV, this translates in higher masses for $\widetilde{\chi}_3^0$, $\widetilde{\chi}_4^0$ and $\widetilde{\chi}_2^{\pm}$ as these mass eigenstates contain the highest higgsino contribution. This A_0 dependence is shown in the right plot of Figure 1.7.

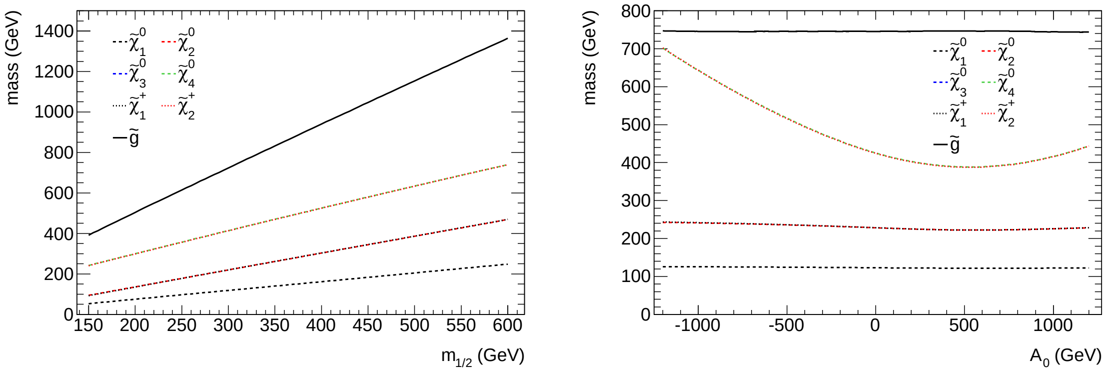

Figure 1.7: The mass of the gluino, neutralinos and charginos in mSUGRA as a function of $m_{\frac{1}{2}}$ (left) and A_0 (right) for $m_0 = 200$ GeV, $\tan(\beta) = 10$, $\mu > 0$ and $A_0 = 0$ GeV (left) or $m_{\frac{1}{2}} = 310$ GeV (right). All masses are calculated by ISAJET [14].

Because the mass of the gluino, the two lightest neutralinos and the lightest chargino are determined almost exclusively by $m_{\frac{1}{2}}$ with a linear dependence on this variable, the ratio $\widetilde{g}$:($\widetilde{\chi}_2^0$, $\widetilde{\chi}_1^{\pm}$):$\widetilde{\chi}_1^0$ is constant throughout the mSUGRA phase-space. This affects the range of possible signatures from SUSY events at the LHC as predicted by mSUGRA, as will be discussed in more detail in the Section 1.3.

Sfermion masses: The masses of the sfermions depend on m_0. When m_0 is much larger than $m_{\frac{1}{2}}$ this dependence is almost linear. However, for sfermion masses smaller than the gaugino masses, interaction terms between the sfermions and the gauginos start to contribute significantly, limiting the minimum effective sfermion masses. This effect is stronger for squarks, as these couple to the heavier gluino, than for sleptons which only couple to the neutralinos and charginos. Therefore squark masses are higher than slepton masses. For this same reason the sfermionic partners to left-handed SM fermions are slightly heavier than the partners of right-handed fermions due to their coupling to the superpartners of the $SU(3)_{\text{left}}$ gauge bosons. Since the sfermion masses are affected by their interactions with the gauginos and higgsinos, their mass also depends (almost linearly) on $m_{\frac{1}{2}}$.

The only difference between sfermions of different families lies in the strength of the Yukawa coupling. Since this coupling is highest for third family fermions the energy dependence for the third family sfermions is stronger than that of the first and second family, leading to smaller masses. As the Yukawa couplings for the first and second family are very small, their effect on the sfermion masses are negligible leading to first and second family fermions masses being degenerate.

Since one of the assumptions of mSUGRA is that all additional SUSY interactions are proportional to the Yukawa coupling with a constant A_0, the third family sfermion masses depend on this constant with lower masses for higher absolute values of A_0. Furthermore these third family sfermions are also affected by $\tan(\beta)$, with high $\tan(\beta)$ leading to smaller masses. This effect is particularly strong for the lightest stau which for high $\tan(\beta)$ can become the LSP.

Figure 1.8 shows the dependence of squark and slepton masses on m_0 (top left and right plot respectively) and the dependence of slepton masses on A_0 (bottom left plot) and $\tan(\beta)$ (bottom right plot). As the masses of the second family sfermions are the same as those of the first family, only the first and third family sfermions are shown.

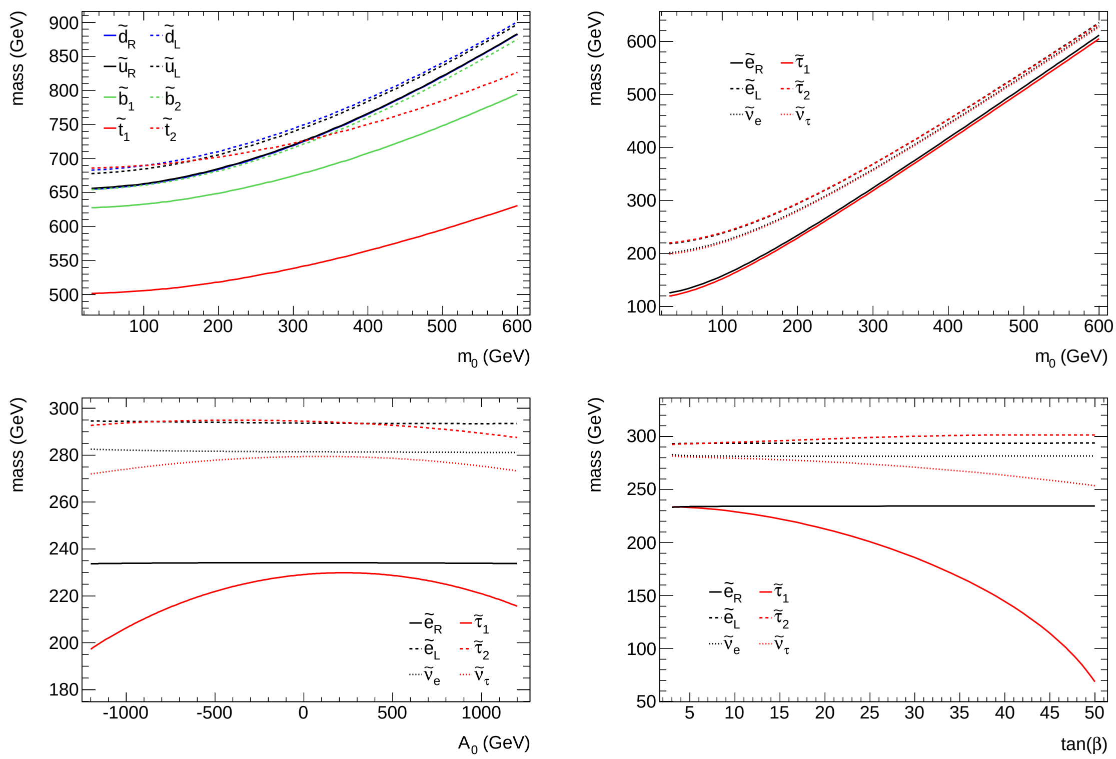

Figure 1.8: Top: The mass of squarks (left) and sleptons (right) in mSUGRA as a function of m_0 for $m_{\frac{1}{2}} = 310$ GeV, $A_0 = 0$ GeV, $\tan(\beta) = 10$ and $\mu > 0$. Bottom: The slepton masses in mSUGRA as a function of A_0 (left) and $\tan(\beta)$ (right) for $m_0 = 200$ GeV, $m_{\frac{1}{2}} = 310$ GeV, $\mu > 0$ and $\tan(\beta) = 10$ (left) or $A_0 = 0$ GeV (right). The second family sfermion masses are equal to their first family counterpart. All masses are calculated by ISAJET [14].

The mSUGRA phase-space

Most of the mSUGRA phase-space has already been excluded by experiments. For relatively low mass mSUGRA the strongest exclusion limits come from direct searches at the LHC [15]. These limits are discussed further in Section 1.3. For higher masses most of the phase-space is excluded since the expected DM contribution from the LSP (in this case $\widetilde{\chi}_1^0$) is higher than measurements indicate [7].

Despite these experimental results we consider mSUGRA in this thesis as it provides a convenient framework in which to present some exclusion limits and compare the results with other analyses. While the assumptions of mSUGRA might not provide a realistic physics model, they are still useful in limiting the SUSY phase-space and producing a wide range of possible SUSY signatures. However, when using mSUGRA as an illustration for the whole SUSY phase-space, it is important to remember the restrictions on the possible mass spectra discussed in this section, which might bias the conclusions.

1.3 Expected supersymmetric signatures at the LHC

Depending on the masses of the SUSY particles, they can be created at proton-proton colliders such as the LHC[4]. The production cross-section and the decay chain for these particles depend strongly on the SUSY mass spectrum and therefore on the phase-space point. As, in general SUSY models, there is no known correlation between the SUSY masses, this mass spectrum is mostly unrestricted except for some experimentally excluded regions, leading to a wide range of possible signatures at the LHC. However, using the property of SUSY that no new forces are introduced, we can determine some typical SUSY signatures which should cover most of the R-parity conserving SUSY phase-space. Some of these typical signatures are described below, motivating our interest in lepton pairs with equal electric charge.

1.3.1 High energetic jets and missing transverse energy

In R-parity conserving SUSY, supersymmetric particles are always produced in pairs which then decay to the LSP. The exact decay chains involved depend on the mass spectrum, but, unless the mass differences are very small, the decay rates are such that all SUSY particles have fully decayed to the LSP and SM particles before reaching a detector.

As we are considering signatures at a proton-proton collider, the production rate for strongly interacting particles is enhanced compared to that of colour neutral particles. Therefore, unless the masses of gluinos and squarks are much higher than that of other sfermions, neutralinos and charginos, the SUSY cross-section at the LHC is dominated by gluino-gluino, gluino-(anti-)squark and (anti-)squark-(anti-)squark production.

Assuming the LSP is a colour neutral particle, a necessary requirement for it to be a DM candidate, the decay chain of each squark must create at least one quark. Similarly, gluino decays produce at least one quark-anti-quark pair. These quarks and anti-quarks

[4] The LHC is discussed in Chapter 2.

are observed as jets in a detector (see Section 2.3.3). If the mass differences involved in the decay steps which created these quarks are reasonably large, the resulting jets will be highly boosted. SUSY events at the LHC are therefore expected to typically contain at least 2, 3 or 4 high energetic jets corresponding to $\tilde{q}\tilde{q}$, $\tilde{q}\tilde{g}$ and $\tilde{g}\tilde{g}$ production respectively.

Independent of the production mechanism, each collision involving SUSY particles results in the creation of two LSPs. If the LSP is both electrically and colour neutral, as suggested by the DM argument, these two particles remain undetected by any detector surrounding the collision. This results in a momentum imbalance in the recorded collision corresponding to the sum of the momenta of the two LSPs, which is detectable as missing transverse energy (see Section 2.3.4). As the originally produced SUSY particle pair is produced back-to-back, a large amount of missing transverse energy is only expected when the mass differences between these particles and the LSP are sufficiently large.

Because of the arguments presented in this section, most searches for SUSY at the LHC look for collisions with high energetic jets and high missing transverse energy [15]. No evidence for SUSY has been found yet. As an example, Figure 1.9 shows the current (end of 2011) exclusion limit obtained by such analyses in ATLAS for one plane in the mSUGRA phase-space. The fixed ratio between the gluino mass and the lighter neutrinos and chargino masses in mSUGRA results in large enough mass differences between the different steps in the gluino decay chain to ensure that high momentum jets and large missing transverse energy are prominent signatures in most of the mSUGRA phase-space.

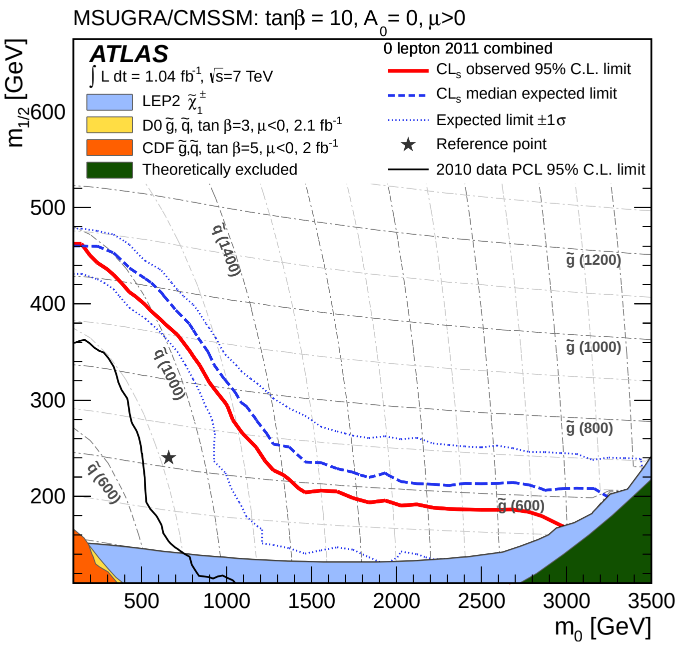

Figure 1.9: The 95% CL excision limit of mSUGRA as a function of m_0 and $m_{\frac{1}{2}}$ for $A_0 = 0$ GeV, $\tan(\beta) = 10$ and $\mu > 0$ obtained by the ATLAS experiment in an analysis based on high momentum jets and large missing transverse energy [15].

1.3.2 Charged leptons

Analyses focussing on high momentum jets and large missing transverse energy have so far found no evidence for physics beyond the SM. This means that, if SUSY exists, either the SUSY masses are higher than the current accessible range, or the mass spectrum is such that SUSY events do not produce the typical signatures described in Section 1.3.1. This can have several reasons including scenarios in which the mass differences between the SUSY particles are not sufficient to produce high energetic jets, or ones in which the gluino and squarks masses are too heavy to be produced at the LHC, leading to a SUSY production process which is limited to sleptons, charginos and neutralinos.

To cover more of the available SUSY phase-space, it is therefore interesting to also consider other possible SUSY signatures. One possibility is to focus on charged leptons which can be produced in the decay chain of SUSY particles. In most of the SUSY phase-space the direct decay of gluinos and squarks to the LSP is suppressed. Most decays will therefore include intermediate stages including sleptons and/or heavier neutralinos and charginos. In the case of decays involving sleptons, leptons are produced to conserve lepton number, while the decays of heavier charginos and neutralinos often produce a Z- or W-boson which can in turn decay to leptons. While neutrinos do not lead to direct signatures in detectors, charged leptons can quite easily be identified. The main advantage of SUSY searches involving leptons is that the SM background is considerably less than for events without leptons. It is therefore possible for such analyses to use less stringent energy requirements on the jets and leptons. However, as a wide range of SM processes leads to signatures including a lepton, these searches still rely on the existence of jets and large missing transverse energy to limit the SM background.

As the branching ratio of gluinos and squarks producing a lepton is lower than the 100% branching ratio for producing jets, searches relying on charged leptons are generally less sensitive than zero lepton searches in the case of SUSY points where the cross-section is dominated by $\widetilde{q}\widetilde{q}$, $\widetilde{q}\widetilde{g}$ and $\widetilde{g}\widetilde{g}$ production, such as for most of the mSUGRA phase-space. They do typically have a higher sensitivity for events including direct slepton, chargino and neutralino production.

1.3.3 Same-sign lepton pairs

As discussed in Section 1.3.2, SUSY decay chains can create charged leptons either by producing them directly in decays involving sleptons, or through the production of W- and Z-bosons. Since, in R-parity conserving SUSY, SUSY particles are always produced in pairs, each SUSY event contains two separate decay chains which could both produce a charged lepton.

The charge of the produced leptons depends on the decay chain and more specifically on the decay step involved in producing the lepton. Typically squark and anti-squarks with positive (negative) charge tend to produce positively (negatively) charged leptons. Gluinos on the other hand are their own anti-particle and have therefore no preference between producing leptons or anti-leptons. As apart from the production mechanism of the two original SUSY particles, the two decay chains are independent, the probability of both decay chains producing a charged lepton of equal charge is equal to that of opposite charge pairs for both $\tilde{g}\tilde{g}$ and $\tilde{q}\tilde{g}$ events. The same is true for the production of sleptons, charginos and heavier neutralinos in association with a gluino. Apart from same-sign dilepton signatures in events involving gluino production, it is also possible to produce such lepton pairs in $\tilde{q}\tilde{q}$ and $\overline{\tilde{q}}\overline{\tilde{q}}$ events. The main production process for such squark pairs and anti-squark pair production at the LHC is shown in Figure 1.10.

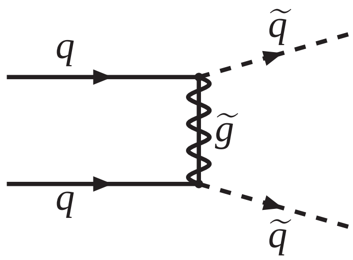

Figure 1.10: The main production process for direct $\tilde{q}\tilde{q}$ production at the LHC.

As an example, Figure 1.11 shows the fraction of events containing high momentum ($p_T > 25$ GeV) same-sign dilepton at the LHC for one plane in the mSUGRA phase-space. Despite the relatively low branching ratios, which are a direct result of the branching ratio of SUSY decays to charged leptons, searches for same-sign lepton pairs are interesting as the background from the SM is small. Such analyses therefore need not include any additional requirements on the event topology, making them sensitive to regions of phase-space without high momentum jets or significant missing transverse energy.

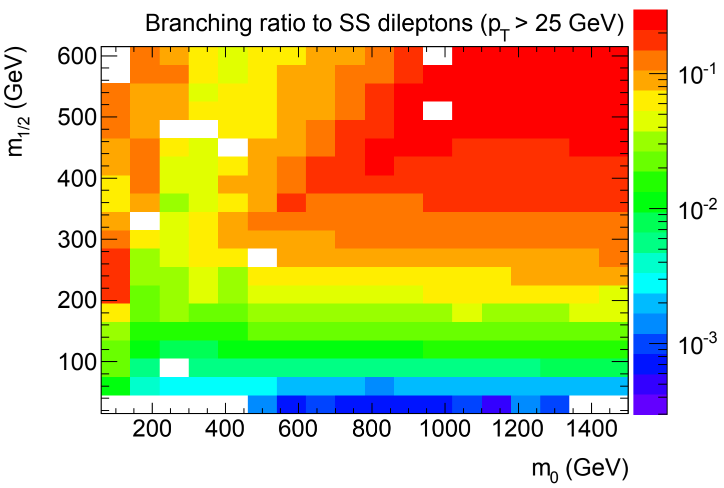

Figure 1.11: The branching ratio of SUSY events producing high momentum ($p_T > 25$ GeV) same-sign lepton pairs in the case of mSUGRA as a function of m_0 and $m_{\frac{1}{2}}$ for $A_0 = 0$ GeV, $\tan(\beta) = 10$ and $\mu > 0$. These values are obtained from simulated events. The samples used are described in Chapter 6.

Outlook

Motivated by the discussion in this chapter, specifically the prediction that supersymmetry could result in events at the LHC with lepton pairs of equal charge, we performed a inclusive same-sign dimuon cross-section measurement, which is presented in Chapter 6. We chose to focus our analysis on the production of muons, as they are experimentally relatively easy to identify and the ATLAS detector is particularly well equipped to detect them. In the following chapters we discuss the ATLAS detector (Chapter 2), its performance for muon reconstruction (Chapter 3) and describe methods to separate muon signatures depending on the muon production mechanism (Chapter 4 and 5) which are then used in the final cross-section measurement.

Chapter 2

Event reconstruction with ATLAS

As discussed in the previous chapter, one way to test for the existence of supersymmetry is to try to create supersymmetric particles in high energy particle collisions. In this thesis we analyse proton-proton collisions created at the Large Hadron Collider (LHC) and detected by the ATLAS detector, in search for such supersymmetric signatures. This chapter provides an introduction to both the LHC (Section 2.1) and the ATLAS experiment (Section 2.2), as well as a general description of how the collected data is used to reconstruct collisions and individual particles used in this thesis (Section 2.3). The ATLAS trigger system (Section 2.4) and simulation software (Section 2.5) is also discussed.

2.1 The Large Hadron Collider

The Large Hadron Collider [16] is an accelerator designed to accelerate and collide protons at a center of mass energy of 14 TeV. This high collision energy, more than seven times the energy of the previously most powerful accelerator in the world, allows for the creation and study of particles with a mass up to a few TeV and is therefore ideal for the search for supersymmetric particles.

The LHC is part of CERN, an international particle physics laboratory, located on the border between Switzerland and France, near Geneva. Apart from protons, the LHC is also able to accelerate and collide lead nuclei. Since no lead collisions are used in this thesis we limit our discussion to proton-proton collisions.

The LHC consists of a 27 km long ring of superconducting magnets designed to control the trajectory of two proton beams, circling in opposite directions along the ring. The protons, grouped in bunches, are first accelerated to an energy of 450 GeV by a chain of smaller accelerators and then injected into the LHC. Each turn around the LHC ring the protons are further accelerated up to their final energy of 7 TeV. At design capacity each proton beam consists of 2808 bunches, each containing 10^{11} protons. The minimum separation time between bunches is 25 ns.

At four different locations along the LHC ring, the two beams can collide, producing $\sqrt{s} = 14$ TeV proton-proton collisions. At design intensity, each bunch crossing results on average in 23 interactions. With a rate of about 40 million bunch crossings per second this leads to a nominal instantaneous luminosity of 10^{34} cm^{-1}s^{-1} per collision site.

Around each of the collisions sites, the detector of one of LHC's four major experiments is located. The four experiments are: ATLAS [17], CMS [18], ALICE [19] and LHCb [20]. ATLAS and CMS are so-called general purpose experiments and use detectors designed for a large variety of physics goals; from testing the SM and finding the Higgs-boson, to searching for new physics beyond the SM. ALICE is built specifically to study heavy-ion collisions, to prove and study the existence of Quark-Gluon-Plasma. LHCb is primarily built to reconstruct B-mesons, for precision measurements of CP-violation, which are sensitive to a large variety of non-SM physics signals.

The LHC in 2010 and 2011

The LHC is operational since December 2009 when the first collisions were created. These first collisions, produced by colliding two proton bunches at injection energies, had a center of mass energy of 900 GeV.

From the 30th of March 2010 until the end of 2011 the LHC has been producing collisions at $\sqrt{s} = 7$ TeV with rapidly increasing instantaneous luminosity. The current plan is to operate at $\sqrt{s} = 8$ TeV in 2012, after which a long shut-down of the machine will enable the preparation for collisions at the design energy of 14 TeV.

All analyses presented in this thesis are performed on the data collected in either 2010 or 2011. The total integrated luminosity of proton-proton collisions in those years is shown as a function of time in Figure 2.1. By the end of 2010 an integrated luminosity of 45.0 pb^{-1} of proton-proton collision data was collected, while in 2011 this was increased to 5.2 fb^{-1}. Since these two years include the starting period of the LHC, the conditions of the LHC beams, both in terms of frequency and intensity, were not constant, resulting in a wide range of recorded instantaneous luminosities. This in turn affects the trigger rates (see Section 2.4) and the average number of collisions per bunch crossings.

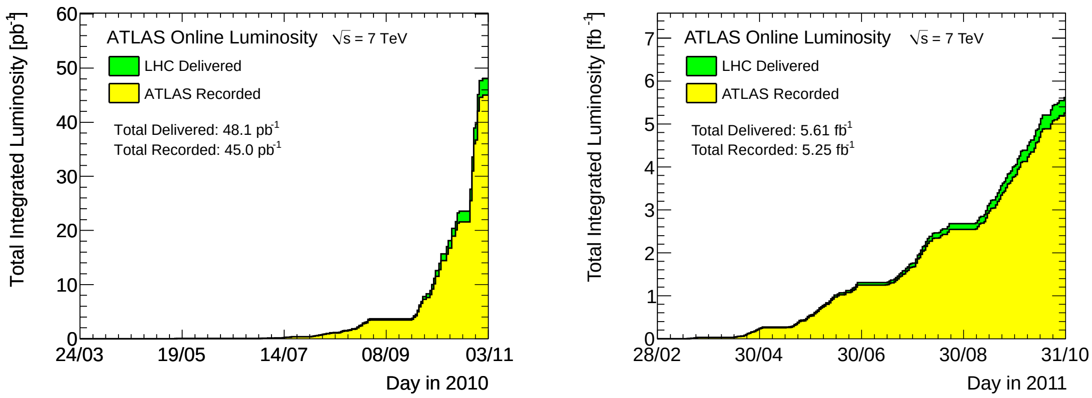

Figure 2.1: The integrated luminosity of proton-proton collisions at $\sqrt{s} = 7$ TeV provided by the LHC and collected by ATLAS in 2010 (left) and 2011 (right) as a function of time.

To facilitate discussions and the comparison of results, the data collected by ATLAS is divided into different data-taking periods in which the beam conditions and the trigger menu are relatively stable. The data periods of 2010 and 2011 are listed in Table 2.1, including the total integrated luminosity, the peak instantaneous luminosity and the resulting peak number of events per bunch crossing for each period.

Year	Period	Dates	Integrated luminosity	Peak instantaneous luminosity	Peak Events/BX
2010	A	Mar 30 - Apr 18	0.1 nb^{-1}	2.22×10^{27} $cm^{-2}s^{-1}$	0.01
	B	Apr 23 - May 16	7.9 nb^{-1}	6.00×10^{28} $cm^{-2}s^{-1}$	0.13
	C	May 18 - Jun 05	7.8 nb^{-1}	2.07×10^{29} $cm^{-2}s^{-1}$	0.17
	D	Jun 24 - Jul 18	311 nb^{-1}	1.58×10^{30} $cm^{-2}s^{-1}$	1.88
	E	Jul 29 - Aug 17	1.12 pb^{-1}	3.91×10^{30} $cm^{-2}s^{-1}$	1.56
	F	Aug 19 - Aug 29	1.96 pb^{-1}	1.02×10^{31} $cm^{-2}s^{-1}$	2.00
	G	Sep 22 - Oct 06	8.81 pb^{-1}	7.01×10^{31} $cm^{-2}s^{-1}$	2.75
	H	Oct 08 - Oct 17	8.81 pb^{-1}	1.47×10^{32} $cm^{-2}s^{-1}$	3.17
	I	Oct 24 - Oct 29	23.0 pb^{-1}	2.03×10^{32} $cm^{-2}s^{-1}$	3.71
2010	Total	Mar 30 - Oct 29	44.1 pb^{-1}	2.03×10^{32} $cm^{-2}s^{-1}$	3.71
2011	A	Mar 13 - Mar 20	8.26 pb^{-1}	1.50×10^{32} $cm^{-2}s^{-1}$	6.93
	B	Mar 21 - Mar 23	16.8 pb^{-1}	2.41×10^{32} $cm^{-2}s^{-1}$	8.39
	D	Apr 14 - Apr 28	177 pb^{-1}	6.57×10^{32} $cm^{-2}s^{-1}$	7.20
	E	Apr 30 - May 03	49.6 pb^{-1}	8.26×10^{32} $cm^{-2}s^{-1}$	7.51
	F	May 15 - May 25	150 pb^{-1}	1.10×10^{33} $cm^{-2}s^{-1}$	7.97
	G	May 27 - Jun 14	555 pb^{-1}	1.26×10^{33} $cm^{-2}s^{-1}$	7.92
	H	Jun 16 - Jun 28	275 pb^{-1}	1.26×10^{33} $cm^{-2}s^{-1}$	6.80
	I	Jul 13 - Jul 29	400 pb^{-1}	1.90×10^{33} $cm^{-2}s^{-1}$	9.14
	J	Jul 30 - Aug 04	233 pb^{-1}	2.02×10^{33} $cm^{-2}s^{-1}$	9.75
	K	Aug 04 - Aug 22	661 pb^{-1}	2.35×10^{33} $cm^{-2}s^{-1}$	11.34
	L	Sep 07 - Oct 05	1570 pb^{-1}	3.28×10^{33} $cm^{-2}s^{-1}$	15.83
	M	Oct 06 - Oct 30	1122 pb^{-1}	3.61×10^{33} $cm^{-2}s^{-1}$	32.08
2011	Total	Mar 13 - Oct 30	5.23 fb^{-1}	3.61×10^{33} $cm^{-2}s^{-1}$	32.08

Table 2.1: A list of the different data periods of proton-proton collisions collected by ATLAS in 2010 and 2011. For each period the corresponding dates and total integrated luminosity of data recorded are also included as well as the peak instantaneous luminosity achieved in that period and the resulting peak number of events per bunch crossing.

2.2 ATLAS

ATLAS is one of the two general purpose experiments at the LHC. Due to its extensive muon system, discussed in Section 2.2.4, the ATLAS detector is ideally suited for physics analyses based on muon identification and reconstruction, such as the analyses presented in this thesis.

2.2.1 General layout of the ATLAS detector

Different technologies are used to optimally identify and reconstruct particles passing though the ATLAS detector. These different technologies can be grouped into three independent subdetectors:

- **The Inner Detector:** The Inner Detector (ID) is the subdetector located closest to the interaction point. Its main purpose is to track the trajectory of charged particles and determine their momentum. Due to its proximity to the interaction point, the ID is used to reconstruct the primary vertex and possible secondary vertices in the event. The ID is discussed in more detail in Section 2.2.2.
- **The Calorimeters:** Surrounding the ID are a combination of electromagnetic and hadronic calorimeters, which measure and absorb the energy of all particles except for muons and neutrino's. These calorimeters are the only subdetectors in ATLAS able to detect photons and neutral hadrons. Furthermore the calorimeters are important for separating electrons and photons from hadrons and for determining the missing transverse energy[1] of the event. The calorimeter system is discussed in Section 2.2.3.
- **The Muon Spectrometer:** The Muon Spectrometer (MS) measures the momentum of charged particles by tracking their trajectory through a magnetic field. Due to its position behind the calorimeters, the only charged particles that reach the MS are muons. This makes the MS a very powerful system in muon identification. The MS is discussed in more detail in Section 2.2.4.

To reconstruct collision events as fully as possible the general layout of ATLAS is chosen to have close to total angular coverage. It consists of a barrel region with detector elements constructed in cylindrical layers around the beam pipe and two end-caps that close up the detector on both sides, built in discs in the transverse plane. The nominal interaction point is in the center of the detector. This design results in the roughly cylindrically shaped detector shown in Figure 2.2. In total the ATLAS detector is 44 m long, 25 m high and weighs 7000 tonnes.

The ATLAS coordinate system

For a more detailed description of the ATLAS detector, and to interpret most of the results in this thesis, knowledge of the ATLAS coordinate system is necessary.

The origin of the ATLAS coordinate system is at the nominal interaction point in the centre of the detector. The z-axis lies along the beam-line and the x- and y-axis define the transverse plain, with the positive x-axis pointing toward the centre of the LHC ring and the positive y-axis pointing upwards.

For most purposes a spherical coordinate system is used. The ϕ-angle is defined in the transverse plane with $\phi = 0$ on the positive x-axis. ϕ runs from $-\pi$ to π with positive/negative values corresponding with the top/bottom half of the detector. The angle to

[1]The missing transverse energy is discussed in Section 2.3.4.

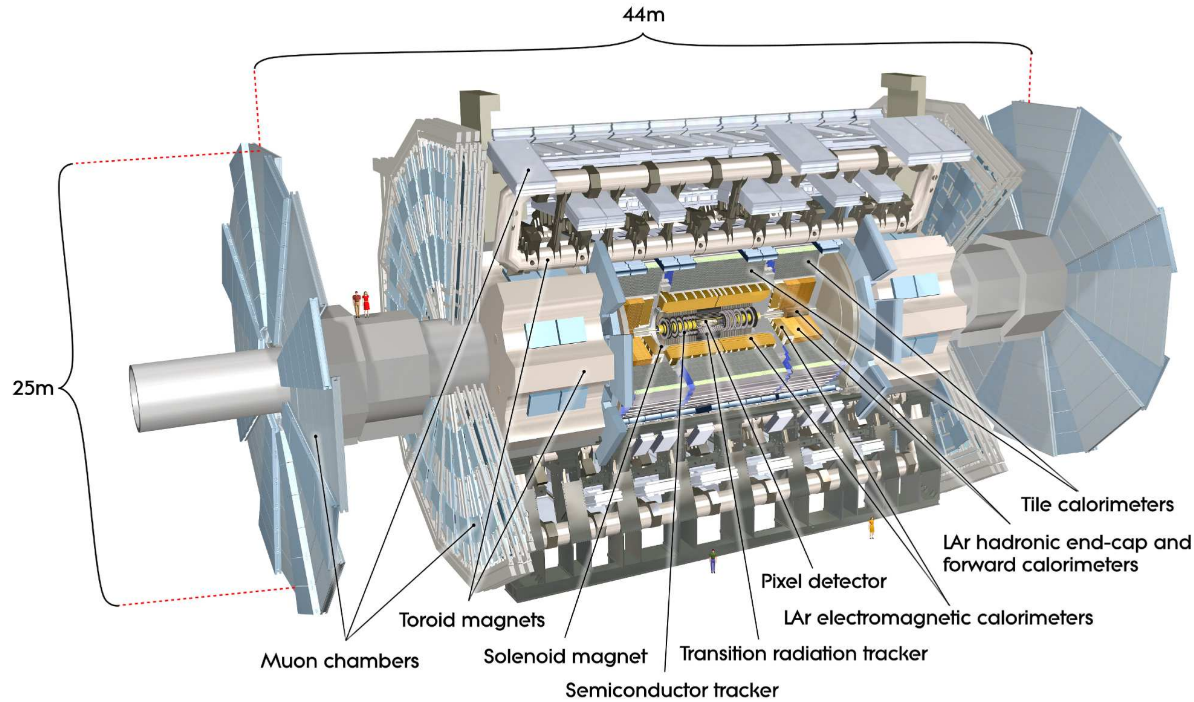

Figure 2.2: Cut-away view of the ATLAS detector [17].

the positive z-axis is denoted as θ, and runs from 0 to π. Instead of θ, the pseudorapidity, η, is often used: $\eta = -\ln(\tan(\frac{\theta}{2}))$, with $\eta = 0$ corresponding to the (z = 0)-plane

2.2.2 The Inner Detector

The ID is designed to reconstruct the trajectory of all charged particles with $|\eta| < 2.5$ and $p_T > 100$ MeV. Relying on a magnetic field of 2 T, generated by a superconducting solenoid magnet surrounding the ID, the ID can measure the momentum of these particles with a design resolution of $\frac{\sigma_{p_T}}{p_T} = 0.05\%\ p_T(\text{GeV}) \oplus 0.1\%$.

To optimise the precision of the track reconstruction while limiting the amount of material and therefore the energy loss and scattering of particles before the calorimeters, different technologies are used to track the particles trough the ID volume. Closest to the interaction point are solid silicon pixels. Their high granularity is necessary to separate hits in events with high track multiplicities and to provide high precision position measurements essential for the reconstruction of vertices. Surrounding the pixel detector is the semi-conductor tracker (SCT), where solid silicon strips give additional 3-D position measurements. The rest of the ID consists of a gaseous detector called the transition radiation tracker (TRT) with a much lower material density than the silicon detectors. This allows the TRT to measure tracks in a large volume. The TRT can only provide 2-D position measurements with a poorer resolution than the silicon detectors, however because of the large number (on average 30) of hits per track over a relatively large distance, the TRT significantly contributes to a good momentum resolution of the tracks. Figure 2.3 shows a cut-away view of the ID.

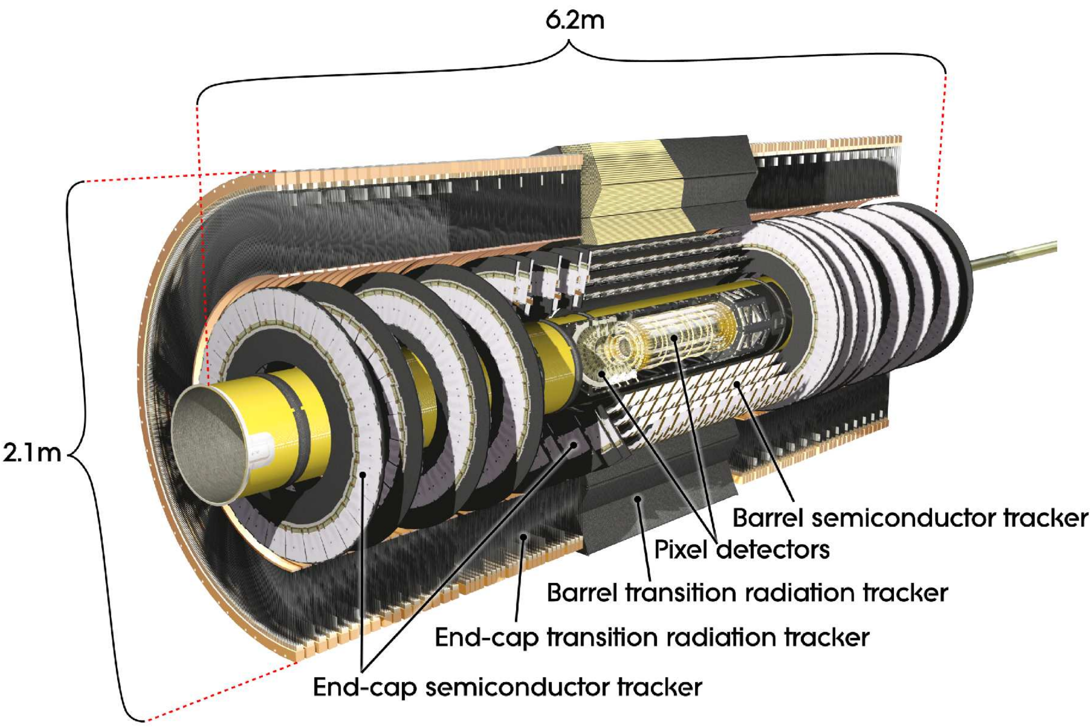

Figure 2.3: Cut-away view of the ATLAS Inner Detector [17].

The pixel detector

The pixel detector tracks the trajectory of charged particles using solid silicon pixel sensors, which operate based on the semiconducting properties of silicon. Each pixel is kept under a voltage of 150 V which ensures that the silicon is fully depleted of free electrons. As charged particles traverse this depleted silicon layer, the atoms are ionized, freeing new electrons. The resulting current is then measured by the pixel electronics. The spacial resolution of the individual pixel sensors is of the order of $10 \times 115\ \mu\text{m}^2$ in $\text{R} - \phi \times \text{z}$.

The first layer of pixels in the barrel region, called the B-layer, is located at only 5.05 cm from the beam line and therefore provides the most important measurement for the reconstruction of primary and secondary vertices in the event. Both the barrel and end-caps of the pixel detector consist of three detector layers.

The measured hit efficiency in the different pixel layers is shown in top left plots of Figure 2.4. Most pixel layers have a hit efficiency of about 99% with a slightly lower efficiency, still over 97%, in the outer end-caps discs due to some dead regions. The measured efficiency of 100% in the B-layer is due to a B-layer hit requirement in the track-selection for this plot.

The SCT

The semi-conductor tracker (SCT), surrounds the pixel detector and is designed to add four additional space-points to each track in the $|\eta| < 2.5$ region. The SCT is based on a similar technology as the pixel detector, but instead of using pixels, it consists of silicon strips. Each silicon strip provides a 2-D position measurement, as no position information along its length is available. Three-dimensional space point are constructed by combining the information of two silicon strip layers. All SCT detector layers are therefore double layered with an angle of 40 mrad between the strips in these layers. On average the SCT provides 8 hits per track, corresponding to four space points with a resolution of approximately 17 μm in the R-ϕ plane and 580 μm in the z- (barrel) or R- (end-caps) direction.

The hit efficiency of the SCT is about 99.9% in the barrel and 99.8% in the end-caps, as shown in Figure 2.4.

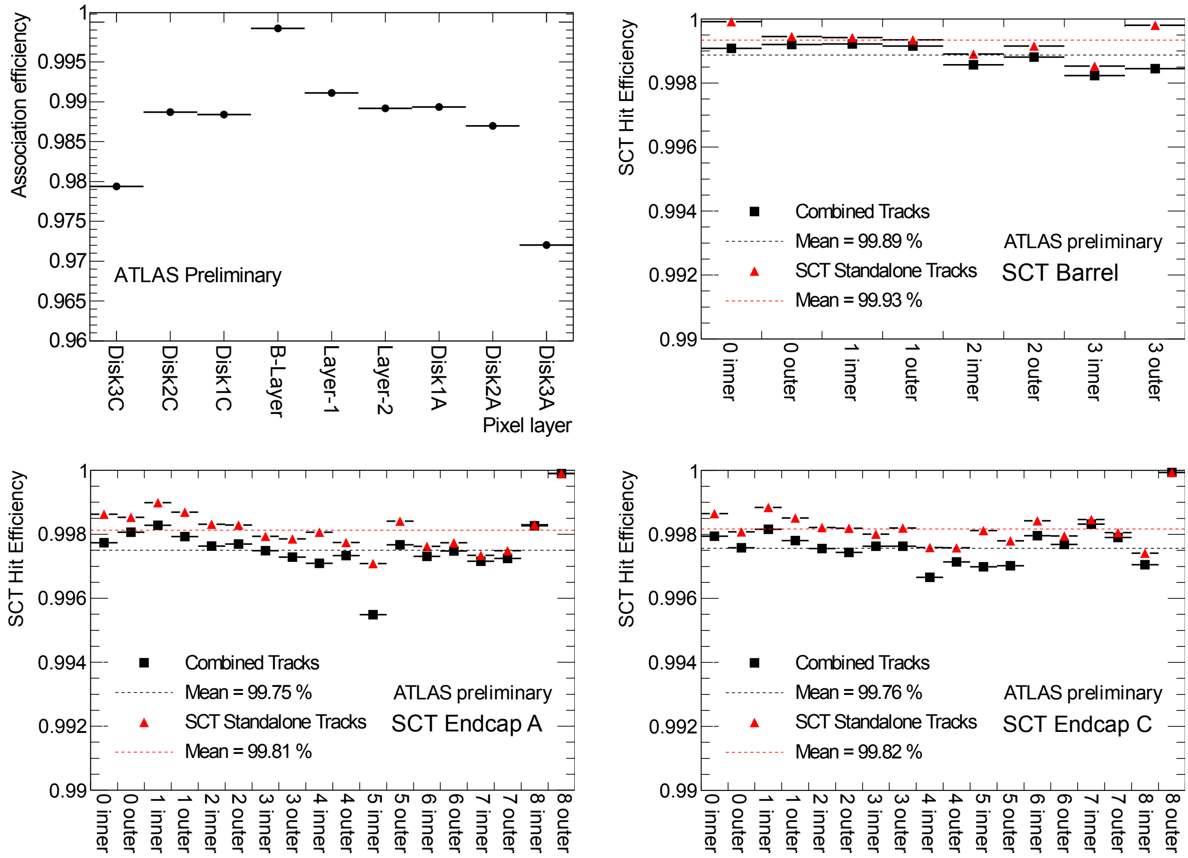

Figure 2.4: The efficiency for a track to have a hit associated when crossing a pixel layer (top left) or a barrel (top right) or end-cap (bottom left and right) SCT layer.

The TRT

Unlike the pixel detector and the SCT, the TRT does not use silicon, but consist of gaseous drift tube elements. These drift tubes, named straws, have a diameter of 4 mm, a length up to 144 cm and are filled with a gas mixture. As charged particles traverse a straw, the gas is ionised along the particle trajectory, and electrons drift under an electric field towards a wire located in the center of the tube. The drift time is used to calculate the distance of closest approach. This leads to a resolution of 130 μm in the direction perpendicular to the straw length. As was the case for the silicon strips, no information about the hit location along the straw length in possible.

In the barrel region the straws are located in layers around the beam-pipe, from a distance of 55.4 to 108.2 cm. The tubes are positioned parallel to the z-axis and therefore do not provide any η information. In the end-caps, which cover the region up to $|\eta| = 2.0$ the straws are mounted radially, pointing away from the beam line. On average the TRT provides 30 to 36 hits per track.

The hit efficiency of the TRT straws depends on the distance between the particle trajectory and the wire. For distances of less than 1 mm this efficiency is approximately 94%.

2.2.3 The calorimeter system

Surrounding the solenoid magnet encompassing the ID, are a number of calorimeters, which measure the energy of strongly and electromagnetically interacting particles. Unlike the ID, the calorimeters are not only able to detect and measure charged particles but also neutral hadrons and photons. Only purely weakly interacting particles, such as neutrinos, pass through the calorimeters undetected.

The main goals of the calorimeters are to measure the energy of individual particles, to help separate electrons and photons from hadrons and to calculate the amount of missing transverse energy, E_T^{miss}, in an event. This last parameter is important, as it is the only way to obtain information about purely weakly interacting particles that otherwise pass though the ATLAS detector undetected.

To ensure maximum angular coverage, necessary to accurately measure E_T^{miss}, the calorimeter system does not only include the usual barrel and two end-caps, which cover the area $|\eta| < 3.2$, but also additional forward calorimeters for the $3.2 < |\eta| < 4.9$ regions. The position of the different calorimeters is illustrated in Figure 2.5.

Operating principle

All the calorimeters of ATLAS are built based on the same detection principle. They contain an absorber material which interacts with incoming particles, causing a shower of new particles. These particles are then measured in an active material. Ideally the amount of created new particles is proportional to the energy of the incoming particle. By alternating layers of absorber and active material, the full length of the shower can be measured. If the sampling fraction of the calorimeter, the fraction of energy measured, is known, the total energy of the incoming particle can be calculated.

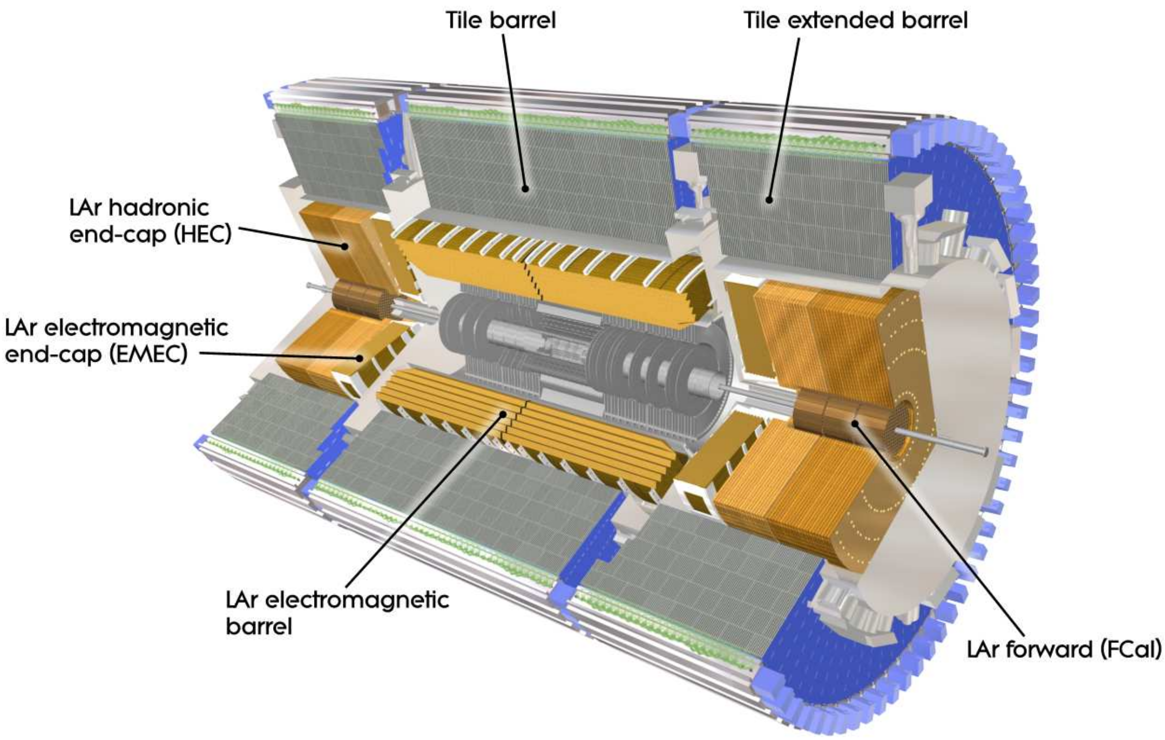

Figure 2.5: Cut-away view of the ATLAS calorimeter system [17].

We distinguish two types of showers: electromagnetic (EM) and hadronic. EM showers are produced by photons and electrons. The photons interact with the electrons in the absorber, creating an electron-positron pair. The electrons and positrons in turn loose energy by ionizing the material, or via bremsstrahlung, creating photons. These processes together produce a shower with an increasing amount of EM particles, with decreasing energy, until all energy is absorbed. Hadrons on the other hand, interact with the material through strong interactions with nuclei. This process scatters the original particle producing a shower of lower energy hadrons. As this typically includes a large number of π^0's, which decay to two photons, hadronic showers also contain an EM component.

As EM showers generally traverse less material than hadronic showers, separate EM calorimeters are used. These calorimeters are used to optimise the spatial and energy resolution for photons and electrons. Only the most energetic EM showers reach the hadronic-calorimeters, located behind the EM-calorimeters. The hadronic-calorimeters have a much stronger absorbing power, ensuring a minimum of punch-troughs to the muon system.

The only charged particles that pass through the calorimeters without loosing all their energy are muons. The reason for this is that, just as for electrons, their dominating source of energy loss in material is through the emission of photons, which is inversely proportional to the particle mass. As muons are much heavier than electrons they only loose a fraction of their energy. On average muons loose about 3 GeV of energy when traversing the calorimeters in the barrel region and about 6 GeV in the end-caps.

Electromagnetic calorimeters

The EM-calorimeters in the barrel, $|\eta| < 1.475$, and the two end-caps, $1.375 < |\eta| < 3.2$, use liquid argon as active material and lead plates as absorber. The total depth of the EM-calorimeter is more than 24 radiation lengths throughout the covered η region, where a radiation length is defined as the average distance over which an electron looses all but $1/e$ of its energy. This ensures that all but the most energetic EM-showers are fully contained in the EM-calorimeters.

The design energy resolution of the EM-calorimeter is $\frac{\sigma_E}{E} = 10\% \sqrt{E} \oplus 0.7\%$ (E in GeV) with a typical granularity of $\Delta\eta \times \Delta\phi = 0.025 \times 0.025$. Full R-$\phi$ coverage is achieved by using accordion shaped absorber plates that remove any gaps between the detector units.

Hadronic calorimeters

The hadronic-calorimeters in the barrel, $|\eta| < 1.7$, and end-caps, $1.5 < |\eta| < 3.2$, are designed to measure the energy of hadronic showers with a resolution of $\frac{\sigma_E}{E} = 50\% \sqrt{E} \oplus 3\%$ (E in GeV). A depth of at least 10 interaction lengths ensures a minimum of punch-troughs to the MS.

The barrel hadronic calorimeter consists of scintillator tiles surrounded by the absorber material, steel. As shown in Figure 2.5, this tile calorimeter is divided into three main parts separated by gaps of at most 60 cm, at $|\eta| \sim 0.9$. These gaps are necessary to leave room for cables from the ID, as well as power supplies for the EM-calorimeter barrel. Part of the reduced resolution in those regions is recovered by plug tile calorimeters and additional scintillator elements.

The hadronic-calorimeter end-caps use liquid argon as active material and copper plates as absorber.

Forward calorimeters

The forward calorimeters, both EM and hadronic, use liquid argon as active material, with copper (EM) or tungsten (hadronic) as absorber. Unlike the more central liquid argon calorimeters, they do not consist of alternating layers or active and absorber material. Instead the liquid argon is limited to small longitudinal holes in the surrounding absorber material. This design limits problems due to ion build-up caused by the high particle fluxes in these forward regions. The forward calorimeters are designed with an energy resolution of: $\frac{\sigma_E}{E} = 100\% \sqrt{E} \oplus 10\%$ (E in GeV).

2.2.4 The Muon Spectrometer

Surrounding the hadronic calorimeters is ATLAS' largest subdetector, the Muon Spectrometer (MS), which measures the momentum of charged particles. Due to its position behind the calorimeters the only charged particles to reach the MS are muons, making the MS a very effective instrument to identify and trigger muons. The general layout of the MS is illustrated in Figure 2.6.

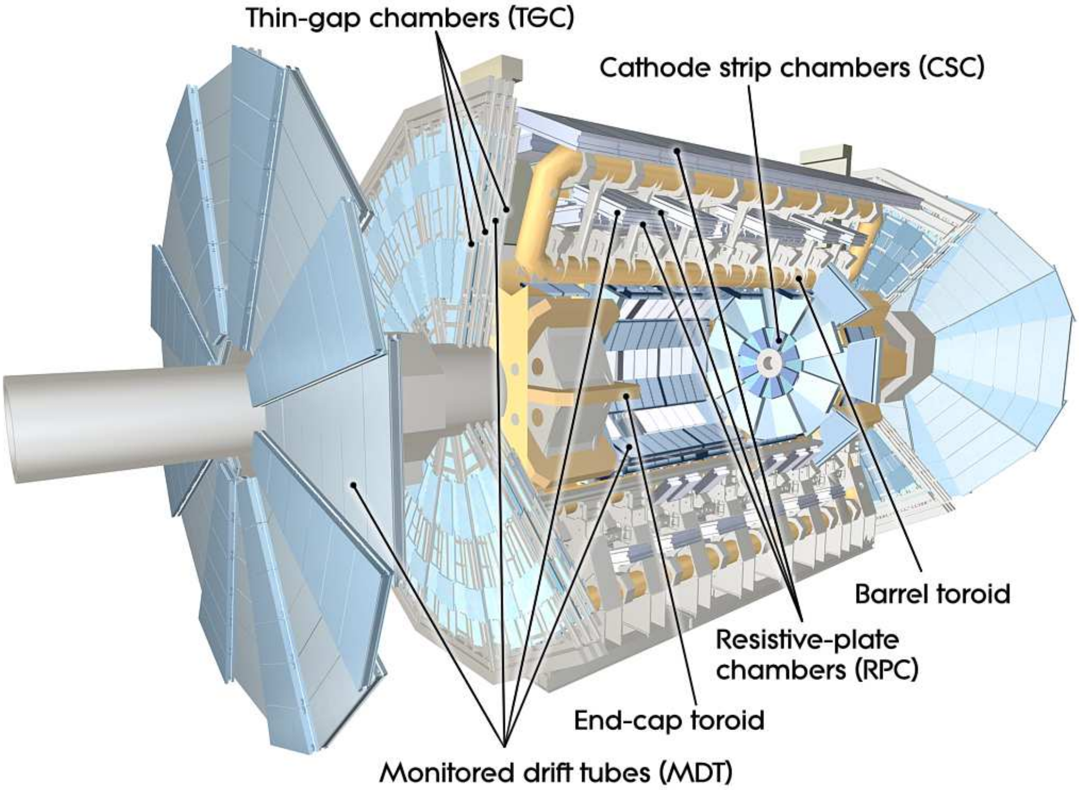

Figure 2.6: Cut-away view of the ATLAS Muon Spectrometer [17].

The MS measures the momentum of charged particles by tracking their trajectory trough a magnetic field. This field is provided by eight barrel and two end-cap superconducting toroid magnets which generate a strong but inhomogeneous magnetic field of 0.15-2.5 T in the barrel and 0.2-3.5 T in the end-caps. By measuring the muon trajectory in at least three different locations in this known magnetic field, the MS is able to provide a momentum measurement which is independent of any other subdetector. Furthermore due to its large size, with a distance between the inner and outer position measurement of at least 5 m, the MS is able to measure the momentum of high energetic muons for which the bending power in the ID is insufficient to provide reliable results. The MS is able to measure muon momenta up to 1 TeV with a resolution of $\frac{\sigma_{p_T}}{p_T} = 10\%$.

Four different technologies are used to provide the required position measurements: Monitoring Drift Tubes (MDTs), Cathode Strip Chambers (CSCs), Resistive Plate Chambers (RPCs) and Thin Gap Chambers (TGCs).

Monitoring Drift Tubes

Monitoring Drift Tubes (MDTs) are used to provide the precision measurement of muon tracks in most of the MS volume. They consist of aluminium tubes with a diameter of 30 mm, filled with a gas mixture. Muons traversing these tubes leave a trail of ionized gas along their trajectory. The freed electrons drift under the influence of an electric field towards a wire located in the center of the tube. The drift time is used to determine the distance of closest approach, resulting in a position resolution of 80 μm in the transverse plane of the tubes. No position determination along the tube length is possible.

The individual tubes are grouped into MDT modules, consisting of two multi-layers of 3 or 4 MDT layers placed slightly apart. This construction leads to a combined resolution of 35 μm per module. As all tubes in the modules are placed parallel to each other, the MDT modules only provide a 2-D position measurement.

Cathode Strip Chambers

Due to the relative long drift time of electrons in the MDTs, they do not function properly at counting rates above 150 Hz/cm^2. Therefore Cathode Strip Chambers (CSCs) are used closed to the beam-pipe, where the particle flux is highest.

The CSCs consist of two layers of strips separated by a gas mixture. Just as with the MDTs the gas get ionized by traversing muons and the freed electrons drift under an electric field to wires located between the strip plates. This in turn induces a charge in the surrounding strips, which is used to measure the position of the muon. By placing a 90° angle between the strip orientation of the two layers, 3-D position measurements can be obtained. The resolution of the CSCs is 40 μm in the direction of the bending plane and 5 mm perpendicular to this plane.

Trigger chambers: Resistive Plate Chambers and Thin Gap Chambers

As the drift time of electrons in the MDTs is approximately 700 ns, and the minimum bunch crossing of the LHC is 25 ns, MDTs can not easily be used in the initial stage of the trigger system. Therefore separate trigger chambers are installed. Two types of trigger chambers are used: Resistive Plate Chambers (RPCs) and Thin Gap Chambers (TGCs).

RPCs consist of two plates kept at a high voltage and separated by a 2 mm gap filled with a gas mixture. As muons ionize the gas, the freed electrons drift within 5 ns toward one of the plates, which in turn induces a charge in metallic strips placed on the outside of the plate. Separate RPCs are used to measure the η and ϕ coordinates of tracks. The obtained position resolution is approximately 10 mm.

TGCs also consist of two plates separated by a gas-mixture which gets ionized by the passage of a muon. An electric field causes the freed electrons to drift towards wires located between the plates, which measure the position coordinate. Just as for the RPCs, different chambers are needed to measure the ϕ and η components. The resolution of the TGCs is 2-7 mm.

Layout of the Muon Spectrometer

Figure 2.6 and 2.7 show the layout of the MS and the approximate position of the individual detector layers. The layout is dominated by the toroid magnets which automatically introduce an eight-fold symmetry in the ϕ direction. This led to a construction based on 16 ϕ-sectors, where 8 small sectors are located around the toroids with 8 large sectors in between. The sectors overlap over small regions of ϕ both to ensure a full ϕ-coverage, and to provide information for sector to sector alignment.

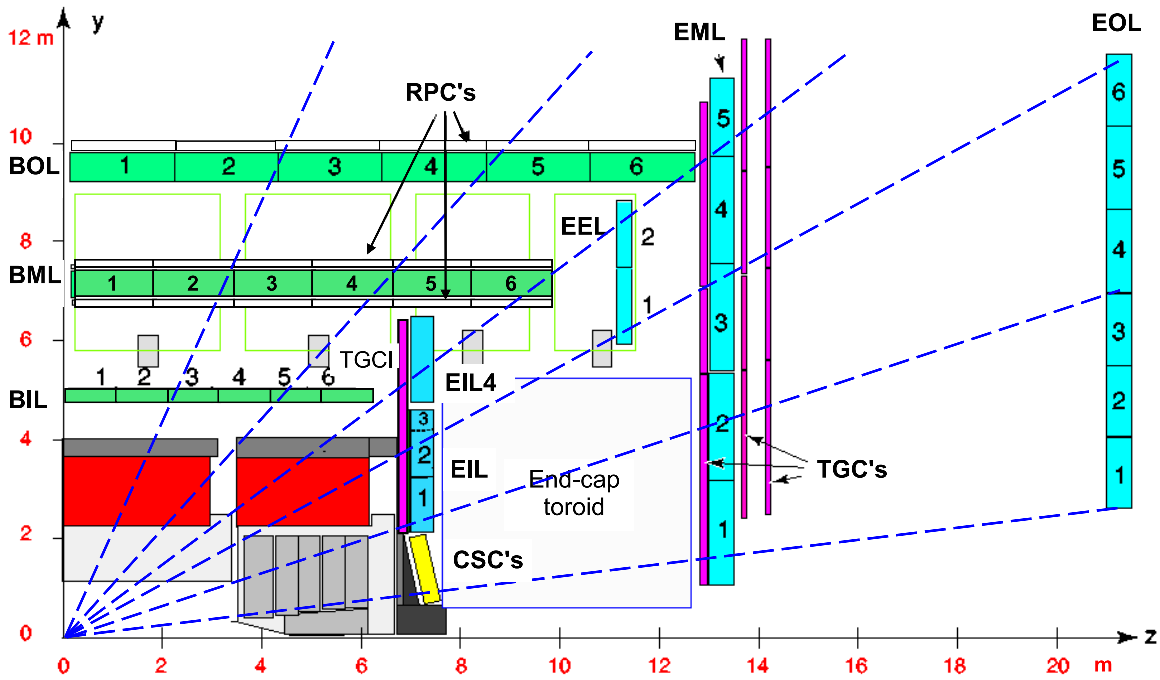

Figure 2.7: Cross-section of the muon system in a plane containing the beam axis [17].

In the barrel region, $|\eta| < 1.05$, both the large and small sectors consist of three layers of MDT modules, positioned at approximately 5.0, 7.5 and 10.0 m from the beam-line, where the exact distance depends on the sector. These modules are positioned to measure the z-coordinate of the tracks, corresponding to the muon bending plane. The ϕ coordinate is provided by the trigger chambers. In the barrel region these are RPCs.

A gap of at most one meter is left between the detector modules in the middle of the barrel ($|\eta| = 0$), to allow room for cables for detectors closer to the interaction point. Unfortunately this gap makes it impossible for the MS to measure high energetic muons at $|\eta| \sim 0$. These muons can only be measured by the ID and the calorimeters.

At the bottom of the detector the MS barrel includes some additional support structure necessary to carry the weight of the ATLAS detector. In these so-called feet regions the acceptance of the MS is somewhat reduced.

The MS end-caps, $1.05 < |\eta| < 2.7$, consist of four disk-shaped detector layers. Three disks provide an inner, middle and outer measurement for forward muons. The fourth disk (named EE), between the inner and outer disk, does not extend to $|\eta| = 2.7$ but provides a third measurement for muons passing though the barrel-end-cap transition regions, which might miss the end-cap outer disk. As in the barrel, MDT chambers provide the track position measurement for most of the MS end-cap volume, with the exception for the region closest to the beam-pipe. On the inner-disk, for $2.0 < |\eta| < 2.7$, CSCs are used, which are better equipped to handle high particle fluxes.

TGCs are used to provide the trigger in most of the end-cap region, as well as to provide a ϕ measurement to be combined with the MDT η precision measurements into 3-D position coordinates. In the region covered by CSCs no separate trigger chambers are necessary, as the CSC drift time is small.

This description of the MS end-caps describes the design layout of the MS. Unfortunately most detector units in the EE disk are not yet installed and will only be added in the next long shut-down of the LHC, scheduled at the end of 2012. Therefore some tracks in the barrel-end-cap transition regions, $1.0 \leq |\eta| < 1.4$, are currently only measured at two positions, leading to a poorer momentum resolution. This is discussed in more detail in Chapter 3.

The MS alignment system

To achieve the design momentum resolution of 10% for muons with an energy of 1 TeV, the position of individual chambers must be known with an accuracy of 30 μm. This high level of alignment precision is partially achieved using an optical alignment system based on measurements from three point straightness monitors: light from an illuminated target is focussed through a lens onto image sensors. By analysing distortions in the recorded image, any shifts of the target relative to the sensor, as well as any rotation along the target-sensor axis, can be calculated. The optical alignment system monitors chamber-to-chamber positions within the MS as well as deformities of the MDT tubes due to gravity. It is designed to measure relative changes in the chamber position with a resolution of 20 μm in the barrel region and 40 μm in the end-caps. The absolute chamber position is less well-measured with a typical accuracy of a few hundred microns.

A track based alignment procedure is used to determine the relative barrel to end-cap position and their position with respect to the rest of the ATLAS detector, as well as to improve on the position determination of the individual MS chambers. Track based alignment of the detector may improve with more data and efforts to improve the alignment are still ongoing. To illustrate the quality of the alignment at the end of 2011, Figure 2.8 shows the uncertainty on the sagitta for tracks passing through the different sectors as a function of η. The yellow bands indicate a spread of 100 μm. With this level of alignment the corresponding uncertainty on the momentum resolution of MS tracks is $\frac{\sigma_p}{p} = 0.13p(\text{TeV})$ in the barrel, $\frac{\sigma_p}{p} = 0.17p(\text{TeV})$ in the MDT end-caps and $\frac{\sigma_p}{p} = 0.15p(\text{TeV})$ in the CSC end-caps.

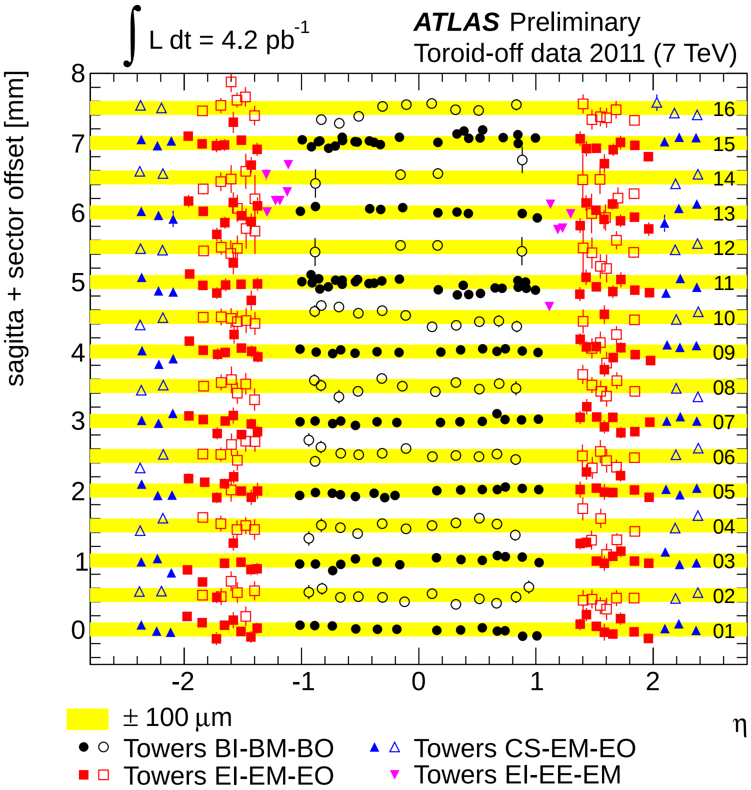

Figure 2.8: The mean value of the sagitta of MS tracks as a function of η for the different MS sectors as obtained from a run in March of 2011 with the toroid magnets off. Open shaped markers indicate the measured values for the small sectors while filled markers correspond to the large sectors. The marker shape and colour separates tracks passing trough barrel towers (black circles), end-caps towers with three MDT layers (red squares) and end-caps towers with the inner layer consisting of CSCs (blue triangles).

2.2.5 The ATLAS detector up to the end of 2011

The ATLAS detector has been operational for a number of years collecting large amounts of data. Before the start-up of the LHC this data was limited to the measurement of muons from cosmic rays, which were used to test, understand and align the detector. In 2010 and 2011 the ATLAS detector was used to record an integrated luminosity of over 5.2 fb^{-1} of collision data, which is over 93% of the integrated luminosity provided by the LHC. The fraction of time that each subdetector system was operational during data-taking is shown in Table 2.2.

2.3 Object reconstruction

The main purpose of ATLAS is to study particles created in the hard scattering of proton-proton collisions. Most of these particles are highly unstable and decay before reaching

detector component	operational
Inner Detector	
Pixel	$\approx 96.4\%$
SCT	$\approx 99.2\%$
TRT	$\approx 97.5\%$
Calorimeter	
Electro-magnetic	$\approx 99.8\%$
Tile calorimeter	$\approx 96.2\%$
Hadronic, end-cap	$\approx 99.6\%$
Forward calorimeter	$\approx 99.8\%$
Muon Spectrometer	
MDT	$\approx 99.7\%$
CSC	$\approx 97.7\%$
RPC	$\approx 97.0\%$
TGC	$\approx 97.9\%$

Table 2.2: The approximate fraction of time that each individual subdetector system was operational during data-taking.

the first detector layer and can therefore only be studied by reconstructing and identifying their longer lived decay products.

In this section we discuss how signals in ATLAS are used to identify and reconstruct muons, vertices and jets and to calculate the missing transverse energy of events. The reconstruction of other particles, such as electrons and photons, is not discussed as these particles are not used in any of the analyses presented in this thesis.

2.3.1 Muons

Muons play a central role in this thesis. In ATLAS they are measured independently by both the ID and the MS, leaving only a small energy deposit in the calorimeters. Therefore the main muon reconstruction algorithms consist of measuring and reconstructing the ID and MS tracks independently and then combining these tracks into so-called combined muons.

Inner Detector tracks

As discussed in Section 2.2.2, the ID consists of three different subdetectors: the pixel, SCT and TRT, where the pixel and SCT detector provide 3-D space-points measurements[2] while the TRT gives 2-D position information. For this reason ID tracks are first identified and reconstructed using only the silicon detectors and then, when applicable, extrapolated

[2] The 3-D space points in the SCT are constructed from hits in two neighbouring layers, as discussed in Section 2.2.2.

to the TRT volume. This is only done if the resulting track has a better χ^2 than the original silicon-only track.

The overall performance of the ID tracking depends on the pseudorapidity and momentum of the ID tracks. Figure 2.9 shows the ID track efficiency for muons with $p_T > 20$ GeV as a function of η. The tracking has an efficiency of 99% in most of the detector with a slightly lower efficiency of 98% in the barrel to end-cap transition regions. The reconstructed track resolution in terms of momentum and impact parameter resolution are discussed in Chapter 3 and 5 respectively.

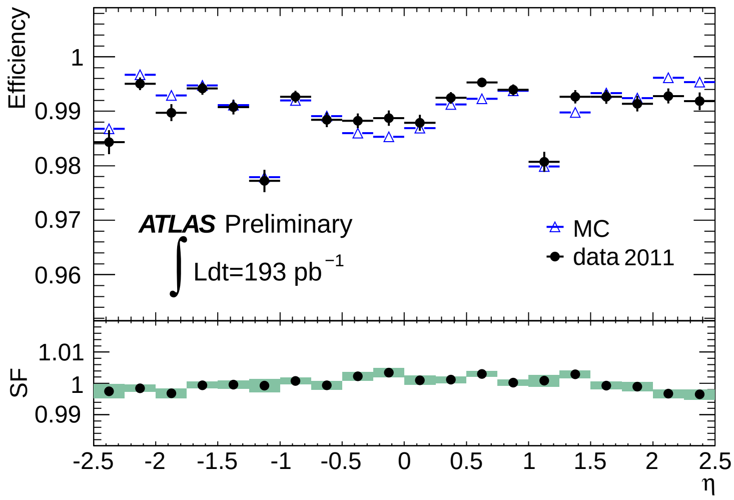

Figure 2.9: The measured ID tracking efficiency for muons with $p_T > 20$ GeV as a function of η in data (black) and simulation (blue).

Muon Spectrometer tracks

As discussed in Section 2.2.4 the MS is designed such that most muons with $|\eta| < 2.5$ and with sufficient energy to traverse the calorimeters are measured by at least three detector stations denoted as the inner, middle and outer stations. Each station consists of 6 to 8 detector modules.

The MS tracking algorithms start by reconstructing track segments within each layer. Different segments are then combined into MS tracks. These tracks can then be extrapolated back to the interaction point to estimate the muon properties before traversing the calorimeters.

Combined muons

Using only the ID information it is not possible to separate muons from other charged particles. However due to its position close to the interaction point and before the calorimeters it is typically able to reconstruct the impact parameter of muon track with better position resolution than the MS. The best reconstructed muon tracks are therefore obtained by combining the stand-alone ID and MS tracks into combined muons.

Two different algorithms are used in ATLAS to reconstruct combined muons. The Staco algorithm uses a statistical method to combine the two individual tracks. The resulting combined muon parameters are a weighted combination of the ID and MS stand-alone parameters. The Muid algorithm on the other hand performs a full refit of the combined muons using the hits of the ID and MS tracks. Both algorithms have similar performance in terms of track resolutions. In this thesis we only use muons reconstructed by the Muid algorithm, which have a slightly better reconstruction efficiency.

Figure 2.10 shows the Muid combined muon reconstruction efficiency for muons with $p_T > 20$ GeV as a function of η (left), as well as the efficiency as a function of p_T for muons from a J/ψ (right). The lower efficiency in the central detector region is due to the gap in the MS at $\eta \sim 0$ discussed in Section 2.2.4. Outside this region the efficiency is almost constant at $\sim 98\%$ for all combined muons with $p_T > 6$ GeV. For low momentum muons the efficiency drops rapidly due to the energy loss of muons in the calorimeters, which results in very low momentum muons either being fully absorbed before reaching the MS or having insufficient energy remaining to reach the middle and/or outer stations.

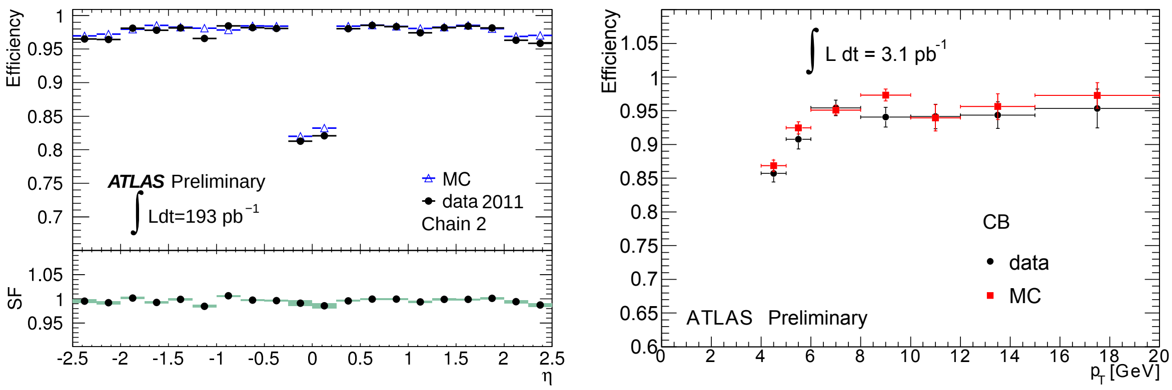

Figure 2.10: Left: The measured Muid combined muon reconstruction efficiency for muons with $p_T > 20$ GeV as a function of η in data (black) and simulation (blue). Right: The measured Muid combined muon reconstruction efficiency for muons from J/ψs as a function of p_T in data (black) and simulation (red).

To provide an estimate of the relative contribution of the ID and MS information to the combined momentum resolution of muon tracks, Figure 2.11 shows the mass resolution of reconstructed combined $\mu^+\mu^-$ pairs in the Z-boson peak in data (black) and simulation (red) as a function of η. The bottom plot shows the resolution obtained using the combined track information, while the top plots show the resolution using only the ID and MS tracks respectively. In this momentum range the combined tracks provide significantly better momentum resolutions than either subdetector alone. For low momentum muons the resolution is dominated by the ID information as the MS track suffers from the uncertainty in the energy loss of the muon in the calorimeters, while at higher momentum the MS resolution dominates due to its larger size and therefore better accuracy on the curvature of the tracks. The momentum resolution of reconstructed muons is discussed in more details in Chapter 3.

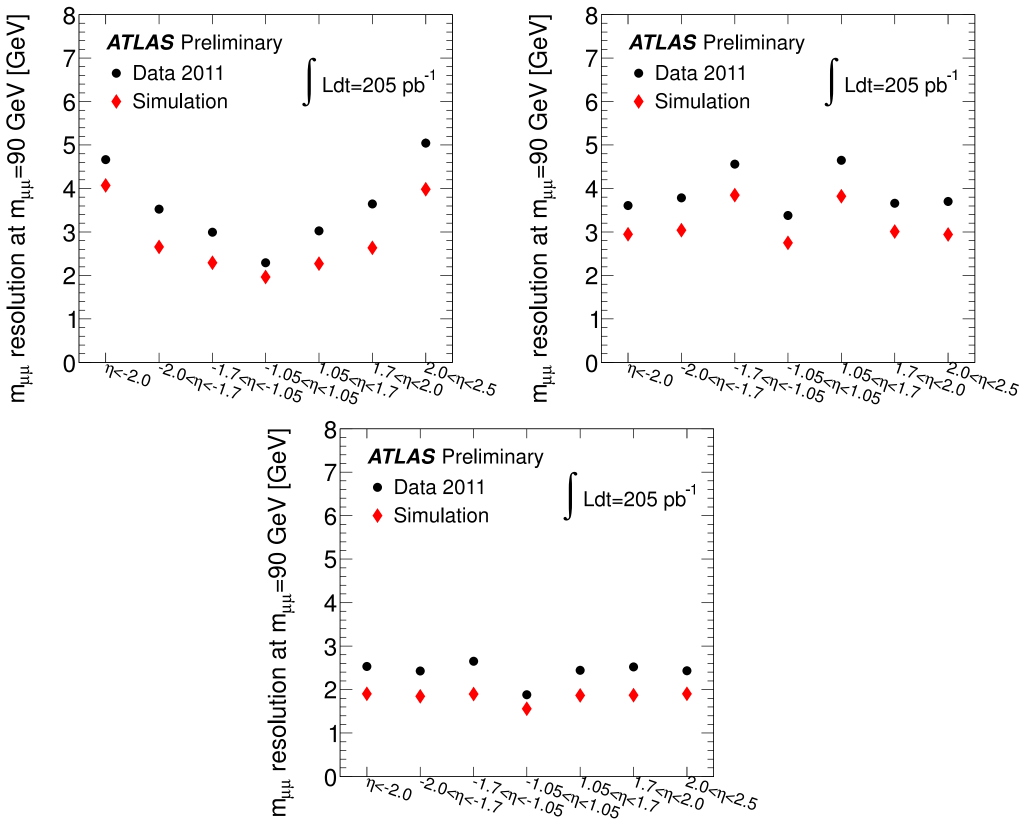

Figure 2.11: The mass resolution in data (black) and simulation (red) of reconstructed combined $\mu^+\mu^-$ pairs in the Z-peak obtained using stand-alone ID (top left), stand-alone MS (top right) and combined muon (bottom) tracks.

Basic muon selection

The following basic muon selection is used for all analyses in this thesis.

- It is a combined muon reconstructed by the Muid algorithm (see Section 2.3.1)
- $|\eta| < 2.5$

Additional selection requirements based on p_T and the number of hits on the muon tracks are also used, but depend on the analysis. These additional requirements are listed per analysis in their corresponding chapter.

2.3.2 Primary Vertex

The primary vertex of an event is reconstructed using the ID tracks created by charged particles. This is done by pre-selecting tracks that are compatible with being produced close to the collision region, the so-called beam spot[3]. Only tracks with $p_T > 400$ MeV, at least 4 hits in the SCT detector and 6 hits in the combined silicon detectors are used.

Each selected track is back-extrapolated to the beam-spot. The z-coordinate of the point of closest approach of the tracks is then used to determine a vertex seed, by looking for the global maximum of this distribution. Tracks close to this seed are combined into a vertex using a χ^2 fitting algorithm. During this process tracks that are incompatible with the fitted vertex by more than approximately 7 σ are excluded from the fit and used to seed a possible new vertex. This process results in a number of possible primary vertices per event. The main primary vertex of the event is defined as the vertex with the highest $\sqrt{\sum p_T^2}$, where the summation is over all tracks used in the vertex fit.

The position resolution of the reconstructed vertices depends on the number of tracks associated to the vertex but also on the momentum of these tracks. This is because higher momentum tracks are straighter and therefore have a better position accuracy on their track extrapolation than lower momentum tracks. Figure 2.12 shows the position resolution in the transverse plane (represented by the x-axis) of reconstructed vertices as a function of $\sqrt{\sum p_T^2}$ (right).

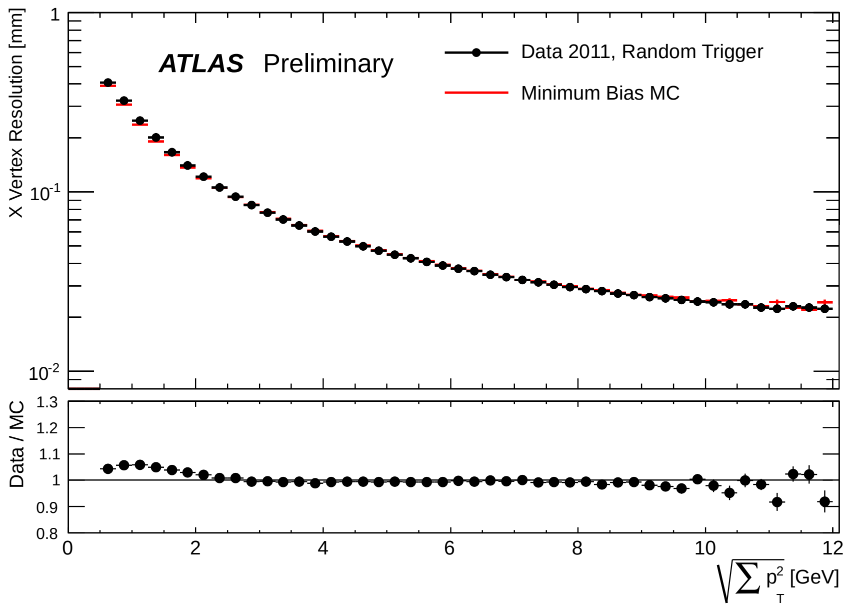

Figure 2.12: The reconstructed vertex position resolution as a function of $\sqrt{\sum p_T^2}$ in data (black) and simulation (red).

[3]The determination of the beam-spot is described in Ref. [21]

Basic primary vertex selection

In this thesis we use the primary vertex reconstruction primarily to calculate the impact parameter of muon tracks. The following basic selection is applied:

- The vertex has the highest $\sqrt{\sum p_T^2}$ in the event.
- The vertex contains at least 3 tracks. (This is to reject vertices reconstructed from cosmic muons.)

2.3.3 Jets

Quarks and gluons are produced in the vast majority of collisions at the LHC. As these particles carry colour charge they are always produced as part of a colour neutral group of particles. Due to the high energy of the collisions, the individual quarks and gluons are typically highly boosted in separate directions, thereby separating colour partners. The energy involved in this process is sufficient to create new coloured particles, which together with the original quarks and gluons produce new colour neutral states. These states then hadronize into hadrons which might in turn decay to other hadrons and leptons. This process results in jets of particles which together provide an estimate for the momentum of the original coloured particle.

Multiple algorithms are used to reconstruct jets. The one used in this thesis is based on combining the information of topological clusters of energy in the calorimeter using an anti-k_T algorithm. As jets typically contain some neutrinos, produced in the decay of hadrons, not all the jet energy can be measured. Therefore the obtained jet energy is corrected using the average fraction of measured energy.

Figure 2.13 shows the energy resolution of reconstructed jets as a function of p_T in data and simulation, calculated using two different techniques [22].

Basic jet selection

In this thesis jets are only used to assign a sign to the transverse impact parameter of muon tracks[4]. We therefore apply a very loose jet selection.

- The jet is reconstructed with an anti-k_T algorithm with parameter R = 0.4, by combining topological clusters in the calorimeters.
- $p_T > 10$ GeV.

2.3.4 Missing transverse energy: E_T^{miss}

Particles that do not carry electric or colour charge, such as neutrinos, do not interact with the ATLAS detector and therefore do not directly produce a measurable signature. The only way to identify the presence of such weakly interacting particles is to measure a

[4]This is described in Section 5.3.

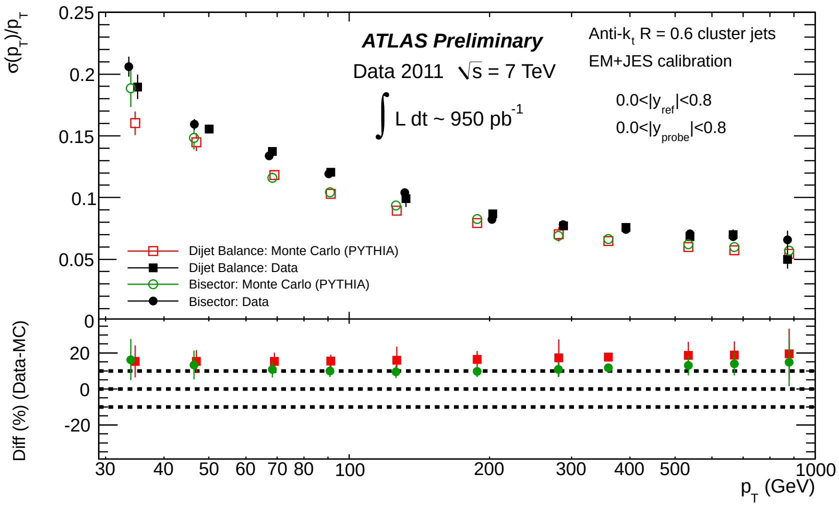

Figure 2.13: The energy resolution of jet reconstructed from topological clusters with a anti-k_T algorithm as a function of p_T for data (filled markers) and simulation (empty marker), calculated using two different techniques described in Ref. [22].

momentum imbalance in the event. Since both the colliding protons do not carry significant transverse momentum, the combined p_T of all particles created in the collisions should be zero. Therefore by combining the momentum of all measured particles in the event, the missing transverse energy can be calculated which ideally corresponds to the total transverse momentum of the weakly interacting particles.

There are multiple methods to calculate the E_T^{miss} of events, which differ from each other in exactly which energy is included in the calculation. The most precise method, and the one used in this thesis, is to add the momenta of reconstructed particles. This E_T^{miss} algorithm adds, in order, the momenta of electrons, photons, taus, jets and muons, making sure that none of the energy in the calorimeters is double counted. After combining the momentum of all reconstructed particles, the remaining energy deposits in the calorimeters are also included. When possible this information is improved using ID tracks. The E_T^{miss} of the event is defined as minus the total measured p_T.

In the analyses presented in this thesis E_T^{miss} is rarely used and none of the conclusions rely on the exact definition of this variable.

2.4 The ATLAS trigger

The subdetectors of ATLAS produce in total approximately 1.5 MB of raw data per event. At nominal instantaneous luminosity the LHC is expected to provide collisions at a rate of approximately 40 MHz. Therefore ATLAS needs to handle a data rate of 50-60 TB/s. Since such a high data rate leads to unrealistic demands of computing power as well as data storage requirements, an online trigger system is used to select interesting events and reduce the event rate to a manageable 200 Hz. This rate is limited by the data storage requirements of accumulated years of data taking.

The ATLAS trigger system consist of three levels:

- **Level 1:** Based on a rough version of the calorimeter information and the MS trigger chambers, regions of interest (RoI) are identified which could indicate high momentum objects such as muons, electrons, photons and jets. Furthermore the total transverse energy is estimated as well as E_T^{miss}. Using this information an event is accepted of rejected, reducing the event rate to 75 kHz. The decision time of the Level 1 trigger is approximately 2.5 μs.

- **Level 2:** The RoIs found by the Level 1 trigger are analysed using the full detector information in these regions. A fast object reconstruction software is used to better determine the object properties and reduce the fake rate. This takes approximately 40 ms and is used to reduce the event rate to 3.5 kHz.

- **Event Filter:** This last trigger level uses the full detector information and runs the full offline object reconstruction and therefore needs an average of 4 s to analyse each event. The event filter reduces the event rate to the final 200 Hz.

2.4.1 The trigger menu and data streams

The exact set of triggers used, the trigger menu, depends on the instantaneous luminosity provided by the LHC. During the first days of data taking the event rate was low enough for each collision events to be recorded and stored. With increasing instantaneous luminosity more selective triggers became necessary.

Most triggers in ATLAS aim at selecting high momentum particles such as muons, electrons, photons, (b-)jets and taus or large E_T^{miss}. The exact requirements of these triggers are time dependent as they need to be adjusted to cope with increasing event rates. This generally results in a higher momentum threshold for the triggered object, but can also include tighter selection properties to reject more fake or badly reconstructed objects. As new tighter triggers are introduced the older triggers are either removed or prescaled with only part of the triggered events analysed and stored.

As most interesting physics signatures do not consist of one very high momentum particle, but of multiple different physics objects, many combination triggers are also used. These triggers require a combination of trigger objects, such as multiple jets or at least 2 muons, allowing events with lower momentum particles to be accepted without introducing too high a trigger rate.

Events passing at least one of the ATLAS triggers are stored in data streams corresponding to the type of trigger used to select the event. For example, events selected using muon triggers and are stored in the muon stream. As events can be triggered by different objects, some events are stored in more than one data stream.

2.4.2 Muon triggers

All analyses presented in this thesis select events using muon triggers [23].

At Level 1 (L1) these triggers are based solely on the information of the RPCs and TGCs in MS barrel and end-caps respectively (see Section 2.2.4). This information is used to construct "roads" connecting hits in different trigger layers. Events are accepted or rejected depending on the p_T of these "roads".

As an example Figure 2.14 shows the trigger efficiency of the L1 muon trigger without any p_T requirement as a function of p_T in the RPC (left) and TGC (right) regions separately. The lower plateau efficiency in the RPC region with respect to the TGC is due to an 80 % geometrical acceptance of the trigger chambers in the MS barrel regions as opposed to almost 100 % in the end-caps. By including a p_T requirement the turn on curve of the efficiency plots is shifted to higher momenta but the plateau efficiency remains unchanged.

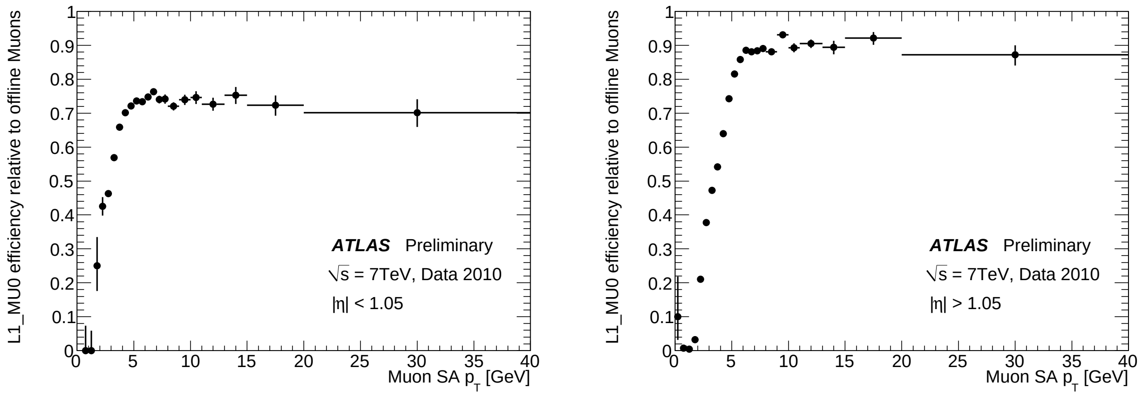

Figure 2.14: The L1 muon trigger efficiency as a function of the offline MS stand-alone (SA) reconstructed p_T for the RPC (left) and TGC (right). No p_T requirement was used in this trigger.

The Level 2 (L2) muon trigger has access to the full MDT and CSC information in the RoI defined by the L1 "roads", as well as to ID tracks and calorimeter information in these regions. Three different L2 muon trigger algorithms are used. The MS only algorithm uses the MDT and CSC information to construct stand-alone MS tracks with a fast tracking algorithm, which provides improved track parameters with respect to the L1 "roads". The muon combined algorithm tries to combine these stand-alone MS tracks with ID tracks. This results in a slightly lower trigger efficiency than the MS only trigger, but the added ID information leads to a more accurate momentum determination and therefore a sharper turn on curve. The third L2 muon trigger algorithm uses calorimeter information to select isolated muons, thereby rejecting most muons produced in jets.

Figure 2.15 shows the efficiency of the L2 MS only (left) and combined muon (right) triggers designed to select muons with a $p_T > 4$ GeV relative to the L1 trigger as a function of p_T of the offline reconstructed muon.

At the Event Filter (EF) level the trigger has access to the full event information. The RoIs defined by the L1 and L2 triggers are fitted using algorithms which are almost identical to the offline muon reconstruction. Three different EF muon trigger algorithms

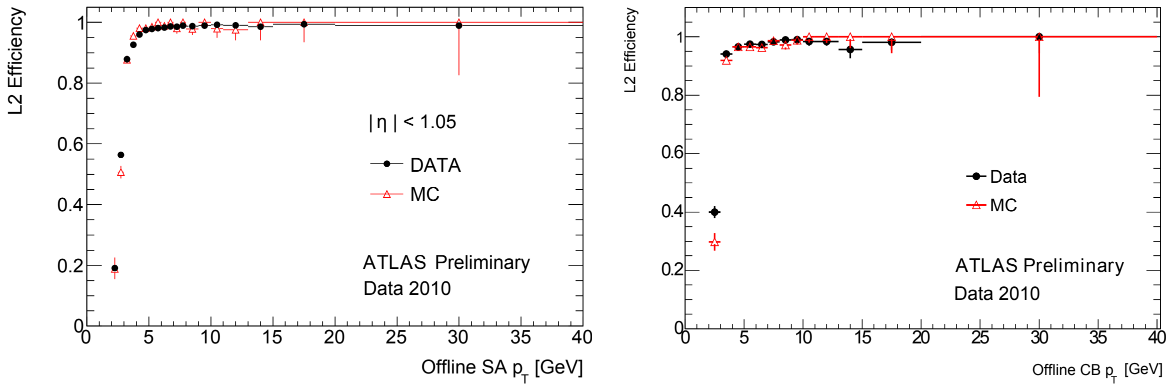

Figure 2.15: The L2 muon trigger efficiency relative to the L1 as a function of the offline reconstructed p_T for the MS only algorithm in the MS barrel (left) as well as for the muon combined algorithm (right). Both triggers are designed to accept muons with $p_T > 4$ GeV.

are used. The MS only algorithm reconstructs MS stand-alone tracks, while two different algorithms reconstruct combined muons. The outside-in algorithm reconstruct muons in the "standard" way starting from MS tracks and combining them with ID tracks, while the inside-out algorithm starts from ID tracks extrapolated to the MS.

Figure 2.16 shows the EF trigger efficiency relative to the L2 for the combined outside-in trigger designed to select muons with $p_T > 4$ GeV as a function of p_T and η of the offline reconstructed combined muon. This trigger is called EF_mu4 and is used for the analysis presented in Chapter 4.

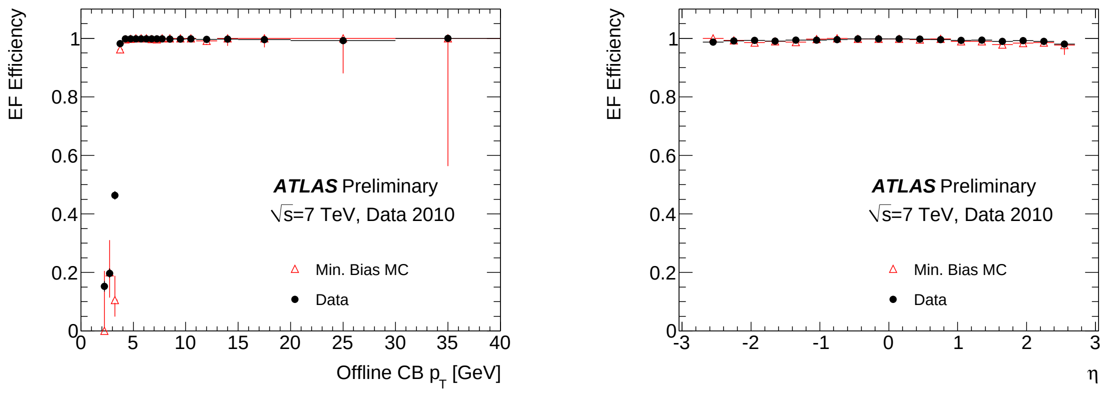

Figure 2.16: The EF muon trigger efficiency relative to the L2 as a function of the offline reconstructed p_T (left) and η (right) for the combined muon outside-in algorithm designed to accept muons with $p_T > 4$ GeV.

2.5 Monte Carlo simulation

To compare the collected data with theoretical expectations, the ATLAS experiment uses simulated events. These simulated samples are not only used to study the expected signatures from different particle production processes but also to study and test the understanding of the ATLAS detector and different reconstruction algorithms by comparing these simulated events with the collected collision data.

The event simulation procedure of ATLAS consists of four separate stages:

- **Event Generation:** The first stage consists of generating the proton-proton interactions. This includes the hard scatter between two constituents of the protons but also the underlying event produced by the proton remnants and the decay and radiation of particles close to the interaction point.

- **Simulation:** The event generators provide a list of outgoing semi-stable particles and their properties. In the simulation stage the propagation of these particles through the ATLAS detector is simulated as well as the decay of longer lived particles such as pions and kaons. The interactions of the particles with the detector material is simulated using the G4ATLAS software, a customized ATLAS version of the GEANT4 software package [24].

- **Digitization:** The interactions between the detector layers and the generated particles are translated to detector signals similar to the raw data produced by the ATLAS detector.

- **Reconstruction:** After the digitization the generated events are run trough the same trigger and offline reconstruction software as actual data events.

The uncertainties on the predictions made by these simulated samples come from uncertainties in the event generation and simulation stages. We therefore discuss these two stages in some more details.

2.5.1 Event generation

Hard interaction

Event generator programs use Monte Carlo (MC) techniques to randomly generate initial hard scatter interactions between the incoming partons in such a way that the phase-space distribution of the produced particles is proportional to the differential cross-section of the generated processes. As these initial interactions happen at the highest energy scale in the event, typically of the order of the mass of the produced particles, $\alpha_S \ll 1$. Therefore the matrix element (ME) can be calculated perturbatively and is relatively well understood. The largest theoretical uncertainties on the calculated cross-section and the kinematics of the hard interactions comes from neglecting higher order corrections in the calculation and from the uncertainty on the Parton Distribution Functions (PDFs) which describe the momentum distributions of the incoming quarks and gluons within the protons.

Most event generators used in ATLAS calculate the ME to leading order (LO), which means that no loop diagrams are included. To correct for the lack of these loop diagrams the cross-section of most processes are also calculated by separate programs to next-to-leading order (NLO) and in some cases even to next-to-next-to-leading order (NNLO). The ratio in cross-section between the LO and NLO calculation is called the K-factor. As for most processes it is computationally too heavy to generate events directly at NLO, events generated by a LO generator are used but weighted by this K-factor. As different loop diagrams lead to different kinematic distributions, the K-factor can depend on the event kinematics. The different event generators and ME calculators used in this thesis are discussed later in this section.

The PDFs are not calculated by the event generators, but are used as an input. As the vast majority of the partons within the protons have a very low energy, the physics within the proton is highly non-perturbative and therefore theoretically not well understood. Different models based on experimental data are used to describe these functions. These models are tuned on data collected both from previous accelerators and from the LHC. By comparing the cross-sections obtained using different PDF models [25–27] we estimate the uncertainty on the MC predictions due to the PDFs. As an example in Chapter 6 we use MC samples of WZ and ZZ diboson production generated at NLO, to estimate the SM contribution to the cross-section of $\mu^{\pm}\mu^{\pm}$ pairs in ATLAS. For these samples the uncertainty on the total cross-section due to higher order terms is estimated to be about 10% while the uncertainty from the PDFs is about 7%.

Parton showering

After the generation of the hard scattering the initial partons and the produced strongly interacting particles can radiate gluons, which in turn can split in additional gluons or quark-anti-quark pairs. As this process involves particles with colour charge, which are confined to remain in colour neutral groups, this process depends on the colour flow of the event and therefore also on the proton remnants which were not part of the hard interaction. This parton radiation typically occurs at a much lower energy than the original hard interaction and can therefore not be described perturbatively. In fact the limit for the number of radiated partons as the momentum and the emission angle of these partons goes to zero, is infinite. To deal with this problem, parton shower generators simulate the emission of new quarks and gluons in an ordered fashion, either by decreasing p_T of the radiated partons or decreasing emission angles. This choice influences the resulting distribution of quarks and gluons in the event as, for example, in the angle ordering scheme, a soft emissions at high angle prevents a subsequent harder emission at smaller angle.

The uncertainty in the modelling of the parton showers affects the final parton distribution in the events and therefore the number, p_T and η distributions of jets. To limit this uncertainty the parton showering models are tuned to jet distributions in data. In this thesis the remaining uncertainty due to parton showering can be neglected because, as mentioned in Section 2.3.3, we only use jets to assign a sign to the impact parameter of muons, but never as part of an event selection.

Hadronization, decay, underlying event and pile-up

After the parton showering the generated quarks and gluons are grouped into colour neutral hadrons (hadronization), which can decay further to (semi-)stable particles. The generated collisions are then combined with an underlying event, which simulates the proton remnants which are not part of the hard scattering. Due to the boost of the incoming protons most particles in the underlying event remain in the beam-pipe. Typically only a "background" of low p_T particles reaches the ATLAS detector. As the analyses presented in this thesis focus on high momentum muons, the underlying event does not significantly affect the results. Pile-up is simulated by adding separately generated events.

Event generators

The event generation stage of the ATLAS simulation procedure is independent of the ATLAS detector, therefore general, experiment-independent generating programs can be used. Currently there are three 'general purpose' generators used in ATLAS which are capable of generating the hard scattering of any SM process at LO, the underlying event and perform the parton showering, hadronization and decay: Pythia [28], Herwig [29] and Sherpa [30]. These three generators differ somewhat in the treatment of the colour flow in the event and the description of the parton showering.

It is possible to interface more specialised programs into these general purpose generators to simulate part of the process. In this thesis we use some simulated samples in which the initial hard scattering is calculated using specialised ME generators. The ME generators used in this thesis are Alpgen [31], MadGraph [32] and MC@NLO [33].

The three general purpose generators can only calculate two-to-one and two-to-two processes within the ME calculation. The decay of these particle as well as the radiation of additional partons is done separately. This means that the originally produced particle or particle-pair is on-shell[5] and that the momentum and angular distribution of the additional partons is determined by the parton showering. Alpgen is designed to handle more complicated parton level configuration in the ME, which means that the radiation of the highest energetic gluons and quarks can be calculated perturbatively. Typically this leads to a more accurate description of additional high momentum jets in the event. The generated events are then processed using the Herwig or Pythia parton showering. To avoid double counting it is important to restrict the generation of hard radiation by the partons showers, as this is already included in the ME calculation. There are multiple approaches to avoid such double counting such as by allocating a negative weight or vetoing events with hard scattering from the parton showering. In ATLAS, Alpgen is primarily used to generate Z+jets, W+jets and $t\bar{t}$+jets events.

MadGraph is also capable of calculating cross-sections for multi particle final states. Although computationally less efficient than Alpgen it is programmed to handle a wider range of processes. In this thesis MadGraph is used to generate the associative production of $t\bar{t}$ with a gauge boson.

MC@NLO includes both real and virtual correction to achieve NLO accuracy in the

[5] A particle is on-shell when $m^2 = E^2 - \vec{p}^2$.

generation of certain processes. In ATLAS, MC@NLO is primarily used to generate $t\bar{t}$ events. It is also used for diboson production.

A list of all simulated samples used in this thesis is given in Appendix A.

2.5.2 Simulation of the ATLAS detector

Because of the uncertainty in the event generation discussed above, we chose, in this thesis, to rely as little as possible on simulated cross-sections and simulated particle distributions. In fact the simulated cross-sections are only used in Chapter 6 to compare independently measured cross-sections with SM and non-SM expectations. In all other analyses in this thesis, simulated samples are only used to describe the reconstruction of muons produced in different decay processes given specific properties for the parent particles. In these cases the production process of the parent particle is mostly irrelevant and the decay of the particles are determined by well known branching ratios and kinematic constraints. The main uncertainty on the resulting simulated signature is then dependent on the accuracy of the simulation of the interactions between the particles and the ATLAS detector.

To simulate the propagation of particles through the detector a GEANT4 description of ATLAS is used. Although this description is highly detailed it is not feasible to perfectly model the material distribution to include, for example, every single cable, or the full details of the magnetic fields. This can lead to some differences in measured resolutions and efficiencies between data and simulation. For example most of the differences in muon momentum resolution in the MS barrel region between data and MC found in Chapter 3 are due to missing material in the simulation.

An additional difference between the GEANT4 description and the real ATLAS detector is that although the position of the detector layer in the simulation can be fixed, their actual positions in ATLAS are not known to infinite precision. Misalignment of the ATLAS detector results in poorer reconstruction resolutions which, by definition, can not be perfectly modelled in the simulation.

With time and data the understanding of the ATLAS detector improves resulting in smaller differences between the simulated and real ATLAS detector. The remaining differences in efficiency and resolution between simulated events and collected data can often be modelled (for example by applying a scale factor or momentum smearing). How this is done for the different distributions used in this thesis is described in the relevant analysis chapters.

Summary

A wide range of Monte Carlo samples have been generated to simulated different types of collision events in ATLAS. The initial hard interaction of these simulated events is calculated using generator programs that determine the differential cross-section of the considered processes perturbatively. The rest of the event, including the parton showering, hadronization and the underlying event are simulated using non-perturbative models.

The main uncertainty on the simulated hard interactions, and therefore on the simulated cross-sections, lies in the accuracy to which the relevant matrix element was calculated. For most processes this calculation is limited to leading-order contributions as higher order contributions are too CPU intensive. When available, these leading-order predictions are then weighted to the next-to-leading order total cross-section. Nevertheless the omission of higher order terms is often the main uncertainty on simulated (differential) cross-sections. Another main uncertainty comes from the PDFs used to describe partons in the colliding protons.

The interactions between the generated particles and the ATLAS detector are simulated to translate the generated events into detector signals. These signals can then be processed by the ATLAS reconstruction software in a similar way are regular collision events. Differences between the model used to describe the ATLAS detector and the actual detector, either due to inaccuracies in the model description or misalignment in the detector, can lead to differences between data and simulations for efficiencies and resolutions.

The Monte Carlo samples used in this thesis are listed in Appendix A.

Chapter 3

Muon momentum scale and resolution from single muons

Measuring the muon momentum scale and resolution in collision data is an important step in the understanding and validation of the ATLAS detector and muon reconstruction performance. In this chapter we present an analysis to measure the muon momentum scale and resolution in ATLAS from an inclusive single muon sample by performing template fits on the relative momentum difference between the Inner Detector (ID) and Muon Spectrometer (MS) momentum measurement of combined muon tracks[1] [34, 35]. This method, described in Section 3.2, was used during the first few months of $\sqrt{s} = 7$ TeV collisions at the LHC and provided the first reliable results on the muon momentum scale and resolution in ATLAS from collision data.

We present the muon momentum scale and resolution in ATLAS as function of p_T and η of the combined muons, as obtained with 1.2 pb^{-1} of collision data. The precise data set and event selection used are described in Section 3.4, while the results are shown and discussed in Section 3.5. This chapter also includes a validation of the method on simulated events and a comparison of the results with other methods.

3.1 Introduction

The expected muon momentum scale and resolution in ATLAS can be determined from the design of the detector and the resolution of the individual hits. The actual scale and resolution may differ from this expectation due to effects such as misalignment or uncertainties in the material distribution or magnetic field description of the detector. To minimise these effects the MS is equipped with an optical alignment system, discussed in Section 2.2.4. Despite this tool, residual misalignment can result in significant differences in muon momentum scale and resolution between data and simulation.

Before the start up of the LHC, muons from cosmic rays were used to further align the detector. Momentum resolution studies preformed with these muons during the first half of 2010 show good agreement between data and simulation [36], indicating an alignment

[1] The definition of combined tracks is given in Section 2.3.1.

not far from design accuracy. However, due to the angular distribution of muons from cosmic rays, only part of the detector could be aligned this way and some remaining differences in scale and resolution between data and simulation were expected in early collision data, especially in the MS end-cap regions.

It is therefore necessary to measure the muon momentum scale and resolution in a data driven fashion directly on collision data. This provides a useful tool for the understanding and commissioning of the ATLAS detector as well as for validating the Monte Carlo simulation. Knowing the scale and resolution in data is also important for most physics analyses involving muons, as they affect both the efficiency of muon selection cuts and distribution shapes.

The standard method to determine the muon momentum scale and resolution in collision data is to study the Z-boson resonance. The scale and resolution are then obtained from the offset of the peak value and the width of this resonance, leading to results such as the ones shown in Section 2.3.1. Unfortunately, during the first months of data taking the available data did not contain sufficient Z-bosons for detailed resolution analyses.

We therefore developed a method to estimate the muon momentum scale and resolution from low momentum single muons by comparing their ID and MS momentum measurements. Due to the high cross-section for such muons, mostly from the decay of heavy flavour quarks, this method was able to obtain the first estimate for the muon momentum scale and resolution in collision data as a function of both p_T and η of the combined muon track with only 17 nb^{-1} of integrated luminosity [34]. This provided the necessary information for the first W- and Z-boson measurements [37] as well as illustrated the state of the ATLAS alignment.

The results shown in this chapter describe the muon reconstruction performance as it was in September of 2010, obtained with approximately 1.2 pb^{-1} of data. This data set, with several million muons passing our basic selection, was chosen because it contains sufficient muons to not be limited by the available luminosity but instead by the number of available simulated events used to describe background distributions.

It is important to note that because this single muon method is based on comparing the momentum measurements of the ID and MS, it provides an estimate for the combined momentum resolution of the two subdetectors (ID $\oplus$ MS) and is not able to decouple the individual resolutions. This combined resolution is not the same as the resolution of combined muons which is always better than that of either stand-alone tracks. However the combined resolution does provide an upper limit for the resolution of combined muons.

3.2 Analysis method

Muons with sufficient energy to pass though the calorimeters ($p_T > 3$ GeV) are usually measured by two independent subdetectors, the Inner Detector (ID) and the Muon Spectrometer (MS). Such combined muons can be used to estimate the muon momentum scale and resolution by studying their momentum imbalance, the relative momentum difference between the ID and MS stand-alone measurements. We do this by performing template fits on the momentum imbalance distribution of combined muon tracks in ATLAS.

3.2.1 The momentum imbalance of combined muon tracks

We defined the momentum imbalance, $\frac{\Delta p}{p}$, of combined muon tracks as:

$$\frac{\Delta p}{p} = \frac{p_{\mathrm{ID}} - p_{\mathrm{MS}}}{p_{\mathrm{ID}}}, \tag{3.1}$$

where p_{ID} is the muon momentum as measured by the ID, while p_{MS} is the momentum of a track reconstructed in the MS back-extrapolated to the primary vertex. p_{MS} includes a correction for the expected muon energy loss through the ATLAS calorimeters.

For muons produced before the first ID layer, such as muons produced in the direct decay of W- and Z-bosons or heavy flavour quarks, the width of the $\frac{\Delta p}{p}$ distribution provides a measure for the combined momentum resolution of both subdetectors (ID $\oplus$ MS). The $\frac{\Delta p}{p}$ value corresponding to the peak of the distribution gives the momentum scale of the ID with respect to the MS.

For muons produced within or behind the ID volume, in the decay of long-lived particles such as pions and kaons, a combined muon is formed by combining a muon track in the MS with and ID track which, either partially or totally, comes from the meson before decaying. As part of the meson energy is transferred to the created neutrino, this introduces a large and positive momentum imbalance due to the energy difference between the meson and the muon.

For simplicity we refer to muons produced in the decay of all pions and kaons as background muons. All other muons are considered part of the signal. Figure 3.1 shows the $\frac{\Delta p}{p}$ distribution of signal and background muons obtained from a simulated di-jet sample[2], illustrating the differences in distribution shape between these muon types.

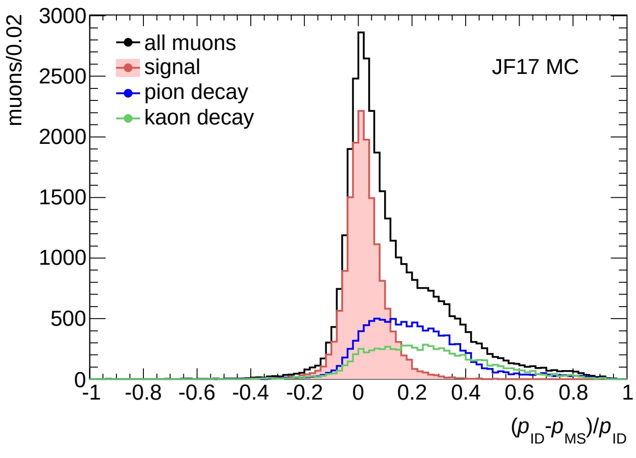

Figure 3.1: The $\frac{\Delta p}{p}$ distribution for muons in the JF17 sample (see Appendix A), separated by muon origin.

[2]The JF17 simulated sample, defined in Appendix A.

The $\frac{\Delta p}{p}$ distribution of muons produced before the ID volume.

For muons produced before the first layer of the ID, signal muons, the shape of the $\frac{\Delta p}{p}$ distribution is a convolution of a Gaussian, due to the instrumental resolutions of both subdetectors, with a Landau distribution, accounting for large energy loss fluctuations in the calorimeters with respect to the average. Given these considerations we use the following convolution function to fit the $\frac{\Delta p}{p}$ distribution:

$$f(\frac{\Delta p}{p};\ \mu_G, \sigma_G, \sigma_L) = \int d\mu_L [G(\frac{\Delta p}{p};\ \mu_G, \sigma_G) \times L(\frac{\Delta p}{p};\ \mu_L, \sigma_L)], \tag{3.2}$$

where μ_G and σ_G are the mean value and the standard deviation of the Gaussian (G), while μ_L is the most probable value of the Landau distribution (L) and σ_L is its width[3].

The muon momentum scale and resolution are obtained by fitting the $\frac{\Delta p}{p}$ distribution of signal muons with this function. The momentum scale corresponds with the $\frac{\Delta p}{p}$ value of the maximum of the fitted signal distribution while the resolution is given by the width of the signal distribution, defined as $\sigma_G + \sigma_L$.

The $\frac{\Delta p}{p}$ distribution of muons from pion and kaon decays

An inclusive sample of relatively low momentum muons, such as the one used in this analysis, contains a significant contribution from pion and kaon decays. This background produces a large tail on the positive side of the $\frac{\Delta p}{p}$ distribution, which is almost impossible to remove. Therefore, instead of trying to reduce this background, we fit its contribution to the $\frac{\Delta p}{p}$ distribution using templates to describe the background shape.

The exact shape of the $\frac{\Delta p}{p}$ distribution of pion and kaon decays depends strongly on the decay distance. We consider three types of decays:

- Early decays: A few percent of the pions and kaons decay before the first pixel layer. Such early decays in flight result in a $\frac{\Delta p}{p}$ distribution which is identical to that of signal muons.
- Late decays: Some pions and kaons, especially with high momentum, reach the calorimeters and loose much of their energy before decaying. The resulting track in the MS is therefore typically of low momentum. As the $\frac{\Delta p}{p}$ definition uses the MS momentum measurement extrapolated to the primary vertex, this momentum is extrapolated to slightly above the expected energy loss in the calorimeters ($\sim$ 3 GeV). The shape of the $\frac{\Delta p}{p}$ distribution for late decays in flight is therefore a peak close to $\frac{\Delta p}{p} = 1 - \frac{3\text{ GeV}}{p_{ID}}$.
- Intermediate decays: Most pions and kaons decay within the ID volume. Their $\frac{\Delta p}{p}$ distribution depends on the flight direction, decay distance and decay-angle but also on the detector and reconstruction performance in combining partial meson/muon

[3]The width of the Landau distribution is defined by the width parameter of the `RooFit::RooLandau` functions from the `RooFit` analysis package [38].

tracks. This results in a broad distribution with $\frac{\Delta p}{p}$ values between that of early and late decays.

The relative contributions of these three types of decays depends on the momentum and angular distribution of the mesons and is different for pions and kaons, although the majority always consists of intermediate decays.

As the shape of the $\frac{\Delta p}{p}$ distribution of pion and kaon decays depends on many variables and is not easily described by a simple analytical expression, we use templates constructed from simulated data to describe this shape.

Extracting the background templates

To build the background templates used to fit the $\frac{\Delta p}{p}$ distribution in data, we select simulated muons from pion or kaon decays using hit based truth matching. The selected reconstructed combined muons should have ID tracks that are either matched to a truth pion or kaon or to a muon produced in the decay of a pion or kaon. The templates of the $\frac{\Delta p}{p}$ distribution are then built using the `RooFit::RooKeysPdf` class from the `RooFit` analysis package [38].

As the $\frac{\Delta p}{p}$ distribution of background muons depends on some of the properties of the reconstructed muons, it is important that the templates are created from simulated events with the same properties as those in the studied data. As we perform the analysis on an inclusive sample of low momentum muons, the templates should be extracted from simulated Minimum Bias events. Unfortunately the available sample has limited statistics and very few muons with a $p_T > 10$ GeV. We therefore use the much larger di-jet sample called JF17[4].

Apart from increased statistics the two samples differ somewhat in the kinematic range of the muons, specifically in the p_T and isolation distribution. This is shown in the left plots of Figure 3.2 which show the normalized p_T and E_T-cone20 (isolation variable)[5] distributions of combined muons in the Minimum Bias and JF17 simulated sample. To ensure that despite these differences the template shapes remain unaffected by the choice in simulated sample, we studied the effect of p_T and E_T-cone20 of the muons on the shape of the $\frac{\Delta p}{p}$ distribution. The top right plot of Figure 3.2 shows the $\frac{\Delta p}{p}$ distribution of background muons for different p_T ranges, while the bottom right plot shows the same for different E_T-cone20 ranges. From these plots we can conclude that the $\frac{\Delta p}{p}$ distribution of background muons does not significantly depend on the muon isolation. However, as expected from the description of the $\frac{\Delta p}{p}$ distribution of pion and kaon decays, the templates do depend on the p_T of the muons. We therefore construct the background templates from the JF17 sample, with the selected muons reweighted to the Minimum Bias p_T spectrum.

To ensure that the templates correctly describe the background $\frac{\Delta p}{p}$ distribution of a given data sample any selection criteria used on the data should in principle also be applied on the simulated samples before building the templates. However, variables that do not influence the physical process of pion and kaon decays and do not affect the muon

[4] Both simulated samples are listed in Appendix A.

[5] E_T-cone20 is defined as the energy deposited in a cone of size $\Delta R = 0.2$ around the muon track.

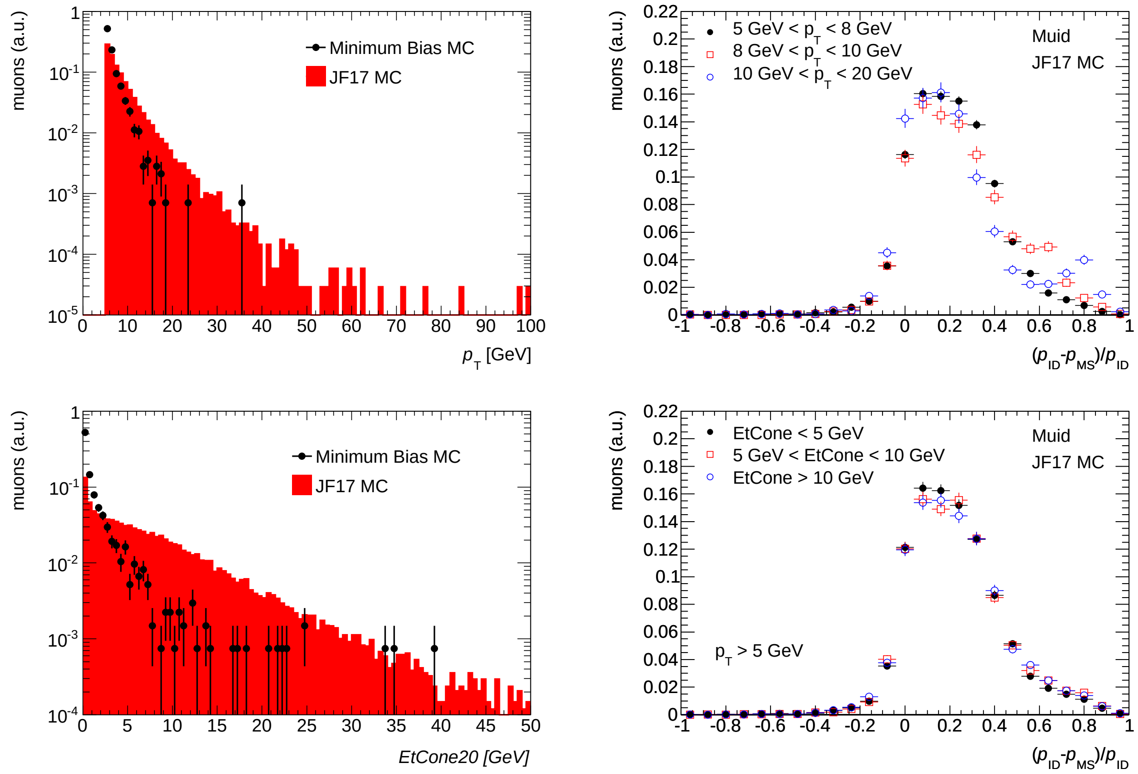

Figure 3.2: Left: The normalized p_T (top) and E_T-cone20 (bottom) distributions for all muons passing the basic selection listed in Section 3.4 in the JF17 simulated sample (red, filled histogram) and the Minimum Bias simulated sample (black points). Right: The $\frac{\Delta p}{p}$ distribution of background muons in the JF17 simulated sample for different p_T (top) and E_T-cone20 (bottom) ranges.

reconstruction in simulation have no effect on the background shape. We therefore do not need to take these variables into account when creating the templates. As the number of available simulated muons often a limiting factor for studying the muon momentum scale and resolution in great detail using this method, this is a definite advantage. For example, the template shapes are independent of the sign of η, the charge and the isolation of the muon.

3.2.2 Fitting the momentum scale and resolution

We fit the $\frac{\Delta p}{p}$ distribution on data to a PDF which is the sum of the signal Landau-Gauss convolution and the obtained background template, leaving the signal to background fraction as a free parameter. In total the fit has 4 free parameters: μ_G, σ_G and σ_L from Equation 3.2 and the signal to background ratio[6]. The best fit parameters are returned

[6]The signal to background ratio is used in Chapter 4 to estimate the pion and kaon fraction of muon samples.

by a likelihood fit to the unbinned $\frac{\Delta p}{p}$ distribution. As an example Figure 3.3 shows the $\frac{\Delta p}{p}$ distribution of muons in data with $|\eta| < 1.05$ for two different p_T ranges: 6 GeV $< p_T <$ 8 GeV and 8 GeV $< p_T <$ 10 GeV. The best-fit to these distributions and the corresponding fitted signal and background components are included.

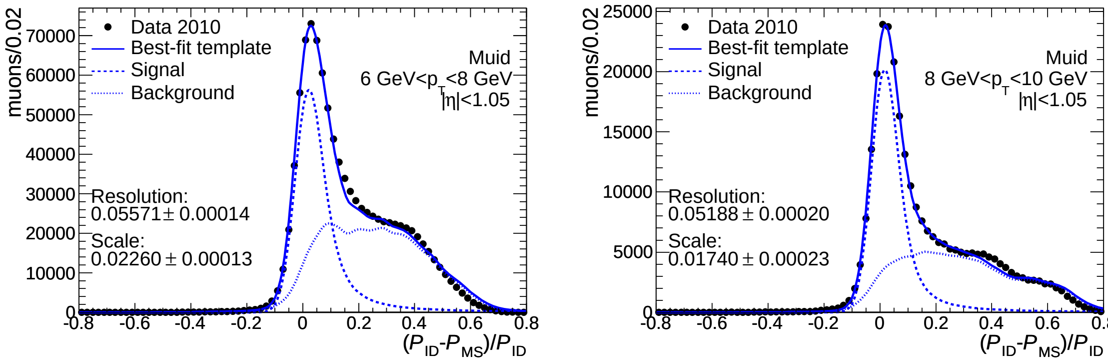

Figure 3.3: The $\frac{\Delta p}{p}$ distribution of muons in data ($\int L \cdot dt \approx 1.2$ pb^{-1}) with $|\eta| < 1.05$ and 6 GeV $< p_T <$ 8 GeV (left) or 8 GeV $< p_T <$ 10 GeV (right). The best-fit function for these distribution (full-line), the signal (dashed-line) and background (dotted-line) components are also displayed.

The momentum scale is obtained by taking the position of the maximum of the signal distribution returned by the fit. The resolution is given by the width of the signal distribution, for which we quote the linear sum $\sigma_G + \sigma_L$, as this is the definition used in earlier resolution analyses based on cosmic muons in ATLAS [36]. Although the fit is not always able to reliably separate the Landau and Gaussian part of the signal distribution, as this depends heavily on the exact shape of background distribution, the fitted combined width of the signal peak is stable.

Shift of the background templates

The simple fitting procedure described so far assumes that the background distribution in data is the same as in simulation. Unfortunately this is only an approximation as both the muon momentum scale and resolution affect the background distribution shape and, as discussed previously, the scale and resolution might not be the same in data and simulation. We therefore need to modify the templates to properly describe the background $\frac{\Delta p}{p}$ distribution in data.

A difference in momentum resolution can be simulated by convoluting of the background distribution with a Gaussian, with the width of the Gaussian depending on the difference in resolution between data and simulation. As the resolution in data is one of the parameter we want to fit, this width should be a free parameter. Unfortunately such a convolution leads to unstable fit results. We therefore do not include a convolution of the background templates in the fitting procedure. This simplification does not significantly affect the fitted scale and resolution as those values are determined from the shape of the peak of the $\frac{\Delta p}{p}$ distribution, which does not strongly depend to the exact background shape. This was confirmed by refitting the $\frac{\Delta p}{p}$ distribution in data using templates convoluted with a Gaussian of fixed width.

Differences in momentum scale between data and simulation lead to shifts of the background template along the $\frac{\Delta p}{p}$-axis. The fitting procedure used in this analysis can be very sensitive to such shifts, as the right-hand side of the $\frac{\Delta p}{p}$ distribution determines the fitted normalization of the background template. A shift of the templates of a few percent can, for example, lead to fits with a fitted background distribution close to zero. In such fits the background tail is fitted by the Landau, resulting in a artificially large estimated scale and resolution. We therefore include this scale dependence of the background distribution by shifting the background templates by the same amount as the signal, μ_G. This is based on the assumption that any detector effects present in data which are not correctly simulated in the Monte Carlo samples can affect the reconstruction performance of either subdetectors as well as the matching between the two stand-alone tracks, but should not affect the physical processes involved. Therefore any shift of the $\frac{\Delta p}{p}$ distribution in data compared to simulation should be independent of the muon origin, which means that the shift of the background distribution should be equal to the difference in scale between data and simulation.

By shifting the background template by the value μ_G we also assume that in the simulation, $\mu_G = 0$, which is valid if the signal distribution in simulation peaks at zero $((\frac{\Delta p}{p})_{max} = 0)$ and that $\mu_G = (\frac{\Delta p}{p})_{max}$. Unfortunately both of these assumptions are only approximately correct. The maximum of the distribution for simulated signal events can be off by up to $1-2\%$. This effect is enhanced further when looking at low p_T Muid muons where the reconstruction algorithm underestimates the energy loss in the calorimeter by ~200 MeV. The assumption $\mu_G = (\frac{\Delta p}{p})_{max}$ is only valid in the limit where $\sigma_G \gg \sigma_L$ and only a pure Gaussian form remains. Otherwise $(\frac{\Delta p}{p})_{max} > \mu_G$. In the fits considered $(\frac{\Delta p}{p})_{max} - \mu_G$ is typically of the same order $0-2\%$. We shift the background by the value μ_G, despite these limitations, because there are insufficient simulated muons to precisely determine the maximum of the signal distribution on Monte Carlo without using a fit, and there is no simple analytical formula to calculate $\mu_G - (\frac{\Delta p}{p})_{max}$. The effect of this choice is taken into account when calculating the systematic uncertainty. How this is done is described in more detail in Section 3.2.3.

3.2.3 Uncertainties on the estimated scale and resolution

In Section 3.2.2 we described how to obtain the best estimate for the muon momentum scale and resolution from inclusive single muon samples. In this section we describe the determination of the uncertainty on this estimate.

Statistical uncertainty

As mentioned in Section 3.2.2 we take the peak value of the signal distribution as the momentum scale and the total width $(\sigma_G + \sigma_L)$ as the resolution. The statistical uncertainty is calculated using a 2-D profile likelihood with μ_G and the combined width $(\sigma_G+\sigma_L)$ as the parameters of interest. As it is not possible to describe the scale value, $(\frac{\Delta p}{p})_{max}$, as a simple analytical function of μ_G, σ_G and σ_L it is difficult to perform a profile likelihood fit on this value. We therefore take the uncertainty on μ_G as the uncertainty on the scale. In cases where the profile likelihood calculation failed to obtain a upper or lower boundary, symmetric errors are assumed.

Systematic uncertainty

There are three systematic uncertainties that can affect the results and need to be quantified:

- The uncertainty on the background template shapes due to the limited number of muons in the Monte Carlo samples,
- The uncertainty on the shift of the background template,
- The uncertainty due to possible differences in the pion to kaon ratio between collision data and simulated events.

Statistical uncertainty on the background template shapes
The fitting procedure of Section 3.2.2 does not take the statistical uncertainty on the background template shapes into account. As there is a factor approximately 150 more muons in the collision data considered in this chapter than in the simulated JF17 sample, this uncertainty is not negligible. To take this uncertainty on the template shape into account we generate a number of toy-Monte-Carlo-templates, which are then used to fit the data. This is done separately for each of the considered kinematic regions.

The toy-MC-templates are created from toy-MC-data sets, which is turn are generated from the original background template. Each toy-MC-data set contains the same amount of muons as the original simulated sample and is therefore statistically equivalent to this original sample. As an example Figure 3.4 shows 300 such toy-MC-templates overlaid with the original background distribution of the JF17 sample for muons with $|\eta| < 1.05$ and 6 GeV< p_T <8 GeV. It also shows the the fits obtained on collision data using these toy-MC-templates, and the resulting measured momentum scales and resolutions.

As can be seen from Figure 3.4 both the scale and resolution distributions are approximately Gaussian. We therefore take the mean value of these distributions as the most probable values for the scale and resolution, and the RMS as the systematic uncertainty due to the template shape. As computation time is a limiting factor when doing unbinned fits on a large amount of data, we perform only 8 fits (7 toy-MC-templates) per kinematic region.

Uncertainty on the shift of the background templates
We shift the background template by an amount equal to μ_G. The reason for this, including its limitations, is discussed in Section 3.2.2. The main problem is that we should shift the background by the value $(\frac{\Delta p}{p})_{max}$ instead of μ_G. To quantify the effect of this approximation on the fitted momentum scale and resolution we consider the difference

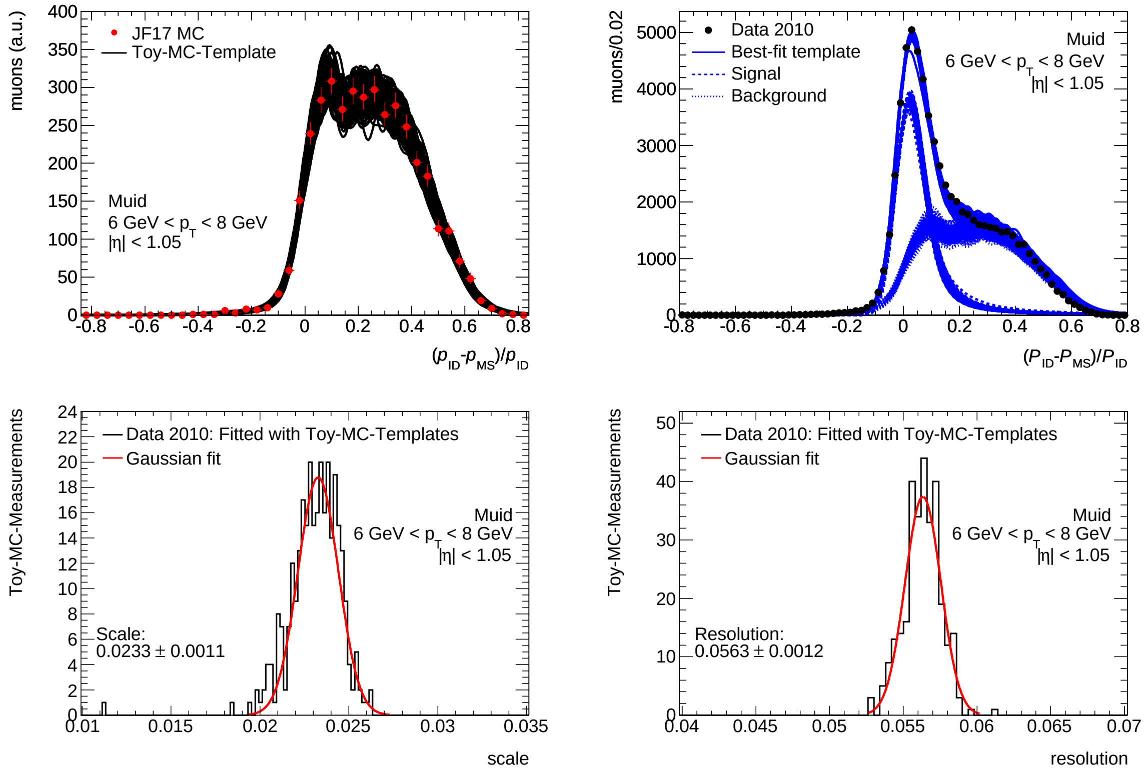

Figure 3.4: Top left: The $\frac{\Delta p}{p}$ distribution of background muons, with $|\eta| < 1.05$ and 6 GeV< p_T <8 GeV, in the simulated JF17 sample (red dots) together with 300 toy-MC-templates (black lines). Top right: The $\frac{\Delta p}{p}$ distribution for muons in collision data ($\int \mathrm{L} \cdot \mathrm{dt} \approx 62\ \mathrm{nb}^{-1}$) passing these same requirements (dots) with the best-fit functions for this distribution using the toy-MC-templates (full-line) and the corresponding signal (dashed-line) and the background (dotted-line) components. Bottom: The muon momentum scale (left) and resolution (resolution) obtained by the 300 fits shown in the top right plot. The red line shows the best Gaussian fit through the distribution.

between $(\frac{\Delta p}{p})_{max}$ and μ_G. We then refit the $\frac{\Delta p}{p}$ distribution shifting the background by a new value $\mu'_G - \mu_G + (\frac{\Delta p}{p})_{max}$ instead of μ'_G, where μ'_G denotes the mean of the fitted signal Gaussian in the refit. The resulting difference in scale and resolution is considered a systematic uncertainty.

In order not to be influenced by the uncertainty from the template shape, this procedure should be repeated for all toy-MC-templates. Unfortunately this is not practical due to the large computing time involved. We therefore perform this second fit on the original template and take the difference between this fit, and the mean of the toy-MC-fits as the uncertainty. If this uncertainty is significantly larger ($> 30\%$) than the uncertainty due to simulated statistics, we perform four additional fits with toy-MC-templates. This is to limit the effect of a fit possibly converging to a local minima giving an unrealistically large systematic uncertainty. The uncertainty is then given by the difference between the mean of these five measurements and the mean from the original fits.

Uncertainty on the background content

The background in this analysis consists of muons from pion and kaon decays. Table 3.1 lists the relative signal, pion and kaon contributions in the Minimum Bias and JF17 simulated samples. The relative pion to kaon ratio of both simulated samples differs by approximately 30%.

	Minimum Bias MC		JF17 MC	
Muon Type	# muons	percentage	# muons	percentage
total	1423	100%	34133	100%
signal	725	51%	15458	46.1%
pion decays	370	26%	10897	31.9 %
kaon decays	328	23%	7517	22.1 %

Table 3.1: Different contributions to the muon content of the simulated Minimum Bias and JF17 sample. The muon selection criteria are given in Section 3.4.1. The signal contribution of both samples is dominated by muons from heavy flavour quark decays.

This uncertainty in the exact background composition affects the template shapes, as muons from pion and kaon decays have slightly different $\frac{\Delta p}{p}$ distributions (see Figure 3.1). To quantify the effect of this uncertainty on the fit results we built two new templates, one where the pion contribution is doubled and one where the kaon contribution is doubled. The difference in scale and resolution obtained when using these templates compared to the best value for the scale and resolution using the toy-MC-templates, is taken as the uncertainty due to the background content. As was the case for the systematic uncertainty due to the relative background shift, we redo these fits four times, using toy-MC-templates, if the uncertainty coming from the background content is at least 30% larger than the uncertainty due to the limited simulated statistics.

Combining the separate uncertainties

For the muon momentum scale and resolution obtained in the collision data we quote the statistical and systematic uncertainty separately. Due to the large difference in muon sample size between the available collision data and the simulated samples used to build the templates, the systematic uncertainty is typically dominated by the uncertainty on the background template shape due to limited simulated statistics. This uncertainty does not only affect the determination of the best fit value, but also the calculation of the other systematic uncertainties, as we are unable to perform sufficient toy-MC-fits to decouple these effects. Because the statistical uncertainty on the background shape is present in all the calculated systematic uncertainties, these uncertainties are highly correlated. We therefore take the maximum of the three uncertainties as the systematic error.

When measuring the muon momentum scale and resolution on the simulated JF17 sample, the background content and the statistical fluctuations in the templates are the same as in the fitted pseudo-data. Therefore no systematic uncertainty due to the background content or the statistical error on the templates needs to be taken into account. In this case we show the combined statistical and systematic uncertainty, by adding the statistical uncertainty and the uncertainty due to the relative background shift in quadrature.

3.3 Validation on simulated Minimum Bias events

To show that our fit is able to correctly separate the signal and background contributions to the $\frac{\Delta p}{p}$ distribution and correctly models the signal shape, we have tested our method on the simulated Minimum Bias sample listed in Appendix A. We fit this sample as if it were data and compare the signal and background components of the fit directly with the true signal and background components of the sample. Figure 3.5 shows the result for four different p_T bins. Both the signal and background distributions are correctly fitted within available statistical uncertainties. Unfortunately this simulated sample does not contain enough muons to test this method separately for different η regions.

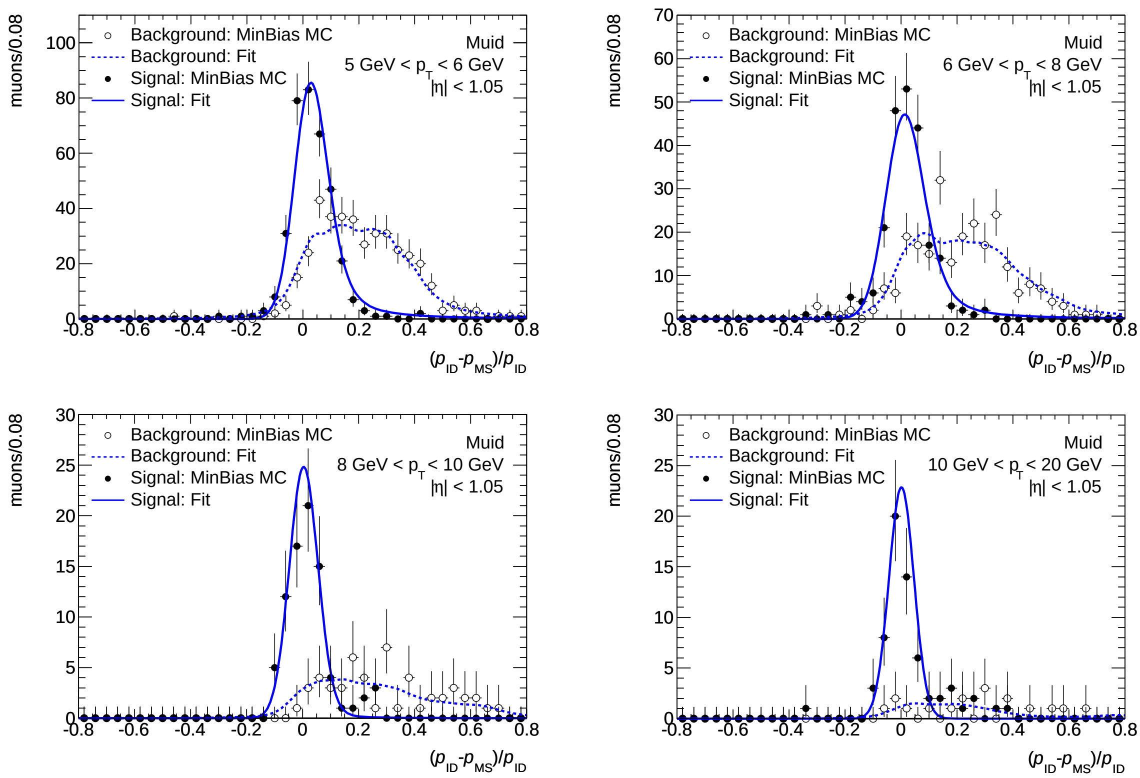

Figure 3.5: Best fit obtained on a simulated Minimum Bias sample, for Muid muons in different p_T ranges. The signal (black dots) and background (white dots) data points are shown separately. Overlain is the signal (full line) and background (dotted line) part of the best fit to the total signal + background distribution.

3.4 Data set and event selection

In this chapter, we analysed a data set corresponding to an integrated luminosity of approximately 1.2 pb^{-1} of collision data at $\sqrt{s} = 7$ TeV. This data set was obtained with stable LHC beams between the 30th of March and the 15th of August 2010, with events passing detector data quality checks and selected on-line by any of the ATLAS muon triggers. The events are reconstructed using the best detector description and reconstruction software available at the time, known as the May 2010 reprocessing.

Collision events are selected if coming from a paired LHC proton bunch. Furthermore each event must contain a minimum of three inner detector tracks associated with a reconstructed primary vertex. These selections are aimed at rejecting muons from cosmic rays.

As mentioned in the previous section, two Monte Carlo samples are used to construct the templates: a Minimum Bias and a di-jet (JF17) sample. Both samples are described in more detail in Appendix A. The JF17 sample is also used to obtain the expected muon momentum scale and resolution from simulation.

3.4.1 Muon Selection

To ensure well reconstructed muon tracks we add the following requirements to the basic muon selection of Section 2.3.1:

- $p_T > 5$ GeV
- At least 1 hit in the pixel detector
- At least 5 hits in the SCT detector

Using this selection the data set used in this chapter contains in total 5.27×10^6 combined muons. The JF17 and Minimum Bias samples contain 3.4×10^4 and 1.4×10^3 combined muons respectively.

3.5 Results

We present our estimate for the muon momentum scale and resolution as a function of p_T and η of the combined muon tracks. These results, obtained from the data set introduced in the Section 3.4, report the state of the muon reconstruction performance as it was in September of 2010. A comparison with the results obtained on the simulated JF17 sample is also included[7].

To interpret these results, it is important to note that the muon momentum scale and resolution shown in this section are obtained from comparing the ID and MS standalone momentum measurements and therefore indicate the relative ID to MS momentum scale and the combined (ID $\oplus$ MS) momentum resolution, which is always larger than

[7] All fits used to obtain the results presented in the section are included in an ATLAS communication note [35].

the momentum resolution of combined muons. Furthermore, since we are looking at the momentum difference between the MS and ID stand-alone measurements, this analysis is not able to decouple the momentum resolution of the two subdetectors. To interpret the results in terms of the individual detector performances we often include an indication for the relative contribution of the two detectors in the text. At the times this analysis was performed, between June and September of 2010, this information was deduced from simulated events. By the end of 2010 this information was confirmed by Z-boson studies such as the results shown in Section 2.3.1.

3.5.1 Momentum scale and resolution as a function of p_T

The p_T dependence of the relative uncertainty on the measured muon momentum, the muon momentum resolution, is of the form:

$$\frac{\sigma_{p_T}}{p_T} = \frac{P_0}{p_T} \oplus P_1 \oplus P_2 \times p_T, \tag{3.3}$$

where the P_0 quantifies the momentum resolution due to the energy loss in material, P_1 quantifies the resolution due to multiple scattering and P_2 is the result of the intrinsic resolution of the individual hits, which starts to dominate the momentum resolution for tracks with $p_T > 100$ GeV.

For muons in the range 5 GeV $\leq p_T \leq$ 20 GeV, the ID momentum resolution is dominated by multiple scattering and is therefore approximately constant as a function of momentum. The size of this resolution depends on η and is approximately 2% at small $|\eta|$ where considerable alignment efforts with cosmic muons where possible, and $\sim 4-5\%$ in the end-caps. The MS stand-alone muon momentum resolution in the barrel region ($|\eta| < 1.05$) is mostly determined by energy loss fluctuations up to a momentum of 10 GeV, leading to a decrease in measured momentum resolution with increasing momentum. Above 10 GeV multiple scattering becomes dominant, reaching a plateau in the resolution at about 5%. In the end-cap regions of the MS ($|\eta| > 1.05$) a minimum p_T requirement of 5 GeV ensures that the momentum of the muons is high enough for the multiple scattering terms to dominate the entire $5-20$ GeV region, resulting in a flat resolution distribution. The size of the momentum resolution in this region is similar to that in the barrel region: $\sim 5\%$.

The muon momentum scale should be zero independent of momentum. However for muons reconstructed by the Muid algorithm, the energy loss in the calorimeters was underestimated by about 200 MeV leading to a none-zero scale in both data and simulation. The relative effect of this underestimation, and therefore the momentum scale, decreases with increasing momentum. This effect was fixed in the November 2010 reprocessing.

The results on the relative momentum scale and resolution are displayed in Figure 3.6 as a function of p_T, for the barrel ($|\eta| < 1.05$) and end-cap ($|\eta| > 1.05$) regions separately. The statistical uncertainties fall within the size of the marker. The systematic uncertainties are given by the light blue rectangles. In the text we always quote the combined statistical and systematic uncertainties. For comparison, we also display the momentum scale and

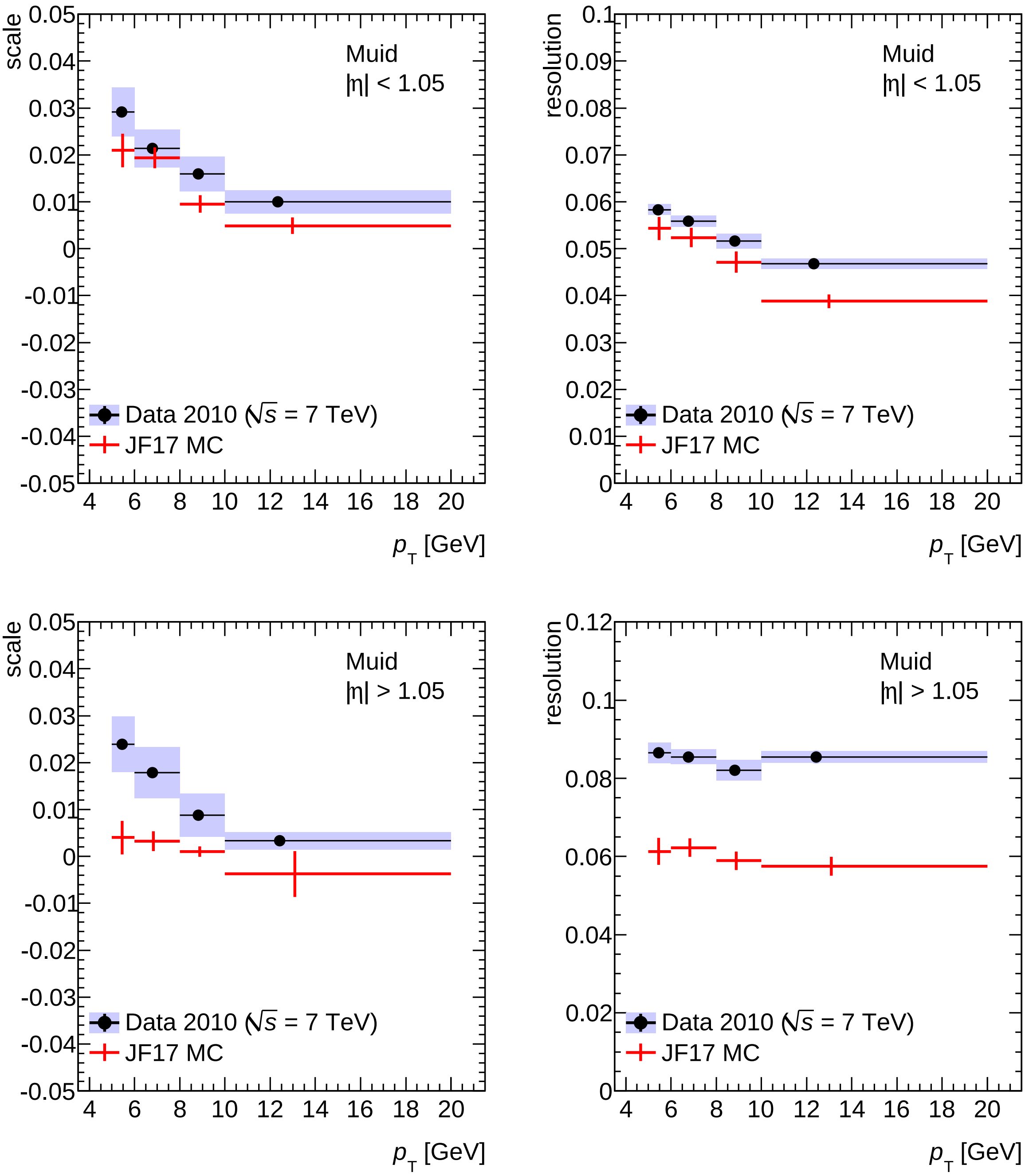

Figure 3.6: The momentum scale (left) and resolution (right) for muons in the barrel ($|\eta| < 1.05$) (top) and end-cap ($|\eta| > 1.05$) (bottom) regions as a function of p_T, for collision data (black dot) and the simulated JF17 sample (red cross). For data the statistical and systematic uncertainties are displayed separately by black lines and light blue rectangles respectively, with the statistical uncertainty falling within the size of the marker. For simulation the red crosses indicate the total uncertainty.

resolution values obtained from the simulated JF17 sample. In this case the red crosses give the combined statistical and systematic uncertainty.

In the barrel region, a good agreement between data and simulation is found. The estimated momentum resolution is between $(5.8 \pm 0.1)\%$ for muons with p_T between 5 and 6 GeV and $(4.7 \pm 0.1)\%$ for muons with p_T between 10 and 20 GeV. The corresponding resolutions in simulation are $(5.4 \pm 0.3)\%$ and $(3.9 \pm 0.1)\%$. This small difference in resolution is primarily due to some missing material in the simulation. Also the scale shows good agreement between data and simulation with a measured scale between the $(2.9 \pm 0.5)\%$ and $(1.0 \pm 0.2)\%$ depending on p_T.

The estimated momentum resolution in the end-caps is constant between the momentum range of 5 to 20 GeV, with a value between $(8.7 \pm 0.3)\%$ (5 GeV $< p_T <$ 6 GeV) and $(8.2 \pm 0.3)\%$ (8 GeV $< p_T <$ 10 GeV). The difference in resolution between data and simulation is much larger ~2-3% than in the barrel. This is not unexpected as, due to geometrical acceptance, the end-caps could not be aligned as precisely using cosmic muons. In more recent data reprocessing the difference between data and simulation is smaller, as can be seen in the plots of Section 2.3.1.

3.5.2 Momentum scale and resolution as a function of η

As discussed in Chapter 2, different technologies are used in the MS to measure muon tracks depending on the spatial direction of the tracks, with MDT chambers covering most of the detector, while CSCs are used in the more forward regions, $|\eta| > 2.0$. For this reason, as well as the geometrical detector layout, the expected nominal muon momentum resolution depends on the detector region. As most of these dependences are independent of ϕ, we study the muon momentum scale and resolution in different η-bins. The results for muons with 5 GeV $< p_T < 20$ GeV are listed in Table 3.2 and shown in Figure 3.7.

	Scale (%)		Resolution (%)	
η-range	Data	Simulation	Data	Simulation
$-2.5 < \eta < -2.0$	1.3±0.1	0.7±0.5	8.1±0.7	6.5±0.3
$-2.0 < \eta < -1.4$	2.1±0.6	−0.4±0.4	8.7±0.3	5.6±0.3
$-1.4 < \eta < -1.05$	5.4±0.7	1.2±0.4	10.2±0.3	7.0±0.4
$-1.05 < \eta < -0.5$	2.5±0.4	1.5±0.2	6.1±0.3	5.8±0.3
$-0.5 < \eta < 0$	2.1±0.3	0.9±0.2	5.6±0.2	4.7±0.3
$0 < \eta < 0.5$	2.2±0.3	1.0±0.2	5.6±0.2	4.8±0.2
$0.5 < \eta < 1.05$	2.7±0.4	1.3±0.2	6.2±0.2	5.4±0.3
$1.05 < \eta < 1.4$	3.2±0.6	0.7±0.2	8.8±0.2	6.9±0.4
$1.4 < \eta < 2.0$	−0.2±0.5	−0.5±0.4	7.6±0.2	5.6±0.3
$2.0 < \eta < 2.5$	1.6±0.2	0.6±0.4	7.9±0.1	6.1±0.3

Table 3.2: The estimated momentum scale and resolution on data and the simulated JF17 sample for different η-regions. The quoted uncertainty contains both statistical and systematic effects.

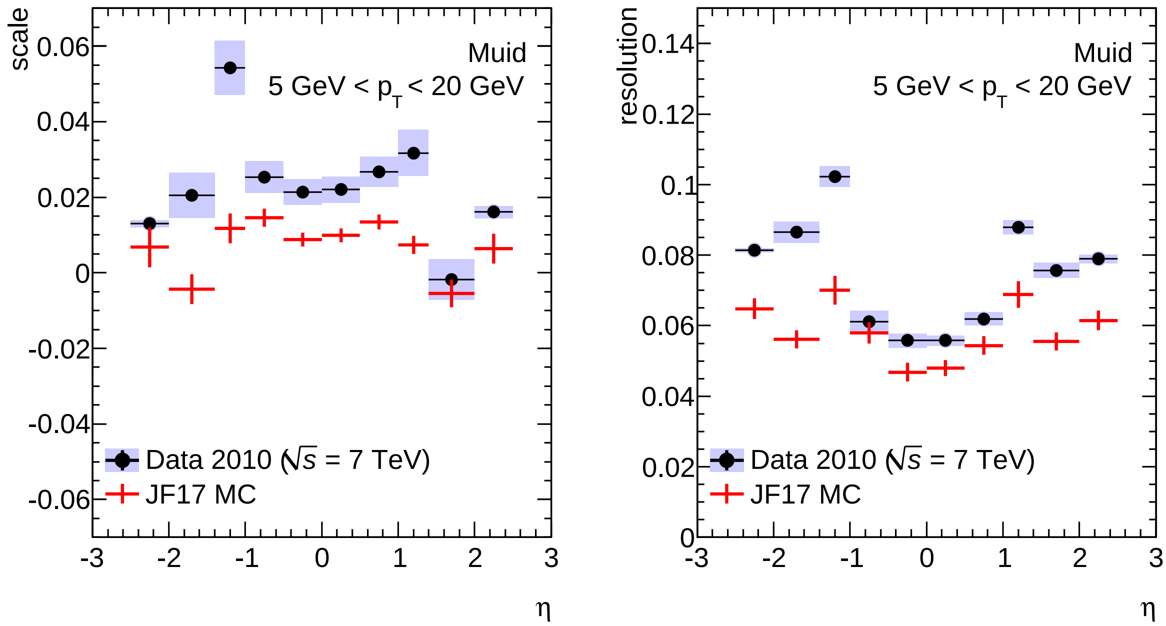

Figure 3.7: The momentum scale (left) and resolution (right) as a function of η, for muons in data (black) and in the simulated JF17 sample (red). For data the statistical and systematic uncertainty are displayed separately by black lines and light blue rectangles respectively, with the statistical uncertainty falling within the size of the marker. For simulation the red cross indicates the total uncertainty.

The barrel region: $|\eta| < 1.05$
All tracks in the barrel region of the MS should pass through three layers of MDT chambers, with the exception of tracks passing through the gap at $\eta \approx 0$. As discussed in Section 3.5.1, the agreement between data and simulation in this region is relatively good, due to alignment efforts performed with muons from cosmic rays. The momentum resolution and scale in the central part of the detector is somewhat better than in the more forward regions of the barrel. This is due to the shorter path through the calorimeters, and therefore smaller energy loss, at small $|\eta|$.

The transition regions: $1.05 \leq |\eta| < 1.4$
The transition regions contain tracks outside the MS barrel region that do not reach the outer MS end-cap ring. These tracks are measured by the inner and middle end-cap rings. In the design of the MS a third measurement should be made in the EE ring (see Figure 2.7), however most EE chambers are not yet installed in ATLAS. Therefore most tracks in the transition regions are reconstructed from only two position measurements, leading to a less precise momentum determination. As the transition regions fall outside the geometrical acceptance of most muons from cosmic rays, and the optical alignment system of the MS does not provide barrel to end-cap alignment, these regions can only be

aligned using collision muons. Therefore, at the time of this study, the difference between data and simulation in both momentum resolution and scale is large and asymmetric in η. This asymmetry in η was not unexpected as the level of random misalignment need not be the same in both regions, however this analysis was one of the first that clearly showed and quantified this effect, giving valuable feed-back for the MS alignment effort. In newer data reprocessing this asymmetry is no longer present. This can be seen in the plots of Section 2.3.1.

The MDT end-cap regions: $1.4 \leq |\eta| < 2.0$
Muons passing through these regions of the MS end-caps are measured by three layers of MDT chambers. The nominal momentum resolution should therefore be similar to that in the barrel region. The large difference between data and simulation in these region is primarily due to misalignment in the ID end-caps, as most of the MS misalignment was removed using the optical alignment system.

The CSC end-cap regions: $2.0 \leq |\eta| < 2.5$
In these regions the momentum measurement in the MS depends on the CSC measurement which is expected to be less precise than that of the MDTs, leading to a slightly worse nominal resolution. The level of misalignment in these regions is similar to that in the $1.4 \leq |\eta| < 2.0$ regions.

3.6 Comparison with other methods

We have cross-checked the results shown in this chapter two other methods used in ATLAS at the time this analysis was performed: the single-sided Gauss method and an analysis performed on muons from cosmic rays.

3.6.1 Comparison with the single-sided Gauss method

The single-sided Gauss method is a simplified version of the template fitting method which does not separate signal and background. The $\frac{\Delta p}{p}$ distribution is fitted with a single Gaussian function. The momentum scale is then defined as the central value of the Gaussian, and the resolution is its half-width. As the background from pions and kaons is prominent at positive values of $\frac{\Delta p}{p}$, the fit is performed on an asymmetric range which varies with the p_T and η bins, chosen in order to minimize the background contamination and to ensure a reasonable fit result in terms of $\chi^2/n.d.f$. As an example the top left plot of Figure 3.8 shows this fit for muons with $|\eta| \leq 1.05$ and 8 GeV$\leq p_T \leq$10 GeV.

As the single-sided Gauss method does not take the background contribution into account, it introduces considerable biases. Most notably, because the background contribution is asymmetric around $\frac{\Delta p}{p} = 0$, the scale is shifted towards positive values. As this shift depends strongly on the chosen fit range, the scale obtained using the single-sided Gauss fit is unreliable.

The obtained resolution is also biased as the fit consists only of a single Gaussian, without a Landau component. This leads to an underestimation of the resolution by about 0.5% to 1%. At higher momenta, where the Landau component becomes less important, this effect is reduced. Despite this clear bias we consider a comparison in the obtained resolution between the two methods meaningful to show that both methods find the same trend for the p_T- and η-dependence of the resolution. The comparison between the single-sided Gauss method and our template based method is shown as a function of p_T and η in Figure 3.8 showing similar distributions for both methods.

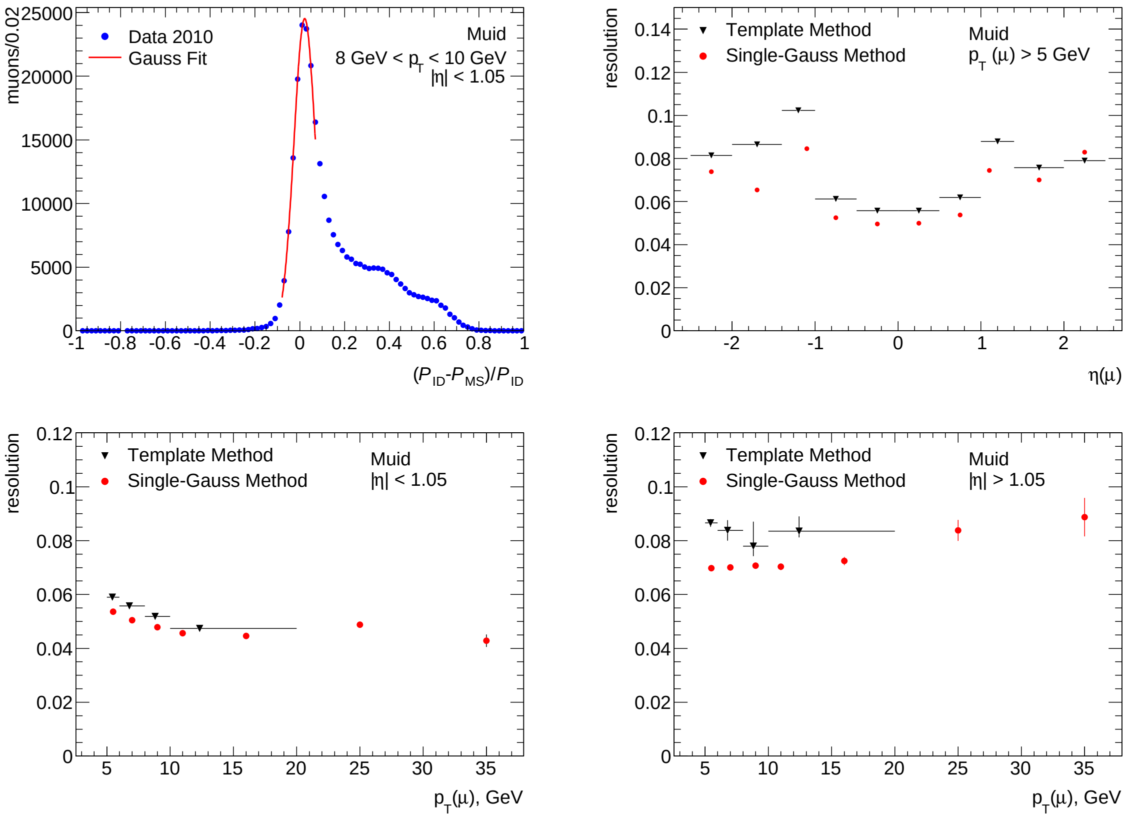

Figure 3.8: The $\frac{\Delta p}{p}$ distribution (top left) for muons in data with 8 GeV$\leq p_T \leq$10 GeV and $|\eta| < 1.05$ (dots) as well as the corresponding single-sided Gauss fit (red line). The muon momentum resolution obtained using the template method (black triangles) and using the single-sided Gauss method (blue dots) is shown as a function of η (top right) and p_T, for muons with $|\eta| < 1.05$ (bottom left) and $|\eta| > 1.05$ (bottom right).

Although the single-sided Gauss method provides less reliable results than the template fitting method, it was heavily used in ATLAS to provide quick first estimates on the resolution. Not only is this method very easy and intuitive to run, it does not rely on Monte Carlo samples and therefore does not suffer from their limited statistics. This is why the single-sided Gauss method in Figure 3.8 could be run on narrower bin sizes and on higher momentum muons than the template fitting method.

3.6.2 Comparison with data from cosmic rays

Cosmic showers produced in the earth's atmosphere are a source of high-energetic muons. Some of these muons reach the ATLAS detector and can be measured by the MS and, if the muon passes trough the center of the detector, by the ID. Such cosmic muons pass trough the entire detector and produce two separate tracks trough the MS, one in the upper and one in the lower hemisphere of the detector. By comparing these two tracks it is possible to estimate the muon momentum resolution in the MS [36].

In Figure 3.9 we compare our results with the best fit to the relative p_T resolution of the MS obtained using cosmic rays [36]. The comparison is unfortunately only possible for muons with $|\eta| < 1.05$, given the reduced geometrical acceptance of the MS end-caps for muons from cosmic rays.

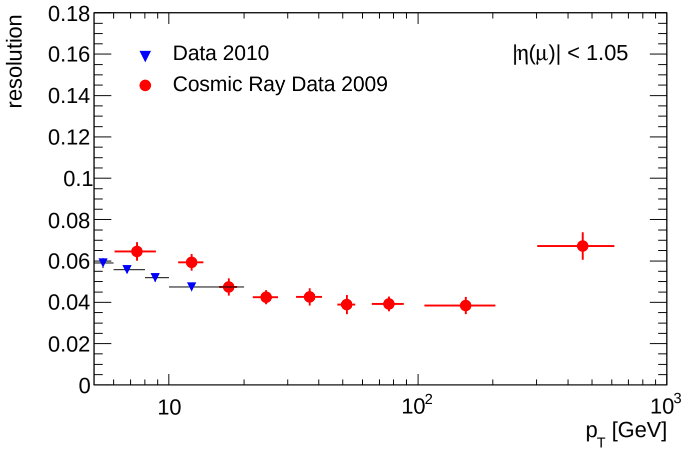

Figure 3.9: The momentum resolution for the MS obtained from cosmic ray muons [36] (red dots) and the the momentum resolution (ID $\oplus$ MS) from collision data using our template method (blue triangles).

Although this comparison is useful as a validation of our method, some differences exist between the two methods which account for the slight difference in results.

- Some improvement on the alignment of the detector was made between the publication of the results from cosmic rays and the results of the template fitting method shown in this chapter.

- The kinematic range of cosmic muons is different than that in collision data. This is especially true for the ϕ distribution since most cosmic muons traverse the detector from top to bottom. Furthermore all collision tracks radiate from the interaction point, which is not true for cosmic muons.

- The results from cosmic ray muons represent the MS stand-alone resolution, while our results estimate the combined resolution (ID $\oplus$ MS). This difference is less than

1% since the MS resolution dominates for low momentum muons in the barrel region (see Section 3.5.1).

- The cosmic analysis applies slightly different selections on the muons (see Ref. [36]).

3.7 Conclusions

We studied the muon momentum scale and resolution in ATLAS using a template method based on fitting the measured relative momentum difference of combined muon tracks in the Inner Detector with respect to the Muon Spectrometer. As this method runs on inclusive samples of low momentum muons, which have a relatively high cross-section, we were able to provide the first reliable data driven results on the muon momentum scale and resolution in the ATLAS collision data [34,35]. These results, discussed in Section 3.5, were used to study the muon reconstruction performance during the first few months of collisions at $\sqrt{s}$=7 TeV.

By estimating the scale and resolution as a function of η (and ϕ) of the muon tracks we were able to identify detector regions with relative better or poorer muon reconstruction performance. In general a good agreement between data and simulation was found in both momentum scale and resolution for muons in the MS barrel regions, indicating a good understanding of the central region of the detector. Despite the calibration and alignment performed on the barrel using muons from cosmic rays, such good agreement in early collision data was not guaranteed. Due to the spatial distribution of cosmic ray muons, which pass through the detector from top to bottom, they could only be used to align some of the ϕ sectors around $\phi = \pm\frac{1}{2}\,\pi$. The alignment of the rest of the detector relied on the relative alignment of the MS optical alignment system. Therefore achieving, in such early collision data, a difference of at most 1 % in both muon momentum scale and resolution between data and simulation, is an impressive result, especially as this difference does not depend significantly on ϕ. The estimated resolution of (4.7 ± 0.1)% for collision muons with $p_T > 10$ GeV is compatible with the resolution measured with cosmic ray muons. The remaining difference between data and simulation is dominated by a slight underestimation of the material distribution in the simulation which is corrected in more recent Monte Carlo samples.

In the end-cap regions we found a larger difference in resolution between data and simulation ($\sim 2-3$%). This is primarily due to misalignment effects, as these regions could not be fully aligned with muons from cosmic rays, although some material was also missing in the simulation. The largest degradation in resolution and scale is in the transition regions ($1.0 \leq |\eta| < 1.4$) as the MS barrel to end-cap alignment is not included in the MS optical alignment system. Most of the discrepancy between data and simulation of the more forward end-cap regions is due to misalignment in the ID, where no hardware oriented alignment exists. From Table 3.2 we can see an asymmetry in the end-cap alignment with a poorer muon reconstruction performance for negative η. By estimating the muon momentum scale and resolution in these regions as a function ϕ we could conclude that this misalignment does not depend on the MS sector.

These results on the state of the muon reconstruction performance could not be used as direct input for the ATLAS alignment, however they did provide useful feedback for the alignment of the MS, and to a lesser degree of the ID, by helping guide the efforts to regions with poorer alignment.

Apart from helping evaluate the muon reconstruction performance, the estimated scale and resolution were also used in physics analyses. Specifically they were used to interpret the results of the first W- and Z-bosons measurements [37] as both the scale and resolution affect the shape of these resonances. Furthermore, by repeating our analysis with different muon selection criteria, such as hit requirements, we were able to quantify the effect of these criteria on the momentum resolution and therefore the width of the resonances. The muon momentum scale and resolution obtained by these first W- and Z-bosons studies are compatible with our results.

Chapter 4

Muons from pion and kaon decays

In the previous chapter we introduced a template fitting method able to estimate the muon momentum scale and resolution in early collision data. Apart from determining the momentum scale and resolution of muons in a certain data sample, this method also automatically estimates the fraction of muons produced in the decay of either a pion or kaon. As muons from π/K-decays form a background for most analyses based on prompt muons, determining this fraction is an important measurement in its own right.

In this chapter we describe a template fitting method, similar to the one from Chapter 3, able to estimate the fraction of muons from pion and kaon decays in a general muon sample. We then apply this method to quantify the contribution of pions and kaons to the invariant mass distribution of muon pairs in ATLAS [39,40]. Understanding this distribution is an important step in understanding the background of any multi-muon analysis, including the same-sign prompt muon cross-section measurement presented in Chapter 6.

4.1 Introduction

The total cross-section of proton-proton interactions at the LHC is dominated by multi-jet events. As jets often include a number of pions and kaons, the total production of light mesons at the LHC is multiple orders of magnitude higher than that of prompt muons. Because both pions and kaons can decay to muons, with a branching ratio of 100% and 63.6% respectively, this results in a large number of muons from π/K decays.

As shown in Chapter 3, the combined pion and kaon contribution to muon samples can be estimated by fitting the $\frac{\Delta p}{p}$ distribution[1] of the combined muons using templates to describe the separate π/K and non-π/K distributions. Performing this analysis on inclusive single muon samples results in plots such as the ones shown in Figure 4.1 [39] which show the estimated non-π/K fraction in these samples as a function of muon p_T. At low momentum more than half the reconstructed muons originate from either a pion or a kaon. This relative contribution decreases rapidly with increasing momentum.

In this chapter we study the π/K contribution to the invariant mass distribution of muon pairs in ATLAS. Figure 4.2 shows this distribution for opposite-sign combined muon

[1] The definition of the momentum imbalance is given in Equation 3.1

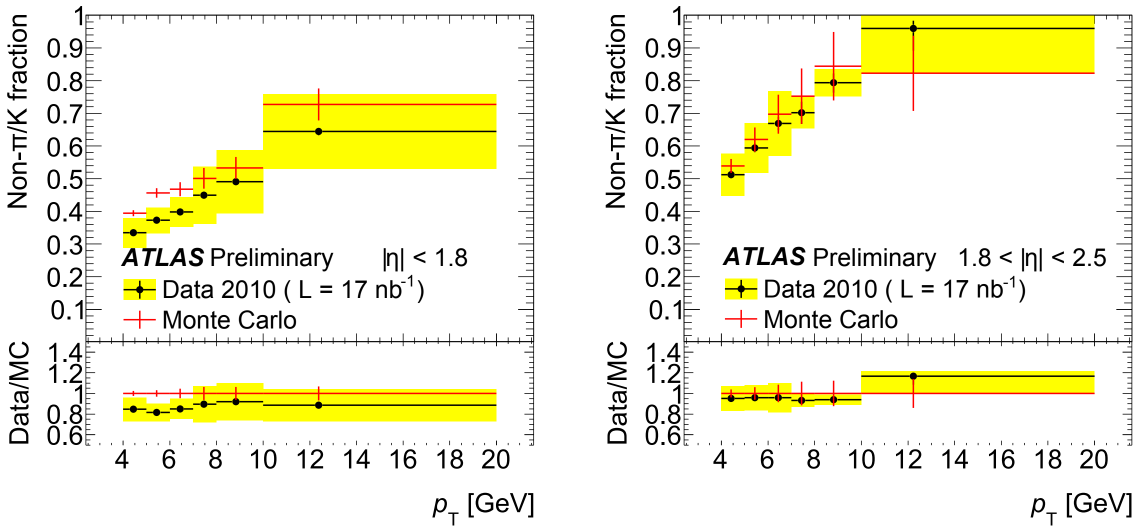

Figure 4.1: The estimated non-π/K fraction as a function of muon p_T in an inclusive single muon sample for two different η regions, compared to the fraction in a simulated Minimum Bias sample. The results are obtained using a template fitting method on the $\frac{\Delta p}{p}$ distribution of the muons [39].

pairs with at least one muon with $p_T > 4$ GeV and the other $p_T > 3$ GeV. This selection is chosen because it is close to the minimum p_T requirement for combined muons and therefore optimal for the study of low mass resonances, which are greatly reduced by stronger p_T requirements on the muons. The invariant mass distribution of Figure 4.2 shows clear peaks at mass values corresponding to particles that can decay to two muons, on top of a smooth continuum distribution. The resonances can be used to calculate the cross-section and decay time of the parent particles.

The smooth distribution underneath these resonances consists mainly of events with two muons produced in two independent decay chains, such as in $b\bar{b}$- or $c\bar{c}$-events with one muon produced in the decay of the quark and the other in the decay of the anti-quark. Another contribution comes from events where the muon pair was produced as part of a three or more body decay of a single particle, such as one muon produced in the direct decay of a b- or c-quark and the other produced in the subsequent decay of the same particle. In both of these cases the dominant contribution consists of muons produced in the direct decay of a b- or c-quarks, but, due to the large cross-section of low momentum muons from pions and kaons, there is also a significant contribution of events where at least one of the muons was produced in a π/K decay. At invariant masses much larger than the $b\bar{b}$ invariant mass the spectrum of Figure 4.2 also contains a significant contribution of muon pairs produced in Drell-Yan processes.

We estimate the π/K fraction of muon samples using a template fitting method similar to the one described in Chapter 3. The differences between both methods, discussed in Section 4.2, are aimed at stabilising the fitted fraction and improving the accuracy of the

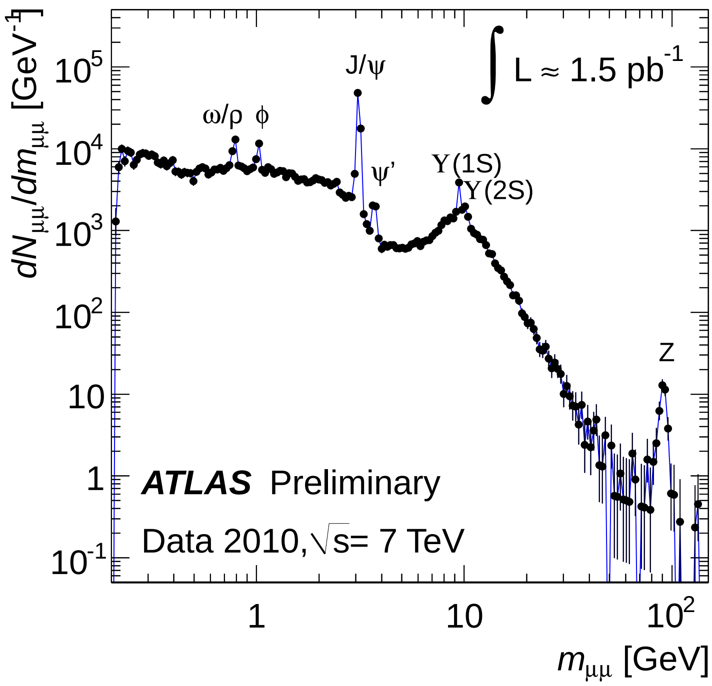

Figure 4.2: The invariant mass distribution of opposite-sign muon pairs in ATLAS. The event selection is given in Section 4.5 [40].

method specifically for low momentum muons. The most notable difference is the use of a second discriminant, called the scattering significance, to help separate π/K decays from other muons.

A statistical method is used to calculate the π/K contribution to muon pair samples. This method, explained in Section 4.3, is first validated on simulated muon pairs (Section 4.4) and then applied on the data set used to obtain Figure 4.2 (Section 4.5). The results, in terms of the estimated π/K contribution to the opposite-sign and same-sign invariant mass distribution of muon pairs in ATLAS, are presented in Section 4.6.

4.2 The π/K fraction in single muon samples

One possible way to estimate the π/K fraction of muon samples is to use the template fitting method described in Chapter 3, which fits the π/K and non-π/K contributions to the $\frac{\Delta p}{p}$ distribution of combined muons. Although this method is able to reliably estimate the π/K fraction of muon samples, it leads to relatively large systematic uncertainties as the fit is not always able to correctly separate the Landau and Gaussian component of the signal distribution (Equation 3.2). This affects the tail of the fitted signal distribution, thereby changing the estimated π/K fraction.

To avoid this uncertainty we use a slightly modified method to estimate the π/K

fraction of muon samples, in which both the templates for muons from pion and kaon decays and other muons are constructed from simulated events. Furthermore we use a second discriminant, called the scattering significance, to increase the discriminating power of the template method.

4.2.1 Discriminants

As discussed in Chapter 3, the long life-time of pions and kaons ensures that the majority of decays occur within or behind the Inner Detector volume. Such late decays in flight result in measured tracks which are partially formed by the meson before decaying and partially by the produced muon, with a discontinuity in both momentum and propagation direction at the decay point due to the emission of a neutrino. Since the tracking algorithms used in ATLAS assume that each track corresponds to one particle, these meson/muon tracks are reconstructed as one track with properties that are some combination of the two real particles. If the angle between the muon and meson trajectory or the momentum difference between both particles is large, the reconstructed track is typically of poor quality (large χ^2) and the track is rejected by the tracking algorithms. In most pion and kaon decays however this emission angle is small and the track is reconstructed as a combined muon.

Based on this information we define two discriminating variables sensitive to discontinuities in the reconstructed muon tracks: The momentum imbalance, $\frac{\Delta p}{p}$, which describes the relative momentum difference between the Inner Detector (ID) and Muon Spectrometer (MS) track and the scattering significance, which describes the probability of a momentum discontinuity within the ID track. The template method used in this chapter is based on a composite discriminant consisting of a linear sum of these two variables. The momentum imbalance, scattering significance and composite discriminant are described separately.

Momentum imbalance

The momentum imbalance, $\frac{\Delta p}{p}$, of combined muons is already introduced in Section 3.2 including a discussion on the difference in $\frac{\Delta p}{p}$ distribution between muons from π/K decays and all other muons. We shall therefore not repeat this discussion here, but focus on the differences between the templates used in Chapter 3 and those used in this chapter.

In this chapter we describe the $\frac{\Delta p}{p}$ distribution of both categories of muons by templates built from simulated events, instead of using the Landau-Gauss convolution of Equation 3.2 for the non-π/K distribution. As both template shapes are affected by the muon momentum scale and resolution, which is different in data and simulation, we modify them by allowing a combined shift of the two templates along the $\frac{\Delta p}{p}$-axis and by performing a convolution of both templates with a Gaussian. The motivation for this is given in Section 3.2.2. Although both the width of the Gaussian and the shift value could be calculated from the difference in scale and resolution obtained in Chapter 3, both variables are left as free parameters. This does not affect the stability of the fit and removes any possible systematic uncertainty due to the uncertainty on the fitted scale and resolution.

Scattering significance

The scattering significance is a measure for the likelihood of a discontinuity in momentum along an ID track. It is measured by fully refitting the track, allowing it to scatter at 8 to 16 distinct positions along its trajectory and then comparing these results with the expected angles due to multiple scattering, determined by the material thickness between the scattering positions. As the analysis performed in this chapter is limited to muons with $|\eta| < 1.05$, for which the TRT detector provides no η information, only scattering along the ϕ-coordinate is used to determine the scattering significance.

This refitting procedure is illustrated in Figure 4.3 which shows schematically the decay of π/K track to a muon track within the ID volume. The left figure indicates the original fitted track while the right figure shows the refitted track which scatters at specified scattering positions.

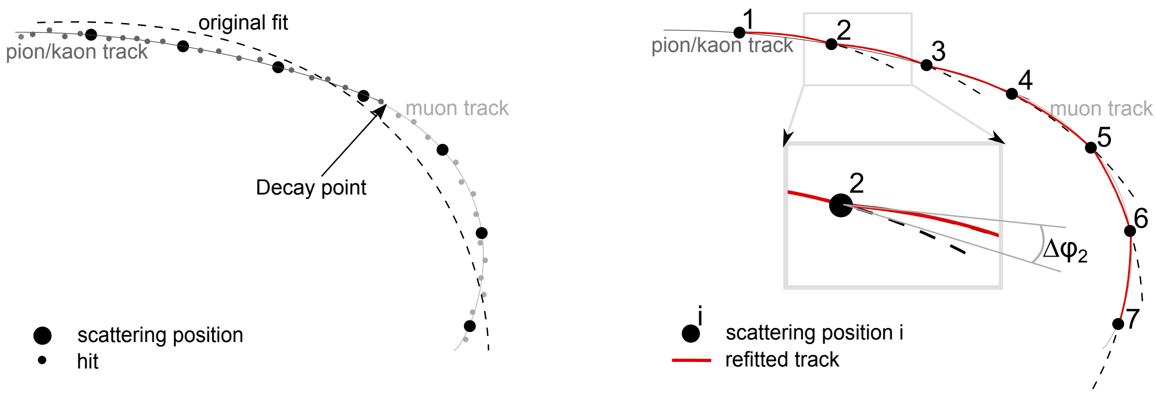

Figure 4.3: A schematic illustration of a π/K track decaying to a muon track within the ID volume with the originally fitted ID track (left) and the refitted track used to calculate the scattering significance (right). The scattering positions are indicated as well as $\Delta\phi_i$ for position 2. The dashed lines in the right image indicate the extrapolation of the fit between positions $i-1$ and i past position i. The angle $\Delta\phi_i$ corresponds to the angle between this extrapolation and the actual fit (the red line) at point i. For scattering positions before the decay point the refitted track is scattered outwards and $\Delta\phi_i > 0$ while after the decay point the scattering is inwards and $\Delta\phi_i < 0$.

We define the signed residual of a track at scatter position i as:

$$s_i \equiv q \frac{\Delta\phi_i}{\phi_i^{\mathrm{msc}}}, \tag{4.1}$$

where q denotes the charge of the track, $\Delta\phi_i$ the fitted scattering angle, obtained by the refit, at position i and ϕ_i^{msc} the expected scattering angle due to multiple scattering. A non-zero scattering angle corresponds to a change in curvature and therefore momentum.

For π/K decays within the ID volume the fitted curvature will generally correspond to a higher momentum before the decay point and a lower momentum after. Therefore s_i

will typically be positive for positions i before the decay point and negative after. This can be seen in Figure 4.3 where $\Delta\phi_i$ and therefore s_i is positive for scattering positions 2, 3 and 4, before the decay point, and negative for position 5 and 6.

Using this information we define the position scattering significance of a track at position k as:

$$S_P(k) \equiv \frac{1}{\sqrt{n}}\left(\sum_{i=1}^{k} s_i - \sum_{j=k+1}^{n} s_j\right), \tag{4.2}$$

where n denotes the total number of scattering layers along the track. Due to the discontinuity in momentum, $S_P(k)$ should be non-zero for scattering positions close to a possible decay point. The scattering significance, S, of the ID track is defined as the maximum $S_P(k)$ along the track trajectory:

$$S \equiv \mathrm{Max}\{S_P(k)\}. \tag{4.3}$$

Composite discriminant

Both the momentum imbalance and the scattering significance of combined muon tracks can be used to differentiate between muons from π/K decays and other muons. The momentum imbalance is particularly useful for high momentum tracks where the momentum difference between the meson and muon is large and the measured ID tracks are typically dominated by the meson, leading to an ID momentum measurement close to the meson momentum. At low momentum the $\frac{\Delta p}{p}$ distribution of muons from π/K decays is narrower, especially due to the requirement that the produced muon must have sufficient energy to traverse the calorimeters to produce a MS track. This effectively introduces a $p_T > 3$ GeV selection cut on the muon, which for low momentum mesons limits the maximum momentum difference between the meson and the muon and thereby the width of the $\frac{\Delta p}{p}$ distribution. The scattering significance on the other hand is most powerful for low momentum tracks, where the decay angle between the meson and the muon is largest.

As both discriminants focus on different sets of muons we use a composite discriminant, c, defined as a linear sum of the absolute value of the momentum imbalance and the scattering significance:

$$c(r) \equiv \left|\frac{\Delta p}{p}\right| + r|S|, \text{ with } r = 0.07 \tag{4.4}$$

The composite discriminant distribution for muons from π/K decays and for all other muons in the JF17 simulated sample[2] are shown in the left plot of Figure 4.4. The value of the coefficient r in Equation 4.4 is chosen such that is maximises the separation power of the composite discriminant. The separation is defined as:

$$\text{separation } s(r) = \int_{-\infty}^{\infty} \frac{\left(f_{\text{other}}(c(r)) - f_{\pi/K}(c(r))\right)^2}{f_{\text{other}}(c(r)) + f_{\pi/K}(c(r))} \mathrm{d}c \tag{4.5}$$

where r denotes the coefficient and $f_{\pi/K}(c(r))$ and $f_{\text{other}}(c(r))$ are the composite discriminant distributions of muons from π/K decays and other muons respectively. The

[2]The JF17 sample is described in Appendix A

optimization curve obtained using the JF17 simulated sample is shown in the right plot of Figure 4.4.

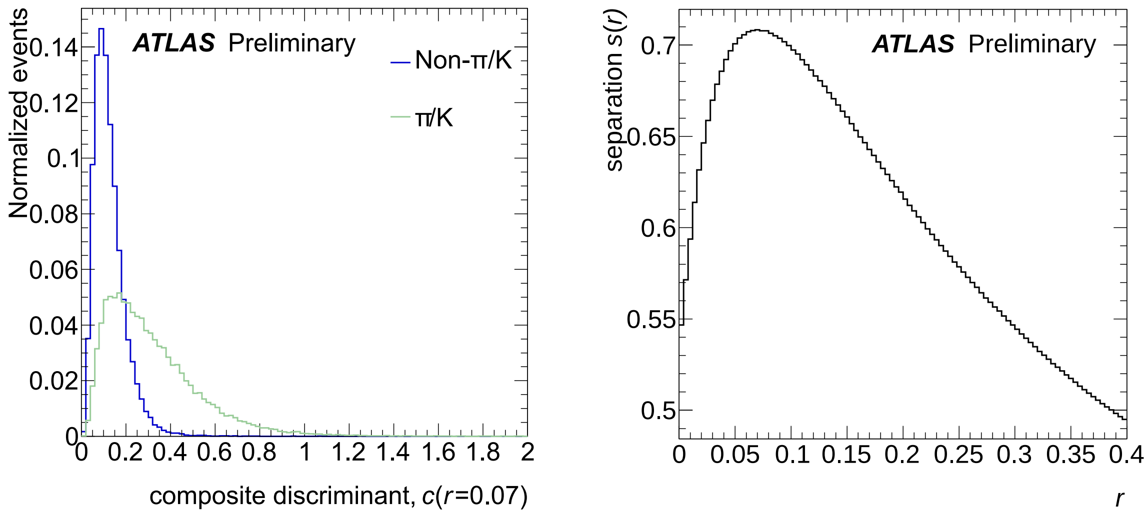

Figure 4.4: Left: The normalized $c(r = 0.07)$ distribution for muons from π/K decays (light green line) and other muons (dark blue line) in the JF17 simulated sample. Right: The separation of the composite discriminant on the JF17 simulated sample as a function of the coefficient r [40].

4.2.2 Fitting the π/K fraction of muon samples

We estimate the π/K fraction of muon samples by performing an unbinned likelihood fit on the composite discriminant distribution of these samples using templates to describe the π/K and non-π/K distributions. The fitted normalization of the templates is used to calculate the π/K fraction.

The templates used in the fit are constructed from simulated muons in the JF17 sample in a similar way as the background templates in Chapter 3. The only difference is that we include a shift of the $\frac{\Delta p}{p}$ distribution as well as a convolution with a Gaussian to account for differences between data and simulation. Therefore each fit has three free parameters: the π/K fraction, the shift value and the width of the Gaussian. The statistical uncertainty on the π/K fraction is given by a profile likelihood fit.

As an example Figure 4.5 shows the composite discriminant distribution for single muons with $|\eta| < 1.05$ and 4 GeV $< p_T <$ 5 GeV in data as well as the best fit and the fitted π/K and non-π/K components.

4.2.3 Systematic uncertainty determination

The evaluation of the systematic uncertainties associated with this analysis, is similar to the procedure used in Chapter 3. We consider three types of systematic uncertainties:

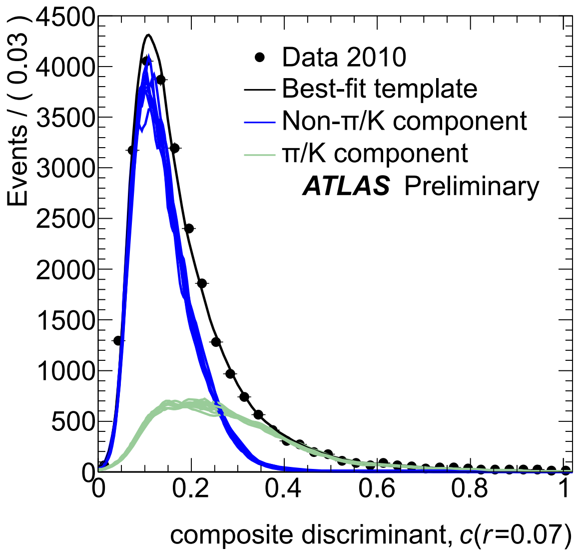

Figure 4.5: The composite discriminant distribution for single muons with $|\eta| < 1.05$ and 4 GeV $< p_T <$ 5 GeV in data (black dots). The best fit of this distribution is given by the black line. The light green and dark blue lines indicate the fitted π/K and non-π/K components respectively, obtained using different toy-MC-templates [40].

- Uncertainty due to limited simulated statistics: We estimate this uncertainty by performing fits using toy-MC-templates, as described in Section 3.2.3.

- Uncertainty due to possible differences in the pion to kaon ratio between collision data and simulated events: This is estimated by performing two additional fits: one with a π/K template with twice the pion content and the other with twice the kaon content. (As described in Section 3.2.3.)

- Uncertainty due to the chosen fitting method: This uncertainty is estimated by performing fits using binned histograms instead of the constructed templates. These results are compared to the π/K fraction obtained from template fits performed with unconvoluted and not shifted templates. The difference between both methods is at most 1%, we therefore add an uncertainty of 1% to all fit results due to this effect. The uncertainty on the fitting method was not considered in Chapter 3 because the results of that analysis are obtained from the properties of the signal template described by a function.

For fits performed on large data samples the uncertainty due to simulated statistics dominates. As this uncertainty is also present in the calculation of the other systematic uncertainties we can use the same argument as in Section 3.2.3 and only quote the largest uncertainty. However all fits performed in this chapter are done on small data samples (narrow invariant mass bins), where this is not the case. We therefore assume no correlation between the systematic uncertainties and add them in quadrature.

4.3 The π/K contribution in dimuon samples

In the previous section we have introduced a template fitting method based on the composite discriminant to estimate the π/K fraction of muon samples. In this section we describe the statistical procedure necessary to apply this method on muon pairs.

The method to estimate the π/K contribution to muon pairs used in this chapter is based on the fact that although the template shapes depend on the properties (p_T and η) of the muon (and meson), they are independent on the topology of the rest of the event. This means that the composite discriminant distribution of muons is independent on the existence or the properties of a second muon.

Given this information we divide all muons in the considered dimuon sample into p_T-η bins and fit the π/K fraction in each bin using the template fitting method described in Section 4.2. The probability of a muon in p_T-η bin i to have been produced in a pion or kaon decay is denoted as ω_i and is equal to the estimated π/K fraction in this bin.

Assuming no correlation between the results in different bins, an assumption which is tested by performing this analysis on simulated muon pairs (Section 4.4), the probability of a muon pair with one muon in bin i and the other in bin j to not contain a muon from either a pion or kaon decay is given by:

$$\omega_{ij}^{(0)} = (1-\omega_i)(1-\omega_j). \tag{4.6}$$

The probability that at least one of the muons is from a pion or kaon decay is therefore given by:

$$\omega_{ij}^{(1+)} = 1-(1-\omega_i)(1-\omega_j). \tag{4.7}$$

Using these probabilities the total number of muons pairs without π/K decays, $N^{(0)}$, and with at least one muon from π/K decay, $N^{(1+)}$, is given by:

$$N^{(0)} = \sum_{ij} \omega_{ij}^{(0)} n_{ij} \qquad \text{and} \qquad N^{(1+)} = \sum_{ij} \omega_{ij}^{(1+)} n_{ij}, \tag{4.8}$$

where n_{ij} is the total number of events with one muon in p_T-η bin i and the other in j.

The uncertainties on $\omega_{ij}^{(0)}$ and $\omega_{ij}^{(1+)}$ are given by:

$$\sigma(\omega_{ij}^{(0)})^2 = \sigma(\omega_{ij}^{(1+)})^2 = \sigma_{\omega_i}^2(1-\omega_j)^2 + \sigma_{\omega_j}^2(1-\omega_i)^2, \quad i \neq j \tag{4.9}$$

where $\sigma_{\omega_i} = \sqrt{\sigma^2_{\omega_i,\mathrm{syst}} + \sigma^2_{\omega_i,\mathrm{stat}}}$, the combined statistical and systematic uncertainty of ω_i.

When both muons are in the same p_T-η bin the estimated π/K fraction for both muons are automatically equal and therefore fully correlated. The uncertainty is then given by:

$$\sigma(\omega_{ii}^{(0)})^2 = \sigma(\omega_{ii}^{(1+)})^2 = 4\sigma_{\omega_i}^2(1-\omega_i)^2. \tag{4.10}$$

The total uncertainty on $N^{(0)}$ and $N^{(1+)}$ are given by:

$$\left(\sigma^{(0)}\right)^2 = \sum_{ij}(\omega_{ij}^{(0)} n_{ij} + n_{ij}^2 \sigma(\omega_{ij}^{(0)})^2, \tag{4.11}$$

$$\left(\sigma^{(1+)}\right)^2 = \sum_{ij}(\omega_{ij}^{(1+)} n_{ij} + n_{ij}^2 \sigma(\omega_{ij}^{(1+)})^2, \tag{4.12}$$

where the first term corresponds to the Poisson uncertainty on the observed number of events and the second term is the propagation of the uncertainty related to the fits.

The π/K contribution to the invariant mass distribution of muon pairs

Equation 4.8, 4.11 and 4.12 give the best estimate and the uncertainty on the π/K contribution to muon pairs. By calculating these values for narrow invariant mass bins it is possible to construct the π/K contribution to the invariant mass distribution of same-sign and opposite-sign muon pairs in ATLAS. The results of this procedure are shown in Section 4.6.

In this chapter we only consider muons within the MS barrel region $|\eta| < 1.05$ where the track quality and therefore the template shapes are relatively well understood. As the template dependence on η in this region is negligible, no binning in η is used.

A fine binning in invariant mass is necessary to observe and study narrow resonances, however it introduces some additional uncertainties. The limited number of events per bin means that most bins have insufficient statistics to perform the full fitting procedure of Section 4.2 without risking unstable fit results. Therefore instead of leaving the shift and the convolution of the $\frac{\Delta p}{p}$ distribution as free parameters we generally use a common value depending on the p_T bin obtained by fitting single muon data samples. Only in bins with more the 500 entries the full fitting method is used. In practise these are only bins in the center of the J/ψ peak.

Using a common value for the shift and convolution of the $\frac{\Delta p}{p}$ distribution independent of the invariant mass bin is based on the idea that the energy-loss of muons is independent on the properties of the second muon and therefore on the true invariant mass of both particles. Unfortunately some dependence on the invariant mass does exist since both the measured invariant mass and the composite discriminant depend on the muon track quality. This introduces an addition systematic uncertainty on the estimated π/K fraction.

To illustrate this, take muon pairs produced in the decay of a J/ψ particle. As the width of the resonance depends strongly on the resolution of the tracks, the track quality of muon pairs with a reconstructed invariant mass in the center of the resonance is generally better than that of muon pairs which are a few sigma away from the central value. Therefore the composite discriminant distribution for J/ψ decays in the center of the resonance is narrower than in the side-bands.

Without compensating for this effect in the template shapes the amount of muons pairs with at least one muon from a pion or kaon decay will be slightly underestimated in the center of resonances and overestimated on the sides. As the amount of over-/underestimation of the events in bin $m_{\mu\mu}$ depends on the number of events in the surrounding bin, at first order this uncertainty is given by the gradient of the number of events in the considered bin. We therefore take the following relative difference in events as the systematic uncertainty due to the uncertainty on the measured invariant mass and add it to quadrature to the other fit uncertainties.

$$\frac{\Delta n}{n} \equiv \frac{n(m'_{\mu\mu}) - n(m_{\mu\mu})}{n(m_{\mu\mu})} \tag{4.13}$$

where $n(m_{\mu\mu})$ denotes the number of events (per mass unit) at mass $m_{\mu\mu}$. Two values of $m'_{\mu\mu}$ are used chosen to represent an overestimation and underestimation of the measured invariant mass by 0.5%.

4.4 Validation

The method described in Section 4.2 and 4.3 is validated on simulated opposite-sign muon pairs in a merged sample of 10 million simulated $b\bar{b}$ and 10 million $c\bar{c}$ events. This sample, denoted as $b\bar{b}/c\bar{c} \rightarrow \mu + X$ is described in more detail in Appendix A. The result of this validation is shown in the left plot of Figure 4.6 which shows the invariant mass distribution (black line/dots) of all muon pairs in the samples as well as the distribution for pairs with zero (dark blue line) and at least one muon from pion or kaon decays (light green line). The estimated distributions for the pairs with and without at least one muon from π/K decays are shown by the light green squares and dark blue triangles respectably. The compatibility between the true and estimated distribution is excellent. This is further illustrated in the right plot of Figure 4.6 which shows the ratio of estimated number of events without muons from π/K decays over the true value, as a function of the invariant mass. The discrepancy at very low invariant mass is mostly due to the fact that these mass-bins are dominated by very low momentum muon tracks where the discriminants are known to be less reliable. The agreement between the true and fitted value for the rest of the distribution proves the validity of this method.

4.5 Data set and event selection

The results shown in this chapter are obtained from data collected by the ATLAS experiment between the 30th of March and the 30th of August 2010[3], passing data-quality cuts and triggered using an event filter trigger for muons with a transverse momentum above 4 GeV (EF_mu4)[4]. For part of the considered period this trigger was prescaled, resulting in 1.5 pb^{-1} of data collected out of 3.4 pb^{-1} delivered integrated luminosity.

The offline event selection requires events with at least three ID tracks associated to the primary vertex and at least one muon pair with the following characteristics:

- Both muons are in the MS barrel region: $|\eta| < 1.05$
- One muon with $p_T > 4$ GeV, the other with $p_T > 3$ GeV
- The ID track of both muons has at least 1 hit in the pixel and 6 hits in the SCT detector

[3]This corresponds to Period A to F of 2010 (see Table 2.1).
[4]The EF_mu4 trigger is described in Section 2.4.2

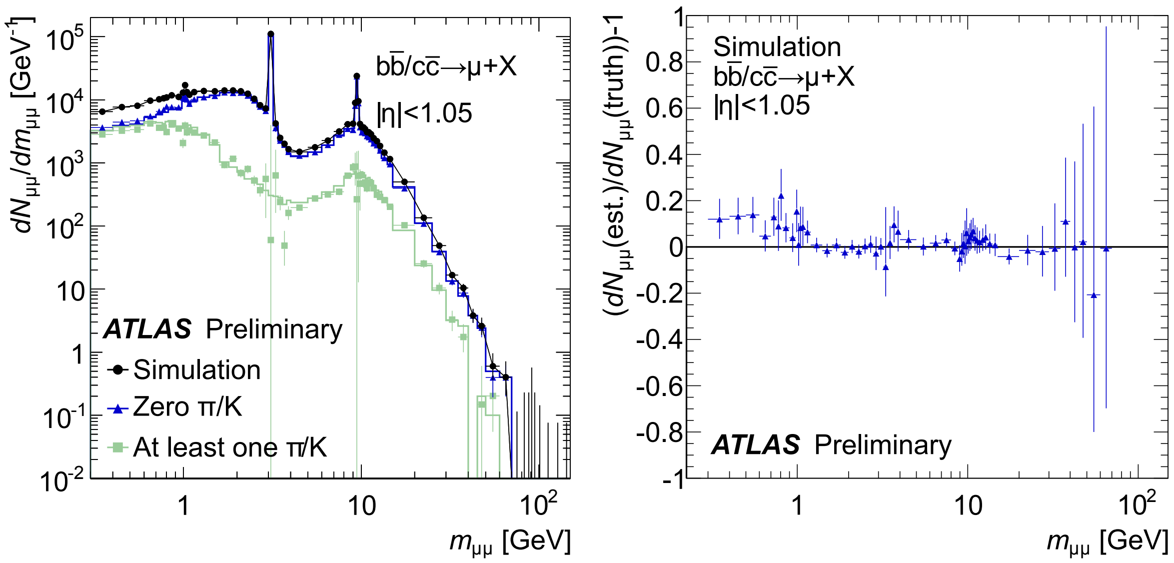

Figure 4.6: Left: The invariant mass distribution of opposite-sign dimuon pairs in the $b\bar{b}/c\bar{c} \rightarrow \mu + X$ simulated sample (black dots) and the separate true and fitted contribution of pairs with (light green line/squares) and without (dark blue line/triangles) at least one muon from pion or kaon decays. Right: The fitted fraction of muon pairs without pions and kaons decays over the true value [40].

- A vertex fit of the two muons has $\chi^2/ndf < 6$, to ensure that both muons are produced in the same interaction

This selection was chosen to minimize the momentum requirement of the muons, while allowing for reasonable efficiency in the muon trigger. The analysis is limited to muons in the MS barrel region with sufficient hits in the pixel and SCT detector, to guarantee a well understood track reconstruction performance. This selection results in a data sample containing 33575 opposite-sign and 8772 same-sign muon pairs.

4.6 Results

Applying the template fitting method described in this chapter on the data sample introduced in Section 4.5 results in the invariant mass distributions of Figure 4.7, where the top plot shows the distribution for opposite-sign muon pairs, and the bottom plot its same-sign equivalent. For both distributions the estimated distribution of pairs with and without at least one muon from a pion or kaon decay is shown as well.

The total fraction of pairs with at least one muon from π/K decays is estimated to be $68 \pm 2\%$ for same-sign and $31 \pm 4\%$ for opposite-sign pairs. The fraction of dimuons where both muons were produced in the decay of a pion or kaon is not shown in Figure 4.7. The total estimated fraction is $22 \pm 2\%$ for same-sign and $5 \pm 1\%$ for opposite-sign pairs.

It can be seen from Figure 4.7 that the π/K contribution produces a smooth background in the invariant mass distributions and that all resonances are clearly produced

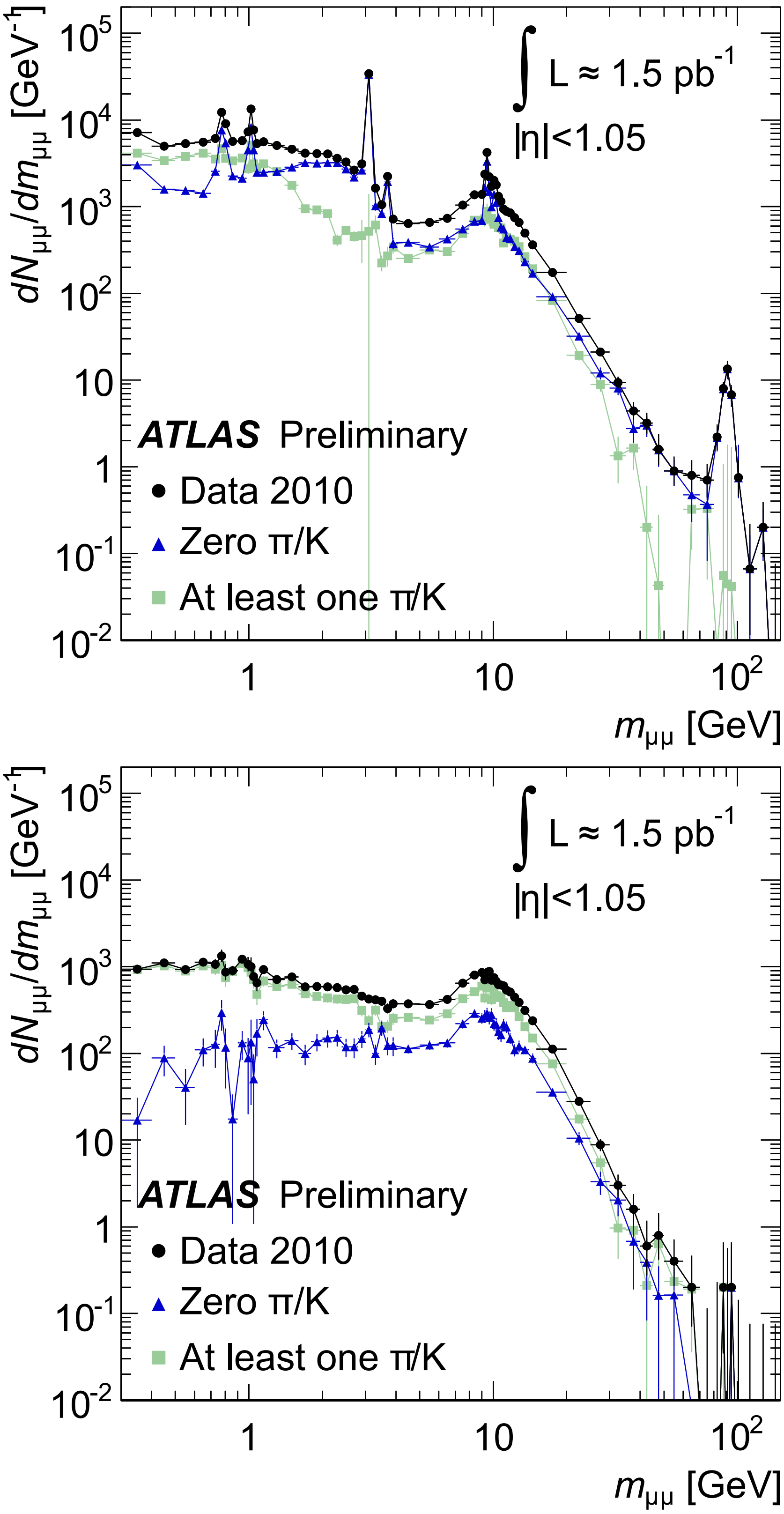

Figure 4.7: The invariant mass distribution of opposite-sign (top) and same-sign (bottom) dimuon pairs in data (black dots) and the fitted contribution for muons pair with (light green squares) and without (dark blue triangles) at least one muon from π/K decays [40].

by two non-π/K muons. The difference in fraction of events with at least one muon from π/K decays between the same-sign and opposite-sign muon pairs is mostly due to the higher cross-section for opposite-sign pairs from prompt muons and muons from the decay of heavy flavour quarks. This can be seen in Figure 4.8 where we plot the difference in distribution between the opposite-sign and same-sign muon pairs for three different mass ranges. The background from π/K decays is the same for the same-sign and opposite-sign muon pairs over most of the invariant mass range, as this background is caused by combining a muon from π/K decays to an unrelated other muon in the event. At very low mass ranges this is no longer the case and more opposite-sign pairs with at least 1 muon from π/K decays were estimated than same-sign pairs. This difference is dominated by decays of charmed and beauty mesons to a lepton and at least one pion or kaon, such as: $D^0 \to K^{\pm}\mu^{\mp}\nu$.

4.7 Conclusion

Muons from pion and kaon decays form a background for any analysis involving prompt muons. In this chapter we introduced a template fitting method to estimate the π/K fraction of muon samples in a data driven fashion. This template method is based on the difference in both the momentum imbalance and the scattering significance of muon tracks from π/K decays and other sources. By using a statistical method we can estimate the π/K contribution to dimuon samples and therefore determine the π/K contribution to the invariant mass distribution of muon pairs in ATLAS. This analysis was validated on simulated $b\bar{b}$ and $c\bar{c}$ events, resulting in excellent agreement between the true and estimated composition of the distributions.

The estimated π/K contribution to the invariant mass distributions in data is shown in Figure 4.7. Apart form the very low mass region ($m_{\mu\mu} < 2$ GeV), the estimated π/K contributions to the opposite- and same-sign invariant mass distributions are equal within statistical errors. Specifically, the smooth distribution for the invariant mass distribution of muon pairs with a least one π/K decay shows no contribution to any of the dimuon resonances. This is not unexpected since, apart from the low mass region, the π/K contribution is dominated by events where a muon from a pion or kaon decay is paired with an independently produced second muon.

In total $68 \pm 2\%$ of the selected same-sign and $31 \pm 4\%$ of the opposite-sign muon pairs contain at least one muon from π/K decays. These numbers illustrate the importance of considering and quantifying the contribution from muons from pion and kaon decays in any multi-muon analysis in ATLAS.

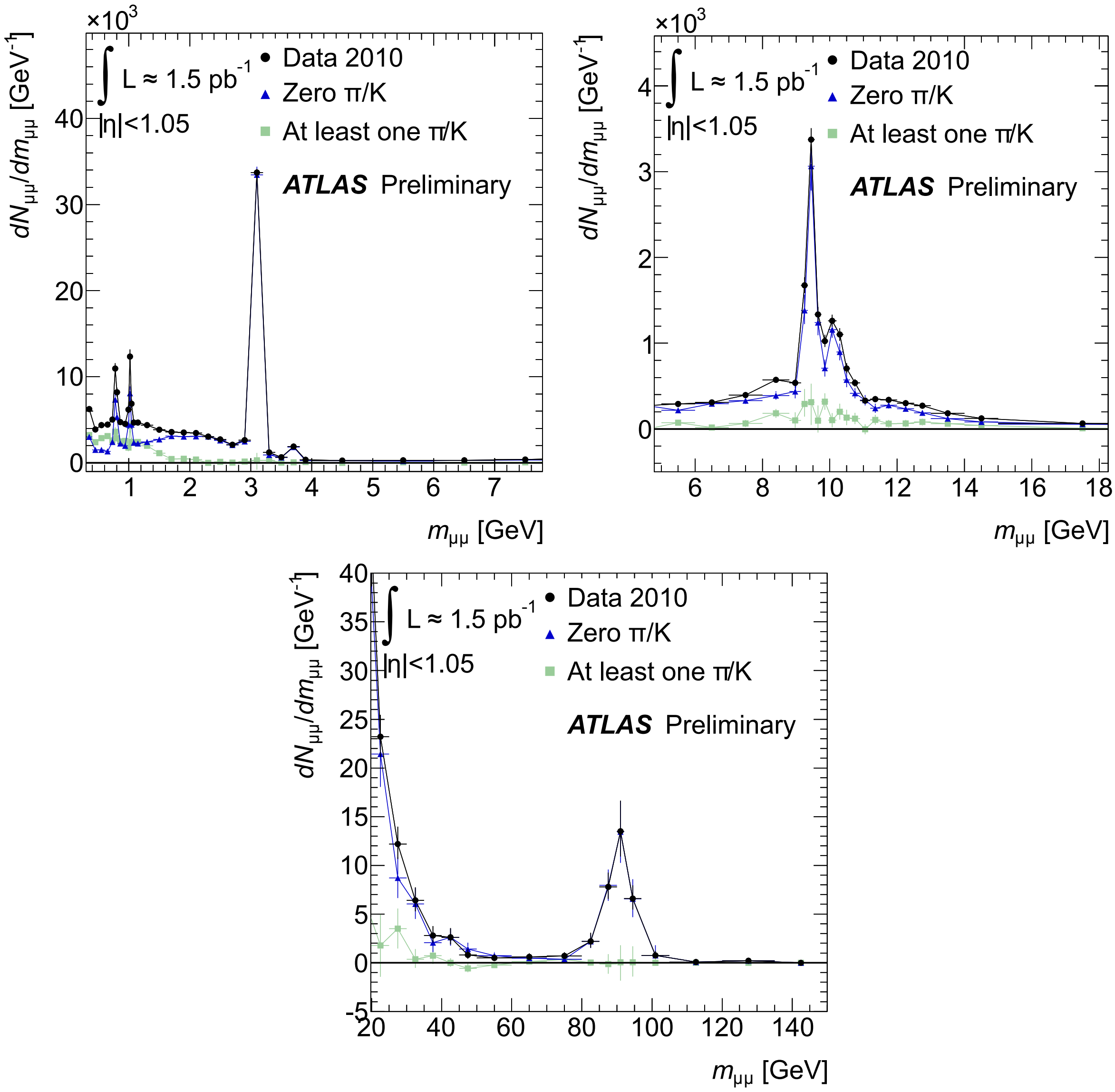

Figure 4.8: The difference in invariant mass distribution between opposite-sign and same-sign dimuon pairs in data (black dots) and the fitted difference for muon pairs with (light green squares) and without (dark blue triangles) at least one muon from π/K decays, for different mass ranges [40].

Chapter 5

Prompt muons

Event topologies containing muons are used in a large variety of physics analyses, from top-physics to searches beyond the SM. Such analyses are in general interested in prompt muons, muons produced at the interaction point. In the case of the Standard Model these are muons produced in the decay of Z- or W-bosons as well as from Drell-Yan processes. All other muons, produced in the decays of b- or c-quarks, taus, pions or kaons, form a background.

In Chapter 4 we used a template fitting method based on the energy-loss and scattering significance of combined muons to estimate the contribution of pion and kaon decays to muon samples. These two variables do not differentiate prompt muons from other non-prompt muons produced before the first detector layer. Therefore, to estimate the prompt fraction of muon samples in a data-driven fashion, we developed an alternative template fitting method [41] based on the transverse impact parameter significance of the muon tracks (d_0-significance), which we describe in this chapter. This method is used in the Chapter 6 to calculate the cross-section of prompt same-sign muon pairs in ATLAS.

5.1 Introduction

Different processes can lead to the creation of muons in ATLAS. Most analyses involving muons are only interested in prompt muons. These analyses generally aim to reject the contribution from other processes, such as from heavy-flavour quark decays, using muon isolation criteria or requiring the muon track to be reconstructed as coming from the primary vertex (small impact parameter). The remaining non-prompt background after such selection cuts is either determined using simulated events or in a data-driven fashion.

In ATLAS, most data-driven methods used for this purpose are based on control regions which are statistically independent of the signal region and chosen to be background dominated. The amount of non-prompt contamination in the signal region is then extrapolated from the control region. These methods, while successful, can be highly model dependent as they rely on knowing how to extrapolate the number of events in the signal region from that of the control regions. This extrapolation may depend on the kinematics of the considered non-prompt processes. Therefore these methods typically need to be validated separately for each definition of the signal region. Furthermore, unexpected processes, such as physics beyond the SM, can influence this extrapolation.

To avoid this model dependence we developed a method which, instead of rejecting non-prompt muons, uses the difference in impact parameter distribution between prompt and non-prompt muons to estimate the prompt fraction of muon samples directly in the signal region. This is done using a template fitting method, similar to the one used in Chapter 4, but based on the d_0-significance of muon tracks. The precise definition of the d_0-significance is given in Section 5.3. In general the d_0-significance distribution depends on the travel distance, and therefore the lifetime, of the muon ancestors. Based on this lifetime we consider five different categories of muons:

- **Prompt muons:** Prompt muons are produced at the interaction point, such as in the direct decay of Z- or W-bosons or in Drell-Yan processes.

- **B-meson decays:** B-mesons can produce muons through the direct decay of b-quarks, as well as though the subsequent decay of c-quarks, taus, pions or kaons.

- **D-meson decays:** D-mesons can produce muons through the direct decay of c-quarks, as well as though the subsequent decay of taus, pions or kaons. In this chapter we consider any muon produced in the decay of a D-meson which is part of a B-meson decay chain, as part of the B-meson decay category.

- **Tau decays:** Taus can also decay to muons. In this category we only consider taus which are not part of a B- or D-meson decay chain.

- **Light meson decays:** As discussed in the previous chapters pions and kaons can also decay to muons. This last category of muons does not include any pions or kaons which are part of a B- or D-meson decay chain. Therefore the definition of light meson decays used in this chapter is different from that of π/K-decays used in Chapter 3 and 4.

The shape of the d_0-significance distribution for each of these categories is discussed in Section 5.4 and 5.5.

An inclusive muon sample typically contains muons from each of these categories with the relative ratios depending on the exact selection criteria of the considered sample. We estimate these ratios by fitting the d_0-significance distribution of the data sample using templates to describe the distribution of the individual categories. This full template fitting method is detailed in Section 5.6, including the building of the templates from simulated events, the fit and the calculation of systematic uncertainties.

One of the main advantages of such a template fitting method is that once the templates and their dependence on the event topology are understood this method is model independent and can therefore be applied on almost any muon sample. This model independence allows us to validate the method on a large variety of different topologies in both simulated events or directly on data. The results of some of these test are presented in Section 5.7.

This flexibility also leads to a large range of possible applications such as: quantifying the background contamination from non-prompt muons in a prompt dominated signal samples such as for $t\bar{t}$ or Z-/W-boson analyses, studying the effect of selection cuts on the prompt muon fraction and searching for a prompt muon signal in a background dominated region, as we do in Chapter 6.

5.2 Data set and event selection

Before going into the details of the template fitting method described in this chapter, we introduce the different data sets, both simulated and from collision data, used in this chapter, as well as define a common muon selection. Stronger selection cuts are implemented in some cases. If so this is indicated in the text.

Data sets

We use simulated samples of the following processes to study the d_0-significance, to build the templates and to validate the method: $t\bar{t}$, $Z \to \mu\mu$, $b\bar{b}$, $c\bar{c}$, $Z \to \tau\tau$ and a di-jet sample known as $JF17$. These samples are listed in Appendix A.

The differences in d_0-significance between data and simulation are studied using approximately 2.5 fb^{-1} of collision data, selected on-line by the any of the ATLAS Muon triggers and passing detector data quality checks, between April 14 and August 22 of 2011[1]. This same data set is also used to validate the method.

Muon selection

The basic muon selection used in this chapter is aimed at selecting muons from W- and Z-bosons decays and therefore has a higher momentum requirement than in the previous chapters. On top op the basic selection defined in Section 2.3.1, we add the following requirements:

- p_T(combined track) > 15 GeV
- p_T(ID track) > 10 GeV
- At least 1 B-layer hit
- At least 3 hits in the pixel detector

The hit requirements ensure a good track position measurement.

Each muon is associated to the closest jet in the event, if any, where the distance between the jet and the muon is defined as: $\Delta R(\mu,\text{jet}) = \sqrt{(\Delta\phi(\mu,\text{jet}))^2 + (\Delta\eta(\mu,\text{jet}))^2}$.

[1]This data period corresponds to period D to K of 2011 (see Table 2.1)

5.3 The d_0-significance variable

The d_0-significance (d_0-sig) of a track is a measure for the likelihood that the track originated from the primary vertex and is therefore ideal to separate prompt from non-prompt muons. It is defined as:

$$d_0\text{-sig} \equiv \frac{d_0}{\sigma_{d_0}},$$

where d_0 denotes the transverse impact parameter of the track, the closest distance in the transverse plane between the extrapolated track and the reconstructed primary vertex, and σ_{d0} is the assigned uncertainty on d_0, containing both the uncertainty from the track and vertex reconstruction. To remove correlations between the track and primary vertex reconstruction, the vertex is refitted without the considered track.

In the case of muons the most precise information to determine the impact parameter in contained in the ID track. We therefore define the d_0-significance of combined muons to be that of their corresponding ID tracks.

Since prompt muons are produced at the interaction point their d_0-significance distribution is relatively narrow, while for muons produced in the decay of longer lived particles this distribution is broader, with long tails depending on the life-time of the parent particle.

The sign of the d_0-significance

The sign of d_0, and therefore of the d_0-significance, is based on the ϕ direction of the track at the point of closest approach to the vertex. This definition results in equal probabilities for tracks with positive and negative d_0, leading to d_0-significance distributions which are symmetric around zero. As this default sign of the d_0-significance holds no discriminating power to separate muons of different origins we redefine the sign with respect to the closest jet. This redefinition, described below, leads to a asymmetric d_0-significance distribution for muons produced in the decay of B- or D-meson while remaining symmetric for all other muons.

In the case of muons produced within a jet, such as in the decay of B- or D-mesons, the muon production vertex is along the jet trajectory. Therefore, bearing resolution effects, the muon track is reconstructed to pass the primary vertex on the same side as the jet direction. We exploit this correlation by redefining the sign of the d_0-significance depending on the spacial direction of the closest jet. In events without jets, the original sign of d_0 is used.

$$d_0\text{-sig} = \begin{cases} +|d_0\text{-sig}| & \text{if } |\phi_0 - \phi(\text{jet})| < \frac{\pi}{2} \\ -|d_0\text{-sig}| & \text{if } |\phi_0 - \phi(\text{jet})| > \frac{\pi}{2} \end{cases}$$

Where ϕ_0 denotes the ϕ component of the impact parameter of the muon and $\phi(\text{jet})$ the ϕ direction of the jet trajectory. Both ϕ_0 and $\phi(\text{jet})$ are illustrated in Figure 5.1.

Variables used to characterise the d_0-significance distributions

From the discussion on the d_0-significance variable given in this section, it is clear that two main properties of d_0-significance distribution which depend strongly on the muon origin

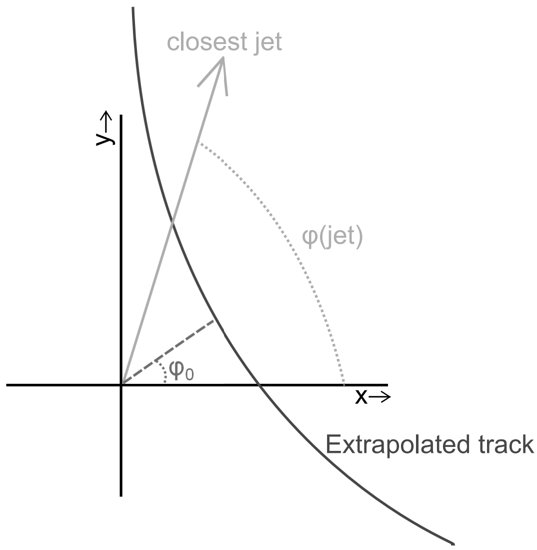

Figure 5.1: An illustration of an extrapolated track trough the transverse plane of the detector, with the refitted primary vertex in the origin. The closest jet trajectory is indicated by an arrow. Both angles ϕ_0 and ϕ(jet) are indicated. This track has a positive d_0-significance.

are its width and asymmetry. We therefore define the following two variables to compare the shape of the d_0-significance distributions of muons with different origins, as well as to study and illustrate possible differences in these distributions depending on muon and event selection criteria:

$$\begin{aligned} W(d_0\text{-sig}) &\equiv \text{mean of the } |\mathrm{d}_0\text{-sig}|\text{-distribution} && \text{(measure for the width)} \\ A(d_0\text{-sig}) &\equiv \text{mean of the } \mathrm{d}_0\text{-sig-distribution} && \text{(measure for the asymetry)} \end{aligned}$$

$W(d_0$-sig) is a measure for the width of the d_0-significance distribution which, contrary to the actual width of the distribution, is independent of the asymmetry. $A(d_0$-sig) on the other hands depends strongly on this asymmetry. In the case of a symmetric d_0-significance distribution $A(d_0\text{-sig}) = 0$.

It is clear that these two variables are insufficient to uniquely define a d_0-significance distribution. Other properties, such as the ratio of muons in the bulk of the distribution compared to the tails, are also important. Nevertheless $W(d_0$-sig) and $A(d_0$-sig) are convenient variables to illustrate differences between d_0-significance distributions.

To show that the d_0-significance variable is useful in separating samples dominated by prompt muons from those with a strong background component from decays of heavy flavour quarks as well as to illustrate the use of $W(d_0$-sig) and $A(d_0$-sig), we consider the invariant mass distribution of $\mu^+\mu^-$-pairs in collision data, shown in Figure 5.2. The Z-boson is clearly visible as a peak around 90 GeV. The Υ resonance at around 10 GeV is also discernible. Both the Z-boson and Υ can decay to a pair of muons which, due to the short lifetime of these resonances, are considered prompt. The rest of the invariant mass distribution is dominated by muons from B-meson decays and, to a lesser degree, from

D-meson decays. The dependence of $W(d_0\text{-sig})$ and $A(d_0\text{-sig})$ on the invariant mass of the muon pair is also shown in Figure 5.2. As expected, the d_0-significance in the Υ and Z-boson mass range is significantly narrower and more symmetric than in the more background dominated regions. This is clearly visible in the $W(d_0\text{-sig})$ and $A(d_0\text{-sig})$ distributions.

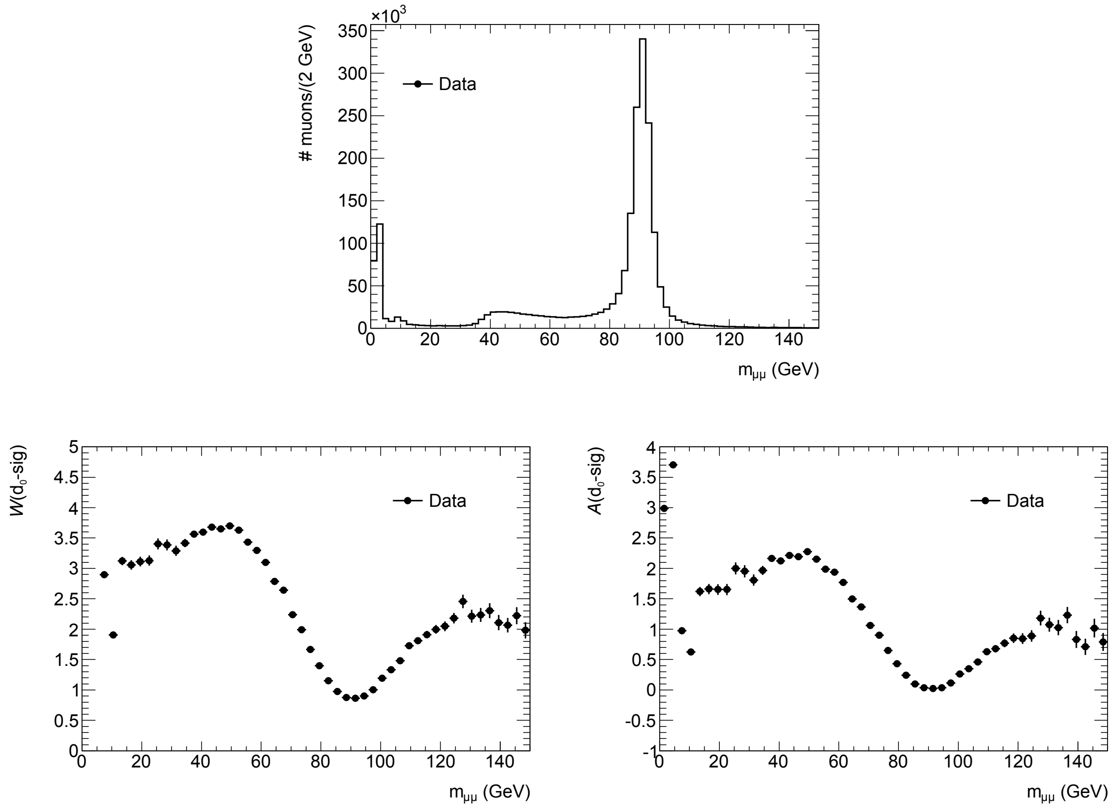

Figure 5.2: Top: The normalized invariant mass distribution of $\mu^+\mu^-$ pairs in collision data. Bottom: The $W(d_0\text{-sig})$ (left plot) and $A(d_0\text{-sig})$ (right plot) distribution for these muons as a function of the invariant mass of the muon pair.

5.4 The d_0-significance distribution in simulation

In the previous section we introduced the d_0-significance variable and discussed in general terms some differences in its distribution depending on the muon origin. In this section we describe the d_0-significance distribution of each muon type in more detail including any dependence of the shape of the distribution on muon characteristics and event topology. This information is essential to construct reliable templates that correctly describe the d_0-significance distribution of each muon type in a selected muon sample. As the templates used in this method are constructed from simulated events we first focus on the distributions of simulated muons. Possible differences between data and simulation are discussed in Section 5.5.

5.4.1 The d_0-significance distribution of prompt muons

Prompt muons are, per definition, produced at the interaction point. Therefore the impact parameter distributions, including d_0, are fully determined by the involved resolutions, including both the resolution effects on the track and vertex reconstruction. This leads to a Gaussian-like d_0 distribution, peaked at zero and with a width approximately equal to the combined track-vertex resolution. This resolution typically depends on the muon characteristics, such as momentum and spacial direction, and on the event topology, such as the number of tracks associated to the primary vertex. If the uncertainty on d_0 is properly calculated it contains these same resolution dependencies, leading to a d_0-significance distribution which is independent of both muon characteristics and event topology and with a width equal to unity. Figure 5.3 shows the d_0-significance distributions for prompt muons from simulated $Z \to \mu\mu$ and $t\bar{t}$ events as well as the d_0 and σ_{d_0} distributions.

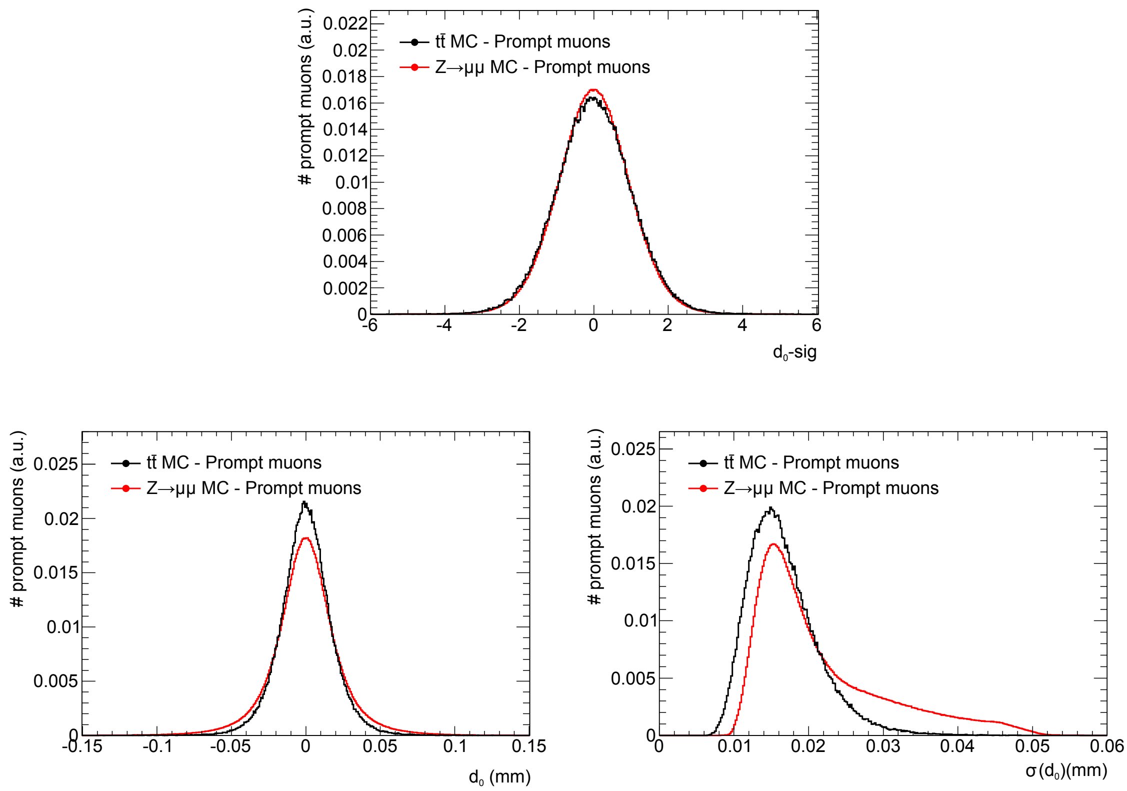

Figure 5.3: The normalized d_0-significance (top plot), d_0 (bottom left plot) and σ_{d_0} (bottom right plot) distributions for prompt muons in $Z \to \mu\mu$ (red) and $t\bar{t}$ (black) simulated events.

Dependences of the d_0-significance distribution of prompt muons.

As discussed previously, the d_0 distribution of prompt muons is purely determined by the track and vertex resolutions. Because these same resolutions are incorporated in the assigned uncertainty, the d_0-significance distribution is independent of muon characteristics and event topology variables. As an example Figure 5.4 shows the $W(d_0\text{-sig})$ distribution for prompt muons from simulated $t\bar{t}$ and $Z \to \mu\mu$ events as a function of p_T and η of the muon track. The flat distributions indicate that the width of the d_0-significance distribution of prompt muons is indeed independent of these variables. Similarly the d_0-significance distribution is independent on the number of hits associated to the muon track or the number of tracks in the event.

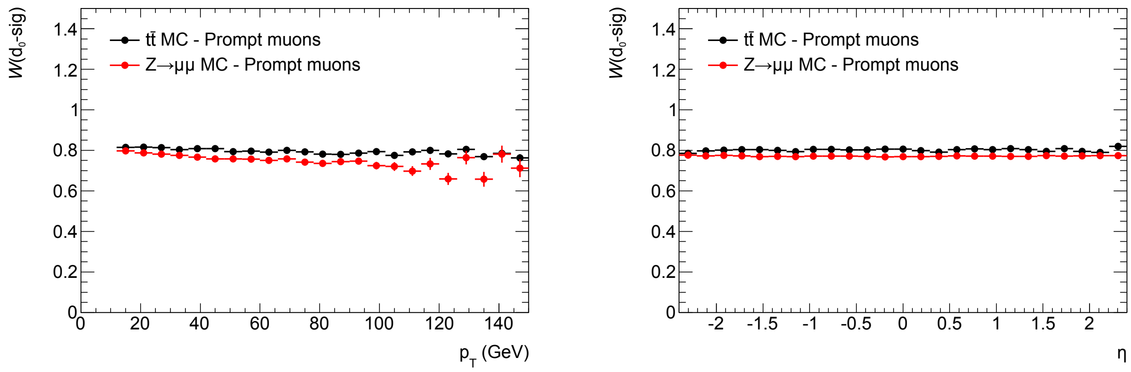

Figure 5.4: The $W(d_0\text{-sig})$ distribution for prompt muons in $Z \to \mu\mu$ (red dots) and $t\bar{t}$ (black dots) simulated events, as a function of p_T (left plot) and η (right plot).

Although the d_0-significance distributions show no dependence on any of the studied variables, there is a slight difference in the width of the d_0-significance distribution between prompt muons from $Z \to \mu\mu$ and $t\bar{t}$ simulated events. This difference is due to the existence of b-jets in the $t\bar{t}$ events as this affects the primary vertex reconstruction. In general the position of the primary vertex is determined by the highest momentum tracks in the event. Because we refit the primary vertex, the prompt muon itself does not contribute. In $Z \to \mu\mu$ events the vertex position is therefore mostly determined by the second prompt muon. In $t\bar{t}$ events on the other hand there is usually only one prompt muon. Without this muon the highest energetic tracks are typically part of the b-jets which, due to the lifetime of the b-quarks, are displaced from the collision spot. This leads to a reconstruction of the primary vertex which is somewhat displaced from the true interaction point. This displacement is not compensated by the assigned uncertainty as it is an actual physical displacement.

Modelling the difference due to the presence of b-jets.

The difference in the d_0-significance distribution between prompt muons in simulated $t\bar{t}$ and $Z \to \mu\mu$ events is due to an additional resolution effect on the vertex position determination in the $t\bar{t}$ sample. Such a resolution effect can be modelled by convoluting the distribution with a Gaussian with a width depending on the size of this additional resolution effect.

To show that the only difference between the two d_0-significance distributions is this resolution effect, and that this can be correctly modelled using a Gaussian distribution, we fit the prompt muon d_0-significance distribution in the $t\bar{t}$ sample using a convoluted template from $Z \to \mu\mu$. The width of the Gaussian is left as a free parameter. The resulting fit, shown in Figure 5.5, describes the $t\bar{t}$ distribution perfectly. The fit is shown with a linear and logarithmic scale on the y-axis to prove that both the peak of the distribution and the tails are correctly described by the template. The fitted width of the Gaussian is 0.280 ± 0.004. This added resolution is incorporated in the systematic uncertainty calculations of the method (see Section 5.6.4).

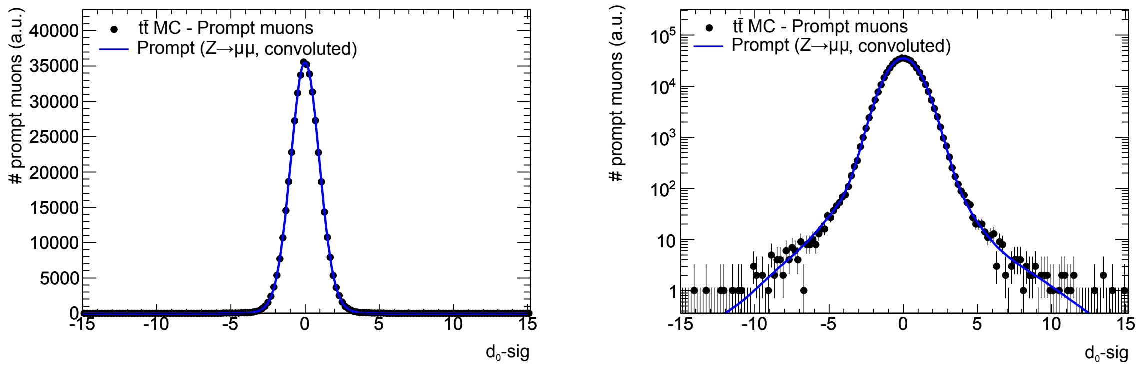

Figure 5.5: The prompt muon d_0-significance distribution in simulated $t\bar{t}$ events (black dots) fitted by a template from prompt muons from simulated $Z \to \mu\mu$ events. The template is convoluted with a Gaussian distribution to model the difference in distributions between the two samples.

5.4.2 The d_0-significance distributions of non-prompt muons

As discussed in Section 5.4.1, the d_0 distribution of prompt muons is purely determined by the involved resolutions. As these resolutions are incorporated in the assigned uncertainty, the d_0-significance distribution is independent of almost all muon characteristics and event topologies. This is not the case for non-prompt muons.

Muons produced in the decay of longer lived particles are created at some distance from the interaction point. The distribution for this distance is given by an exponential function with a width depending on both the lifetime and Lorentz boost of the parent particle. The true impact parameter (without resolution effects) of non-prompt muons varies, depending on the emission angle, between zero, if the muon is emitted in the same direction as the parent particle, and this decay distance, if the muon is emitted perpendicular to propagation direction of the parent particle. This is illustrated in Figure 5.6. The angular distribution of the muon relative to the parent particle is affected by the Lorentz boost. In more boosted systems the muons are emitted closer to the momentum axis of the parent particle. This effect reduces the dependence of the the muon impact parameter on the momentum of the parent particle.

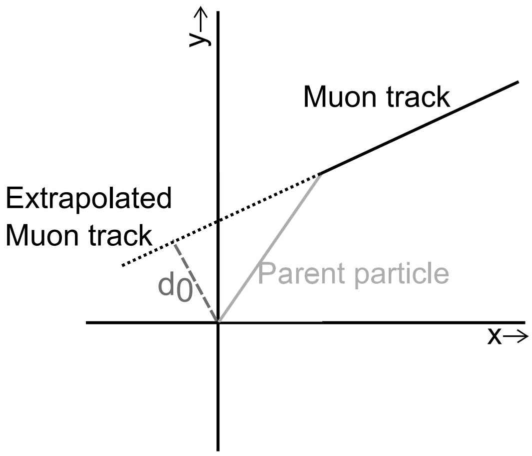

Figure 5.6: An illustration of a muon track, produced in the decay of parent particle. The true d_0 is indicated.

The measured d_0 distribution and therefore the measured d_0-significance of non-prompt muons depends both on the true d_0 distribution and the involved resolutions. As mentioned in the introduction we consider four types of non-prompt muons:

- **B-meson decays:** For muons produced in the decay of B-mesons, the true d_0 distribution is broad due to the relative long life time of the mesons, leading to a d_0-significance distribution with is significantly wider than that for prompt muons. As both the true impact parameter of the muon and the b-jet direction are along the meson trajectory the d_0-significance distribution is strongly asymmetric with the majority of muons having a positive d_0-significance. The top left plot of Figure 5.7 shows the normalized d_0-significance distributions for muons from B-meson decays from simulated $b\bar{b}$ and $t\bar{t}$ events. The difference between the two samples is primarily due to the difference in p_T distributions of the B-mesons, as discussed later in this section.

- **D-meson decays:** Muons in the D-meson decay category have a d_0-significance distributions which is very similar to that from B-meson decays. Due to the shorter lifetimes of D-mesons the distribution is generally narrower than that for B-mesons. The top right plot of Figure 5.7 shows the normalized d_0-significance distribution for muons from D-meson decays from simulated $c\bar{c}$ and $t\bar{t}$ events.

- **Tau decays:** Although taus can travel some distance before decaying, their decay distance is typically much shorter than that of B- and D-mesons. The d_0-significance distribution of tau decays is therefore narrower than that of B- and D-meson decays. For taus that decay leptonically and are not part of a B- or D-meson decay, the impact parameter of the resulting muons is uncorrelated to nearby jets. Therefore the d_0-significance distribution for muons in this category is symmetric around zero, as shown in the bottom left plot of Figure 5.7 for muons produced in tau decays in simulated $Z \to \tau\tau$ and $t\bar{t}$ events.

- **Light meson decays:** The lifetime of light mesons is such that a large fraction of them decay after reaching the ID volume. In this case the ID track, used to calculate the d_0-significance, is (partially) formed by the meson track. As the mesons considered in this category are not part of either of a B-meson, D-meson or tau decay chain they can be considered prompt. Therefore muons from light meson decays have a d_0-significance distribution which is very similar to that of prompt muons. Unfortunately this means that the template fitting method described in this chapter is unable to separate light meson decays from the prompt muons. The bottom right plot of Figure 5.7 shows the d_0-significance distribution for muons from light meson decays in a simulated $JF17$ and $t\bar{t}$ sample.

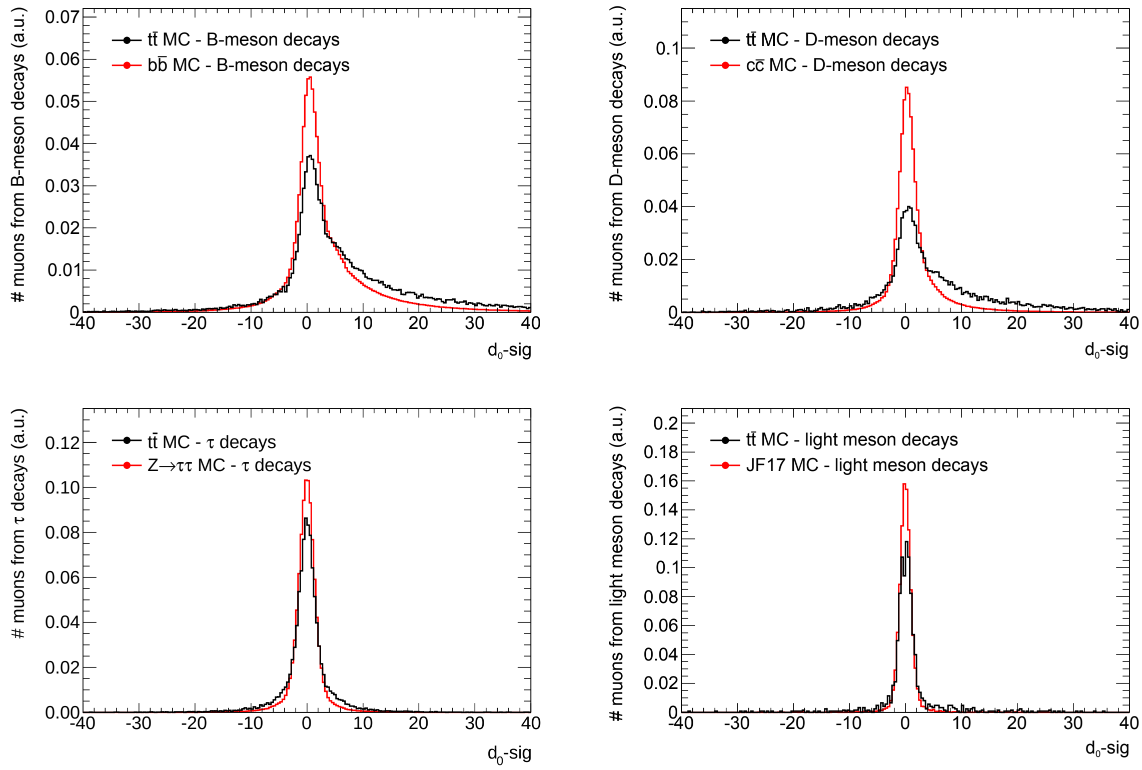

Figure 5.7: The normalized d_0-significance distributions for muons from B-meson (top left plot), D-meson (top right plot), tau (bottom left plot) and light meson (bottom right plot) decays in simulated events.

Dependence on the properties of the closest jet

Muons from tau and light meson decays are independent of any jet, therefore their d_0-significance distribution and that of prompt muons does not depend on jet characteristics. This is not the case for muons from B- and D-mesons decays. These decays depend on the characteristics of the original meson and therefore of the resulting b- or c-jet.

Dependence on the p_T of the closest jet

Figure 5.8 shows the dependence of the d_0-significance distribution for muons from B- and D-meson decays on the p_T of the closest jet, by plotting $W(d_0\text{-sig})$ and $A(d_0\text{-sig})$ as a function of this jet p_T for muons from simulated $b\bar{b}$, $c\bar{c}$ and $t\bar{t}$ events. The steep distributions indicates a strong dependency, with a wider and more asymmetric d_0-significance distributions for high jet momenta. Due to the longer lifetime of B-mesons compared to D-mesons this effect is more pronounced in B-meson decays.

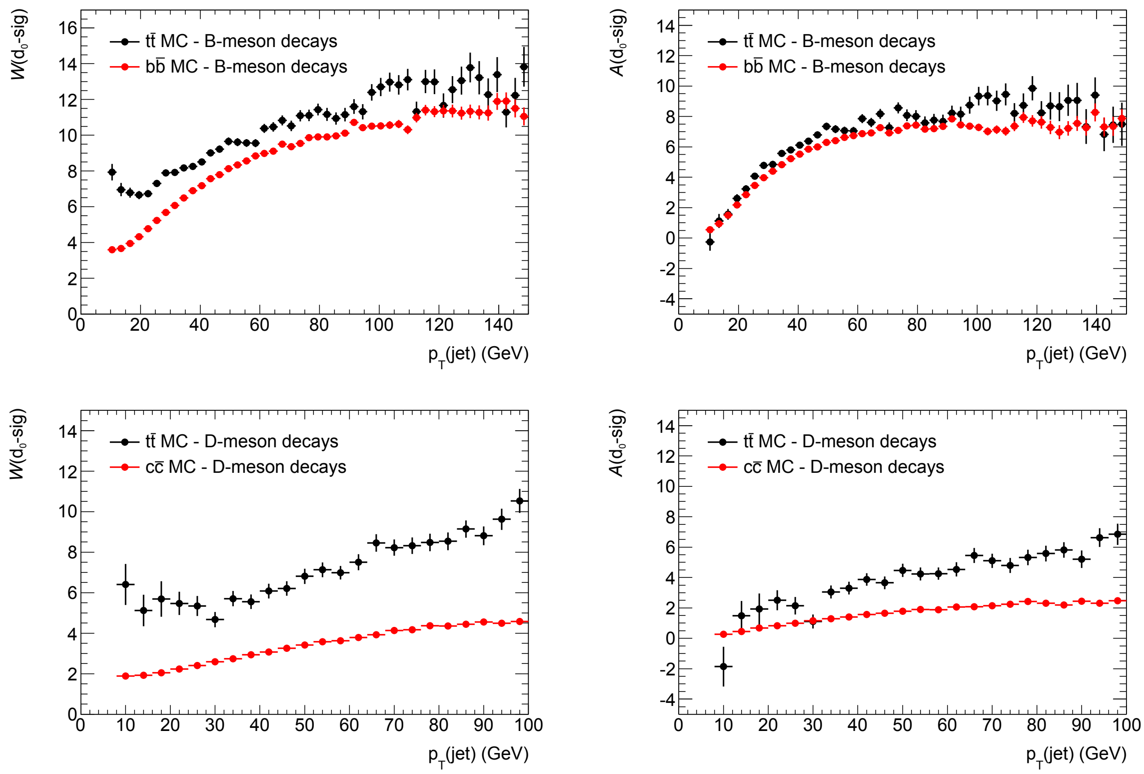

Figure 5.8: $W(d_0\text{-sig})$ (left plots) and $A(d_0\text{-sig})$ (right plots) as a function of the p_T of the closest jet for muons from B- (top plots) and D-meson decays (bottom plots) in simulated $b\bar{b}/c\bar{c}$ (red dots) and $t\bar{t}$ (black dots) events.

The difference in jet momenta between the different simulated samples accounts for most of the difference in the d_0-significance. This can be seen from Figure 5.9 which show the d_0-significance distributions for muons from B- (left plot) and D-meson (right plot) decays in simulated $b\bar{b}$, $c\bar{c}$ and $t\bar{t}$ events with the muons in the $b\bar{b}$ and $c\bar{c}$ sample reweighted to have the same closest jet p_T distribution as the muons of the same category in the $t\bar{t}$ sample. In order to simplify further discussions we refer to these reweighted $b\bar{b}$ and $c\bar{c}$ samples as $\langle b\bar{b}\rangle_{\text{rw}}$ and $\langle c\bar{c}\rangle_{\text{rw}}$ respectively.

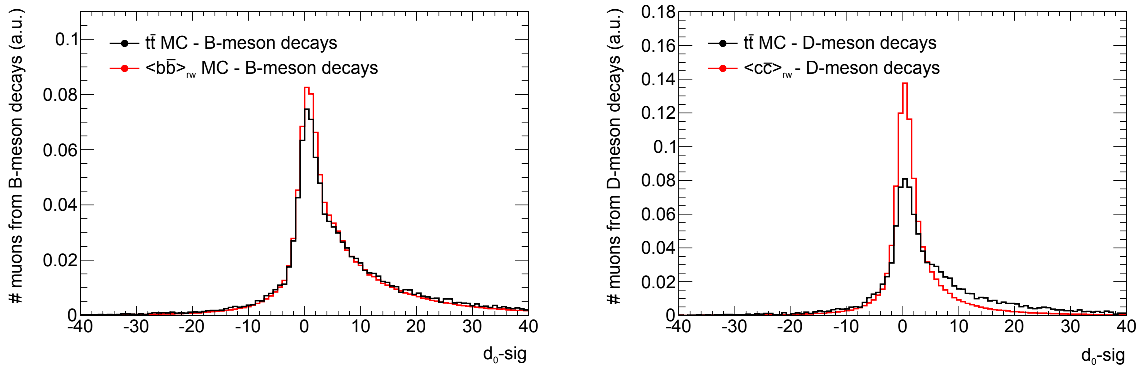

Figure 5.9: The normalized d_0-significance distributions for muons from B- (left plot) and D-meson (right plot) decays in simulated $b\bar{b}$, $c\bar{c}$ (red line) and $t\bar{t}$ (black line) events. The muons in the $b\bar{b}/c\bar{c}$ samples are reweighted to the have the same closest jet p_T distribution as in the $t\bar{t}$ sample.

Dependence on the distance to the closest jet

The d_0-significance of muons from B- and D-meson decays does not only depend on the momentum of the original meson but also on the emission angle of the muon relative to meson trajectory. Figure 5.10 shows the distribution for the angle between the muon and the closest jet for B- and D-meson decays in the $\langle b\bar{b}\rangle_{\rm rw}$, $\langle c\bar{c}\rangle_{\rm rw}$ and $t\bar{t}$ simulated sample.

As can be seen from Figure 5.10 most muons in B-meson and D-meson decays are produced within a distance of $\Delta R(\mu,\text{jet}) = 0.4$ to the nearest jet. The tails beyond this distance are due to muons for which the corresponding b- or c-jet was not properly reconstructed or did not have a high enough momentum to pass our selection criteria. These muons are therefore assigned to an unrelated jet. Apart from the difference in the tails, the distributions for each muon type are the same between the different samples. This is not surprising as the angular distribution of the muon emission depends purely on the kinematics involved and is therefore fixed by the momentum of the meson.

The d_0-significance distribution for B- and D-meson decays depends strongly on the emission angle. This can be seen in Figure 5.11 which shows $W(d_0\text{-sig})$ and $A(d_0\text{-sig})$ as a function of the angle between the muon and the closest jet for B-meson decays in the $\langle b\bar{b}\rangle_{\rm rw}$ and $t\bar{t}$ simulated samples.

Dependence on isolation

Isolation criteria are often used to reject muons from B- and D-meson decays where the isolation is defined as the amount of energy in a cone around the muon. For muons from B- and D-meson decays the amount of energy in this cone is typically high since the muons are generally produced within a jet. The actual amount of energy depends on the momentum of the closest jet and on the angle between the muon and this jet. Therefore any dependence of the d_0-significance distribution on the isolation is already taken into account by the dependence on the jet p_T.

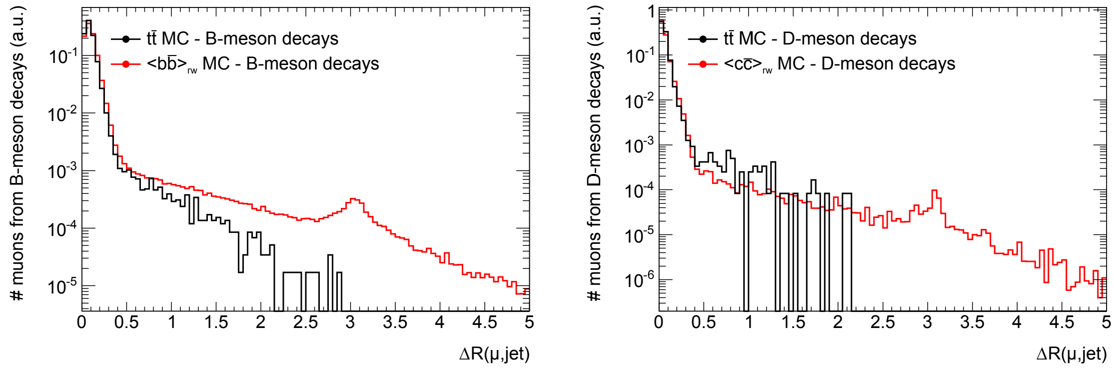

Figure 5.10: The $\Delta R(\mu,\text{jet})$ distribution for muons from B- (left plot) and D-meson decays (right plot) in simulated $b\bar{b}/c\bar{c}$ (red) and $t\bar{t}$ (black) events. The muons in the $b\bar{b}/c\bar{c}$ samples are reweighted to have the same closest jet p_T distribution as in the $t\bar{t}$ sample.

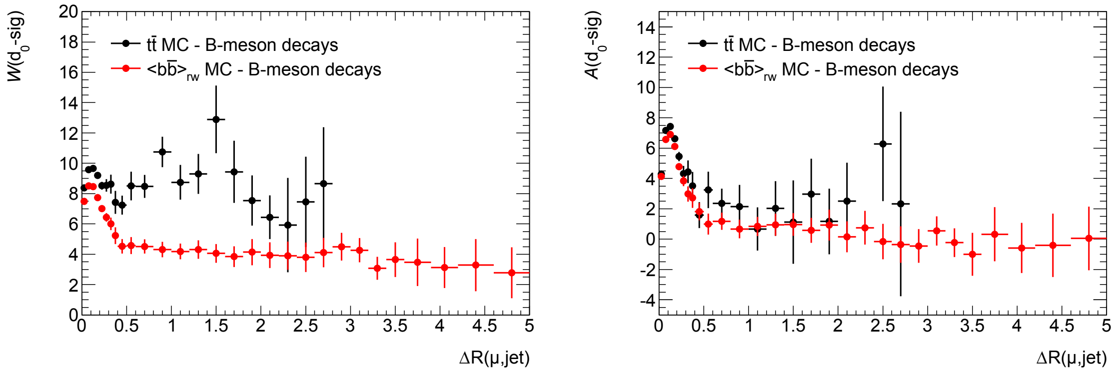

Figure 5.11: $W(d_0\text{-sig})$ (left plot) and $A(d_0\text{-sig})$ (right plot) as a function of the angle to the closest jet for muons from B-meson decays in simulated $b\bar{b}$ (red dots) and $t\bar{t}$ (black dots) events. The muons in the $b\bar{b}$ sample are reweighted to have the same closest jet p_T distribution as in $t\bar{t}$ sample.

Dependence on other jet dependent quantities

Apart from the jet dependent quantities mentioned so far, other possible event and muon selection criteria can affect the d_0-significance distribution by affecting the b- and c-jets. Two such variables are b-tagging on the closest jet and the difference in momentum between the ID and the MS track of the muon.

A cut on any of the b-tagging variables affects the type of b- or c-jets that remain in the sample, either by cutting on its decay distance trough a secondary vertex requirement or by requiring a muon with certain characteristics to be part of the jet. Either type of b-tagging affects the d_0-significance distribution of the muons from B- and D-meson decays.

The difference in momentum between the muons ID and MS track is used to remove muons from light meson decays. As some of the muons from B- and D-meson decays are produced through the creation of a light meson, such a cut affects the kinematic by which the remaining muons are produced in the B- and C-mesons decay chains, thereby changing the shape of the d_0-significance distribution.

Dependence on σ_{d_0}

The assigned uncertainty on d_0 is based on the resolution of the track and vertex reconstruction. For non-prompt muons the d_0 distribution depends both on the resolution and on a real physical displacement. In the d_0-significance this physical displacement is divided by the uncertainty. Therefore a larger uncertainty leads to non-prompt distributions with shorter tails.

Figure 5.12 shows the dependence of the d_0-significance distribution on the assigned uncertainty for the four types of non-prompt muons, by plotting $W(d_0\text{-sig})$ and $A(d_0\text{-sig})$ as a function of the uncertainty for muons from B- and D-meson decays and $W(d_0\text{-sig})$ as a function of this same variable for tau and light meson decays. As the d_0-significance distribution of tau and light meson decays is symmetric around zero the $A(d_0\text{-sig})$ distribution for these muons is not relevant.

Figure 5.12 shows a strong dependence of the d_0-significance distribution of non-prompt muons on the assigned uncertainty. The exception is for muons from light meson decays. As discussed previously the d_0-significance of muons from light meson decays is dominated by prompt tracks, where the meson track is misidentified as the muon ID track. Therefore the impact parameter for muons from light meson decays does not include a true physical distance but is determined by the involved resolutions, leading to a d_0-significance distribution which is independent of the assigned uncertainty.

Dependence on muon characteristics

The d_0-significance distribution for all four types of non-prompt muons are independent of other muon characteristics, such as p_T, angular distributions and number of hits associated to the track.

Summary: the d_0-significance distribution in simulated events

The d_0-significance distribution of prompt muons in simulated samples has a Gaussian-like shape centred around zero with a width approximately equal to unity. The distribution is independent of almost all muon characteristics and event topology variables, with the exception of a small dependence on the presence of b-jets in the event. In events containing b-jets the distribution is slightly wider. This can be modelled by convoluting the distribution in events without b-jets with a Gaussian distribution. To quantify this effect we fitted the width of this Gaussian by comparing the prompt muon d_0-significance distribution in simulated $Z \to \mu\mu$ and $t\bar{t}$ events. A width of 0.280 ± 0.004 was fitted. This value is used in the systematic uncertainty calculations of the method (see Section 5.6.4).

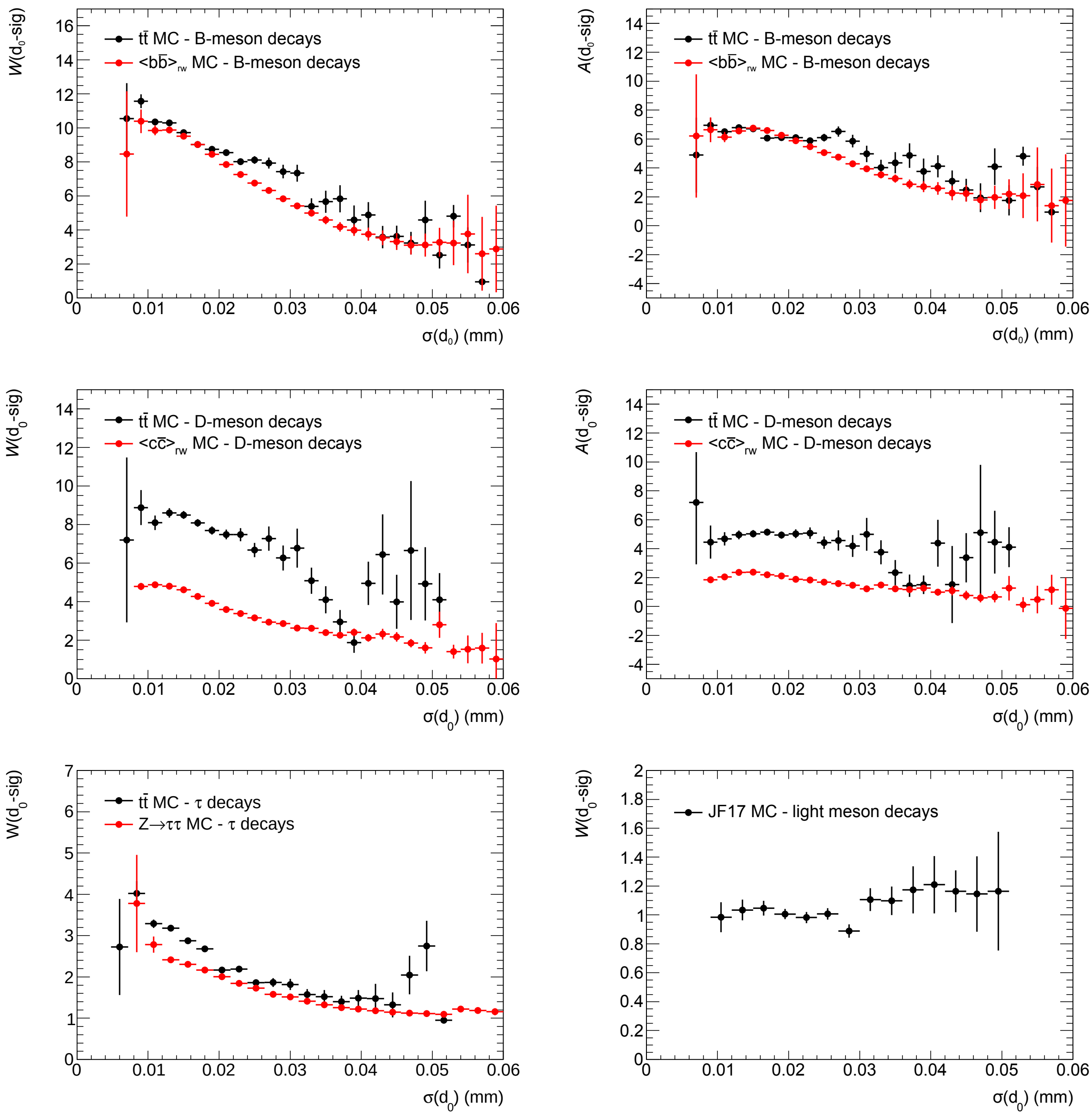

Figure 5.12: $W(d_0\text{-sig})$ (top/middle left plot) and $A(d_0\text{-sig})$ (top/middle right plot) as a function of σ_{d_0} for muons from B-/D-meson decays in simulated $b\bar{b}/c\bar{c}$ (red dots) and $t\bar{t}$ (black dots) events. The muons in the $b\bar{b}$ and $c\bar{c}$ samples are reweighted to the p_T distribution of the closest jet in $t\bar{t}$ events. The bottom left plot shows the $W(d_0\text{-sig})$ distributions for tau decays as a function of σ_{d_0} in simulated $Z \to \tau\tau$ (red dots) and $t\bar{t}$ (black dots) events while the bottom right plot shows the same distribution for muons from light meson decays from the simulated $JF17$ sample.

We consider four types of non-prompt muons: B-meson, D-meson, tau and light meson decays. The d_0-significance distribution for light meson decays is very similar to that of prompt muons, making it impossible to separate these two contributions based on this variable. The d_0-significance distributions of the other three categories of non-prompt muons differ significantly from that of prompt muons being broader and, in the case of B- and D-meson decays, asymmetric.

The d_0-significance distributions for muons from B- and D-meson decays depend on the properties of the original mesons. This results in a dependence on both the p_T of and distance to the closest jet. Consequently this also results in a dependence on the isolation of the muon. Furthermore the non-prompt muon distributions for all categories except light meson decays depend on the assigned uncertainty. There is no strong dependence on any other muon property. These dependencies are taken into account when constructing the templates (see Section 5.6).

5.5 Differences between data and simulation

In the previous section we described the d_0-significance distributions for each muon type and their dependences on muon characteristics and event topology. This was done for simulated muons. Unfortunately some effects, such as misalignment or inaccuracies in the detector simulation, can lead to differences in the d_0-significance distribution between data and simulation. To build reliable templates to fit on data samples, it is necessary to map these differences and model their effects on the d_0-significance distribution accurately.

5.5.1 Modelling differences in the d_0-significance distributions

Some detector effects, such as misalignment, are not the same in data and simulation and result in additional resolution effects on the d_0 distribution in data. Ideally these effects are translated to a corresponding larger assigned uncertainty, leaving the d_0-significance distribution (at least for prompt muons) unchanged. However, if the assigned uncertainty on d_0 does not (fully) account for these resolution effects, the d_0-significance distribution in data is wider than in simulation. This widening can, at first order, be simulated by convoluting the distributions from simulation with a Gaussian.

The width of the Gaussian and its dependence on muon characteristics and event topology is determined by comparing the prompt d_0-significance distribution in simulated $Z \to \mu\mu$ events with that of muons in collision data which pass a tight Z- or W-boson selection. This is done in Section 5.5.2. We assume that the measured differences are independent of the muon origin and that therefore we can modify the d_0-significance distributions for the non-prompt muons by convoluting them with this same Gaussian. This assumption is based on the idea that misalignment effects affect the track reconstruction independently of which processes occurred close before reaching detector.

Testing the modification of the non-prompt muon distributions in a similar way is very difficult, as it requires an almost pure data sample containing only one type of non-prompt muons. Therefore we do not validate the modified non-prompt distributions independently, but only as part of the overall method validation presented in Section 5.7.

5.5.2 Differences for prompt muons

To study possible differences in the d_0-significance between collision data and simulation we use two data samples with a high prompt muon content. The first sample is aimed at selecting muons from Z-boson decays, while the second uses a W-boson selection. The selection criteria are:

Z-boson selection:

- The event contains one $\mu^+\mu^-$ pair with an invariant mass between 88 and 94 GeV.
- $p_T > 20$ GeV, for both muons
- $\Delta R(\mu,\text{jet}) > 0.6$, for both muons and all jets.
- No third isolated ($\Delta R(\mu,\text{jet}) > 0.6$) muon ($p_T > 20$ GeV) in the event.

The purity of this Z-boson sample is about 98-99% as can be estimated from an invariant mass distribution for muons passing this Z-boson selection (without the invariant mass cut).

W-boson selection:

- The event must contain at least one muon with $p_T > 20$ GeV.
- $\Delta R(\mu,\text{jet}) > 0.6$, for all jets.
- The muon track must contain at least 6 hits in the SCT detector
- $E_T^{Miss} > 25$ GeV
- $M_T(\mu, E_T^{Miss}) > 40$ GeV

where $M_T(\mu, E_T^{Miss})$ denotes the transverse mass of the muon and missing transverse energy. There is no easy way to determine the prompt muon fraction in this sample, but we expect it to have a purity of more than 95%.

The d_0-significance distributions for muons passing the Z- and W-boson selection in data as well as for prompt muons in simulated $Z \to \mu\mu$ events are shown in Figure 5.13. The distributions in data are indeed wider than that in simulation, consistent with the effect of remaining alignment issues. The difference between the two data samples indicates that the difference between data and simulation is not universal. Before studying this dependence we show that we can successfully model the difference between data and simulation using a convolution with a Gaussian.

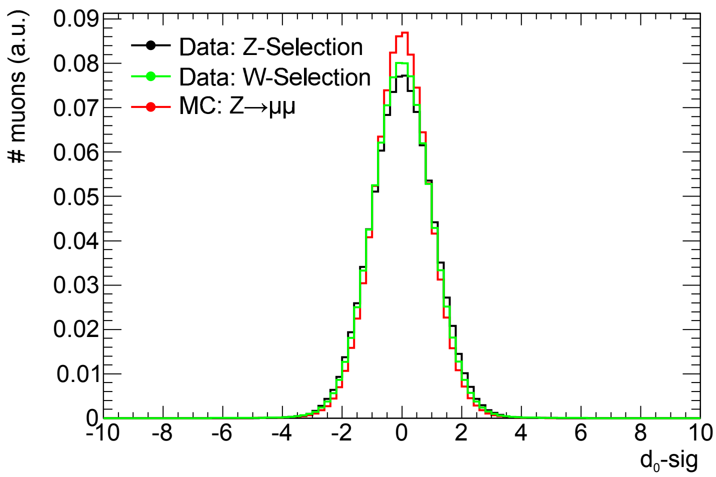

Figure 5.13: The d_0-significance distribution for muons passing the Z- (black line) and W-boson selection (green line) in data as well as for prompt muons from simulated $Z \to \mu\mu$ (red line) events.

Testing the modelling of the differences between data and simulation

We fit the d_0-significance distribution of muons in data passing this Z- and W-boson selection separately using a prompt template from a simulated $Z \to \mu\mu$ sample and non-prompt templates from simulated $b\bar{b}$, $c\bar{c}$ and $Z \to \tau\tau$ events for muons from B-meson, D-meson and tau decays respectively. Each template is convoluted with the same Gaussian distribution. The width of the Gaussian is left as a free parameter but the prompt muon fraction in both fits is fixed to be more than 95% in order to limit the freedom of the fit. The result of the fit on the Z-boson and W-boson selection are shown in Figure 5.14. In both cases the modified templates fit the data within statistical fluctuations, both in the peak of the distribution and the tails, indicating that the proposed modification to the templates can model the differences between data and simulation correctly. The sigma of the Gaussian is fitted to be 0.400 $\pm$ 0.004 for the Z-boson selection and 0.275 $\pm$ 0.002 for the W-boson selection, showing a clear difference between the two samples. This is investigated in Section 5.5.3.

5.5.3 Dependencies of the differences

The main difference between the two data samples introduced in Section 5.5.2 lies in the event topology, notably in the number of high energetic tracks in the events. This difference is responsible for most of the differences in d_0-significance distributions between the two samples.

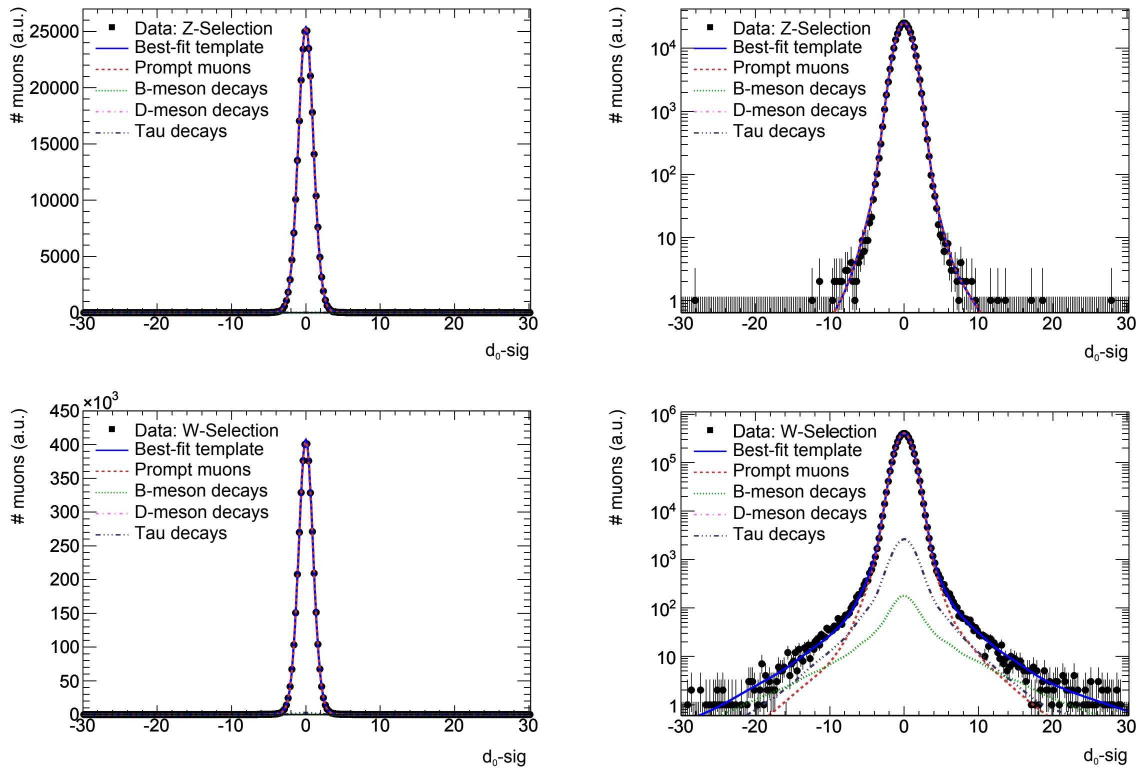

Figure 5.14: The d_0-significance distribution for muons passing the Z-boson (top) and W-boson (bottom) selection of Section 5.5.2 in data (black dots) fitted by a template from prompt muons from simulated $Z \to \mu\mu$ events. The template is convoluted with a Gaussian to account for the difference in distributions between data and simulation. The fits are shown with both linear (left) and logarithmic (right) scales on the y-axis to show the compatibility of the fit in both the peak region and in the tails.

Dependence on event topology

Detector effects, such as misalignment, affect the reconstruction of all tracks in the event which in turn affect the primary vertex reconstruction. This can lead to an underestimation of the vertex position uncertainty, especially in events with high momentum tracks where the assigned uncertainty is typically small.

The primary vertex reconstruction is generally dominated by the highest momentum tracks in the event which contain the necessary amount of hits in the silicon detectors. As we use a refitted vertex to calculate the d_0-significance, the muon track itself does not contribute. For most events passing the W-boson selection this means that this refitted vertex only contains low momentum tracks, while for muons passing the Z-boson selection the refitted vertex always contains the second high momentum muon track.

To show that this difference in number of high momentum tracks in the event is responsible for the difference in d_0-significance distribution between the two data samples, we add the following requirement to the W-boson selection:

- The event must contain at least 2 ID-tracks with $p_T > 15$ GeV, at least 1 B-layer, 3 pixel and 4 SCT hits[2].

The result of fitting the d_0-significance distribution of this modified W-boson selections using the same fitting procedure as in Section 5.5.2 is shown in Figure 5.15. The fitted width for the Gaussian is 0.393 ± 0.006, compatible with the results for the Z-boson selection.

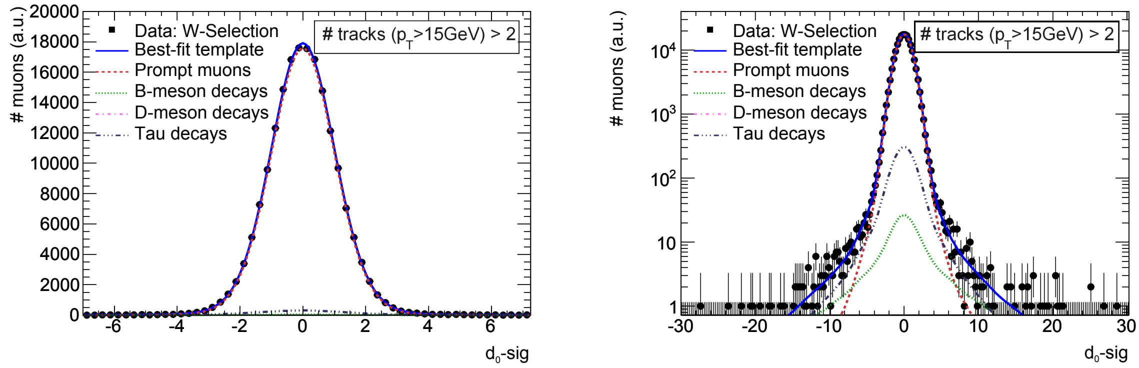

Figure 5.15: The d_0-significance distribution for muons passing the W-boson selection of Section 5.5.2 in events with at least 2 ID-tracks with $p_T > 15$ GeV, at least 1 B-layer, 3 pixel and 4 SCT hits. The data (black dots) is fitted with a template from prompt muons from simulated $Z \to \mu\mu$ events. The template is convoluted with a Gaussian to account for the difference in distributions between data and simulation. The fit is shown with both linear (left) and logarithmic (right) scales on the y-axis to show the compatibility of the fit in both the peak region and in the tails.

Dependence on muon characteristics

The differences between data and simulation are independent of most muon characteristics. This is shown in Figure 5.16 which shows the $W(d_0\text{-sig})$ distribution for prompt muons in $Z \to \mu\mu$ simulated events (red dots) and muons passing the Z-boson (black dots) and W-boson (green dots) selection in data, as a function of different muon track characteristics. To remove any dependence on the event topology only events with a second ID track with $p_T > 15$ GeV and at least 1 B-layer, 3 pixel and 4 SCT hits were used in the data selections. The difference in $W(d_0\text{-sig})$ between the two data samples is due to the difference in purity.

The strongest dependence in Figure 5.16 is for muons with $p_T < 40$ GeV in the W-boson selection. This dependence is also due to the purity of the data sample, with more non-prompt contamination at lower momenta. The bulk of the d_0-significance distribution

[2]The requirement for 4 SCT hits is due to the requirement for tracks in the primary vertex reconstruction (Section 2.3.2).

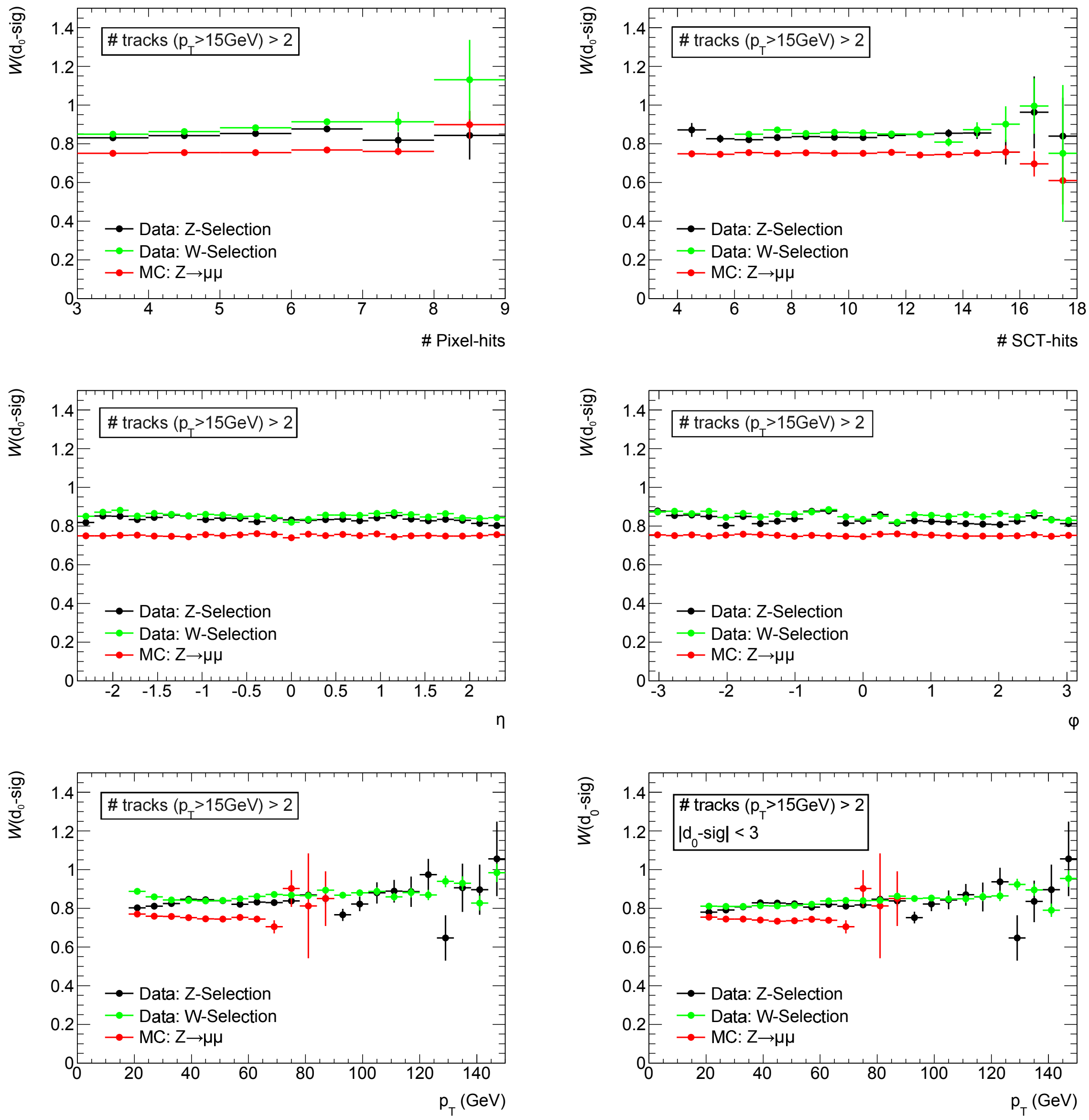

Figure 5.16: The $W(d_0\text{-sig})$ distribution for prompt muons in $Z \to \mu\mu$ simulated events (red dots) and muons passing the Z-boson (black dots) and W-boson (green dots) selection of Section 5.5.2 in data, as a function of the number of hits in the pixel- (top left plot) and SCT- (top right plot) detector as well as η (middle left plot), ϕ (middle right plot) and p_T (bottom left plot) of the muon track. Only muons in events with at least 2 tracks with $p_T > 15$ GeV and at least 1 B-layer, 3 pixel and 4 SCT hits were considered. The bottom right plot shows the $W(d_0\text{-sig})$ distribution as a function of p_T for these same muons with $|d_0\text{-sig}| < 3$.

does not depend on p_T as can be seen in the bottom right plot of Figure 5.16 where we show the $W(d_0\text{-sig})$ distribution for muons with $|\mathrm{d_0\text{-}sig}| < 3$.

The only real dependence of the prompt d_0-significance distribution in data is a slight dependence on the number of pixel hits associated to the muon track.

5.5.4 Pile-up

As can be seen from Table 2.1 most events at the LHC contain multiple interactions. The average number of additional collisions per bunch-crossing, pile-up, depends on the data taking period.

In this method we define a single vertex to be the primary vertex. As discussed in Section 2.3.2 this is the vertex with the highest $\sum p_T^2$. The d_0-significance of each muon track is defined with respect to this primary vertex. Therefore any muon track, both prompt or non-prompt, produced at another vertex, typically has a high d_0-significance.

Since the d_0-significance distribution of muons from pile-up collisions depends on the beam conditions as well as the type of pile-up collisions, it is not realistic to build a reliable template to describe this distribution. When the fraction of muons produced in pile-up collisions is small, these muons are absorbed by the different non-prompt templates and fitted as part of the background. This might affect the relative ratios between the non-prompt templates but does not affect the fitted prompt fraction as the prompt template is significantly narrower than the non-prompt distributions.

If the fractions of muons from pile-up collisions is high enough to significantly affect the shape of the d_0-significance distribution of the data sample, the non-prompt templates might no longer be able to absorb this difference, leading to unstable fits. To check whether this is the case for the data sample used in the chapter, we show, in Figure 5.17, the d_0-significance distribution for a prompt dominated sample, defined by the Z-selection of Section 5.5.2 and a non-prompt dominated sample, for different data periods. The non-prompt dominated sample is defined as non-isolated muons ($\Delta R(\mu,\text{jet}) < 0.4$) in $\mu^+\mu^-$ pairs with an invariant mass between 40 and 60 GeV. Despite the difference in the maximum number of pile-up collisions per bunch-crossing between the considered data periods there is no significant difference in the shape of the d_0-significance distribution, with the exception of a handful of muons in Period K with high d_0-significance in the prompt dominated sample. These are too few muons to affect the fit results.

We therefore conclude that, for the data period considered in this thesis, this template fitting method does not suffer from pile-up. However it is important to note that our definition of prompt muon is only with respect to the primary vertex. Any "prompt" muon produced at a pile-up vertex is considered non-prompt.

Summary: differences between data and simulation

There are some differences in the d_0-significance distribution between data and simulation. These differences are of the form of additional resolution effects in data and can be modelled by convoluting the distributions from simulation with a Gaussian. The size of the additional resolution effects and therefore the width of the Gaussian depends on the

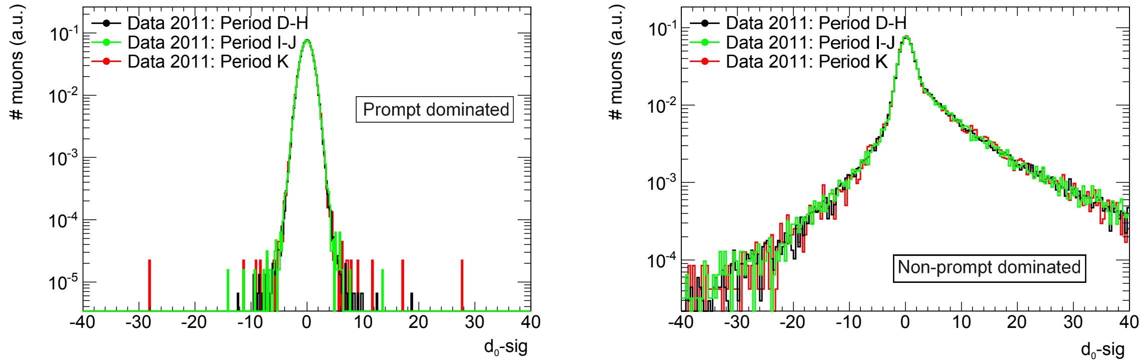

Figure 5.17: The d_0-significance distribution for muons passing the Z-boson selection of Section 5.5.2 (left) and for non-isolated muons ($\Delta R(\mu,\text{jet}) < 0.4$) in $\mu^+\mu^-$ pairs with an invariant mass between 40 and 60 GeV (right) for different data periods in 2011. The definition of the data periods is given in Table 2.1.

event topology, most notably on the presence of additional high momentum tracks in the event. These are the tracks which typically provides the strongest constrain on the vertex position. For events with at least 2 ID-tracks with $p_T > 15$ GeV, at least 1 B-layer, 3 pixel and 4 SCT hits, the sigma of the Gaussian is fitted to be 0.400 ± 0.004.

5.6 Method description

In the previous sections we described the properties of the d_0-significance distribution for different types of muons. The differences between these distributions can be used to determine the prompt muon fraction of muon samples using a template fitting method, similar to the methods used in Chapter 3 and 4.

5.6.1 Building the templates from simulation

We build templates from simulated events. Muons from each category are selected using hit based truth matching between the reconstructed muons and the corresponding truth particles. The templates are built from the d_0-significance distribution of these selected muons.

Muon types

We build templates for the following four muon categories:

- **Prompt:** The prompt muon template is built from simulated $Z \to \mu\mu$ events using reconstructed muons which are matched directly to truth muons whose parent particle (closest ancestor which is not a muon itself) is a Z-boson.

- **B-meson decays:** This category contains muons whose corresponding truth particle have a B-meson or b-quark as ancestor. The templates are built from simulated $b\bar{b}$ events. Templates from $t\bar{t}$ events are used in the systematic uncertainty calculations.

- **D-meson decays:** This category contains muons whose corresponding truth particle have a D-meson or c-quark as ancestor but are not part of the B-meson category. The templates are built from simulated $c\bar{c}$ events. Templates from $t\bar{t}$ events are used in the systematic uncertainty calculations.

- **Tau decays:** This category contains reconstructed muons which are matched directly to truth muons whose parent particle (closest ancestor which is not a muon itself) is a tau. Muons that are part of either the B- or D-meson category are excluded. The templates for tau decays are built from simulated $Z \to \tau\tau$ events. Templates from $t\bar{t}$ events are used in the systematic uncertainty calculations.

In Section 5.1 we defined one additional type of non-prompt muons; light meson decays. We do not build templates for this category because, as shown in Section 5.4.2, the d_0-significance distribution of light meson decays is very similar to that of prompt muons. Therefore the fit on the d_0-significance is not able to consistently separate these two types of muons. As muons from light meson decays with a high momentum are quite rare, we choose not to include a light meson template to the fit. The small contribution from light meson decays is fitted as prompt and should be evaluated separately using a different method.

Template dependencies

In Section 5.4 it was shown that the d_0-significance distributions in simulation depend on some muon characteristics and event topology. To keep the method process independent it is necessary to include these dependencies in the constructed templates. There are two ways to achieve this.

For some dependencies it is sufficient to apply the same selection criteria on the simulated muons used to construct the templates as on the final data sample. This approach is used for variables whose distribution is independent of the hard interaction of the event, such as the number of hits associated to the muon track. These model independent variables are expected to be the same in data and simulation, therefore any dependence on these variables present in the data sample is automatically included in the templates.

Other variables depend strongly on the event type. For these variables it is necessary to split the data into bins and build different templates for each bin. In practice we bin the templates of the non-prompt muons in bins of σ_{d_0}. The B- and D-meson templates are also binned depending on the p_T of the closest jet. All other dependencies are incorporated using the selection criteria. Specifically this includes the dependence of the B- and D-meson templates on $\Delta R(\mu,\text{jet})$, isolation and other jet related variables, as the distribution for these variables are fixed by the p_T of the closest jet.

5.6.2 Modifying the templates

As discussed in Section 5.5 the d_0-significance distribution in data differs from that in simulation. To account for these differences we modify the templates by convoluting them with a Gaussian which represents the additional resolution effects in data which are not fully included in simulation. The width of the Gaussian is determined by fitting a convoluted prompt template on muons passing the Z-boson selection of Section 5.5.2. As motivated in Section 5.5.1, the same Gaussian is then used to modify both the prompt and non-prompt templates.

The slight dependence of the d_0-significance in data on the number of pixel hits is taken into account by applying the same pixel requirement when determining the Gaussian width as in the final data sample. The dependence on the existence of additional high energetic tracks in the event in taken into account in the systematic uncertainty calculation.

5.6.3 Performing the template fit

The data is binned depending on the p_T of the closest jet and on σ_{d_0} of the muon track. For each bin, an fit is performed on the unbinned d_0-significance distribution of the data sample using the modified templates discussed in Sections 5.6.1 and 5.6.2. The relative normalisation between the four types of muons is left free.

Using the fitted normalisations and the number of muons per bin it is simple to compute the overall estimated number of muons of each category. The statistical uncertainty is computed from the uncertainty on the normalisations given by the individual fits as well as the number of events per bin.

5.6.4 Systematic uncertainties

We consider two sources of systematic uncertainty:

- **Uncertainty due to the choice of simulated sample for the templates.**

  We quantify the effect of this uncertainty by fitting each bin with templates built from simulated $t\bar{t}$ events.

- **Uncertainty in the differences between data and simulation.**

  This is quantified by changing the width of the Gaussian used to describe these differences. Specifically we use the width and corresponding uncertainty fitted on the W-boson selection in Section 5.5.2 to define a lower limit for this width. Since, in this thesis, we use this method solely on di-muon events we use the results fitted with the modified W-boson selection of Section 5.5.3 which requires the existence of a second high momentum track. As upper limit for the width of the Gaussian we combine the fitted effect of b-jets on the prompt d_0-significance distribution discussed in Section 5.4.1 with the difference between data and simulation, by adding the two measured widths in quadrature.

  Each bin is refitted using the lower and the upper limit for the width of the Gaussian.

For each type of systematic uncertainty we calculate the total estimated prompt and non-prompt contributions to the data sample. As the correlation between the two types of systematic uncertainty is difficult to ascertain we also estimated to effect of the combined systematic uncertainty by varying the width of the Gaussian used to modify the templates from $t\bar{t}$ events. As it is unnecessary to account for the existence of b-jets twice, the upper limit for the Gaussian in this case is defined as the fitted width using the Z-boson selection plus the corresponding uncertainty.

This procedure results in five new sets of muon ratios, based on:

- $t\bar{t}$ templates
- the lower limit on the Gaussian width on the default templates
- the upper limit on the Gaussian width on the default templates
- the lower limit on the Gaussian width on the $t\bar{t}$ templates
- the upper limit on the Gaussian width on the $t\bar{t}$ templates

We take the smallest and largest values for each ratio as the systematic uncertainty. Typically these are given by using the lower limit on the Gaussian width with the regular templates and the upper limit with the $t\bar{t}$ templates.

5.7 Validation and results

To show that the method gives reliable results we apply the method on different muon samples, both simulated and from collision data, and compare the measured prompt and non-prompt fractions with expectations. From the large number of possible tests we have chosen to test this method on the following muon samples:

- Different combination of simulated events, to test the fit stability. (Section 5.7.1)
- Simulated $t\bar{t}$ events, to test the full method on simulated events. (Section 5.7.2)
- The $\mu^+\mu^-$ invariant mass spectrum in data, to test the full method on data. (Section 5.7.3)

5.7.1 Stability checks on simulation

To test the precision by which the fit can separate muons from different origins as well as the stability of the fit, we fit different combinations of simulated $Z \to \mu\mu$, $b\bar{b}$, $c\bar{c}$ and $Z \to \tau\tau$ events using templates built from these same samples. Since the templates automatically describe the "data" perfectly we do not need to either bin the data or calculate systematic uncertainties. The templates are statistically independent of the "data" points.

Fits on simulated samples with prompt muons

Figure 5.18 summarises the results of fitting different samples all containing 500 prompt muons and different combinations of non-prompt muons. The error bars only reflect the uncertainty on the relative normalisation of the templates, returned by the fit.

The results of these fits are compatible with the true number of muons in each sample, with the majority of fits returning values which are within one standard deviation of the true value for each muon type. Statistically the most significant deviation is for the fits with 1500 muons from D-meson decays where the prompt fraction is underestimated, although this deviation still falls within two standard deviations. Since all these fits contain the same 1500 muons from $c\bar{c}$ events the results are highly correlated. Repeating these fits with a statistically independent second selection of muons from D-meson decays returns results which are within one standard deviation of the true prompt fraction. We therefore conclude that the fit is stable and able to correctly separate prompt from non-prompt muon contributions.

Fits on simulated samples without prompt muons

To check the reliability of the fit in separating the contributions of the different non-prompt muon types, we performed the same fits on samples without prompt muons but with different combinations of non-prompt muons. The result are shown in Figure 5.19. As expected all fits return a prompt muon contribution which is within one standard deviation of zero with an uncertainty on the prompt fraction of a few percent. However it is clear that the fit has some problems in separating muons between the different non-prompt processes. This translates to large and correlated uncertainties for the non-prompt contributions but also in results that differ from the true contribution by a few standard deviations. For example, the contribution from D-meson decays is typically underestimated and fitted as partially B-meson decays and partially tau decays. This is not unexpected as the bulk of the d_0-significance distributions for all three types of non-prompt muons is similar, with the main differences being the length and relative contribution of the tails. This instability in the fit does not threaten the estimation of the prompt muon fraction as the d_0-significance distribution for prompt muons is narrower than for all types of non-prompt muons.

5.7.2 Validating the method on simulated $t\bar{t}$ events

We fit the muon content of a simulated $t\bar{t}$ sample using the full method described in Section 5.6 but without the distortions to the template used to model the differences between data and simulations.

As we calculate the systematic uncertainty using templates from this same $t\bar{t}$ sample the results are biased. This test is meant to provide an estimation of the size of this systematic uncertainty.

In total the $t\bar{t}$ sample contained $5.66 \cdot 10^5$ muons that pass our selection: $4.36 \cdot 10^5$ prompt muons, $7.7 \cdot 10^4$ muons from B-meson decays, $1.6 \cdot 10^4$ from D-meson decays,

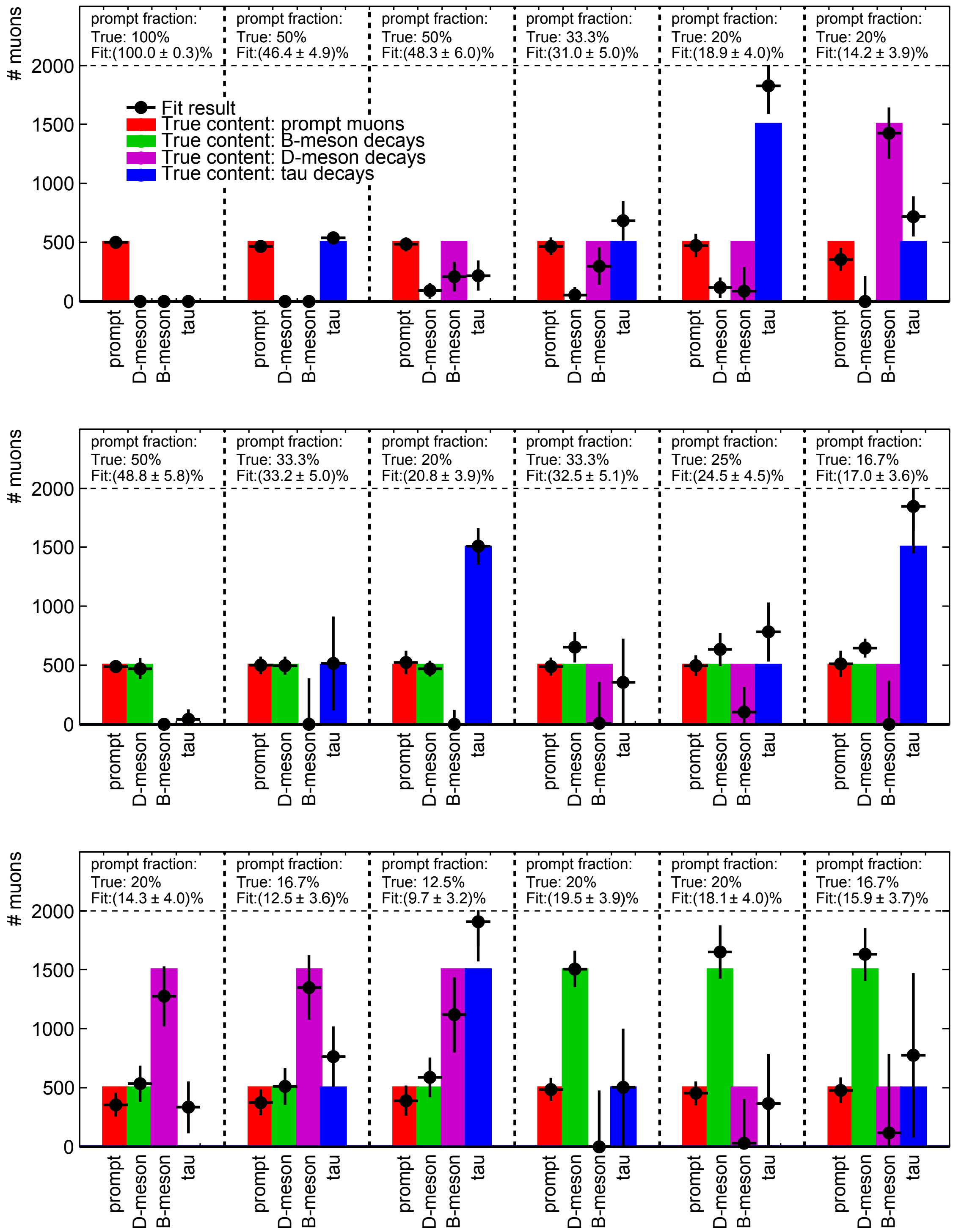

Figure 5.18: The true (filled bars) and estimated (black dots) number of prompt muons, B-meson decays, D-meson decays and tau decays for different combinations of muons from simulated $b\bar{b}$, $c\bar{c}$ and $Z \to \tau\tau$ samples and 500 prompt muons from $Z \to \mu\mu$ simulated events. The fits are performed using templates built from these same simulated samples, but statistically independent from the fitted data. The error bars indicate the uncertainties returned by the fit.

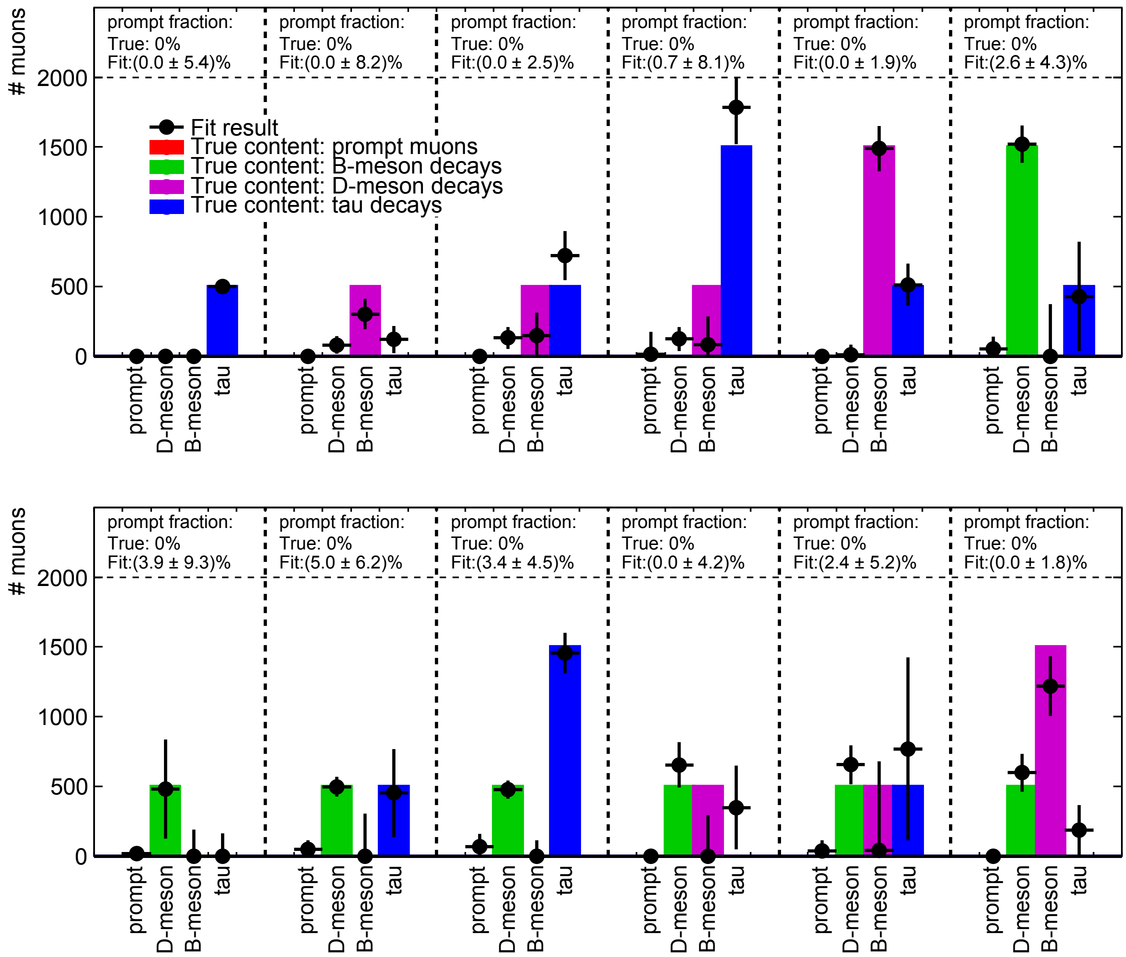

Figure 5.19: The true (filled bars) and estimated (black dots) number of prompt muons as well as B-meson, D-meson and tau decays for different combinations of muons from simulated $b\bar{b}$, $c\bar{c}$ and $Z \to \tau\tau$ samples. The fits are performed using templates built from these same simulated samples and simulated $Z \to \mu\mu$ events, but statistically independent from the fitted data. The error bars indicate the uncertainties returned by the fit.

$3.5 \cdot 10^4$ from tau decays and $0.2 \cdot 10^4$ from light meson decays. This corresponds with a prompt muon fraction of 77.1 %.

Using our template method we estimate a prompt muon fraction of $0.728 \pm 0.001 \pm 0.054$, compatible with the true value. The first uncertainty represents the statistical uncertainty calculated using the uncertainty on the relative template normalisation returned by the fit, while the second uncertainty is the estimated systematic uncertainty calculated using the procedure of Section 5.6.4. The total number of muons of each category, estimated by this method, are listed in Table 5.1, together with the individual bin results. The estimated prompt muon fraction in each bin is compatible with the true value. The same is true for most non-prompt estimates although, just as in Section 5.7.1, the systematic uncertainty can be more than 100% and some significant deviations exist.

$\sigma_{d_0}(\mu\text{m})$		Prompt	B-meson decay	D-meson decay	Tau decay
Total					
	true	436472	76743	16372	34937
	fit	$(412 \pm 1 \pm 31) \cdot 10^3$	$(125 \pm 1 \pm 82) \cdot 10^3$	$(6 \pm 1 \pm 20) \cdot 10^3$	$(23 \pm 1 \pm 31) \cdot 10^3$
$0 <$ Closest jet p_T (GeV) < 20					
$0-20$	true	207682	2390	162	15143
	fit	$(2037 \pm 6 \pm 46) \cdot 10^2$	$(46 \pm 5 \pm 38) \cdot 10^2$	$(0 \pm 3 \pm 29) \cdot 10^2$	$(172 \pm 5 \pm 37) \cdot 10^2$
$20-30$	true	48149	1268	57	5376
	fit	$(469 \pm 3 \pm 21) \cdot 10^2$	$(26 \pm 27 \pm 20) \cdot 10$	$(28 \pm 7 \pm 23) \cdot 10^2$	$(495 \pm 80 \pm 35) \cdot 10$
$30-40$	true	3214	103	10	389
	fit	$(315 \pm 5 \pm 19) \cdot 10$	$0 \pm 13 \pm 37$	$(16 \pm 13 \pm 7) \cdot 10$	$(41 \pm 13 \pm 15) \cdot 10$
> 40	true	253	18	2	46
	fit	$250 \pm 10 \pm 75$	$0 \pm 6 \pm 0$	$0 \pm 62 \pm 0$	$69 \pm 69 \pm 73$
$20 <$ Closest jet p_T (GeV) < 30					
$0-20$	true	41545	6422	438	2912
	fit	$(413 \pm 3 \pm 10) \cdot 10$	$(100 \pm 5 \pm 62) \cdot 10$	$(0 \pm 4 \pm 21) \cdot 10$	$(0 \pm 1 \pm 31) \cdot 10^2$
$20-30$	true	9610	2712	203	1059
	fit	$(922 \pm 19 \pm 94) \cdot 10$	$(30 \pm 3 \pm 11) \cdot 10^2$	$(146 \pm 32 \pm 77) \cdot 10$	$(0 \pm 4 \pm 93) \cdot 10$
$30-40$	true	620	174	7	78
	fit	$(45 \pm 5 \pm 15) \cdot 10$	$(3 \pm 5 \pm 14) \cdot 10$	$(40 \pm 7 \pm 35) \cdot 10$	$0 \pm 23 \pm 62$
> 40	true	61	20	2	12
	fit	$44 \pm 12 \pm 2$	$0 \pm 39 \pm 19$	$51 \pm 60 \pm 40$	$0 \pm 44 \pm 19$
$30 <$ Closest jet p_T (GeV) < 50					
$0-20$	true	35817	18495	1831	2503
	fit	$(323 \pm 2 \pm 48) \cdot 10^2$	$(27 \pm 0 \pm 16) \cdot 10^3$	$(0 \pm 0 \pm 45) \cdot 10^2$	$(0 \pm 0 \pm 65) \cdot 10^2$
$20-30$	true	9519	5586	807	1028
	fit	$(87 \pm 1 \pm 16) \cdot 10^2$	$(83 \pm 1 \pm 49) \cdot 10^2$	$(0 \pm 0 \pm 14) \cdot 10^2$	$(0 \pm 0 \pm 20) \cdot 10^2$
$30-40$	true	821	309	58	81
	fit	$(61 \pm 6 \pm 19) \cdot 10$	$189 \pm 83 \pm 11$	$(48 \pm 9 \pm 37) \cdot 10$	$(0 \pm 2 \pm 18) \cdot 10$
> 40	true	61	60	9	9
	fit	$(0 \pm 11 \pm 3) \cdot 10$	$19 \pm 32 \pm 29$	$(12 \pm 10 \pm 9) \cdot 10$	$0 \pm 14 \pm 40$
Closest jet p_T (GeV) > 50					
$0-20$	true	63328	33296	10242	4586
	fit	$(52 \pm 0 \pm 13) \cdot 10^3$	$(60 \pm 0 \pm 42) \cdot 10^3$	$(0 \pm 0 \pm 11) \cdot 10^3$	$(0 \pm 0 \pm 18) \cdot 10^3$
$20-30$	true	14495	5495	2381	1549
	fit	$(128 \pm 1 \pm 20) \cdot 10^2$	$(113 \pm 13 \pm 81) \cdot 10^2$	$(0 \pm 0 \pm 23) \cdot 10^2$	$(0 \pm 0 \pm 39) \cdot 10^2$
$30-40$	true	1176	338	142	144
	fit	$(106 \pm 7 \pm 15) \cdot 10$	$(55 \pm 14 \pm 34) \cdot 10$	$(21 \pm 13 \pm 6) \cdot 10$	$(0 \pm 3 \pm 26) \cdot 10$
> 40	true	111	57	21	22
	fit	$39 \pm 29 \pm 24$	$30 \pm 37 \pm 15$	$(15 \pm 45 \pm 10) \cdot 10$	$0 \pm 13 \pm 68$

Table 5.1: The true and estimated number of prompt, B-meson decays, D-meson decays and tau decays in a simulated $t\bar{t}$ sample. The results are listed separately for each fitted closest jet p_T and σ_{d_0} bin. The first uncertainty is statistical and only contain the uncertainty on the relative normalisation of the templates, returned by the fit. The second uncertainty denotes the systematic uncertainty.

The uncertainties listed in Table 5.1 are obtained using the procedure described in this chapter, which only provides symmetrical uncertainties. This is in many cases only an approximation of the actual uncertainty range and suggests the possibility of non-physical negative contributions. While this is obviously inaccurate the listed uncertainties give an indication of the precision of each fit and can be used to validate the general method, which is our primary goal at this point. When using this template method in an actual physics analysis, as done in Chapter 6 a more precise uncertainty determination is used, removing this problem.

5.7.3 Fitting the di-muon invariant mass distribution in data

To show that this template fitting method gives reliable results on collision data we estimate the prompt and different non-prompt contributions to the opposite-sign di-muon invariant mass spectrum. By fitting different invariant mass bins separately we can validate our method on samples with different prompt to non-prompt ratios. The consistency of the fit results can then be checked by considering the fitted invariant mass distributions of the individual contributions.

We select muons which pass the following di-muon selection:

- It is part of a $\mu^+\mu^-$ pair.
- The event does not contain a third muons passing the selection of Section 5.2.

Figure 5.20 shows the invariant mass distribution, $m_{\mu\mu} > 20$ GeV, for muons passing this di-muon selection as well as the the fitted contributions to each bin. The plotted uncertainties only contain the statistical uncertainty.

As expected the Z-boson peak in the mass range of 80-100 GeV consists almost purely of prompt muons. The region with invariant mass between 20 and 80 GeV is dominated by muons from B-meson decays but also contains quite a large prompt muon contribution. These can be muons from W-boson decays or from Z-boson decays where the second muon remained undetected either by passing outside the selected η range or through one of the cracks of the detector. These single muons are then paired with muons from B-meson decays to form di-muon pairs.

The individual invariant mass distributions for prompt and B-meson decays, including systematic uncertainty are shown in Figure 5.21. As expected, for the non-prompt muons the systematic uncertainty can be large. This uncertainty is dominated by the uncertainty of using the template from simulated $t\bar{t}$ events instead of those of $b\bar{b}$, $c\bar{c}$ and $Z \rightarrow \tau\tau$.

From the smooth invariant mass distribution of the different muon contributions it is clear that the method gives consistent results from one invariant mass bin to the next. To test that the actual measured prompt muon fraction is accurate we redo the fitting procedure separately for isolated muons ($p_T$cone20$/p_T(\mu) < 0.1$) and not isolated muons ($p_T$cone20$/p_T(\mu) > 0.1$), where $p_T$cone20 denotes the summed p_T of tracks, excluding the muon itself, in a cone $\Delta R(\mu, \text{jet}) < 0.2$ around the muon track. No isolation requirement is added to the second muon in the event. The results are shown (without systematic uncertainty) in Figure 5.22. As expected the entire invariant mass distribution for isolated

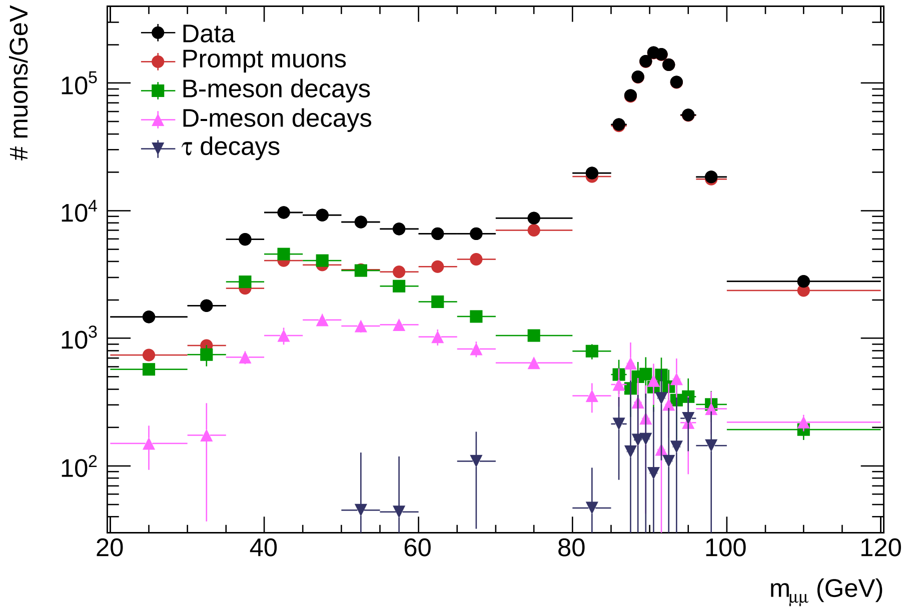

Figure 5.20: The invariant mass distribution of muon pairs for muons in data passing the di-muon selection of Section 5.7.3 (black dots) as well as the estimated prompt (red dots), B-meson decay (green square), D-meson decay (pink upwards-pointing triangles) and tau decay (dark blue downwards-pointing triangles) contributions to this spectrum. The plotted uncertainties are statistical.

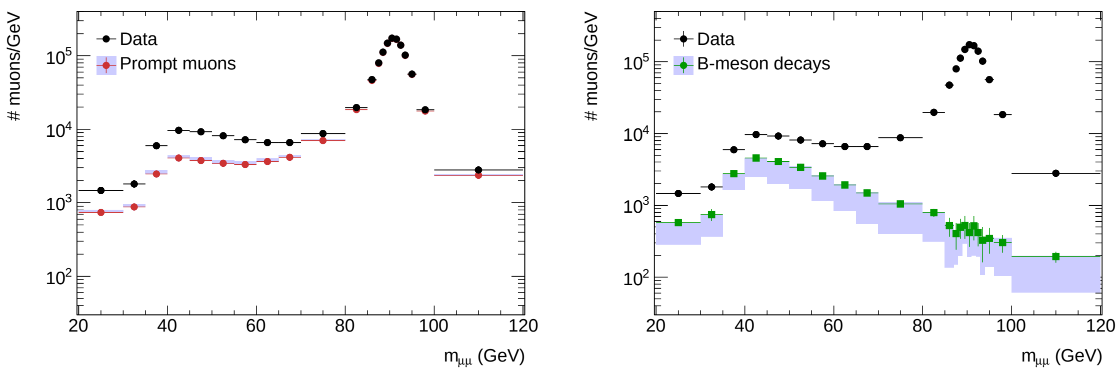

Figure 5.21: The invariant mass distribution of muon pairs for muons in data passing the di-muon selection of Section 5.7.3 (black dots) as well as the estimated prompt (left plot) or B-meson decay (right plot) contribution to this spectrum. The light blue squares indicate the calculated systematic uncertainty.

muons is prompt dominated. The not isolated distribution is still prompt dominated in the Z-boson mass range, however most of the prompt contribution of the 20-80 GeV mass

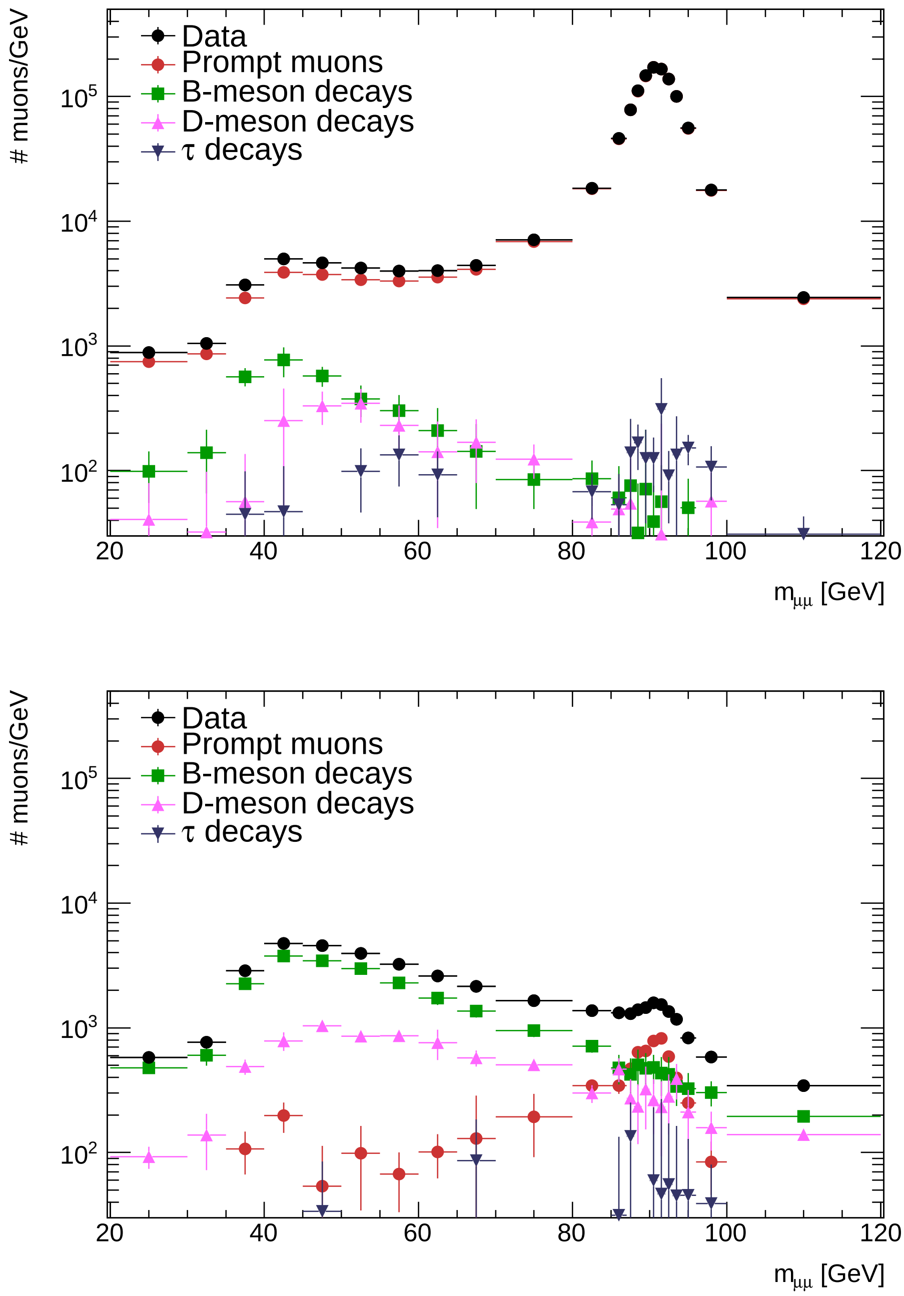

Figure 5.22: The invariant mass distribution of muon pairs for isolated ($p_T$cone20$/p_T(\mu) < 0.1$) muons (top plot) and not isolated ($p_T$cone20$/p_T(\mu) > 0.1$) muons (bottom plot) in data passing the di-muon selection of Section 5.7.3 (black dots) as well as the estimated prompt (red dots), B-meson decay (green square), D-meson decay (pink upwards-pointing triangles) and tau decay (dark blue downwards-pointing triangles) contribution to this spectrum. The plotted uncertainties are statistical.

range is removed. The total contribution of isolated and not isolated muons for each muon type is consistent with the total distribution in Figure 5.20.

The invariant mass distribution for the low mass region (1 GeV $< m_{\mu\mu} <$ 20 GeV) is shown in Figure 5.23. Both the total invariant mass distribution and that of the individual components is less smooth than in the higher mass region. This is due to large amount

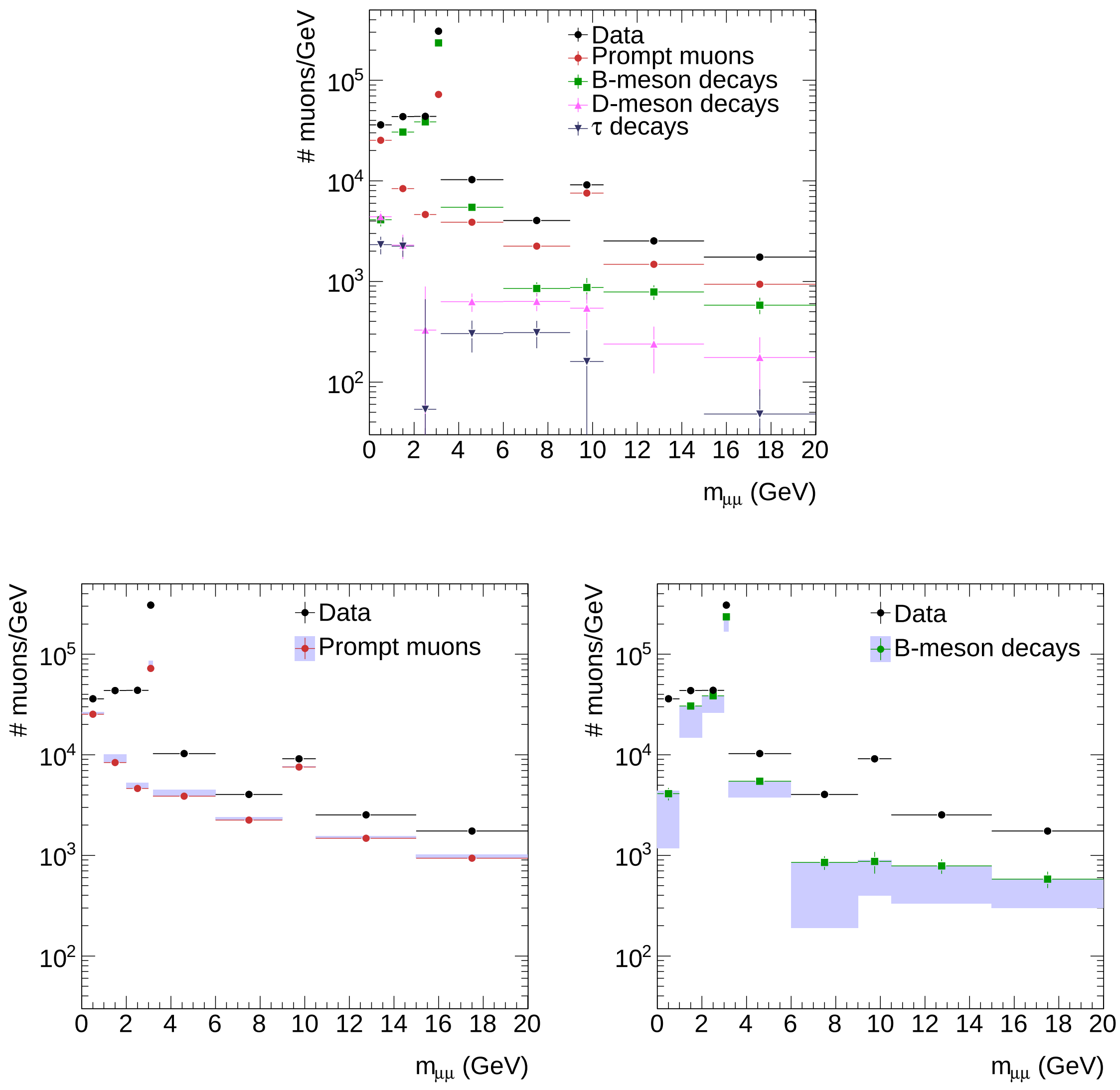

Figure 5.23: Top: The invariant mass distribution of low mass muons pairs for muons in data passing the di-muon selection of Section 5.7.3 (black dots) as well as the estimated prompt (red dots), B-meson decay (green square), D-meson decay (pink upwards-pointing triangles) and tau decay (dark blue downwards-pointing triangles) contribution to this spectrum. The plotted uncertainties are statistical. Bottom: The same invariant mass distribution with only the prompt (left) or B-meson decay (right) component. The light blue rectangle denotes the systematic uncertainty.

of different processes that contribute in this region including: resonances, Drell-Yan and muon pairs produced within the same jet. It is however clear from Figure 5.23 that the Υ resonance at $m_{\mu\mu} \sim 9.5$ GeV is properly fitted as prompt. The J/ψ resonance at $m_{\mu\mu} \sim 3$ GeV on the other hand is only partially fitted as prompt. This is expected as due to the minimum p_T requirement of the muons, this di-muon selection only selects highly boosted J/ψ's, many of which are themselves produced within a b-jet and therefore non-prompt.

We conclude that using the template fitted method described in this chapter we can accurately separate the prompt muon contribution to this di-muon invariant mass distribution.

5.8 Conclusion

The d_0-significance distribution for muons depends strongly on the muon origin. For prompt muons this distribution is narrow, symmetric and peaks at zero. It is independent of almost all muon characteristics and event topologies and relatively simple to study directly on collision data by considering muons that pass a tight Z- or W-boson selection. For muons produced in the decay of longer lived particles the d_0-significance distribution is wider and in the case of B- or D-meson decays, highly asymmetric.

These differences in the distributions can be used to estimate the prompt muon fraction of generic muon samples. We have presented a template method which fits the d_0-significance distribution of muon samples using templates to describe the individual contributions from prompt muons as well as muons from B-meson, D-meson and tau decays. The method was tested on a variety of muon samples, both from simulation and collision data. The prompt muon fraction resulting from these fits, described in Section 5.7, are, in the case of simulated samples, consistent with the truth results. The results on data agree with expectations and are consistent with each other.

This method is in principle also capable of separating the individual contributions of muons from B-meson decays, D-meson decays and tau decays. However this separation is less precise and reliable than the prompt muon fraction estimation. The reason for this is that depending on the event topology the B- and D-meson decay templates are very similar. Furthermore the templates for tau decays can have a similar width as the bulk of the B- and D-meson distributions in case of low momentum mesons. Due to these similarities in the templates the relative non-prompt ratios depend strongly on the precise non-prompt template shapes leading to large systematic uncertainties. This does not affect the prompt muon fraction estimation, because the prompt template is always narrower than that of any of the non-prompt shapes.

We conclude that this template method, based on the d_0-significance of muon tracks, is a reliable method to estimate the prompt muon fraction in a large variety of muon samples.

Chapter 6

Prompt same-sign muon pairs

A wide range of proposed extensions to the Standard Model, including supersymmetry, predict enhanced rates for collision events at the LHC containing two prompt leptons with equal electric charge. As the SM cross-section for such signatures in relatively small, prompt same-sign (SS) dilepton cross-section measurements can be used to search for new physics beyond the SM.

In this chapter we use the template fitting method of Chapter 5 and the knowledge of muons from pion and kaon decays of Chapter 4 to determine the cross-section for inclusive prompt SS dimuon events in ATLAS and compare the result with SM predictions. As the main SM contribution to the prompt SS dimuon cross-section comes from WZ and ZZ diboson production where both bosons decay to muons, we also consider the subset of prompt SS dimuon events with a third opposite-sign muon, to determine the Z+prompt muon cross-section.

Using these prompt SS dimuon and Z+prompt muon cross-sections, it is possible to exclude some phase-space of the proposed new physics models. As an example, in Section 6.5, we determine limits in the mSUGRA[1] phase-space.

6.1 Introduction

In the SM, prompt high momentum muons are almost exclusively produced in the decay of gauge bosons, specifically: Z- and W-bosons as well as offshell photons (γ^*), where a Z or γ^* decays to $\mu^+\mu^-$ and $W^\pm$ to $\mu^+\nu_\mu$ or $\mu^-\overline{\nu}_\mu$ depending on the charge of the W-boson. Top-quarks can also lead to prompt muons due to their decay to a W-boson and a b-quark with a branching ratio of close to 100%. The muon is then produced in the subsequent decay of the W-boson. As none of these SM particles result in the production of two SS prompt muons, events which contain at least two muons of equal charge can only be created in events with at least two gauge bosons.

The main SM contribution to the SS prompt muon cross-section comes from $(Z/\gamma^*)W^\pm$ and $(Z/\gamma^*)(Z/\gamma^*)$ diboson production. The cross-section for these two processes is taken from simulation and, for γ^* masses above 20 GeV, is approximately 17.5 and 5.7 pb

[1] mSUGRA is introduced in Section 1.2.5

respectively. With a branching ratio of $Z/\gamma^* \rightarrow \mu^+\mu^-$ of 3.366% and of muonic decays of W-bosons of 10.56%, this leads to SS prompt muon pair cross-section contributions of 62.1 and 6.5 fb respectively. Apart from these two main channels there is also a small contribution from $W^\pm$W$^\pm$ which can be produced together with two (anti-)quarks in events where the two (anti-)quarks scatter through the exchange of a gluon in a t-channel diagram and both (anti-)quarks radiate a W-boson. The last SM contribution comes from the associative production of gauge bosons with a $t\bar{t}$ pair. All other SM sources of SS prompt muon pairs are negligible.

SS dimuon signatures in new physics models

Several new physics models can also give rise to final states with prompt SS muon pairs. One of these models is supersymmetry which is described in Chapter 1. Other models include: universal extra dimensions [42], left-right symmetric models [43–46], Higgs triplet models [47–49], little Higgs models [50], fourth-family quarks [51] and flavour changing neutral current [52–57]. The production process and the rate by which these models create prompt SS dimuons depends on the new physics model and typically on the phase-space point within the model. In some cases the SS muon pair is produced in the decay of a single double charged particle such as a doubly charged Higgs-boson, but in other models, such as for R-parity conserving SUSY, the two muons are produced in two somewhat independent decay chains. As discussed in Section 1.3, in most of the SUSY phase-space a significant contribution to the prompt SS muon cross-section comes from diboson events, similar as in the SM, except that the bosons are produced in the decay of SUSY particles.

Analysis method

Although we use SUSY to motivate our search for prompt SS muon pairs in ATLAS and we compare our results with expectations from mSUGRA, our primary goal is to test the SM with the least possible bias from theoretical expectations. We therefore measure the inclusive cross-section for prompt SS dimuons in a fiducial volume chosen to minimise the restrictions on the muons while ensuring a proper event reconstruction in ATLAS. As discussed in Chapter 2, this means that both muons must be within the MS volume ($|\eta| < 2.5$) and at least one of the muons must fall within the trigger range $|\eta| < 2.4$. We further require that both muons have $p_T > 25$ GeV. This is both to limit the background of non-prompt muons and to ensure a well understood trigger rate. Apart from these basic restriction on p_T and η of the muons no other requirement is put on either the kinematics of the muon pair or the rest of the event.

The main challenge of measuring such an inclusive prompt SS muon pair cross-section lies in understanding the background from muon pairs where one or both muons are non-prompt. We estimate this background using the template fitting method described in Chapter 5 which allows us to separate prompt muons from muons produced in the decay of B- and D-mesons as well as τs without making any assumptions on the kinematics of these background events. By considering high momentum muons ($p_T > 25$ GeV) we automatically reject almost all muons produced in the decay of prompt pions and kaons. Any possible remaining contribution from this category of muons is estimated by considering the $\frac{\Delta p}{p}$ value (see Equation 3.1) of the muons, as motivated in Chapter 4.

Another possible background to prompt SS muon pairs comes from prompt opposite-sign muon pairs where the charge of one of the muon was misidentified. We limit this contribution by requiring that the independent charge measurements of the ID and MS tracks obtain the same charge. The remaining contribution is estimated from simulation and tested using muons from Z-boson decays and is shown to be negligible [58].

Previous analyses in ATLAS

The analysis presented in this chapter provides an alternative to previously performed prompt SS dimuon searches in ATLAS [58] which only considered isolated muons. Apart from this isolation criteria on the muons the main difference between the methods lies in the estimation of the non-prompt background. In Ref. [58] this contribution is estimated by extrapolating from the number of events in control regions, while we fit this contribution directly in the signal region, thereby removing any dependence on the kinematics of these background events. In Section 6.6 we compare the sensitivity of the two methods.

6.2 Data set and muon selection

The cross-section measurements presented in this chapter are performed on the data collected in Period D to K of 2011. This is the same data set as used in Chapter 5, except that we require the data to pass some additional basic data-quality cuts[2], resulting in an integrated luminosity of 2.28 ± 0.08 fb^{-1} [59].

6.2.1 Trigger

The events are selected using Event Filter level triggers designed to select single high momentum muons. Specifically we require the events to be selected by either a combined muon EF trigger for muons with $p_T > 18$ GeV (EF_mu18_MG) or a MS only EF trigger for muons with $p_T > 40$ GeV and $|\eta| < 1.05$ ($EF\_mu40\_MSonly\_barrel$)[3]. The use of this second trigger is to compensate for a small decline in the EF_mu18_MG trigger efficiency for muons in the barrel regions with a momentum of more than 200 GeV. Although this trigger was added for completeness it does not significantly affect the results presented in the chapter, as such very high momentum muons are very rare. In data-taking Periods J and K of 2011 the EF_mu18_MG was prescaled. Therefore in these periods the $EF\_mu18\_MG\_medium$ trigger was used instead, which has slightly higher quality cuts on the muon tracks.

The trigger efficiency with respect to the offline reconstruction for the combination of the EF_mu18_MG and $EF\_mu40\_MSonly\_barrel$ triggers is shown in Figure 6.1. In the

[2]These additional requirements are implemented in the form of a *Good Run List* which rejects events obtained when one or more of the subdetector was not working optimally. The main cause in the luminosity drop introduced by this *Good Run List* is due to some problems in the liquid argon calorimeters.

[3]The ATLAS muon triggers are described in Section 2.4.2.

barrel region $|\eta| < 1.05$ (left plot) the efficiency is given as a function of η and ϕ and holds for muons with $p_T > 20$ GeV, corresponding with the momentum plateau region. The low efficiency bins at negative ϕ are due to the feet regions of the MS. In the end-cap regions, $1.05 < |\eta| < 2.4$, (right plot) the trigger efficiency does not significantly depend on either η or ϕ and is therefore given as a function of p_T. The trigger does not extend beyond $|\eta| = 2.4$.

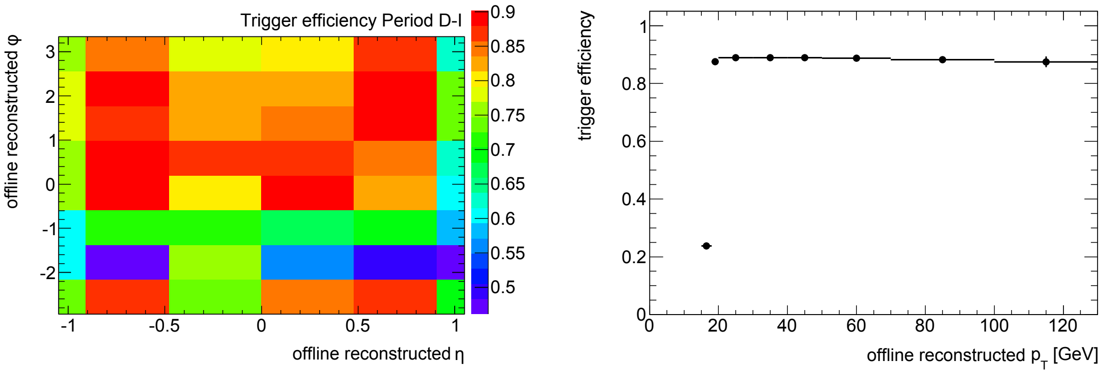

Figure 6.1: The trigger efficiency with respect to the offline reconstruction for the combination of the *EF_mu18_MG* and *EF_mu40_MSonly_barrel* triggers for combined muons in the barrel region ($|\eta| < 1.05$) as a function of η and ϕ (left plot) and in the end-cap regions ($1.05 < |\eta| < 2.4$) as a function of p_T (right plot). The efficiency in the barrel region holds for muons with $p_T > 20$ GeV.

6.2.2 Muon Selection

To ensure a high quality on the selected muon tracks, as well as to use the same muon selection as used to obtain the muon trigger efficiencies the following requirements were added to the basic muon selection of Section 2.3.1:

- $p_T > 15$ GeV
- $z_0 < 10$ mm (to limit the number of tracks from pile-up collisions)
- The charge of the ID and MS track must be the same (to ensure an accurate charge measurement).
- At least 1 B-layer hit, if a B-layer hit is expected.
- At least 2 pixel hits, where dead pixels along the track are considered as hits.
- At least 6 SCT hits, where dead strips along the track are considered as hits.
- The number of holes (missing hits) in the pixel and SCT track is smaller than 3.

- If $|\eta| < 1.9$, at least 6 TRT hits and/or outliers hits, where the number of TRT outliers hits is less the 90% of the total.

- If $|\eta| > 1.9$, the number of TRT outliers hits should be less the 90% of the total TRT hits if the track has at least 6 TRT hits and/or outliers hits.

This corresponds to the minimum muon requirements used in this chapter. In most cases we use a stronger p_T requirement ($p_T > 25$ GeV) to limit the non-prompt background as well as to be in the plateau region of the selected triggers. The minimum p_T requirement of each selected muon is always indicated in the text.

Muon reconstruction efficiency

The reconstruction efficiency for muons passing this selection is shown in Figure 2.10 where the reconstruction efficiency is given by the fraction of true muons above a given momentum threshold which are properly reconstructed. As we want to relate reconstructed muons with their reconstructed properties to the original true muons, we use a slightly modified definition of the reconstruction efficiency given by the number of reconstructed muons with a reconstructed $p_T > 15$ or 25 GeV in a certain detector region over the number of true muons with a true $p_T > 15$ or 25 GeV in the same detector region. This definition of the reconstruction efficiency depends slightly on the muon reconstruction resolutions and kinematic distributions of the muons. Specifically it includes some threshold effects such as reconstructed muons with a higher (lower) momentum than the true momentum, leading to a higher (lower) efficiency. In case of a flat momentum distribution these two contributions would cancel, but depending on the steepness of the p_T distribution at the p_T threshold this effect could result in ”efficiencies” larger than one.

The reconstruction efficiency for muons with $p_T > 15$ GeV is given in Figure 6.2 as a function of η. The efficiency is obtained from a high statistics sample of simulated $Z \to \mu^+\mu^-$ events and is corrected for differences in efficiency and momentum resolution between data and simulation. To quantify the dependence of the muon reconstruction efficiency on the kinematic distribution of the muons the results are compared with the efficiency obtained from simulated ZZ and ZW events. The values obtained by the three samples agree within statistics, showing no significant dependence on possible threshold effects.

From Figure 6.2 it is clear that the muon reconstruction efficiency depends on η, with a much lower efficiency in at $\eta \sim 0$ due to a gap in the MS as was discussed in Section 2.3.1. The efficiency in the MS barrel to end-cap transition regions (around $|\eta| = 1.2$)is also somewhat lower than in the rest of the MS region. Apart from this dependence on η the muon reconstruction efficiency also depends on ϕ, specifically on whether the track was reconstructed in a small or large MS segment or in the overlap regions between segments. Furthermore the reconstruction efficiency is lower in the MS feet regions. For each of these different ϕ regions the differences in efficiency between data and simulation was obtained separately and incorporated in the distributions of Figure 6.2. In this chapter we do not use the ϕ dependence of the efficiency explicitly since events in ATLAS are essentially ϕ

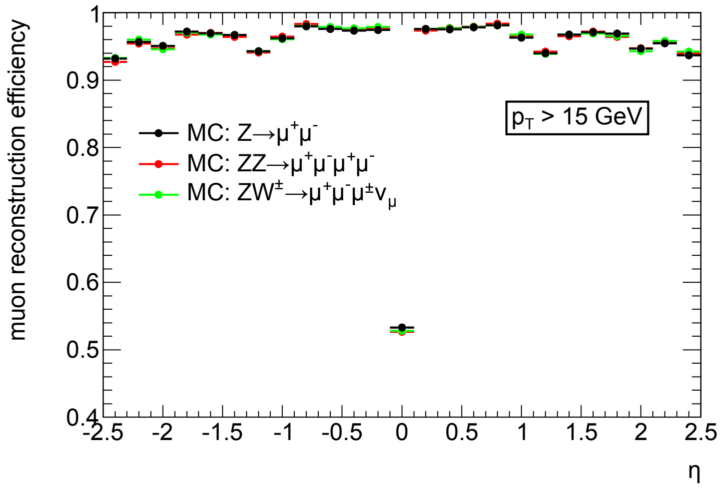

Figure 6.2: The reconstruction efficiency for muons passing the selection of Section 6.2.2, given by the fraction of reconstructed muons with $p_T > 15$ GeV over true prompt muons with $p_T > 15$ GeV, as a function of η, obtained simulated Z, ZZ and ZW samples. The efficiencies are corrected for differences between data and simulation.

symmetric and therefore the ϕ distribution of muons in all simulated samples and in data should be the same.

As shown in Figure 2.10, for muon with $p_T > 15$ GeV, the reconstruction efficiency is independent of the muon transverse momentum. We therefore only need to take the η dependence of the muon reconstruction efficiency into account.

6.2.3 Monte Carlo samples

To compare the measured cross-sections in this chapter with theoretical expectations we rely on simulated events to obtain the total and fiducial theoretical cross-sections from SM and SUSY processes. These simulated samples are all listed in Appendix A, while the generating procedure is described in Section 2.5.

Standard model processes

The production of $(Z/\gamma^*)(Z/\gamma^*)$ and $(Z/\gamma^*)W^\pm$ events is generated at NLO with a total cross-section of 5.7 and 17.5 pb respectively. The uncertainty on this cross-section, taken from Ref. [58], is 12%: 10% due to higher order corrections and 7% from the PDFs.

For $W^\pm W^\pm$ production we use a sample generated at LO. It has a cross-section of 221 fb with an estimated K-factor of 1.0 ± 0.5. Unfortunately the only available sample contains a filter requiring two jets of at least 20 GeV. Without this added requirement the cross-section for $W^\pm W^\pm$ production is 287 fb. As we do not include any jet requirements in our analysis, we reweight the available sample to this total cross-section. This is based on the assumption that the jet-filter does not affect the kinematics on the muons, which unfortunately is not true. However the uncertainty due to this assumption should fall well within the 50% uncertainty from the K-factor.

The last category of SM events which contribute to the prompt SS dimuon cross-section are $t\bar{t}W^{\pm}$ and $t\bar{t}Z$ production. These samples are also generated at LO, with an estimated cross-section of 208 and 177 fb respectively. The estimated K-factor for these samples is 1.30 ± 0.65.

These different contributions to the prompt SS dimuon cross-section are discussed further in Section 6.3.6 and listed in Table 6.2.

SUSY processes

To estimate the SUSY prompt SS dimuon cross-section for the mSUGRA plane defined by $A_0 = 0$ GeV, $\tan(\beta) = 10$ and $\mu > 0$ we use the 350 samples of the mSUGRA grid defined in Appendix A. These samples are generated at LO and corrected to the NLO cross-section calculated by Prospino [60,61], a program specialized in the calculation of SUSY cross-sections. These corrections are done separately for all SUSY points and each production process and are therefore typically different for, for example, $\tilde{g}\tilde{g}$ and $\tilde{g}\tilde{q}$ production. The cross-section estimation for gluino and squark production is further improved to the next-to-leading-log order, which incorporates some additional NNLO effects, using Nll-fast [62–66]. The uncertainty on the cross-section is obtained by varying the PDF between CTEQ [25] and MSTW [27] and varying the uncertainties on both these PDF due to the uncertainty on α_s and on the scale-factor used to separate perturbative and non-perturbative processes.

As an indication for the cross-section and the relative uncertainties, Figure 6.3 shows the estimated mSUGRA fiducial cross-section for prompt SS muon pairs with $p_T(\mu) > 25$ GeV in the ATLAS detector acceptance and the relative uncertainty on this cross-section for each point on the mSUGRA grid.

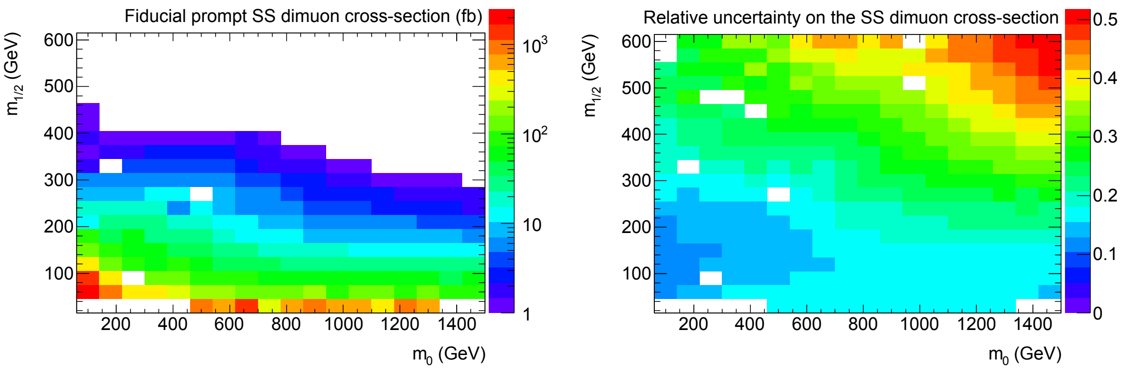

Figure 6.3: The estimated mSUGRA fiducial cross-section for prompt SS muon pairs with $p_T(\mu) > 25$ GeV in the ATLAS detector acceptance in fb (left) and the relative uncertainty on this cross-section (right) for each point on the mSUGRA grid discussed in Section 6.2.3. This grid is defined in the mSUGRA plane with $A_0 = 0$ GeV, $\tan(\beta) = 10$ and $\mu > 0$.

6.3 Prompt SS muon pair cross-section

The main goal of this analysis is to determine the fiducial cross-section for inclusive, prompt, SS, high momentum ($p_T > 25$ GeV) muon pairs in the ATLAS detector acceptance (one muon with $|\eta| < 2.4$ due to the trigger acceptance and the other muon with $|\eta| < 2.5$). We do this by selecting SS muon pairs passing these requirements and fitting the prompt fraction for each muon. The number of events where both muons are prompt can then be estimated from these fitted fractions. As we are interested in the inclusive fiducial cross-section, we do not put any further requirements on the selected events. Specifically this means that besides the selected muon pair the event can contain additional leptons and/or jets.

The most straightforward way to estimate the probability that both muons in a selected muon pair are prompt is to multiply the prompt probability of the first muon with that of the second. This is the approach used in Chapter 4 to estimated the pion and kaon contamination to dimuon pairs. It is based on the assumption that the prompt fraction of both muons are uncorrelated. In Chapter 4 this assumption, which we tested on simulated events, was possible because, except for the very low invariant mass region, the production of π/K and non-π/K muons is independent. Unfortunately this is not true for prompt and non-prompt muons as, for example, $t\bar{t}$ events can lead to signatures with one prompt muon and one non-prompt muon with equal charge. In these types of events the probability for the second muon to be prompt is dependent on whether the first muon was prompt or not. Therefore if, for example, we measure a prompt fraction of 20% for both muons, the fraction of events where both muons were prompt could be 4%, if the prompt fractions are uncorrelated, but could also be 0%, if all prompt muons are produced in combination with a non-prompt muon. This dependence on the correlation between the prompt fraction of the muons is taken as a systematic uncertainty. To limit the relative size of this uncertainty, we use a tight selection on one of the muons such that its prompt fraction is close to one.

This tight selection on one of the selected muons is achieved using both an isolation cut and a cut of the d_0-significance on the most isolated muon. To quantify the effect of these added selection criteria and therefore to be able to estimate the cross-section without isolation or impact parameter restrictions, we correct the obtained cross-section using the efficiency of the d_0-significance cut. As discussed further in Section 6.3.2 this efficiency is obtained from the prompt muon templates. The effect of the isolation cut is quantified by estimating separately the fiducial cross-section for events with at least one muon isolated, and events with both muons isolated. The isolation independent cross-section is then estimated using these two values.

6.3.1 Event selection

We apply the following event selection:

- The event contains at least one $\mu^{\pm}\mu^{\pm}$ pair.

- The most isolated muon is denoted as μ_1 and the other as μ_2, where the isolation is given by p_T-cone40/p_T.[4]

- $p_T > 25$ GeV, for both muons.
- At least one muon is isolated: p_T-cone40/$p_T < 0.08$, for μ_1.
- If the event contains more than one $\mu^\pm\mu^\pm$ pair passing these selections, the pair with the most isolated second muon, μ_2, is selected.
- One of the selected muons is matched to a trigger object ($\Delta R < 0.15$) and has $|\eta| < 2.4$.
- The most isolated muon is produced close to the interaction point: $-2 < d_0$-sig < 1, for μ_1.

As mentioned previously, the isolation and impact parameter requirements on the most isolated muon are necessary to ensure a high prompt fraction for this muon. To estimate the efficiency of the isolation cut, we also consider the subset of events where the second muon, μ_2, is isolated (p_T-cone40/$p_T < 0.08$).

The cut-flow for this selection is given in Table 6.1. In total there are 1118 events that pass our event selection, of which 94 have both muons isolated. The invariant mass distribution for all SS muon pairs with $p_T > 25$ GeV is shown in Figure 6.4 together with the distribution for events with one or both muons isolated.

Cut	# events
At least one $\mu^\pm\mu^\pm$ pair	77126
$p_T > 25$ GeV for both muons	8809
$\|\eta\| < 2.4$ for at least one muon	8808
μ_1 is isolated	1657
muon matched to a trigger object	1649
$-2 < d_0$-sig$(\mu_1) < 1$	1118
μ_2 is isolated	94

Table 6.1: The cut-flow for the event selection of Section 6.3.1 on the data set described in Section 6.2.

6.3.2 Cross-section measurement

To estimate the fiducial cross-section for inclusive prompt, SS, high momentum ($p_T >$ 25 GeV) muon pairs in the ATLAS detector acceptance, we first determine the cross-sections for events where at least one of the muons is isolated and for events where both muons are isolated. The cross-sections for these two subset of events are then used to calculate the cross-section independent of isolation criteria.

[4] p_T-cone40 is defined as the sum of the p_T of all tracks in a cone with angle 0.4 around the muon.

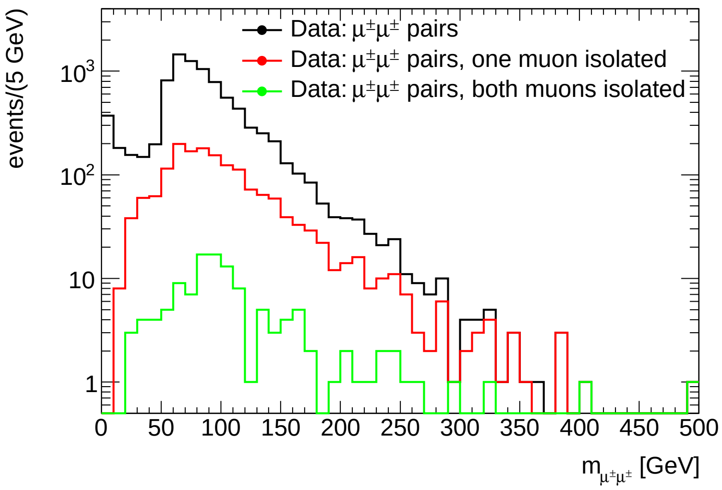

Figure 6.4: The invariant mass distribution of high momentum ($p_T(\mu) > 25$ GeV) $\mu^{\pm}\mu^{\pm}$ pairs in the data sample of Section 6.2 (black lime) as well the distribution for the subset of muon pairs with one (red line) or both (blue line) muons isolated (p_T-cone40$/p_T < 0.08$).

The number of signal events in the selected data sample where at least one of the selected muons is isolated is obtained by calculating, for each event separate, the probability that both muons are prompt. This probability is corrected for the trigger and muon reconstruction efficiency as well as for the applied d_0-significance cut on μ_1. This leads to the following expression for the cross-section:

$$\sigma^{\text{fid}}_{\text{SS}:\mu_1=\text{isolated}} = \frac{1}{\mathscr{L}} \sum_{\text{events}} \frac{\mathscr{P}_{\mu_1}(\mu_1) \cdot \mathscr{P}_{\mu_2}(\mu_2)}{\varepsilon_{\text{trigger}}(\mu_1, \mu_2) \cdot \varepsilon_{\text{reco}}(\mu_1) \cdot \varepsilon_{\text{reco}}(\mu_2) \cdot \varepsilon_{d_0\text{-sig}}}, \tag{6.1}$$

where $\mathscr{L}$ denotes the integrated luminosity, $\varepsilon_{\text{trigger}}$ and $\varepsilon_{\text{reco}}$ the trigger and muon reconstruction efficiencies, $\varepsilon_{d_0\text{-sig}}$ the efficiency of the d_0-significance cut on μ_1 and $\mathscr{P}_{\mu_1}$ and $\mathscr{P}_{\mu_2}$ give the probability that μ_1 and μ_2 are prompt.

In Equation 6.1 we assume that the probability that both muons are prompt is equal to $\mathscr{P}_{\mu_1}(\mu_1) \cdot \mathscr{P}_{\mu_2}(\mu_2)$. As mentioned before this is based on the assumption that $\mathscr{P}_{\mu_1}(\mu_1)$ and $\mathscr{P}_{\mu_2}(\mu_2)$ are uncorrelated. We quantify the uncertainty due to this assumption on the measured cross-section by considering the case where the prompt fraction of μ_1 and μ_2 are fully anti-correlated. In this case the $\mathscr{P}_{\mu_1}(\mu_1) \cdot \mathscr{P}_{\mu_2}(\mu_2)$ term in Equation 6.1 should be replaces by $\mathscr{P}_{\mu_1}(\mu_1) + \mathscr{P}_{\mu_2}(\mu_2) - 1$ in events with $\mathscr{P}_{\mu_1}(\mu_1) + \mathscr{P}_{\mu_2}(\mu_2) > 1$ and by zero otherwise. This corresponds to the minimum number of prompt muons pairs possible given $\mathscr{P}_{\mu_1}(\mu_1)$ and $\mathscr{P}_{\mu_2}(\mu_2)$.

$\mathscr{P}_{\mu_1}$ and $\mathscr{P}_{\mu_2}$:

The probability that μ_1 is prompt, $\mathscr{P}_{\mu_1}$, is determined by fitting the d_0-significance distribution for μ_1 (without the d_0-significance cut) using the template fitting method of

Chapter 5. The result of the fit is shown in the left plot of Figure 6.5. The prompt probability of each individual muon is obtained from the fitted fraction of the prompt PDF over the total distribution at the d_0-significance value corresponding to that of the muon. The statistical uncertainty on this value is obtained using a profile likelihood on the signal fraction of the fit. The systematic uncertainty calculation is described in Chapter 5. The right plot of Figure 6.5 gives $\mathscr{P}_{\mu_1}$ as a function of the d_0-significance.

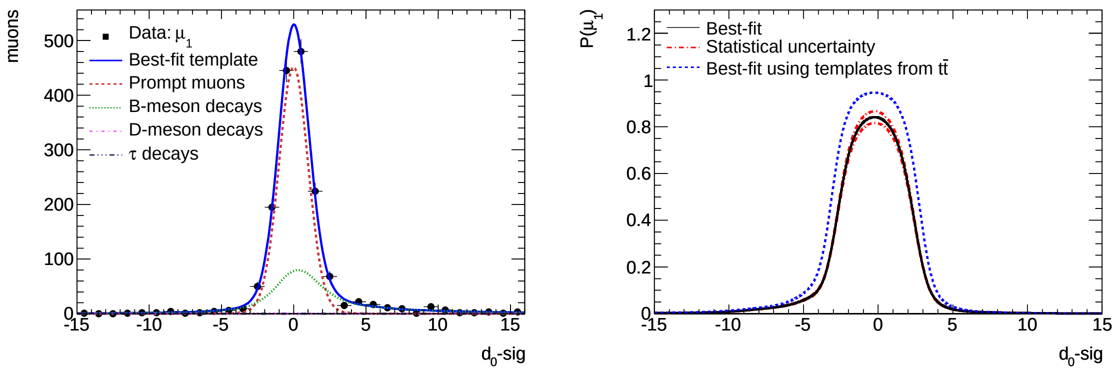

Figure 6.5: Left: The d_0-significance distribution for μ_1 in the event selection of Section 6.3.1 without the d_0-significance cut, fitted using the template fitting method of Chapter 5. Right: $\mathscr{P}_{\mu_1}$ as a function of the d_0-significance of μ_1. The red lines denote the statistical uncertainty while the blue line gives the systematic uncertainty obtained from using templates constructed from simulated $t\bar{t}$ events.

The probability that μ_2 is prompt, $\mathscr{P}_{\mu_2}$, is determined in a similar way by fitting the d_0-significance distribution for μ_2. This is done separately for three bins depending on the p_T of the closest jet to the muon track, where this p_T is taken to be zero in events without any jets[5]. The result of these fits are shown in Figure 6.6. The majority of prompt muons have a closest jet p_T of less than 20 GeV. For these muons the value for $\mathscr{P}_{\mu_2}$ is plotted as a function of the d_0-significance in the top right plot of figure Figure 6.6. We did not bin the fits for μ_1 in a similar way as the isolation criteria on this muon remove most of the correlation between the impact parameter distribution of the muon and the properties of the nearest jet.

The template fitting method of Chapter 5 is able to separate the prompt muon contribution from muons from B-meson, D-meson and τ decays. Unfortunately it is not able to differentiate between prompt muons and prompt pions and kaons. As this contribution to high momentum muons is expected to be very small, we do not consider prompt pions and kaons in the determination of $\mathscr{P}_{\mu_1}$ and $\mathscr{P}_{\mu_2}$. The systematic uncertainty due to this omission is quantified by calculating the cross-section after rejecting muons with $\frac{\Delta p}{p} > 0.5$. The use of the $\frac{\Delta p}{p}$ value[6] is motivated in Chapter 4. For all cross-sections measured in this chapter, the uncertainty from prompt pions and kaons turns out to be negligible.

[5] This binning in p_T(jet) is motivated in Chapter 5
[6] See Equation 3.1.

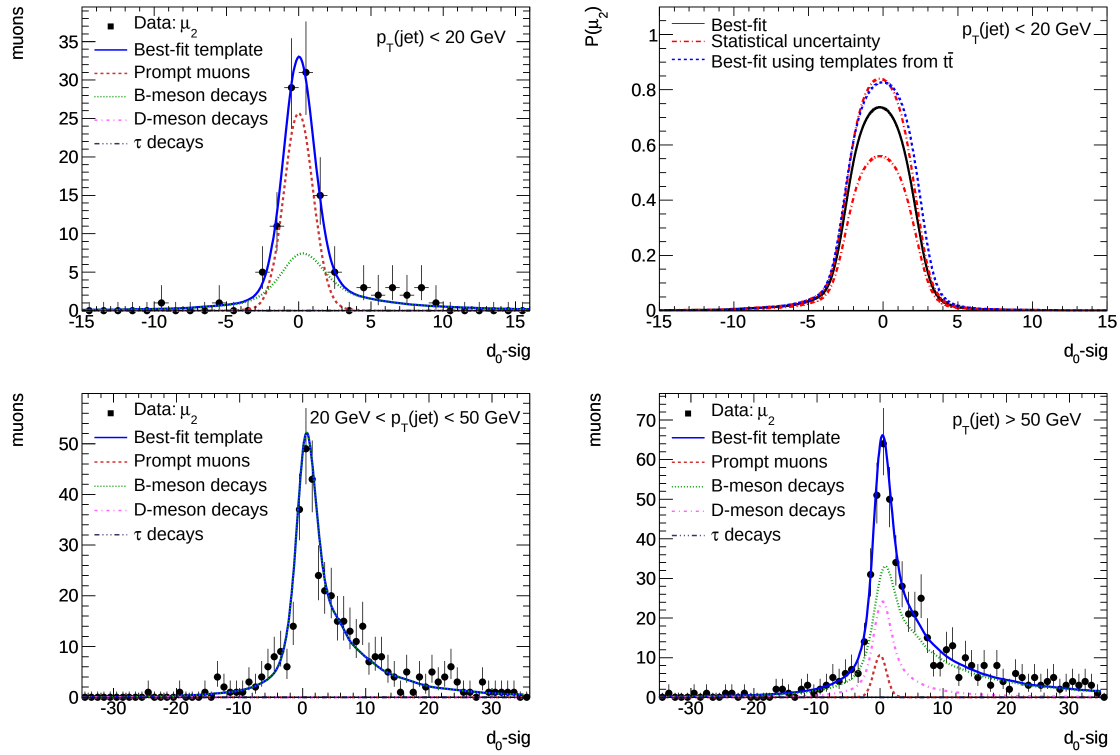

Figure 6.6: Top left and bottom: The d_0-significance distribution for μ_2 in the event selection of Section 6.3.1 fitted using the template fitting method of Chapter 5 for different bins in closest jet p_T. Top right: $\mathscr{P}_{\mu_2}$ as a function of the d_0-significance of μ_2 for muons whose closest jet has a $p_T < 20$ GeV. The red lines denote the statistical uncertainty while the blue line gives the systematic uncertainty obtained from using templates constructed from simulated $t\bar{t}$ events.

$\mathscr{L}$, $\varepsilon_{\mathbf{reco}}$, $\varepsilon_{\mathbf{trigger}}$ and $\varepsilon_{d_0\text{-}\mathbf{sig}}$:

As mentioned in Section 6.2 the integrated luminosity of the selected data sample is 2.28 fb^{-1} with an uncertainty of 3.7% [59].

The muon reconstruction efficiency for each muon is taken from Figure 6.2 and depends on η. The trigger efficiency of the event depends on p_T, η and ϕ of both muons, as well as on the data period. The efficiency to trigger at least one muon is:

$$\varepsilon_{\text{trigger}}(\mu_1,\mu_2) = 1-(1-\varepsilon_{\text{trigger}}(\mu_1))(1-\varepsilon_{\text{trigger}}(\mu_2)),$$

where the efficiency per muon is discussed in Section 6.2.1. As we require the trigger object to be matched with a muon with $|\eta| < 2.4$ the trigger efficiency for muon with $|\eta| > 2.4$ is automatically zero. The binning used for the muon trigger and reconstruction efficiency is the same binning as shown in Figure 6.1 and 6.2. For all cross-section measurements performed in this chapter the uncertainty from the trigger and reconstruction efficiency turns out to be negligible.

$\varepsilon_{d_0\text{-sig}}$ is taken from the prompt template and is the same for all events ($80 \pm 1\%$). The uncertainty is included by the use of different templates to estimate the uncertainty on $\mathscr{P}_{\mu_1}$ and is therefore correlated with the systematic uncertainty on the fit result.

6.3.3 Result for events with at least one muon isolated

Using Equation 6.1 we can extract the fiducial cross-section for prompt, SS, high momentum ($p_T > 25$ GeV) muon pairs in the ATLAS detector acceptance (one muon with $|\eta| < 2.4$ and the other muon with $|\eta| < 2.5$) with at least one of the muons isolated:

$$\sigma^{\text{fid}}_{\text{SS}:\mu_1=\text{isolated}} = 48^{+23}_{-10}(\text{stat})^{+33}_{-17}(\text{syst}) \text{ fb}.$$

The statistical uncertainty contains both the Poisson uncertainty on the number of events, calculated by adding the contribution of each event in quadrature, and the uncertainty on the fit results due to statistical fluctuations in the signal shape. As discussed in Section 6.3.2 this second uncertainty, which dominated the total statistical uncertainty, is obtained from a profile likelihood on the prompt fraction in the fits for $\mathscr{P}_{\mu_1}(\mu_1)$ and $\mathscr{P}_{\mu_2}(\mu_2)$. The upper limit on the systematic uncertainty is dominated by the choice in the templates used in the d_0-significance fits. As discussed in Chapter 5 this uncertainty is estimated by using templates constructed from simulated $t\bar{t}$ events. The lower limit on the systematic uncertainty is dominated by the uncertainty in the correlation between $\mathscr{P}_{\mu_1}(\mu_1)$ and $\mathscr{P}_{\mu_2}(\mu_2)$. All other uncertainties are negligible.

6.3.4 Result for events with both muons isolated

We determine the cross-section for events in which both muons are isolated using the same approach as for events with at least one muon isolated. The corresponding fits on the d_0-significance distributions of μ_1 and μ_2 are shown in Figure 6.7.

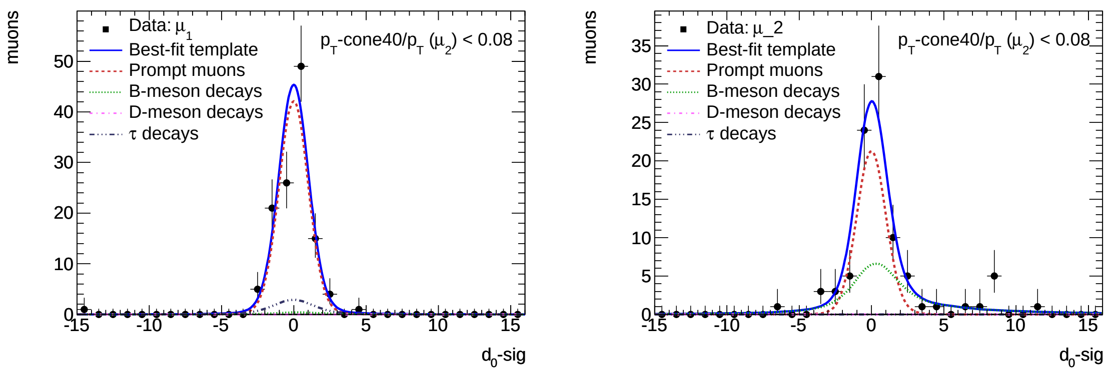

Figure 6.7: The d_0-significance distribution for μ_1 (left) and μ_2 (right) in the event selection of Section 6.3.1 with both muons isolated. The left plot does not include the d_0-significance cut on μ_1. Both distributions are fitted using the template fitting method of Chapter 5.

The estimated fiducial cross-section for the subset of events in which both muons are isolated is:

$$\sigma^{\text{fid}}_{\text{SS}:\mu_1,\mu_2=\text{isolated}} = 32^{+7}_{-9}(\text{stat})^{+7}_{-2}(\text{syst})\text{ fb}.$$

The statistical uncertainty is still dominated by the uncertainties on $\mathscr{P}_{\mu_1}$ and $\mathscr{P}_{\mu_2}$ returned by the fits. The upper limit on the systematic uncertainty is caused by the effect of changing the templates used in the d_0-significance fits to templates constructed from simulated $t\bar{t}$ events. The lower value on the systematic uncertainty is a combination on the uncertainty to how we combine $\mathscr{P}_{\mu_1}(\mu_1)$ and $\mathscr{P}_{\mu_2}(\mu_2)$ (1.4 fb), the systematic uncertainty on the d_0-significance fits (1.2 fb) and the uncertainty on the integrated luminosity (1.1 fb).

The relative uncertainties for this cross-section measurement are significantly smaller than the uncertainties on $\sigma^{\text{fid}}_{\text{SS}:\mu_1=\text{isolated}}$ despite a difference in statistics of about an order of magnitude. For the statistical uncertainty, this is because the uncertainty is not dominated by the Poisson term but by the effect of the statistical uncertainty of the d_0-significance distribution shapes on the fitted prompt fractions. This uncertainty is dominated by statistical uncertainties in the tails of the distributions and is therefore relatively larger for more non-prompt dominated muon samples. As the prompt fraction for μ_2 and to a lesser degree for μ_1, is significantly higher with the additional isolation requirement on the second muon, this leads to corresponding smaller uncertainties.

The more prompt dominated muon selections are also the reason for the smaller systematic uncertainties, as the shape of the prompt template is more stable and better understood than the different non-prompt template shapes which depend on the properties of the nearby jets and on the uncertainty on d_0 (see Chapter 5). Therefore the systematic uncertainty on the fits due to our choice in templates is smaller with a relative smaller non-prompt contribution. Also the uncertainty due to combining $\mathscr{P}_{\mu_1}(\mu_1)$ and $\mathscr{P}_{\mu_2}(\mu_2)$ into the probability of two prompt muons, is much smaller for $\sigma^{\text{fid}}_{\text{SS}:\mu_1,\mu_2=\text{isolated}}$ than for $\sigma^{\text{fid}}_{\text{SS}:\mu_1=\text{isolated}}$ due to the prompt fraction of almost 100% on μ_1 shown in Figure 6.7.

6.3.5 The SS prompt dimuon cross-section

Using the cross-sections obtained for events with at least one and with both muons isolated, we estimated the isolation independent fiducial cross-section for prompt SS dimuons in ATLAS.

Assuming that for signal events the probability that one of the muons is isolated is independent of whether the other muon is also isolated the following equations hold:

$$\begin{aligned}\sigma^{\text{fid}}_{\text{SS}:\mu_1,\mu_2=\text{isolated}} &= \varepsilon^2_{\text{isolation}}\sigma^{\text{fid}}_{\text{SS}} \\ \sigma^{\text{fid}}_{\text{SS}:\mu_1=\text{isolated}} &= (2\varepsilon_{\text{isolation}} - \varepsilon^2_{\text{isolation}})\sigma^{\text{fid}}_{\text{SS}}.\end{aligned}$$

Therefore:

$$\sigma^{\text{fid}}_{\text{SS}} = \frac{(\sigma^{\text{fid}}_{\text{SS}:\mu_1,\mu_2=\text{isolated}} + \sigma^{\text{fid}}_{\text{SS}:\mu_1=\text{isolated}})^2}{4\sigma^{\text{fid}}_{\text{SS}:\mu_1,\mu_2=\text{isolated}}} \tag{6.2}$$

Using Equation 6.2 we estimate the fiducial cross-section for inclusive prompt, SS, high momentum ($p_T > 25$ GeV) muon pairs in the ATLAS detector acceptance to be:

$$\sigma_{\mathrm{SS}}^{\mathrm{fid}} = 50^{+24}_{-11}(\mathrm{stat})^{+43}_{-20}(\mathrm{syst})\ \mathrm{fb}.$$

The statistical uncertainty is obtained by using the same relative uncertainty as on $\sigma^{\mathrm{fid}}_{\mathrm{SS}:\mu_1=\mathrm{isolated}}$. This is motivated by the observation that the statistical uncertainties of $\sigma^{\mathrm{fid}}_{\mathrm{SS}:\mu_1=\mathrm{isolated}}$ and $\sigma^{\mathrm{fid}}_{\mathrm{SS}:\mu_1,\mu_2=\mathrm{isolated}}$ are highly correlated. Since the relative uncertainty on $\sigma^{\mathrm{fid}}_{\mathrm{SS}:\mu_1=\mathrm{isolated}}$ is much larger it dominates the uncertainty on $\sigma^{\mathrm{fid}}_{\mathrm{SS}}$. The upper value of the systematic uncertainty is obtained from evaluating Equation 6.2 with the results using templates from simulated $t\bar{t}$ events. The lower value of the systematic uncertainty corresponds to the lower systematic limit for $\sigma^{\mathrm{fid}}_{\mathrm{SS}:\mu_1,\mu_2=\mathrm{isolated}}$ as it is impossible for the total fiducial cross-section to be smaller than $\sigma^{\mathrm{fid}}_{\mathrm{SS}:\mu_1,\mu_2=\mathrm{isolated}}$.

6.3.6 Comparison with SM predictions

Using the MC samples and cross-sections given in Section 6.2.3 we estimate the theoretical, SM, fiducial cross-section for prompt SS dimuons at the LHC to be:

$$\sigma^{\mathrm{fid}}_{\mathrm{SS:SM}} = 39.3 \pm 4.5\ \mathrm{fb}.$$

The contributions from the individual SM processes are listed in Table 6.2. In calculating the uncertainty on the total fiducial cross-section we assume the uncertainty on the cross-section of the $ZW^{\pm}$ and ZZ samples to be fully correlated. The same holds for the uncertainty on the K-factor of the $t\bar{t}W$ and $t\bar{t}Z$ cross-sections. All other uncertainties are assumed to be uncorrelated.

Process	$\sigma^{\mathrm{fid}}_{\mathrm{SS:SM}}$ (fb)
$ZW^{\pm}$	29.3 ± 3.5
ZZ	4.9 ± 0.6
$W^{\pm}W^{\pm}$	2.0 ± 1.0
$t\bar{t}W$	2.0 ± 1.0
$t\bar{t}Z$	1.1 ± 0.6
Total	39.3 ± 4.5

Table 6.2: The theoretical prediction from the SM for $\sigma^{\mathrm{fid}}_{\mathrm{SS:SM}}$ for different processes.

Combining this theoretical SM cross-section with our measured cross-section we conclude that the non-SM contribution to the fiducial prompt SS dimuon cross-section is:

$$\sigma^{\mathrm{fid}}_{\mathrm{SS:non\text{-}SM}} = 10^{+49}_{-24}\ \mathrm{fb},$$

showing no indication of physics beyond the SM. The uncertainty on $\sigma^{\mathrm{fid}}_{\mathrm{SS:non\text{-}SM}}$ is obtained from combining the theoretical uncertainty with the statistical and systematic uncertainty on the measured cross-section in quadrature.

6.3.7 95% CL upper limit

The values for the cross-sections shown so far are quoted with our best estimate for a 1σ uncertainty, approximately corresponding to a 68% confidence level (CL). When interpreting these results for the exclusion of new physics models, the 95% CL upper limit is more commonly used. As some of the systematic uncertainties are highly non-Gaussian we can not simply multiply the quoted uncertainties by a factor of 1.664 to obtain this upper limit. Instead we recalculate all separate uncertainties for this 95% CL limit before combining them. This includes using a wider range for the width of the Gaussian used to convolute the templates for the d_0-significance fits (see Section 5.6.1).

The uncertainty due to the possible correlations between the prompt probability of both muons, and the uncertainty in the choice of templates ($t\bar{t}$ versus non-$t\bar{t}$) is not increased compared to the 68% CL values. The reason for this is that these uncertainties are already estimated by looking at the full range of possibilities. In the case of the correlation between the prompt probability of the two muons we consider the case of fully anti-correlated probabilities to calculate the uncertainty. As it is impossible for these muons to be more than 100% anti-correlated, increasing this uncertainty is unrealistic. Similarly, the uncertainty due to the choice in templates reflects the uncertainty in the type of background events. The normal templates represent the simplest event topologies while the $t\bar{t}$ templates corresponds to the most complex SM events, involving a wide range of different particles. Therefore, varying between the two sets of templates already incorporates all possible SM backgrounds.

As we have no easy way to estimate the background composition of our data selection we can not build a likelihood function for the uncertainty from our choice in templates. Using the most conservative approach we therefore estimate the 95% CL upper limit to the fiducial cross-section of prompt SS dimuons in ATLAS, by calculating this cross-section and the upper limit using only templates from $t\bar{t}$. The best estimate for this cross-section is 93 fb with a 95% CL upper limit of 130 fb. This difference is dominated by the statistical uncertainties on the fits. Using the SM cross-section discussed in Section 6.3.6, this leads to a 95% CL upper limit to the non-SM contribution to $\sigma_{\mathrm{SS}}^{\mathrm{fid}}$ of 91 fb. In Section 6.5 we use this value to determine exclusion limits in the mSUGRA phase-space.

6.4 The Z+prompt muon cross-section

The largest SM contribution to the prompt SS dimuon cross-section comes from ZW and ZZ production. We therefore also determine the cross-section for the subset of prompt SS dimuon events with a third opposite-sign muon ($p_T > 15$ GeV, $|\eta| < 2.5$), such that one $\mu^+\mu^-$ is produced in the decay of a Z-boson with invariant mass between 81.2 and 101.2 GeV. We determine this Z+prompt muon cross-section by selecting a high purity sample of Z-boson candidates and determining the prompt fraction for the third muon using the template fitting method of Chapter 5.

6.4.1 Event selection

We apply the following Z-boson selection:

- The event contains at least one $\mu^+\mu^-$ pair with invariant mass between 81.2 and 101.2 GeV.
- $p_T cone40/p_T(\mu) < 0.08$, for both muons in the $\mu^+\mu^-$ pair.
- d$_0$-sig < 5, for both muons in the $\mu^+\mu^-$ pair.
- If the events contains more than one $\mu^+\mu^-$ pair, the pair with invariant mass closest to 91.2 GeV is chosen.

Furthermore the events must pass these additional selections:

- The event contains at least one additional muon ($p_T > 15$ GeV), denoted as μ_3.
- $p_T > 25$ GeV, for both muons in the $\mu^\pm\mu^\pm$ pair.
- $|\eta| < 2.4$, for one of the muons in the $\mu^\pm\mu^\pm$ pair.
- If the events contains more than one possible candidate for μ_3, the most isolated muon is chosen.
- One of the three selected muons is matched to a trigger object ($\Delta R < 0.15$) and has $p_T > 20$ GeV and $|\eta| < 2.4$.

Applying this event selection on the data sample introduced in Section 6.2 results in 136 selected events. The cut-flow for is shown in Table 6.3.

Cut	# events
At least one $\mu^\pm\mu^\pm$ pair	77126
$p_T > 25$ GeV, for both muons in $\mu^\pm\mu^\pm$	8809
$\lvert\eta\rvert < 2.4$, for one muon in $\mu^\pm\mu^\pm$	8808
Additional opposite-sign muon	614
81.2 GeV $< m_{\mu^+\mu^-} <$ 101.2 GeV	213
One of the muon is matched to a trigger object	213
$p_T cone40/p_T(\mu) < 0.08$, for both muons in $\mu^+\mu^-$	136
$\lvert d_0\text{-sig}\rvert < 5$, for both muons in $\mu^+\mu^-$	136

Table 6.3: The cut-flow for the event selection of Section 6.4.1 on the data set described in Section 6.2.

6.4.2 Cross-section measurement

The fiducial cross-section for the associated $Z \to \mu^+\mu^-$ plus additional prompt muon production is calculated by combining the purity of the Z-boson selection with the prompt fraction of μ_3 and correcting the event weight with the trigger and reconstruction efficiency as well as with the selection efficiency on the Z-boson. This leads to the following formula:

$$\sigma^{\mathrm{fid}}_{\mathrm{Z}+\mu} = \frac{1}{\mathscr{L}} \sum_{\mathrm{events}} \frac{\mathscr{P}_{\mathrm{Z}}}{\varepsilon_{\mathrm{iso}}} \frac{\mathscr{P}_{\mu_3}(\mu_3)}{\varepsilon_{\mathrm{trigger}}(\mu_Z^+, \mu_Z^-, \mu_3) \cdot \varepsilon_{\mathrm{reco}}(\mu_Z^+) \cdot \varepsilon_{\mathrm{reco}}(\mu_Z^-) \cdot \varepsilon_{\mathrm{reco}}(\mu_3) \cdot \varepsilon_{m_Z}(\mu_Z^+, \mu_Z^-)}, \tag{6.3}$$

where $\mathscr{P}_Z$ denotes the purity of the Z-selection, $\varepsilon_{\mathrm{iso}}$ the efficiency of the isolation and impact parameter cut on the muons from the Z-boson candidate and ε_{m_Z} the efficiency of the invariant mass cut.

The value for the luminosity as well as for the trigger and reconstruction efficiency are already discussed in Section 6.3.2. The only difference is that the trigger efficiency now includes the probability that the third muon is triggered, provided that $p_T > 20$ GeV and $|\eta| < 2.4$.

$\mathscr{P}_Z$ and $\varepsilon_{\mathrm{iso}}$:

We estimate the purity of the Z-boson selection, $\mathscr{P}_Z$, and the efficiency of the combined isolation and impact parameter cuts, $\varepsilon_{\mathrm{iso}}$, from the invariant mass distribution of the Z-boson candidates (without the in invariant mass cut). Figure 6.8 shows this distribution for Z-boson candidates without (left plot) and with (right plot) the muon isolation and d_0-significance requirements. We estimate the number of signal events in the considered invariant mass range by fitting these distributions using a exponential function to describe the background and Breit-Wigner convoluted with a Gaussian for the signal. The Breit-Wigner peak value and width are fixed to the Z-boson mass (91.2 GeV) and width (2.5 GeV) while the mean of the Gaussian is set to zero. The resulting fits are included in Figure 6.8. The purity of the selected Z-boson candidates corresponds to the number of signal events in the mass range over the total number of events: $\mathscr{P}_Z = 0.897 \pm 0.022 \pm 0.023$, where the first uncertainty denotes the statistical uncertainty from the fit while the second uncertainty denotes the systematic uncertainty due to our choice in fitting function. This systematic uncertainty was obtained from fitting the distributions using only a simple Gaussian distribution with a mean value of 91.2 GeV for the signal. The fitted efficiency for the applied isolation and d_0-significance cuts, is equal to the ratio between the number of signal events, in mass range between 81.2 and 101.2 GeV, between the two plots in Figure 6.8: $\varepsilon_{\mathrm{iso}} = 0.840 \pm 0.047 \pm 0.002$.

In Equation 6.3 we are interested in the ratio $\frac{\mathscr{P}_Z}{\varepsilon_{\mathrm{iso}}}$. In this case the number of signal events after the isolation and impact parameter cuts is no longer relevant. $\frac{\mathscr{P}_Z}{\varepsilon_{\mathrm{iso}}}$ equals the total number of events in the applied Z-boson selection (both signal and background) over the number of signal events in the invariant mass range between 81.2 and 101.2 GeV before the isolation and d_0-significance requirements. Using this ratio we estimate $\frac{\mathscr{P}_Z}{\varepsilon_{\mathrm{iso}}}$ to be $1.07 \pm 0.05 \pm 0.03$.

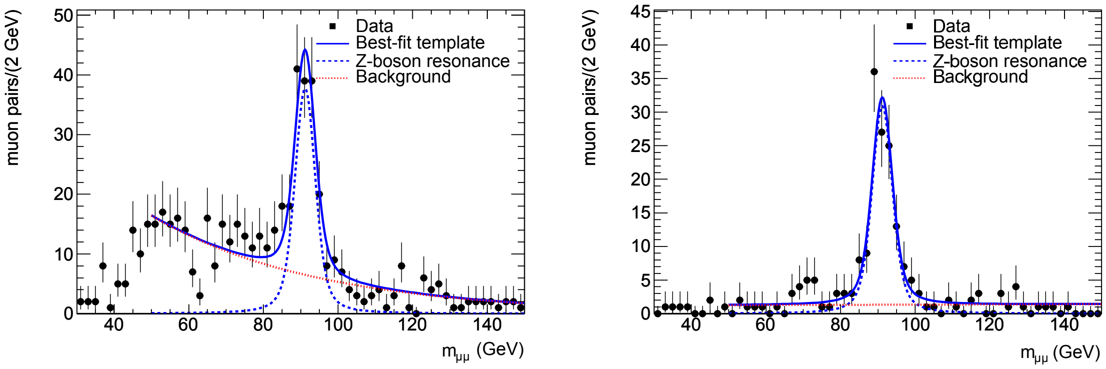

Figure 6.8: The invariant mass distribution for the Z-boson candidates in the selection of Section 6.4.1 without (left plot) and with (right plot) the muon isolation and impact parameter requirement. The distributions are fitted using a exponential function for the background and a Breit-Wigner convoluted with a Gaussian for the signal.

$\mathscr{P}_{\mu_3}$:

The prompt probability of the third muon, $\mathscr{P}_{\mu_3}$, is determined by fitting the d_0-significance distribution of μ_3. The result of this fit is shown in Figure 6.9 as well as the $\mathscr{P}_{\mu_3}$ distribution as a function of the d_0-significance. Similar as in Section 6.3.2 the possible contamination from prompt pions and kaons is estimated by considering the effect of rejecting muons with $\frac{\Delta p}{p}$>0.5 on the obtained cross-section and turns out to be negligible.

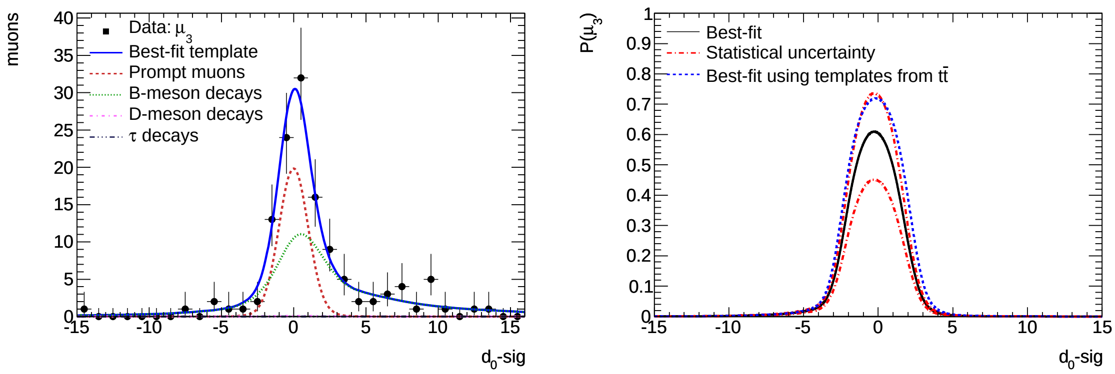

Figure 6.9: Left: The d_0-significance distribution for μ_3 in the event selection of Section 6.4.1, fitted using the template fitting method of Chapter 5. Right: $\mathscr{P}_{\mu_3}$ as a function of the d_0-significance of μ_3. The red lines denote the statistical uncertainty while the blue line gives the systematic uncertainty obtained from fitting the distribution using templates constructed from simulated $t\bar{t}$ events.

$\varepsilon_{m_Z}(\mu_Z^+,\mu_Z^-)$:

$\varepsilon_{m_Z}(\mu_Z^+,\mu_Z^-)$ represents the difference in the efficiency of the invariant mass cut between the true and reconstructed invariant mass of the Z-boson. It is defined as the fraction of reconstructed Z-bosons with a reconstructed invariant mass between 81.2 and 101.2 GeV over those with a true Z-mass, obtained from combining the true muon momenta, in this mass range. The value for $\varepsilon_{m_Z}(\mu_Z^+,\mu_Z^-)$ is obtained from simulated $\mathrm{Z}\to\mu^+\mu^-$ events in which the momentum resolution of the muons was corrected for differences between data and simulation. It is approximately 0.99 with a slight dependence on the momentum resolution of the two muons in the Z-boson selection. As the momentum resolution of muons depends on the detector region, $\varepsilon_{m_Z}(\mu_Z^+,\mu_Z^-)$ was calculated separately for muons in the MS barrel region ($|\eta|<1.05$), the transition region ($1.05<|\eta|<1.7$), the MDT end-cap region ($1.7<|\eta|<2.0$) and the CSC end-cap region ($2.0<|\eta|<2.5$). The obtained values were confirmed using simulated ZZ and ZW events.

Since both $\varepsilon_{m_Z}(\mu_Z^+,\mu_Z^-)$ and the muon reconstruction efficiency depend on the muon momentum resolution their uncertainties are correlated. Furthermore while evaluating the uncertainty on $\sigma^{\mathrm{acc}}_{\mathrm{Z}+\mu}$ due to the different efficiencies it is, in principle, important to remember that the efficiency uncertainties for muons in the same p_T, η and ϕ bin are fully correlated, although both uncertainties turn out to be negligible.

The Z-boson+prompt muon cross-section

Using Equation 6.3 we measure an fiducial associated cross-section for $\mathrm{Z}\to\mu^+\mu^-$ with an additional prompt muon within the ATLAS detector acceptance of:

$$\sigma^{\mathrm{fid}}_{\mathrm{Z}+\mu} = 29.0^{+5.0}_{-9.6}(\mathrm{stat})^{+4.6}_{-1.3}(\mathrm{syst})\ \mathrm{fb}.$$

The statistical uncertainty is dominated by the uncertainty in the d_0-significance fit for μ_3 ($^{+3.7}_{-9.0}$ fb) and to a lesser extend on the Poisson uncertainty (± 3.1 fb) and the statistical uncertainty on $\frac{\mathscr{P}_Z}{\varepsilon_{\mathrm{iso}}}$ (± 1.5 fb). The relevant contributions to the systematic uncertainty are from the systematic uncertainty of $\mathscr{P}_{\mu_3}$ ($^{+4.4}_{-0.7}$ fb), the luminosity (± 1.0 fb) and the systematic uncertainty on $\frac{\mathscr{P}_Z}{\varepsilon_{\mathrm{iso}}}$ (± 0.8 fb)

6.4.3 Comparison with SM predictions.

As mentioned previously, the only SM contributions to the Z-boson plus prompt muon cross-section come from ZZ, ZW and $t\bar{t}Z$ production. The theoretical prediction from the SM for the cross-section of this subset of prompt SS dimuon events is:

$$\sigma^{\mathrm{fid}}_{\mathrm{Z}+\mu,\mathrm{SM}} = 29.2 \pm 3.4\ \mathrm{fb}.$$

The contribution of the individual processes are listed in Table 6.4.

We conclude that our measurement of the fiducial cross-section for the associative $Z\to\mu^+\mu^-$ plus prompt muon production is compatible with the SM value. The non-SM

Process	$\sigma^{\text{fid}}_{\text{Z}+\mu,\text{SM}}$ (fb)
$ZW^{\pm}$	23.6 ± 2.8
ZZ	4.6 ± 0.6
$t\bar{t}Z$	0.9 ± 0.4
Total	29.2 ± 3.4

Table 6.4: The theoretical prediction from the SM for $\sigma^{\text{fid}}_{\text{Z}+\mu,\text{SM}}$ for different processes.

contribution to this cross-section is estimated to be:

$$\sigma^{\text{fid}}_{\text{Z}+\mu,\text{non-SM}} = -0.2^{+7.6}_{-10.6} \text{ fb.}$$

6.5 Exclusion limits on the mSUGRA phase-space

It is possible to use the measured cross-section quoted in this chapter to reject some new physics models. As an example we use the 95% CL upper limit for the non-SM fiducial cross-section of SS prompt muon pairs given in Section 6.3.7 to calculate limits in the mSUGRA phase-space[7] plane defined by $A_0 = 0$ GeV, $\tan(\beta) = 10$ and $\mu > 0$.

The expected SUSY cross-section for this signature is obtained using the simulated mSUGRA sample described in Section 6.2.3. Due to the relatively small branching ratio of SUSY events producing two prompt SS muons and the limited amount of events generated (between 25000 and 10000 per SUSY point), only 0 to about 100 events pass our selection per SUSY point. The leads to non-negligible statistical uncertainties on the expected fiducial cross-sections. To reduce these uncertainties we also consider prompt electron production, thereby increasing the available Monte Carlo statistics by a factor of four. This addition is justified because in mSUGRA the decay steps producing the two SS leptons are independent and muon and electron production is nearly identical (since smuons and selectrons have the same mass).

The resulting limit on the mSUGRA phase-space plane defined by $A_0 = 0$ GeV, $\tan(\beta) = 10$ and $\mu > 0$ as a function of m_0 and $m_{\frac{1}{2}}$ is given in Figure 6.10. The region of $m_{\frac{1}{2}} < 60$ GeV is excluded independent of m_0. For low values of m_0 the lower limit on $m_{\frac{1}{2}}$ to about 150 GeV at $m_0 = 100$ GeV.

6.6 Conclusion and discussion

Using the template fitting method of Chapter 5 we were able to determine the fiducial cross-section for inclusive prompt, SS, high momentum ($p_T > 25$ GeV) muon pairs in the ATLAS detector acceptance (one muon with $|\eta| < 2.4$ due to the trigger acceptance and the other muon with $|\eta| < 2.5$). The measured cross-section of $\sigma^{\text{fid}}_{\text{SS}} = 50^{+24}_{-11}(\text{stat})^{+43}_{-20}(\text{syst})$ fb

[7] The mSUGRA phase-space is discussed in Chapter 1.

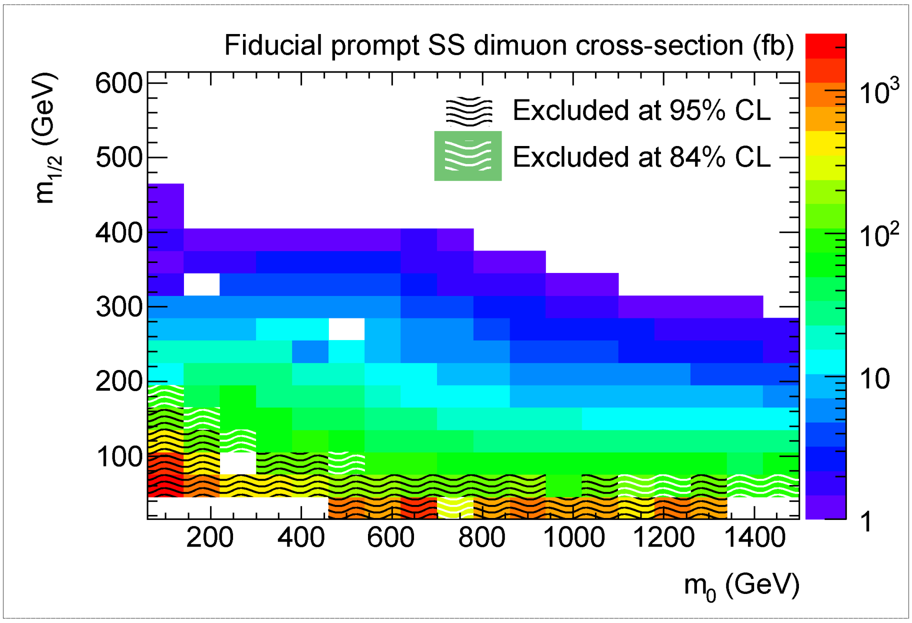

Figure 6.10: The 95% and 84% CL exclusion limit in the mSUGRA plane defined by $A_0 = 0$ GeV, $\tan(\beta) = 10$ and $\mu > 0$, as a function m_0 and $m_{\frac{1}{2}}$ obtained using the measured fiducial SS prompt dimuon cross-section measured in this chapter.

was obtained without making any assumptions on the kinematics of either signal or background events and is independent of simulated cross-sections. This value is consistent with the expected SM cross-section obtained from simulations: $\sigma^{\rm fid}_{\rm SS:SM} = 39.3 \pm 4.5$ fb.

As a wide range of new physics models, including supersymmetry, predict enhanced rates for prompt SS dimuon production at the LHC, we can use the 95% CL upper limit to the non-SM contribution of this cross-section to exclude part of the models. This limit is estimated to be 91 fb. As an example we calculated the 95% CL exclusion limit for one plane in the mSUGRA phase-space (see Figure 6.10).

6.6.1 Comparisons with other ATLAS results

The analysis used to obtain the cross-sections and exclusion limits presented in this chapter was developed to be as data-driven and model independent as possible. Although this specific analysis has not previously been performed, other methods have been used in ATLAS to calculate similar quantities. In this section we compare our analysis with other ATLAS results.

The prompt SS dimuon cross-section measurement

This specific cross-section for inclusive prompt SS dimuons in the ATLAS detector acceptance has not been measured previously. The most general similar analysis previously performed in ATLAS is the measurement of the cross-section for prompt SS dimuons for isolated muons with $p_T > 20$ GeV [58]. Apart from the isolation criteria the main difference between that analysis and the one presented in this thesis is that the former estimates the non-prompt background by extrapolating the number of events from control regions to the signal regions, while we fit the prompt content directly in the signal region. The 95% confidence level upper limit quoted in Ref. [58] for the non-SM contribution to the fiducial cross-section is 58 fb for $m_{\mu^\pm\mu^\pm} > 15$ GeV. From Figure 6.4 we can see that this invariant mass cut should have no significant effect on the cross-section. This limit is more stringent than our upper limit of 91 fb. This is primarily because the amount of background and therefore the uncertainty on this background is much smaller for isolated muons than for all muons. This upper limit of 58 fb can therefore be more closely compared to the uncertainty on the cross-section for two isolated muons obtained in this analysis, $\sigma^{\text{fid}}_{\text{SS:}\mu_1,\mu_2=\text{isolated}} = 32^{+7}_{-9}(\text{stat})^{+7}_{-2}(\text{syst})$ fb, which also shows significantly smaller uncertainties than $\sigma^{\text{fid}}_{\text{SS}}$. We use the same isolation criteria on these muons as in Ref. [58].

Despite the smaller uncertainties on the cross-section for isolated muons we chose to present our results independent of muon isolation, as the isolation of prompt muons depends heavily on the event topology, specifically on the number and distributions of jets in the event. These jet distributions, obtained from simulation, not only depend on the type of interaction (the hard scatter) but also on the amount and type of pile-up events, on the amount and hardness of parton radiation (parton showering) and on the underlying event. As discussed in Section 2.5 these last processes are non-perturbative and therefore can introduce a large uncertainty on the simulated distributions. However, it should be noted that despite these theoretical uncertainties, prompt SS dimuon cross-sections for isolated muons currently lead to more stringent limits on new physics models. For this reason we chose to only compute the limits for the mSUGRA phase-space shown in Figure 6.10. With increased luminosity this isolation independent measurement should become more competitive, as more statistics would reduce both the statistical and systematic uncertainty on the d_0-significance fits performed in this analysis. This reduction in the systematic uncertainty with increased statistics is because we would be able to bin the data in more narrow bins in closest jet p_T and σ_{d_0} (discussed in Chapter 5), thereby limiting the difference in results due to the choice in templates, which is currently the main systematic uncertainty.

The exclusion limits on the mSUGRA phase-space

Apart from the isolated SS dimuon cross-section measurement of Ref. [58] there are also a wide range of analyses in ATLAS aimed at testing more specific new physics models. Most relevant for this discussion are the analyses based on high momentum jets and large missing transverse energy that currently provides the best limits on the mSUGRA phase-space [15]. These limits, shown in Figure 1.9, are a lot stronger than the limits provided by our prompt SS dimuon cross-section. The reason for this, discussed in more detail in Chapter 1, is that the mSUGRA mass spectrum always results in signatures with high energetic jet and large missing transverse energy, which might not hold for the entire SUSY phase-space. On the other hand the branching ratio for the production of SS dimuons is probably more representative for SUSY in general.

Although more model specific analyses can produce stronger limits for specific new physics models, they might not be able to cover the full phase-space of new physics possibilities, which is why we chose to leave our analyses as model independent as possible.

The Z+prompt muon cross-section measurement

Apart from the fiducial inclusive prompt SS dimuon cross-section discussed above we also measured the cross-section for prompt SS dimuon events which are part of the Z+prompt muon cross-section. The measured fiducial cross-section for this process is $\sigma^{\mathrm{fid}}_{\mathrm{Z}+\mu} = 29.0^{+5.0}_{-9.6}(\mathrm{stat})^{+4.6}_{-1.3}(\mathrm{syst})$ fb which is in agreements with the expected SM cross-section of $\sigma^{\mathrm{fid}}_{\mathrm{Z}+\mu,\mathrm{SM}} = 29.2 \pm 3.4$ fb.

We performed this measurement mainly as a cross-check for our SS prompt dimuon cross-section measurement as most of the SM contribution to $\sigma^{\mathrm{fid}}_{\mathrm{SS}}$ comes from ZZ and $ZW^{\pm}$ pair production. However this cross-section by itself could be used to exclude new physics models, as some of these model, including supersymmetry, also increase the Z+prompt muon production cross-section.

It is important to note that the measurement performed in the chapter is not the most accurate method to determine either the ZW or ZZ cross-section in ATLAS. Analyses which use the existence of a fourth muon in ZZ events [67] or missing E_T in ZW events [68] are able to further reduce the systematic uncertainties while those using both decay channels to muons and electrons increase the available statistics by a factor close to four. However, as we are using this Z-boson plus prompt muon cross-section measurement to search for new physics, we choose to leave this analysis fully independent of the production mechanism of the third prompt muon.

6.6.2 Possible improvements

The fiducial prompt SS dimuon cross-section measurement described in this chapter uses a template method to separate the prompt muon signal from the non-prompt background. The main drawback of such template fitting methods is that they need a minimum number of events to provide reliable fit results. The main advantage is that the method is fully model independent, allowing the same analysis to be used in different signal regions. With more statistics it would therefore be possible to measure the inclusive prompt SS dimuon cross-section using this method as a function of the invariant mass of the muon pair, or separately for different event topologies, such as depending on the missing transverse energy of the event. This last suggestion would for example significantly increase the sensitivity of this method for models, such as mSUGRA, which also predict large missing transverse energy. With the integrated luminosity of data available for this thesis, the amount of selected SS muon pairs was unfortunately insufficient to perform such more specific analyses.

Appendix A

Simulated samples

A wide range of different simulated samples are used throughout this thesis. They are all listed below:

- Minimum Bias: A sample of non-diffractive minimum-bias events, generated using PYTHIA.
- JF17: A sample of simulated di-jet events. The events were selected at generator level to contain one jet with $E_T^{cell} > 17$ GeV, where E_T^{cell} is the generated transverse energy in a region of approximate size $\Delta\eta \times \Delta\phi = 0.12 \times 0.12$. The event generation was done using PYTHIA.
- $b\bar{b}/c\bar{c} \to \mu + X$: A merged sample of 10 million simulated $b\bar{b}$ and 10 million $c\bar{c}$ events, where each event contains at least one true muon with $p_T > 4$ GeV. This samples were generated by PYTHIA using the Minimum Bias generation settings and filtering events at truth level to contain a $b\bar{b}/c\bar{c}$ pair.
- $t\bar{t}$: This sample was generated using HERWIG, with the ME calculated by MC@NLO. It includes a filter at generator level guaranteeing that at least on of the W-bosons created in the decay of the top- or anti-top-quark decays to leptons.
- $b\bar{b}$: The $b\bar{b}$ sample used in this thesis is generated by PYTHIA, filtered to contain at least one true muon with $p_T > 15$ GeV.
- $c\bar{c}$: The $c\bar{c}$ sample used in this thesis is also generated by PYTHIA, filtered to contain at least one true muon with $p_T > 15$ GeV.
- $Z \to \mu\mu$: This sample is generated using HERWIG, with the ME calculated by ALPGEN. The produced Z-boson is not required to be on-shell. This sample also contains $\gamma^* \to \mu\mu$ for photon masses larger than 20 GeV
- $Z \to \tau\tau$: Similar as $Z \to \mu\mu$.
- ZZ: This sample is generated by HERWIG with the ME calculated by MC@NLO. Apart from Z-bosons this sample also contains the production of γ^* for photon

masses larger than 20 GeV. Only events where both Z/γ^*s decay to electrons or muons are included.

- ZW: Similar to ZZ, this sample is generated by Herwig with the ME calculated by MC@NLO. Apart from ZW production it also contains $\gamma^* W$ events for photon masses larger than 20 GeV. Only events where both bosons decay to electrons or muons are included. ZW^+ and ZW^- events are generated separately.

- $W^\pm W^\pm$: Same-sign W-bosons are produced in association with two jets. This $W^\pm W^\pm jj$ sample is generated by Pythia with the ME calculated by MadGraph. A filter of 20 GeV is put on both jets.

- $t\bar{t}W$: The associated production of $t\bar{t}$ with a W-boson is generated by Pythia with the ME calculated by MadGraph. This is done separately for events with zero and at least one additional high momentum parton, where the highest momentum parton is included in the ME calculation.

- $t\bar{t}Z$: The associated production of $t\bar{t}$ with a Z-boson is also generated by Pythia with the ME calculated by MadGraph. This is done separately for events with zero and at least one additional high momentum parton, where the highest momentum parton is included in the ME calculation.

- mSUGRA grid: The generation of SUSY events is done using Herwig while the SUSY masses are calculated using ISAJET7.80 [14]. This grid is defined for the mSUGRA plane with $A_0 = 0$ GeV, $\tan(\beta) = 10$ and $\mu > 0$ and consist of 350 point in the remaining m_0-$m_{\frac{1}{2}}$ plane, with m_0 varying between 100 and 1460 GeV and in steps of 80 GeV and $m_{\frac{1}{2}}$ varying between 30 and 600 GeV and in steps of 30 GeV. The number of events generated per SUSY point depends on the cross-section and lies between 25000 and 10000 events.

Bibliography

[1] S.L. Glashow, *Partial Symmetries of Weak Interactions*, Nucl. Phys. **22** (1961) 579.

[2] J. Goldstone, A. Salam and S. Weinberg, *Broken Symmetries*, Phys. Rev. **127** (1962) 965.

[3] S. Weinberg, *A Model of Leptons*, Phys. Rev. Lett. **19** (1967) 1264.

[4] The ATLAS Collaboration, *An update to the combined search for the Standard Model Higgs boson with the ATLAS detector at the LHC using up to 4.9 fb^{-1} of pp collision data at $\sqrt{s} = 7$ TeV* (2012), ATLAS-CONF-2012-019.

[5] The ATLAS Collaboration, *Combined search for the Standard Model Higgs boson using up to 4.9 fb^{-1} of pp collision data at $\sqrt{s} = 7$ TeV with the ATLAS detector at the LHC*, Phys. Lett. B **710** (2012) 49.

[6] The CMS Collaboration, *Combined results of searches for the Standard Model Higgs boson in pp collisions at $\sqrt{s} = 7$ TeV*, Phys. Lett. B **710** (2012) 26.

[7] NASA, *WMAP Cosmological Parameter Model: lcdm+sz+lens Data: wmap5*, http://lampda.gsfc.nasa.gov/product/map/dr3/params/lcdm_ sz_ lens_ wmap5.cfm.

[8] V.A. Gol'fand and E.P. Likhtman, *Extensions of the Algebra of Poincare Group Generators and Violation of P Invariance*, JETP Lett. **13** (1971) 323.

[9] D. Volkov and V.P. Akulov, *Possible Universal Neutrino Interactions*, JETP Lett. **16** (1972) 438.

[10] J. Wess and B. Zumino, *Supergauge Transformations in Four Dimensions*, Nucl. Phys. **B70** (1974) 139.

[11] P.W. Higgs, *Broken Symmetries, Massless Particles and Gauge Fields*, Phys. Rev. Lett. **12** (1964) 132.

[12] The Super-Kamiokande Collaboration, *Search for Proton Decay via $p \to e + \pi^0$ and $p \to \mu + \pi^0$ in a Large Water Cherenkov Detector*, Phys. Rev. Lett. **102** (2009) 141801.

[13] S.P. Martin, *A supersymmetry primer* (2011), arXiv:hep-ph/9709356.

[14] S.D. Protopopescu H. Bear, F.E. Paige and X. Tata, *ISAJET 7.48: A Monte Carlo event generator for* pp, $\overline{p}p$ *and* e^+e^- *interactions* (2000), arXiv:hep-ph/00001086v1.

[15] The ATLAS Collaboration, *Search for squarks and gluinos using final states with jets and missing transverse momentum with the ATLAS detector in* $\sqrt{s} = 7$ *TeV proton-proton collisions* (2011), arXiv:hep-ph/1109.6572, CERN-PH-EP-2011-145.

[16] L. Evans and P. Bryant, *LHC Machine*, Journal of Instrumentation **3** (2008) 8001.

[17] The ATLAS Collaboration, *The ATLAS experiment at the CERN Large Hadron Collider*, Journal of Instrumentation **3** (2008) 8003.

[18] The CMS Collaboration, *The CMS experiment at the CERN LHC*, Journal of Instrumentation **3** (2008) 8004.

[19] The ALICE Collaboration, *The ALICE experiment at the CERN LHC*, Journal of Instrumentation **3** (2008) 8002.

[20] The LHCb Collaboration, *The LHCb detector at the LHC*, Journal of Instrumentation **3** (2008) 8005.

[21] The ATLAS Collaboration, *Characterization of Interaction-Point Beam Parameters Using the pp Event-Vertex Distribution Reconstructed in the ATLAS Detector at the LHC* (2010), ATLAS-CONF-2010-027.

[22] The ATLAS Collaboration, *Jet energy resolution and selection efficiency to track jets from in-situ techniques with the ATLAS detector using proton-proton collisions at a center of mass energy* $\sqrt{s} = 7$ *TeV* (2010), ATLAS-CONF-2010-054.

[23] The ATLAS Collaboration, *Performance of the ATLAS Muon Trigger in p-p collisions at* $\sqrt{s} = 7$ *TeV* (2010), ATLAS-CONF-2010-095.

[24] The geant4 collaboration and S. Agostinelli, *Geant4-a simulation toolkit*, Nuclear Instruments and Methods in Physics Research A **506** (2003) 250.

[25] J. Pumplin, D.R. Stump, J. Huston, H.L. Lai, P. Nadolsky and W.K. Tung, *New generation of parton distributions with uncertainties from global QCD analysis*, JHEP **0207** (2002) 012.

[26] A. Shvertsnev and R. Thorne, *Parton distributions for LO generators*, Eur. Phys. J. C **55** (2008) 553.

[27] A.D. Martin, W.J Stirling, R.S. Thorne and G. Watt, *Parton distributions for the LHC*, Eur. Phys. J. C **63** (2009) 189.

[28] T. Sjostrand, S. Mrenna and P. Skands, *PYTHIA 6.4 Physics and Manual*, JHEP **0605** (2006) 026, arXiv:hep-ph/0603175v2.

[29] G. Corcella, I.G. Knowles, G. Marchesini, S. Moretti, K. Odagiri, P. Richardson, M.H. Seymour and B.R. Webber, *HERWIG 6.4: an event generator for Hadron Emission Reactions With Interfering Gluons (including supersymmetric processes)*, JHEP **0101** (2001) 020, arXiv:hep-ph/0011363v3, arXiv:hep-ph/0210213v2.

[30] T. Gleisberg, S. Hoeche, F. Krauss, M. Schoenherr, S. Shumann, F. Siegert and J. Winter, *Event generation with SHERPA 1.1*, JHEP **0902** (2009) 007, arXiv:hep-ph/08114622v1.

[31] M.L. Mangano, M. Moretti, F. Piccinini, R. Pittau and A. Polosa, *ALPGEN, a generator for hard multiparton processes in hadronic collisions*, JHEP **0307** (2003) 001, arXiv:hep-ph/0206293v2.

[32] J. Alwall et al., *MadGraph/MadEvent v4: The new web generation*, Nucl. Phys. B **0709** (2007) 028.

[33] S. Frixione and B.R. Webber, *Matching NLO QCD computations and parton showering simulations*, JHEP **0206** (2002) 029, arXiv:hep-ph/0204244.

[34] The ATLAS Collaboration, *Muon Reconstruction Performance* (2010), ATLAS-CONF-2010-064.

[35] N. Ruckstuhl and G. Salamanna, *Muon momentum scale and resolution measurements with inclusive muons from* $1.2\ pb^{-1}$ *of collision data at* $\sqrt{s} = 7$ *TeV* (2010), ATL-COM-PHYS-2010-708.

[36] The ATLAS Collaboration, *Commissioning of the ATLAS Muons Spectrometer with Cosmic Rays* (2010), arXiv:1006.4384v2.

[37] The ATLAS Collaboration, *Measurement of the* $W \to l\nu$ *and* $Z/\gamma \to ll$ *production cross sections in proton-proton collisions at* $\sqrt{s} = 7$ *TeV with the ATLAS detector*, JHEP **1012** (2010) 060.

[38] W. Verkerke and D. Kirkby, *The RooFit toolkit for data modelling*, http://www.slac.standford.edu/econf/C0303241/proc/papers/MOLT007.PDF.

[39] The ATLAS Collaboration, *Extraction of the prompt muon component in inclusive muons produced at* $sqrt(s)$*=7TeV* (2010), ATLAS-CONF-2010-075.

[40] The ATLAS Collaboration, *Di-muon composition in ATLAS at 7 TeV* (2011), ATLAS-CONF-2011-003.

[41] N. Ruckstuhl, *Extracting the prompt muon fraction using a template fit on the d0-significance* (2011), ATL-COM-PHYS-2011-538.

[42] J. Alwall, P. Schuster and N. Toro, *Simplified models for a first characterization of new physics at the LHC*, Phys. Rev. D **79** (2009) 075020.

[43] J.C. Pati and A. Salam, *Lepton number of the fourth ”color”*, Phys. Rev. D **10** (1974) 275.

[44] R.N. Mohapatra and J.C. Pati, *Left-right gauge symmetry and an ”isoconjugate” model of CP violation*, Phys. Rev. D **11** (1975) 566.

[45] G. Senjanovic and R.N. Mohapatra, *Exact left-right symmetry and spontaneous violation of parity*, Phys. Rev. D **12** (1975) 1502.

[46] T. Rizzo, *Doubly charged Higgs bosons and lepton-number-violation processes*, Phys. Rev. D **25** (1982) 1355.

[47] H. Georgi and M. Machacek, *Doubly charged Higgs bosons*, Nucl. Phys. B **262** (1985) 463.

[48] J.F. Gunion, R. Vega and J. Wudka, *Higgs triplets in the standard model*, Phys. Rev. D **42** (1990) 1673.

[49] J.E. Cieza Montalvo, N.V. Cortez, J. Sa Borges and M.D. Tonasse, *Searching for doubly charged Higgs bosons at the LHC in a 3-3-1 model*, Nucl. Phys. B **796** (2008) 422.

[50] N. Arkani-Hamed et al., *The minimal moose for a little Higgs*, JHEP **0208** (2002) 021.

[51] P.H. Frampton, P.Q. Hung and M. Sher, *Quarks and leptons beyond the third generation*, Phys. Rept **330** (2000) 263.

[52] S. Jung, H. Murayama, A. Pierce and J.D. Wells, *Top quark forward-backward asymmetry from new t-channel physics*, Phys. Rev. D **81** (2010) 015004.

[53] J. Cao, Z. Heng, L. Wu and J.M. Yang, *Top quark forward-backward asymmetry at the Tevatron: A comparative study in different new physics models*, Phys. Rev. D **81** (2010) 014016.

[54] D. Choudhury, R.M. Godbole, S.D. Rindani and P. Saha, *Top polarization, forward-backward asymmetry and new physics*, Phys. Rev. D **84** (2011) 014023.

[55] J. Cao, L. Wang, L. Wu and J.M. Yang, *Top quark forward-backward asymmetry, FCNC decays and like-sign pair production as a joint probe of new physics* (2011), arXiv:hep-ph/1101.4456v3.

[56] B. Bhattacherjee, S.S. Biswal and D. Ghosh, *Top quark forward-backward asymmetry at Tevatron and its implications at the LHC*, Phys. Rev. D **83** (2011) 091501.

[57] E.L. Berger, G.H. Cao, C.R. Chen, C.S. Li and H. Zhang, *Top quark forward-backward asymmetry and same-sign top quark pairs*, Phys. Rev. Lett. **106** (2011) 201801.

[58] The ATLAS Collaboration, *Search for anomalous production of prompt like-sign muon pairs and constraints on physics beyond the Standard Model with the ATLAS detector* (2011), arXiv:1201.1091, CERN-PH-EP-2011-219.

[59] The ATLAS Collaboration, *Luminosity determination in pp collisions at* $\sqrt{s} = 7$ *TeV using the ATLAS detector in 2011* (2011), ATLAS-CONF-2011-116.

[60] M. Spira W. Beenakker, R. Hopker and P.M. Zerwas, *Squark and gluino production at hadron colliders*, Nucl. Phys. B **492** (1997) 051.

[61] T.Plehn M. Spira W. Beenakker, M. Kramer and P.M. Zerwas, *Stop production at hadron colliders*, Nucl. Phys. B **515** (1998) 003.

[62] A. Kulesza and L. Motyka, *Threshold resummation for squark-antisquark and gluino-pair production at the LHC*, Phys. Rev. Lett. **102** (2009) 111802.

[63] A. Kulesza and L. Motyka, *Soft gluon resummation for the production of gluino-gluino and squark-antisquark pairs at the LHC*, Phys. Rev. D **80** (2009) 095004.

[64] M. Kramer A. Kulesza E. Laenen W. Beenakker, S. Brensing and I. Niessen, *Soft-gluon resummation for squarks and gluino hadroproduction*, JHEP **0912** (2009) 041.

[65] M. Kramer A. Kulesza E. Laenen L. Motyka W. Beenakker, S. Brensing and I. Niessen, *Squark and gluino hadroproduction*, Int. J. Mod. Phys. A **26** (2011) 2637.

[66] M. Kramer A. Kulesza E. Laenen W. Beenakker, S. Brensing and I. Niessen, *Supersymmetric top and bottom squark production at hadron colliders*, JHEP **1008** (2010) 098.

[67] The ATLAS Collaboration, *Measurement of the* ZZ *production cross section and limits on anomalous neutral triple gauge couplings in proton-proton collisions at* $\sqrt{s} = 7$ *TeV with the ATLAS detector*, Phys. Rev. Lett. **108** (2012) 041804.

[68] The ATLAS Collaboration, *Measurement of the* $W^{\pm}Z$ *production cross section and limits on anomalous triple gauge couplings in proton-proton collisions at* $\sqrt{s} = 7$ *TeV with the ATLAS detector* (2011), arXiv:hep-ph/1111.5570, CERN-PH-EP-2011-184.

Summary

All elementary particles known today and their interactions are described by the Standard Model. While some of these particles, such as electrons, are abundantly found in nature, the heavier particles of the Standard Model are unstable and decay almost immediately after production. To study these particles they first need to be created in particle collisions. This can for example be done using particle accelerators.

At present the most powerful accelerator in the world is the Large Hadron Collider (LHC) at CERN, near Geneva. It collides protons at an energy of 7 TeV and is capable of producing particles with a mass of at most a few TeV. As the heaviest Standard Model particle, the top-quark, is approximately 175 GeV (0.175 TeV), this means that the LHC can produce all Standard Model particles. Furthermore it can be used to search for new theoretical particles predicted by a variety of proposed extensions to the Standard Model. To study the produced particles the collision regions of the LHC are surrounded by detectors. In this thesis we analyse events recorded using the ATLAS detector.

Since the majority of particles, including most proposed non-Standard Model particles, decay almost immediately, only their more stable decay products reach the detector. In this thesis we have chosen to focus on one of the possible decay products, the muon. This semi-stable particle can travel up to a few hundred meters before decaying, while losing only a relatively small amount of energy when traversing materials. It is therefore the only charged particle to reach the outermost edge of the detector, making it relatively easy to identify. As muons can be produced in the decay of a wide range of different particles, they are an essential part of many analyses. In this thesis we first study the muon reconstruction performance in ATLAS during the first few months after the start-up of the LHC. We then describe two methods that can be used to classify muon contributions depending on the muon production mechanism. Finally we study events in ATLAS with two muons of equal charge in a search for physics beyond the Standard Model.

Muon reconstruction performance

Before using muons in physics analyses, it is important to know the performance of the muon reconstruction procedure in ATLAS. This not only affects the accuracy of such physics analyses, but also provides useful information and validation of the current understanding of the detector. One of the major benchmarks for determining this performance is to estimate the accuracy with which the ATLAS reconstruction software reconstructs the momentum of muons: the muon momentum resolution.

In Chapter 3 we describe a method to estimate the muon momentum resolution based on the information that muons in ATLAS are measured independently by two subdetectors: the Inner Detector and the Muon Spectrometer. As both subdetectors give an independent momentum estimate the relative difference between these measurements can be used as a measure for the momentum resolution, provided both subdetectors measured the same particle. This is the case if the muon was produced before reaching the innermost detector. Unfortunately, inclusive samples of low momentum muons, the only samples available in the first month of collision data, also contain a large fraction of muons that were produced in the decay of longer lived particles, such as pions and kaons, which often travel some distance through the detector before decaying. In these cases part of the track reconstructed by the Inner Detector was not produced by the muon, but by its parent particle, and has a different (larger) momentum than the track in the Muon Spectrometer. The measured momentum difference for these background muons therefore does not provide an accurate measure for the momentum resolution.

To separate the effect of signal muons, produced before the Inner Detector, and these background muons we study the distribution of the relative momentum difference between the Inner Detector and the Muon Spectrometer measurements and fit this distribution using separate functions to model the signal and background contributions. Two examples of such fits are shown in Figure 3.3. The momentum resolution can then be obtained from the fitted shape of the signal distribution.

Using this method we conclude that in the spring and summer of 2010 the muon momentum resolution achieved by the ATLAS experiment was close to the expected resolution for muon tracks passing through the center region of the detector. In the more forward region the difference between the obtained resolution in data and simulation was larger. This was not unexpected because, at the time, the detector was less well aligned in these forward regions, translating to a larger inaccuracy in the estimated momentum. Using the results of this analysis we were able to indicate which parts of the detector suffered the most from misalignment. This helped in obtaining a better understanding of the detector and therefore a better momentum resolution in the future. At present most of the difference in the momentum resolution between data en simulation has been corrected for.

Muon origin

A wide range of different processes can produce muons in proton-proton collisions. The vast majority of muons are either produced in the decay of b- and c-quarks, which typically travel a few millimetres before decaying, or, as discussed above, in the decay of pions and kaons. While muons produced from b- and c-quarks can be used to identify the flavour of these quarks, most analyses involving muons purely focus on muons produced directly at the interaction point, prompt muons, such as through the decay of Z- and W-bosons. It is therefore useful to be able to separate muons depending on their origin.

While it is usually not possible to determine the origin of an individual muon, by considering specific distributions it is possible to quantify the relative contribution of different muon types in general muon samples. For example, the method to estimate the muon momentum resolution mentioned above, fits the relative momentum difference between the

Inner Detector and Muon Spectrometer momentum measurements. This distribution is significantly different for muons from pion and kaon decays than for all other muons. By fitting this distribution using different templates to describe the shape of the two independent contributions, while leaving the relative normalisation of both contributions free, we can extract the ratio of muons in the sample produced in pion and kaon decays. In Chapter 4 we use this method, extended to also exploit some differences in the Inner Detector tracks, to estimate the pion and kaon contribution of di-muon events in ATLAS.

For high momentum muons, the relative contribution of muons from pion and kaon decays decreases rapidly, and we are more interested in separating prompt muons from muons produced in the decay of b-quarks, c-quarks or taus. As all these muons are produced before reaching the Inner Detector, the momentum difference between the Inner Detector and Muon Spectrometer can not be used to separate these contributions. We instead use the fact that for non-prompt muons the measured track, when extrapolated back to interaction region, does not point to the collision spot. The smallest distance between the extrapolated track and the fitted collision spot is called the impact parameter. The impact parameter significance, which is the impact parameter divided by its uncertainty, is a measure for the probability that the track originated at the interaction point. As b-quarks, c-quarks and taus have different lifetimes and therefore travel different distances before decaying, the impact parameter significance distributions of these three types of muons and prompt muons differ significantly. A template fitting method based on this parameter is therefore able to estimate the fraction of prompt muons in muon samples. This method is described and validated in Chapter 5.

Prompt same-sign muon pair cross-section

We use our knowledge on how to separate the contribution of different muon types to estimate the cross-section of events containing two prompt muons with the same electric charge, same-sign muons. According the Standard Model same-sign muon pairs can only occur through the production of at least two bosons, either a W-boson with a Z-boson or two Z-bosons[1]. While such events do occur, the corresponding cross-section is small. On the other hand, a wide range of theories for physics beyond the Standard Model predict that additional particles might result in an enhanced production rate for same-sign muon pairs at the LHC.

Using the template fitting methods described in this thesis we estimated the cross-section for prompt same-sign high momentum muons[2] in ATLAS to be:

$$\sigma_{\mathrm{SS}}^{\mathrm{fid}} = 50^{+24}_{-11}(\mathrm{stat})^{+43}_{-20}(\mathrm{syst})\ \mathrm{fb}.$$

This is in agreement with the theoretical Standard Model cross-section of

$$\sigma_{\mathrm{SS:SM}}^{\mathrm{fid}} = 39.3 \pm 4.5\ \mathrm{fb},$$

showing no evidence for physics beyond the Standard Model.

[1]The Z-bosons can also be replaced by off-shell photons.
[2]The exact selection criteria are listed in Chapter 6.

Samenvatting

Alle elementaire deeltjes die momenteel bekend zijn en hun interacties worden beschreven door het Standaard Model. Hoewel sommige van deze deeltjes, zoals het electron, in groten getale om ons heen te vinden zijn, zijn de zwaardere deeltjes van Het Standaard Model instabiel en vallen ze vrijwel meteen nadat ze geproduceerd worden uit elkaar. Om deze deeltjes te bestuderen moeten ze eerst gemaakt worden in botsingen van deeltjes. Dit kan bijvoorbeeld gedaan worden met behulp van deeltjesversnellers.

Momenteel is de Large Hadron Collider (LHC) op CERN, dichtbij Genève, de krachtigste versneller ter wereld. De LHC botst protonen op elkaar met een energie van 7 TeV en is in staat om deeltjes te produceren met massa's tot enkele TeV. Gezien het zwaarste deeltje uit het Standaard Model, de top-quark, een massa heeft van 175 GeV (0.175 TeV), betekent dit dat de LHC alle deeltjes van het Standaard Model kan produceren. Daarnaast kan de LHC worden gebruikt om te zoeken naar theoretische deeltjes die voorspeld worden door een heel aantal mogelijke uitbreidingen van het Standaard Model. Om de geproduceerde deeltjes te bestuderen, zijn de regio's rondom de botsingen in de LHC omgeven door detectoren. In dit proefschrift analyseren we botsingen geregistreerd met de ATLAS detector.

Omdat de meeste deeltjes, inclusief de meerderheid van de voorgestelde niet-Standaard Model deeltjes, vrijwel direct vervallen, bereiken enkel de stabielere vervalproducten de detector. We hebben gekozen om ons in dit proefschrift te richten op één van de mogelijke vervalproducten, het muon. Dit semi-stabiele deeltje kan tot enkele honderden meters afleggen voordat het vervalt, en verliest slechts een klein gedeelte van zijn energie terwijl het door materiaal heen beweegt. Het is dan ook het enige geladen deeltje dat de buitenste rand van de detector bereikt en daarom is het relatief makkelijk te identificeren. Omdat muonen geproduceerd kunnen worden in het verval van een breed scala aan verschillende deeltjes, zijn ze een essentieel onderdeel van veel analyses. In dit proefschrift bestuderen we eerst de muon reconstructie prestaties in ATLAS gedurende de eerste paar maanden na het opstarten van de LHC. Vervolgens beschrijven we twee methoden die gebruikt kunnen worden om de bijdrage van verschillende muon productie mechanismes te classificeren. Tenslotte bestuderen we botsingen in ATLAS met twee muonen met gelijke lading, met als doel het zoeken naar nieuwe fysica voorbij het Standaard Model.

Muon reconstructie prestaties

Voordat muonen in fysische analyses gebruikt kunnen worden, is het belangrijk om te weten hoe goed de prestaties van de muon reconstructie procedure in ATLAS zijn. Dit beïnvloed niet alleen de nauwkeurigheid van zulke fysische analyses, maar het levert ook nuttige informatie over en validatie van onze huidige kennis over de detector. Een van de belangrijkste benchmarks voor het bepalen van de prestaties is het schatten van de nauwkeurigheid waarmee de ATLAS reconstructie software de impuls van de muonen reconstrueerd: de muon impuls resolutie.

In Hoofdstuk 3 beschrijven we een methode om de muon implus resolutie te bepalen gebaseerd op het gegeven dat muonen in ATLAS onafhankelijk door twee subdetectoren worden gemeten: de Inner Detector en de Muon Spectrometer. Omdat beide subdetectoren een onafhankelijke schatting voor de impuls geven, kan het relatieve verschil tussen de twee metingen gebruikt worden als een maat voor de impuls resolutie, verondersteld dat beide subdetectoren hetzelfde deeltje hebben gemeten. Dit is het geval als het muon geproduceerd werd voordat het de binnenste detector heeft bereikt. Helaas bevat een selectie van lage impuls muonen, de enige selectie die beschikbaar was met de eerste maand aan botsingsdata, ook een grote fractie muonen die geproduceerd zijn in het verval van lang levende deeltjes, zoals pionen en kaonen, die vaak enige afstand door de detector afleggen voor ze vervallen. In deze gevallen is de baan die door de Inner Detector is gereconstrueerd niet geproduceerd door het muon, maar door zijn moederdeeltje en heeft het een andere (grotere) impuls dan de baan in de Muon Spectrometer. Het gemeten impulsverschil voor deze achtergrond-muonen levert daarom geen nauwkeurige maat voor de impuls resolutie.

Om het effect van de signaal-muonen, geproduceerd voor het bereiken van de Inner Detector, en eerdergenoemde achtergrond-muonen te scheiden, bestuderen we de verdeling van het relatieve impulsverschil tussen de metingen van de Inner Detector en de Muon Spectrometer en fitten we deze verdeling met behulp van aparte functies die de bijdragen van het signaal en van de achtergrond modelleren. Twee voorbeelden van dergelijke fits zijn te zien in Figuur 3.3. De impuls resolutie wordt verkregen uit de vorm van de signaal verdeling.

Met behulp van deze methode concluderen we dat in het voorjaar en in de zomer van 2010 de muon impuls resolutie behaald door het ATLAS experiment dicht bij de verwachte resolutie ligt, voor muon banen die door het middelste gedeelte van de detector gaan. In de voorwaartste regio was het verschil tussen de resolutie verkregen uit de data en die uit de simulaties groter. Dit is niet onverwacht, gezien op dat moment de detector in deze voorwaartste regio niet zo goed was uitgelijnd, wat leidt tot een grotere onnauwkeurigheid in de schatting van de impuls. Met behulp van de resultaten van deze analyse zijn we in staat geweest om aan te geven welke gedeeltes van de detector het meest beïnvloed werden door de foutieve uitlijning, wat hielp om de detector beter te begrijpen en wat betekent dat we in de toekomst een betere impuls resolutie kunnen behalen. Inmiddels is het grootste gedeelte van het verschil in impuls resolutie tussen data en simulaties gecorrigeerd.

Muon productie processen

Een breed scala aan verschillende processen kan muonen produceren in ATLAS. De overgrote meerderheid van de muonen worden geproduceerd of in het verval van b- en c-quarks, die zich doorgaans enkele milimeters verplaatsen alvorens te vervallen, of, zoals hierboven besproken, in het verval van pionen en kaonen. Hoewel muonen die geproduceerd zijn uit b- en c-quarks gebruikt kunnen worden om de smaak van de quarks te identificeren, richten de meeste analyses omtrent muonen zich puur op muonen die direct op het interactiepunt worden geproduceerd, de zogenaamde prompte muonen, bijvoorbeeld uit het verval van Z- en W-bosonen. Het is daarom nuttig om onderscheid te maken tussen muonen op basis van hun herkomst.

Hoewel het normaal gesproken niet mogelijk is om de herkomst van een individueel muon te bepalen, is het wel mogelijk om de relatieve bijdrage van de verschillende muon types in de algemene muon selecties te kwantificeren. Bijvoorbeeld, de methode om de muon impuls resolutie te schatten, zoals hierboven genoemd, fit het relatieve impuls verschil tussen de impuls metingen van de Inner Detector en de Muon Spectrometer. Deze verdeling is significant anders voor muonen uit het verval van pionen en kaonen dan voor alle andere muonen. Door deze verdeling te fitten met behulp van verschillende sjablonen die de vorm van de twee onafhankelijke bijdrages beschrijven, maar de relatieve normalisatie vrij laten, kunnen we de fractie van muonen in een selectie die geproduceerd zijn door verval van pionen en kaonen bepalen. In Hoofdstuk 4 gebruiken we deze methode, uitgebreid om ook gebruik te maken van verschillen tussen banen in de Inner Detector, om een schatting te maken van de bijdrage van pion en kaon verval in botsingen met twee muonen in ATLAS.

Voor muonen met een hoge impuls neemt de relatieve bijdrage van pion en kaon verval snel af en zijn we meer geïntereseerd in het scheiden van prompte muonen en muonen die geproduceerd zijn in het verval van b-quarks, c-quarks en taus. Omdat al deze muonen geproduceerd worden voordat ze de Inner Detector bereiken, kan het impuls verschil tussen de Inner Detector en de Muon Spectrometer niet worden gebruikt om deze bijdragen te scheiden. In plaats daarvan maken we gebruikt van het feit dat een gemeten baan van een niet-prompt muon, wanneer deze terug naar de interactie regio geëxtrapoleerd wordt, niet in de richting van de botsingslocatie wijst. De kleinste afstand tussen de geëxtrapoleerde baan en de botsingslocatie wordt de impact parameter genoemd. De impact parameter significantie, dat wil zeggen, de impact parameter gedeeld door zijn onzekerheid, is een maat voor de waarschijnlijkheid dat de baan is begonnen bij het interactiepunt. Omdat b-quarks, c-quarks en taus verschillende levensduren hebben en daarom verschillende afstanden afleggen alvorens te vervallen, verschillen de impact parameter significantie verdelingen van deze drie types muonen en die van prompte muonen flink. Een sjabloon fit methode gebaseerd op deze parameter kan daarom worden gebruikt om de fractie van prompte muonen te schatten. Deze methode wordt beschreven en getest in Hoofdstuk 5.

Werkzame doorsnede van prompte same-sign muonen paren

We gebruiken onze kennis over het scheiden van de bijdragen van verschillende muon types om de werkzame doorsnede van botsingen met twee prompte muonen met gelijke elektrische lading, same-sign muonen, te schatten. Volgens het Standaard Model komen same-sign muonen alleen voor bij de productie van tenminste twee bosonen, W-bosonen, Z-bosonen of off-shell fotonen, waar beide bosonen vervallen naar muonen[3]. Hoewel dergelijke botsingen plaatsvinden, is de bijbehorende werkzame doorsnede klein. Aan de andere kant is er een breed scala aan theorieën voor fysica voorbij het Standaard Model die voorspellen dat extra deeltjes mogelijk resulteren in een verhoogde productie van same-sign muonen paren in de LHC.

Gebruikmakend van de sjabloon fit methodes die in dit proefschrift zijn beschreven hebben we de werkzame doorsnede voor prompte same-sign muonen met hoge impuls[4] in ATLAS geschat op:

$$\sigma_{\mathrm{SS}}^{\mathrm{fid}} = 50^{+24}_{-11}(\mathrm{stat})^{+43}_{-20}(\mathrm{syst})\ \mathrm{fb}.$$

Dit is in overeenstemming met de theoretische werkzame doorsnede in het Standaard Model van

$$\sigma_{\mathrm{SS:SM}}^{\mathrm{fid}} = 39.3 \pm 4.5\ \mathrm{fb},$$

wat geen bewijs voor fysica voorbij het Standaard Model laat zien.

[3]Twee W-bosonen met tegenovergestelde elektrische lading kunnen niet leiden tot een paar van same-sign muonen.

[4]De precieze selectie criteria zijn genoemd in Hoofdstuk 6.

Acknowledgements

As is traditional at the end of a thesis, I would like to thank everyone who helped me get to this point. I just spent the last four and bit years doing the type of work I have always wanted to do. Overall it has been a lot of fun. This does not mean that there weren't periods of frustration and unhappiness when I was either stuck in an analysis or fed-up with writing yet another chapter. Sharing my concerns, but also the moments of triumph when things were working perfectly, with the people around me is what got me through these last few years. I would therefore like to thank everyone who had to endure me complaining or jumping around in excitement and basically to everyone who shared part of the last four years with me.

There are few people I would like to thank personally, starting with my promotor Stan Bentvelsen and my supervisor Ivo van Vulpen.

Stan, ontzettend bedankt voor je steun en inzet, vooral gedurende de laatste maanden met onze wekelijkse besprekingen. Ondanks de tijdsdruk die er speelde heb je me nooit onder druk gezet of me schuldig doen voelen als ik weer eens compleet verkeerd had ingeschat hoeveel tijd ik nodig zou hebben voor een bepaalde taak. Ongeacht hoe ik me voelde aan het begin van elke bespreking, vertrok ik altijd weer hoopvol en gemotiveerd.

Ivo, jou wou ik ook in het bijzonder bedanken. Ik had me serieus geen betere begeleider kunnen voorstellen. Je hebt er altijd voor gezorgd dat ik het meeste uit mijn promotie traject zou krijgen als ik kon, door me de vrijheid te geven onderzoeken te doen die ik zelf graag wou doen, door erop te staan dat de service tasks die ik voor ATLAS moest doen ook voor mij interssant en nuttig zouden zijn, maar ook bijvoorbeeld door te regelen dat ik op tijd een verlenging ging aanvragen en een vervolg contract zou krijgen. Sorry voor alle mails vol spellingsfouten die je in de loop der jaren hebt moeten doorworstelen :).

Guiseppe, you might not have officially been my supervisor, but I have learned a lot from you (and not just Italian swear words). Working with you was always a lot of fun and I have missed it since then. I am very happy that you agreed to be part of my committee.

I am a firm believer that to be productive it is important to enjoy going to work every day. For me that enjoyment came to a large extent from spending time with my colleagues. So to all my past and current colleagues, thank you for all the fun coffee/cola breaks, lunch breaks and borrels!

There are a few additional colleagues I would like to thank in particular. First of all my two paranymphs, John and Ido, who were there every step of the way. We started working around the same time, moved to Geneva at the same time and started writing at approximately the same time. John, Ido, jullie hebben mijn promotie traject zeker een stuk gezelliger gemaakt. Ik ben erg blij dat jullie allebei bereid zijn om naast me te staan/zitten terwijl ik het afrond.

The year I spent at CERN was work-wise very exciting, especially with the LHC just starting up. However being away from my family, friends and mostly Gideon was not always easy. A lot of that was compensated by the great company I had at CERN consisting of (among others) Ido, John, Marcel, Rikard, Ivan, Giuseppe, Lucie en Robin (sorry if I forgot to mention someone). Thanks for all the dinners and occasional game nights! An additional thanks to Marcel and Rikard. I owe this thesis to the two of you. It was during some long dicussions with you after such dinners that I came up with the main ideas behind all the analyses included in this thesis. Without the two of you (and large quantities of beer and wine) my thesis would have looked very differently.

Daniel, jouw moet ik hier natuurlijk ook even noemen. Ik heb me wel eens afgevraagd of jouw aanwezigheid op Nikhef een positive of negative invloed heeft gehad op mijn productiviteit. Het valt niet te ontkennen dat onze ”koffie pauzes” de neiging hadden een beetje lang door te lopen, en dat we ook om de pauzes heen wel erg veel tijd aan het kletsen waren. Maar ik moet ook zeggen dat in periodes waar ik niets anders moest doen dan schrijven en ik het gevoel had dat dingen niet opschoten, diezelfde pauzes één van de dingen waren die me de motivatie gaven om toch door te ploeteren. Dus bedankt voor de achievements, WWRD?s (What Whould Rodney Do?), de lange diccusies over sci-fi en natuurlijk stoeptegels :).

Buiten collega’s om zijn er nog een hoop mensen die ik dankbaar ben, om meer redenen dan ik hier op kan noemen. Ik hoop dat ik het deze mensen vaak genoeg duidelijk heb gemaakt dat ze dit al weten. Ik zal me daarom hier beperken tot het bedanken van mijn familie, Mamsk, Yv, Kar, maar ook Karin, Jan en Veron, voor hun steun en liefde en mijn naaste vrienden, Mark, Ilaan, Maaike, Ernst en Nora voor alle gezelligheid. Bedankt Vincent en natuurlijk Esther voor de prachtige kaft!

Gideon, je valt zowel onder familie als vrienden en zoveel meer. Hoewel je dit al weet wil ik je nogmaals bedanken voor alles wat je voor me hebt gedaan om dit proefschrift mogelijk te maken. Van nooit moeilijk doen over de ”Year of Hell” tot het regelen van zoveel dingen gedurende de laatste maanden zoals de printer, hoofdstukken nakijken en zoveel meer. Thanks for keeping me sane.

Thanks again to everyone,

Nicole, 17-05-2012